Power Control of Virtual Oscillator Controlled Inverters in Microgrids

Muhammad Ali

A thesis submitted in fulfillment of the requirements for the degree of

Doctor of Philosophy

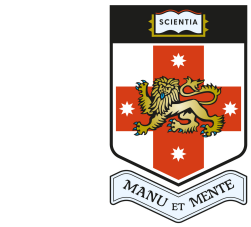

UNSW
SYDNEY

School of Electrical Engineering and Telecommunications

Faculty of Engineering

The University of New South Wales

September 2020

Thesis/Dissertation Sheet

Surname/Family Name	:	**ALI**
Given Name/s	:	**MUHAMMAD**
Abbreviation for degree as given in the University calendar	:	**PhD**
Faculty	:	**Engineering**
School	:	**Electrical Engineering and Telecommunications**
Thesis Title	:	**Power Control of Virtual Oscillator Controlled Inverters in Microgrids**

Abstract

This thesis focuses on power control of multiple parallel-connected virtual oscillator-controlled inverters in an islanded microgrid. The proposed power dispatch technique simultaneously regulates both the active and reactive power of multiple parallel-connected virtual oscillator-controlled inverters. The proposed technique enables better energy source utilisation, increased efficiency, and reduced line losses and stress on the distribution network. The control laws are derived, and power security constraints are presented to determine the feasible operating region. Moreover, a filter and line parameter design procedure is discussed for non-dispatched inverters to share the power demand proportionally. The local stability of the system with 1-D manifold of equilibria is also established.

The existing actual and averaged VOC models do not take into account the inverter non-linearities, including the voltage loss/gain due to the dead-time, and semi-conductor voltage-drop. Considering this, secondary voltage and current control loops are proposed to compensate for these unmodelled inverter non-linearities. Experimental results demonstrate that the proposed secondary control loops enable the virtual oscillator-controlled inverters to follow the desired droop-characteristics.

Moreover, in contrast to the existing literature, a new version of the averaged VOC model is derived for inverters with current feedback after the output *LC/LCL* filter. The corresponding VOC parameter design procedure is presented. Further, the proposed power dispatch technique is extended to this new version of averaged VOC dynamics. The updated control laws and power security constraints are derived to determine the feasible operating region. Simulation results demonstrate that the proposed new version of averaged VOC model more accurately predicts the actual VOC dynamics than the existing averaged VOC model for an inverter with current feedback after the output *LC/LCL* filter.

Finally, a system of heterogeneously controlled inverters with two different types of control techniques: i) virtual oscillator control and ii) droop control is considered. It is demonstrated that the two heterogeneous inverter controllers can be designed to share the power proportionally. Further, the effects of VOC design parameter ε on the system's harmonic profile and transient response are investigated.

The proposed research work demonstrates the significance and potential of dispatchable inverter control techniques for microgrids powered by distributed energy resources.

FOR OFFICE USE ONLY Date of completion of requirements for Award:

ORIGINALITY STATEMENT

‘I hereby declare that this submission is my own work and to the best of my knowledge it contains no materials previously published or written by another person, or substantial proportions of material which have been accepted for the award of any other degree or diploma at UNSW or any other educational institution, except where due acknowledgement is made in the thesis. Any contribution made to the research by others, with whom I have worked at UNSW or elsewhere, is explicitly acknowledged in the thesis. I also declare that the intellectual content of this thesis is the product of my own work, except to the extent that assistance from others in the project's design and conception or in style, presentation and linguistic expression is acknowledged.’

Signed …….....

Date September 13, 2020 …….....

COPYRIGHT STATEMENT

Signed ……

Date September 13, 2020 ……

AUTHENTICITY STATEMENT

Signed ……

Date September 13, 2020 ……

INCLUSION OF PUBLICATIONS STATEMENT

UNSW is supportive of candidates publishing their research results during their candidature as detailed in the UNSW Thesis Examination Procedure.

Publications can be used in their thesis in lieu of a Chapter if:

- The student contributed greater than 50% of the content in the publication and is the "primary author", i.e. the student was responsible primarily for the planning, execution and preparation of the work for publication
- The student has approval to include the publication in their thesis in lieu of a Chapter from their supervisor and Postgraduate Coordinator.
- The publication is not subject to any obligations or contractual agreements with a third party that would constrain its inclusion in the thesis

Please indicate whether this thesis contains published material or not.

☐ *This thesis contains no publications, either published or submitted for publication*

☒ *Some of the work described in this thesis has been published and it has been documented in the relevant Chapters with acknowledgement*

☐ *This thesis has publications (either published or submitted for publication) incorporated into it in lieu of a chapter and the details are presented below*

CANDIDATE'S DECLARATION

I declare that:

- I have complied with the Thesis Examination Procedure
- where I have used a publication in lieu of a Chapter, the listed publication(s) below meet(s) the requirements to be included in the thesis.

Name	Signature	Date
Muhammad Ali		September 13, 2020

This thesis is dedicated to
my parents
for their love and support.

Abstract

This thesis focuses on the power control of multiple parallel-connected virtual oscillator-controlled inverters in an islanded microgrid. The proposed power dispatch technique can simultaneously regulate both the active and reactive power of multiple parallel-connected virtual oscillator-controlled inverters. The proposed technique enables better energy source utilisation, increased efficiency, and reduced line losses and stress on the distribution network. The control laws are derived to determine the control inputs corresponding to a particular power set-point for each dispatched inverter. Further, power security constraints are presented to determine the feasible operating region. Using these security constraints, it can be determined a-priori if a particular power set-point can be achieved. In order to determine the control inputs and feasible operating region, a numerical iterative method is proposed to solve the non-linear power flow equations with the virtual oscillator controller (VOC) dynamics included. Moreover, a filter and line parameter design procedure is discussed for non-dispatched inverters to share the remaining power demand proportionally. The local stability of the system with 1-D manifold of equilibria is also established. The proposed technique is validated through simulation and experimental results for a number of power dispatch scenarios and load transients.

The existing actual and averaged VOC models do not take into account the inverter non-linearities, including the voltage loss/gain, due to the dead-time and semi-conductor voltage-drop present in an inverter. Considering this, inner voltage and current control loops are proposed to compensate for these unmodelled inverter non-linearities. Experimental results demonstrate that the proposed inner control loops enable the virtual oscillator-controlled inverters to follow the desired droop-characteristics and to minimise the mismatch in the control inputs between the simulation and experimental results for power dispatch.

Moreover, the existing averaged VOC model either does not take into account inverters with current feedback after the output LC/LCL filter or assumes the output filter to be inductive only. In order to address this limitation, a new version of the averaged VOC model is derived, taking into account the current feedback after

the output LC/LCL filter. The corresponding VOC parameter design procedure is also presented. Further, the proposed power dispatch technique is extended to this new version of averaged VOC dynamics, and updated control laws are derived. In order to determine the feasible operating region, updated power security constraints are also derived. Simulation results demonstrate that the proposed new version of the averaged VOC model more accurately predicts the actual VOC dynamics than the existing averaged VOC model for an inverter with current feedback after the output LC/LCL filter.

Finally, a system of heterogeneously controlled inverters with two different types of control techniques: i) virtual oscillator control and ii) droop control, is considered. It is demonstrated that the two heterogeneous inverter controllers can be designed to share the power proportionally. Further, the effects of VOC design parameter ϵ on the system's harmonic profile and transient response are investigated. The proposed control strategy is validated through simulation results for synchronisation and power sharing capability, and source and load transients.

The proposed research work demonstrates the significance and potential of the dispatchable inverter control techniques for microgrids powered by distributed energy resources.

List of Publications

This thesis is based on the following published, accepted and under review journal articles and conference papers.

1. Journal Articles

1.1 **M. Ali**, J. Li, L. Callegaro, H. I. Nurdin, and J. E. Fletcher, "Regulation of active and reactive power of a virtual oscillator controlled inverter," *IET Generation, Transmission & Distribution*, vol. 14, no. 1, pp. 62–69, 2019. (from Chapter 3)

1.2 **M. Ali**, H. I. Nurdin, and J. E. Fletcher, "Dispatchable virtual oscillator control for single-phase islanded inverters: Analysis and experiments," to appear in *IEEE Transactions on Industrial Electronics*, [Online] Available: doi: 10.1109/TIE.2020.2991996. (from Chapter 4)

2. Conference Papers

2.1 **M. Ali**, H. I. Nurdin, and J. E. Fletcher, "Output power regulation of a virtual oscillator controlled inverter," in *2018 IEEE 18th International Power Electronics and Motion Control Conference (PEMC)*, pp. 1085–1090, IEEE, 2018. (from Chapter 3)

2.2 **M. Ali**, H. I. Nurdin, and J. E. Fletcher, "Simultaneous regulation of active and reactive output power of parallel-connected virtual oscillator controlled inverters," in *IECON 2018-44th Annual Conference of the IEEE Industrial Electronics Society*, pp. 4051–4056, IEEE, 2018. (from Chapter 4)

2.3 **M. Ali**, A. Sahoo, H. I. Nurdin, J. Ravishankar, and J. E. Fletcher, "On the

power sharing dynamics of parallel-connected virtual oscillator-controlled and droop-controlled inverters in an ac microgrid," in *IECON 2019-45th Annual Conference of the IEEE Industrial Electronics Society*, vol. 1, pp. 3931–3936, IEEE, 2019. (from Chapter 7)

2.4 **M. Ali**, H. I. Nurdin, and J. E. Fletcher, "Synthesizing averaged virtual oscillator dynamics to control inverters with an output lcl filter," accepted in *IECON 2020-46th Annual Conference of the IEEE Industrial Electronics Society*, IEEE, 2020. (from Chapter 5)

Acknowledgements

My three and a half years at UNSW evolved around a lot of beautiful people who kept me motivated, positively influenced my thinking, and assisted and advised me along the PhD pathway that concluded with the submission of this thesis. I am really grateful to all these people who made this journey pleasant and momentous.

First of all, I would like to sincerely thank Professor John E. Fletcher, my primary supervisor, and Dr. Hendra I. Nurdin, my joint supervisor, for their continual guidance, technical support, dedicated supervision and encouragement throughout my PhD studies at UNSW. I really appreciated the way they demonstrated how to be a good researcher to me through their critical thinking approach, rigorous analysis and arguments, precise and coherent writing skills, and determination for their persistent research. Further, I would like to thank my supervisors for their critical feedback and proof reading of my published research work. I am hopeful that my relationship will continue with the supervisors.

I would also like to thank the A. W. Tyree Foundation for their funding contributions to support my PhD research work. Further, I would like to thank the Australian Government for partially supporting my research work through the Australian Research Council's Discovery Projects Funding Scheme under Project DP180103200. The views expressed herein are those of the authors and are not necessarily those of the Australian Government or Australian Research Council.

Furthermore, I would like to thank the School of Electrical Engineering and Telecommunications and UNSW for providing me this exceptional opportunity with an outstanding learning environment and state-of-the-art resources to conduct the research work during my doctoral studies. I also enjoyed the amazing opportunity to work as a Casual Academic during my PhD studies at UNSW. This helped me in my professional development and in developing my teaching skills in an academic setting.

I would like to thank Mr. Jiacheng Li, Dr. Leonardo Callegaro and Mr. Baburaj Karanayil for their guidance and technical assistance in progressing my familiarity with the Renewable Energy and Microgrid Research Lab in the Tyree Energy Technologies Building at UNSW. I would also like to extend my appreciation to Dr. Zhan Shi for the productive discussions we had on the research challenges.

I had an awesome opportunity to collaborate with my talented colleagues to carry out the research activities and publish the research findings while working towards the completion of my PhD studies. I would like to thank the co-authors of my publication [1], Mr. Jiacheng Li and Dr. Leonardo Callegaro, for their technical assistance and help in the development of a microgrid prototype for conducting the experiments. Further, I would like to acknowledge the co-authors of my publication [2], Mr. Animesh K. Sahoo and his PhD supervisor, Associate Professor Jayashri Ravishankar, for working on the droop control part of the publication.

I would like to thank my loving and wonderful PhD colleagues Dr. Saad Irtza, Mr. Jawad Ahmed, Mr. Sanaullah, Mr. Farhan Ahmad, Dr. Tariq Nazir, Mr. Muhammad Talal, Mr. Awais Ahmad, Mr. Animesh K. Sahoo and Mr. Ayyoob Hamza for productive and relaxing tea/coffee breaks during which we discussed our professional careers, research activities and hobbies.

I would also like to thank my caring UNSW and Sydney friends who were always there to support me during the bad times and divert my attention when I most needed it throughout the journey of my PhD. Moreover, I would like to thank them for the fun-filled cherished moments we had together and making them memorable life events.

Finally, I would like to express my deepest gratitude to my parents, especially my mother, for her continual support, encouragement and motivation during the tough times of my doctoral studies.

Contents

List of Figures

List of Tables

Nomenclature

$\Re\{.\}$	The real part of a complex number $\{.\}$
$\bar{(.)}$	The complex conjugate of the number $(.)$
$\jmath$	$\sqrt{-1}$
$\mathbb{R}$	The set of real numbers
$\mathbb{R}^n$	A real coordinate space of dimension n
$\mathbb{R}_+$	The set of positive real numbers
$\mathbb{Z}$	The set of integers
$\mathbb{Z}_{\geq 0}$	The set of non-negative integers
$\otimes$	Kronecker product
$\overline{(.)}$	The ac-cycle averaged value of the variable $(.)$
$\overrightarrow{(.)}$	The phasor associated with a time-domain variable $(.)$
$\searrow$	The decrease in variable from an initial positive value towards zero

Acronyms

AC	Alternative Current
DC	Direct Current
DSP	Digital Signal Processor
DSTATCOM	Distributed Static Reactive Power Compensator
dVOC	dispatchable VirtuaI Oscillator Control
IEEE	Institute of Electrical and Eletronics Engineering
IET	Institute of Engineering and Technology
IGBT	Insulated Gate Bipolar Transistor
MPP	Maximum Power Point
MPPT	Maximum Power Point Tracking
ODE	Ordinary Differential Equation
PCC	Point of Common Coupling
PI	Proportional Integral
PLL	Phase-Locked Loop
PR	Proportional-Resonant
PV	Photo-voltaic
PWM	Pulse Width Modulation
RES	Renewable Energy Source
RMS	Root Mean Square
ROCOF	Rate of Change of Frequency
SOGI	Second Order Generalised Integrator
SOS	Sum-of-Squares

THD	Total Harmonic Distortion
TI	Texas Instruments
uVOC	unified Virtual Oscillator Control
VO	Virtual Oscillator
VOC	VirtuaI Oscillator Controller
VSG	Virtual Synchronous Generator
VSI	Voltage Source Inverter

Chapter 1

Introduction

Considering the impact of global warming and efforts to reduce dependence on fossil fuels, the world is increasingly moving towards renewable energy sources (RESs). Being green and environmentally friendly, renewable energy source integration into the power system has increased tremendously over the past few years. The continual increase in the penetration of renewable energy sources into the power system has resulted in the need for intelligent and efficient control strategies to better utilise the available energy sources. With advanced control strategies capable of power dispatch, and smart load flow planning, the system's efficiency can be increased with reduced line losses and stress on the distribution network.

Microgrids have gained a lot of attention as a power grid concept for remote and rural communities [3–6]. Microgrids rely on locally available renewable energy sources and can be tied to a conventional power grid. A microgrid saves the cost associated with long transmission lines for the remote areas and enhances the system's reliability through multiple distributed energy generation sources. There exists a number of inverter control techniques for microgrids including conventional droop control [7–11], proportional-resonant (PR) control [12–15] and recently proposed, virtual oscillator control (VOC) [16–20]. The existing control techniques can be used to regulate the system's voltage and frequency within the desired range, and

enable the inverters to share power proportional to their power ratings.

The high penetration of renewable energy sources, intermittent by nature and with low inertia, into the power systems over the past few years has necessitated the development of advanced inverter control techniques to control and stabilise these renewable energy sources with varying dynamical behaviour [21–27]. Dispatchable generation is one of the main challenges (e.g. reduced inertia, harmonic distortion, voltage and frequency stability [28–30]) associated with a microgrid i.e. the inverter control techniques should be advanced enough to independently regulate the output power of each energy source present in the system. Unfortunately, most of the existing inverter control techniques lack this capability [7–20].

With the increased penetration of renewable energy sources, proportional power sharing is not always desirable [1, 31–33]. There are a number of factors behind the motivation of dispatchable generation. For example, solar photo-voltaic panels should be utilised at maximum capacity when it is sunny. Similarly, maximum power should be extracted from the wind turbines when it is windy. This helps in better energy source utilisation and enhances the efficiency of the overall system. Another important aspect is to fulfil the load demand from the nearest generation source. This has a significant impact on reducing line losses and stress on the distribution network.

1.1 Research Motivations and Objectives

The major motivations and objectives behind the reported research work in this thesis are based on the following knowledge gaps that are identified from the literature review in Chapter 2.

1.1.1 Knowledge Gap 1

1.1.1.1 Problem Statement

The first problem concerns lack of power dispatch capability in most of the existing virtual oscillator based inverter control techniques to simultaneously regulate both the active and reactive output power of multiple parallel-connected inverters and achieve the desired power set-points in a microgrid.

Dispatchable generation has become of vital importance with the increased integration of renewable energy sources in the power system [1, 31–33]. Unlike conventional energy sources (burning fossil fuels, one of the main sources of green-house gas emissions), proportional power sharing between the generation sources may not always be desirable. Most of the existing virtual oscillator based inverter control techniques lack this capability and there exists a knowledge gap for dispatchable inverter control techniques as reviewed in Chapter 2.

The research objectives and main contributions of the proposed research work in this thesis relevant to this problem statement as follow.

1.1.1.2 Research Objectives

A dispatchable inverter control technique is proposed to simultaneously regulate both the active and reactive output power of multiple parallel-connected virtual oscillator-controlled inverters in an islanded microgrid. The output power is regulated for m-controlled inverters while the remaining n-uncontrolled inverters share the power proportionally in a system of $m+n$ parallel-connected inverters to a constant impedance or/and constant power load. The output power is regulated by tuning the current and voltage gains of the virtual oscillator-controlled inverters using the PI controllers according to the desired power set-points.

1.1.2 Knowledge Gap 2

1.1.2.1 Problem Statement

The problem is lack of power security constraints defining the feasible operating region, and control laws to achieve the desired power set-points in case of dispatchable generation for virtual oscillator-controlled inverters.

When we talk about dispatchable generation, we should be able to determine the power security constraints defining the feasible power set-points that can be achieved by parallel-connected virtual oscillator-controlled inverters in a power system. Further, the existence of control laws is crucial to determine the controller parameters corresponding to the desired power set-points. There exists a knowledge gap in specifying the feasible operating region for the virtual oscillator-controlled inverters.

The research objectives and main contributions of the proposed research work in this thesis relevant to this problem statement are as follow.

1.1.2.2 Research Objectives

A set of power security constraints is derived to determine the feasible operating region. Dispatchable generation requires the knowledge of achievable power set-points a-priori in order to plan the optimal power generation and load flow. In addition to power security constraints, the control laws are proposed to determine the control parameters corresponding to the desired power set-points. An iterative numerical method is proposed to solve the load flow analysis including the virtual oscillator controller dynamics to determine the feasibility of a particular power set-point, and corresponding control parameters.

1.1.3 Knowledge Gap 3

1.1.3.1 Problem Statement

The problem is lack of a compensation technique to nullify the effects of virtual oscillator-controlled inverter non-linearities including the voltage loss/gain at every switching cycle due to the dead-time, semi-conductor voltage-drop, and inverter side filter inductor voltage-drop. These unmodelled non-linearities avoid the virtual oscillator-controlled inverters to follow the desired embedded droop-characteristics. Further, the existing virtual oscillator control literature does not take into account the inverters with current feedback after the output LC/LCL filter.

The existing actual and average VOC models do not take into account the inverter non-linearities including the voltage loss/gain at each switching cycle due to the dead-time, and semi-conductor voltage-drop that varies as a function of device conduction current. Further, the virtual oscillator controller does not take the output voltage as a feedback. This results in the voltage appearing at the output filter capacitor to be different from the modulation signal being generated by the virtual oscillator controller and prevents the inverter from following the desired embedded drop-characteristics. Moreover, while dispatching the virtual oscillator-controlled inverters, these non-linearities result in an offset error in the control inputs between the simulation and experimental results, as discussed in Chapter 4. A knowledge gap exists for a compensation technique that can be used to avoid these effects due to the virtual oscillator-controlled inverter non-linearities.

In addition to above, the existing averaged VOC model [19] is derived assuming the current feedback before the output LC/LCL filter or assuming the output filter is inductive only. In contrast, this is not the case for practical inverters in general. An output LC/LCL filter is always considered an integral part of most of the inverters. Further, the current feedback before the output LC/LCL filter contains a

lot of switching harmonics. There exists a knowledge gap to consider the inverter output LC/LCL filter while deriving the averaged VOC model so that the inverter's behaviour can be analysed more precisely when there is current feedback after the output LC/LCL filter with fewer harmonics as compared to the current feedback before the output LC/LCL filter.

The research objectives and main contributions of the proposed research work in this thesis that are relevant to this problem statement are as follow.

1.1.3.2 Research Objectives

In order to compensate for the virtual oscillator-controlled inverter non-linearities including the voltage loss/gain at every switching cycle due to the dead-time, semiconductor voltage-drop and inverter side filter inductor voltage-drop, inner voltage and current control loops are proposed. These inner control loops compensate for the virtual oscillator-controlled inverter non-linearities and enable the inverters to follow the desired embedded droop-characteristics. Further, a new version of averaged VOC dynamics is derived for an inverter with current feedback after the output LC/LCL filter. The proposed averaged VOC model takes into account the effects of output LC/LCL filter and predicts the actual virtual oscillator dynamics more accurately than the existing averaged VOC model.

1.1.4 Knowledge Gap 4

1.1.4.1 Problem Statement

The problem is lack of research work on microgrids with heterogeneously controlled inverters and to enable optimal power sharing between these inverters.

With the increased penetration of renewable energy sources, the inverters in a power

system are not necessarily to be controlled using the same control technique. Unfortunately, most of the existing inverter control literature considers all the inverters present in the system to be controlled using the same control technique. There exists a knowledge gap to address the systems with inverters controlled using heterogeneous control techniques, and investigating a system parameter design procedure to make these heterogeneously controlled inverters work in parallel while sharing the load demand optimally.

The research objectives and main contributions of the proposed research work in this thesis relevant to this problem statement are as follow.

1.1.4.2 Research Objectives

A system of heterogeneously controlled inverters is investigated. Two types of inverter control techniques, including the droop control and the virtual oscillator control, are considered. It is demonstrated that by properly designing the controller parameters for both of the inverter control techniques, proportional power sharing between these inverters can be achieved.

1.2 Thesis Organisation

The thesis is organised into eight chapters. A brief description of these chapters is as follows.

1.2.1 Chapter 1: Introduction

In this chapter, an overview of the problem statements and research motivations is presented. The knowledge gaps are identified, and the major contributions are linked to these knowledge gaps. Further, the thesis outline is presented at the end

with a brief description of each chapter.

1.2.2 Chapter 2: Literature Review

This chapter starts with an overview of a microgrid, its modes of operation, and the potential benefits and challenges associated with it. The existing inverter control techniques for parallel-connected inverters in a microgrid to regulate the system's voltage and frequency are discussed. A brief overview of the advanced control techniques to overcome the challenges of accurate reactive power sharing and complex line impedance is also presented. Moreover, the existing control hierarchy including primary, secondary and tertiary control loops is presented. In addition to that, the existing literature on power flow analysis and determining the feasible operating region of a power system is discussed. The recently proposed virtual oscillator control (based on the Van der Pol oscillator) that is the main focus of this thesis is presented and analysed in detail. The virtual oscillator control structures, averaged model, parameter design procedure, synchronisation conditions, and the existing literature on the dispatchable virtual oscillator control are presented and compared with our proposed dispatchable inverter control technique. Some other versions of the virtual oscillator, including oscillators with dead-zone non-linearity and oscillators with a pure sinusoidal output (without the harmonic components), are also presented. Moreover, the sum-of-squares technique used to establish the system's stability by constructing a polynomial Lyapunov function, and center manifold theory to analyse the stability of systems with a manifold of equilibria, are discussed.

1.2.3 Chapter 3: Regulation of Active and Reactive Power of a Virtual Oscillator-Controlled Inverter

This chapter proposes a dispatchable inverter control technique for an islanded inverter connected to an RL load. The output power is dispatched by tuning the current feedback gain using a PI controller. Local stability of the system is investigated using the system linearisation and eigenvalues analysis. The constraints are derived on the system parameters which ensures the local stability of the system under parametric variations. Moreover, the global stability of the system is determined by constructing a polynomial Lyapunov function using the sum-of-squares technique for a particular choice of power set-point. The proposed dispatchable inverter control technique and analytical analysis are validated through the simulation and experimental results for a number of active and reactive power dispatch scenarios.

This chapter is based on conference paper [31] and journal article [1]. This chapter addresses Knowledge Gap 1.1.1.

1.2.4 Chapter 4: Dispatchable Virtual Oscillator Control for Single-Phase Islanded Inverters: Analysis and Experiments

In this chapter, the power dispatch technique presented in Chapter 3 is extended to a general case of m-controlled and n-uncontrolled inverters in a system of parallel-connected $m + n$ virtual oscillator-controlled inverters. The power is dispatched for the m-controlled inverters according to the desired power set-points for each controlled inverter while the remaining n-uncontrolled inverters share the power proportionally. In contrast to Chapter 3, the simultaneous regulation of both the active and reactive power is achieved by tuning both the current and voltage gains

of the virtual oscillator controller. In order to tune the current and voltage gains, two PI controllers are used for each controlled inverter.

In order to plan the optimal operation of a power grid with dispatchable energy generation sources, knowledge of feasible operating region is of vital importance. A set of power security constraints is derived defining the feasible power set-points that can be achieved with the proposed power dispatch technique. Using these constraints, it can be determined a-priori if a particular power set-point is achievable or not. An iterative numerical method is developed including the VOC dynamics to solve the load flow analysis and determine the feasible operating region. The control laws are also presented to determine the control inputs corresponding to a particular power set-point. Further, a line and filter parameter design procedure is discussed to enable the n-uncontrolled inverters to share the power proportionally. The proposed power dispatch technique is validated through simulation and experimental results for a number of power dispatch scenarios, load transients and security constraint violations.

This chapter is based on conference paper [32] and journal article [33]. This chapter addresses the Knowledge Gap 1.1.1 and Knowledge Gap 1.1.2.

1.2.5 Chapter 5: Synthesising Averaged Virtual Oscillator Dynamics to Control Islanded Inverters with an Output *LCL* Filter

This chapter presents a new version of averaged VOC dynamics with current feedback after the output LC/LCL filter (see Appendix A for a detailed derivation). The existing VOC model either assumes the current feedback before the output LC/LCL filter or assumes the filter to be inductive only. A VOC parameter design procedure is presented based on the proposed new version of averaged VOC dynamics to enable

the virtual oscillator-controlled inverter to follow the desired droop-characteristics, and maintain the output voltage and frequency with the desired range. Moreover, the dispatchable inverter control technique proposed in Chapter 4 is extended to this new version of averaged VOC dynamics, and corresponding control laws and power security constraints (to determine the feasible operating region) are derived. The proposed new version of averaged VOC dynamics is validated through simulation results for a number of scenarios. Further, the stability of the high voltage solution of the proposed new version of averaged VOC dynamics is established in Appendix B.

This chapter is based on conference paper [34]. This chapter partially addresses the Knowledge Gap 1.1.3.

1.2.6 Chapter 6: Inner Control Loops to Compensate for Inverter Non-linearities Occurring in Virtual Oscillator Controlled Inverters

This chapter proposes inner voltage and current control loops to compensate for the inverter non-linearities including voltage loss/gain at each switching cycle due to the dead-time, semi-conductor voltage-drop, and inverter side filter inductor voltage-drop. Neither the existing actual or the averaged VOC models takes into account these inverter non-linearities. As a result, the virtual oscillator-controlled inverter does not exhibit the desired embedded droop-characteristics. The proposed inner control loops enable the virtual oscillator-controlled inverter to overcome these non-linearities and generate the desired voltage at the output LC/LCL filter capacitor according to the modulation signal generated by the virtual oscillator controller. Further, these inner control loops minimise the steady-state offset error in the control inputs between the simulation and experimental results, as discussed in Chapter 4. The proposed inner voltage and current control loops to compensate for the inverter

non-linearities are validated through simulation and experimental results for a number of scenarios including black-start operation, synchronisation and power sharing capability, verifying the embedded droop-characteristics, and power dispatch.

This chapter partially addresses the Knowledge Gap 1.1.3.

1.2.7 Chapter 7: Power Sharing Dynamics of Parallel Connected Virtual Oscillator Controlled and Droop Controlled Inverters in an AC Microgrid

This chapter investigates a system of heterogeneously controlled inverters. The inverters are controlled using two different control techniques including droop control and virtual oscillator control. It is demonstrated that the two heterogeneously controlled inverters can be made to work in parallel and to share the power proportionally if the controller parameters are designed properly. The parallel operation of heterogeneously controlled inverters is validated through simulation results for a number of scenarios demonstrating synchronisation capability and system's response under source and load transients.

This chapter is based on conference paper [2]. This chapter addresses the Knowledge Gap 1.1.4.

1.2.8 Chapter 8: Conclusion and Future Directions

This chapter concludes the thesis while highlighting the significance of the proposed research work and outlines the potential future research work.

1.3 Conclusion

The problem statements and research motivations are presented. Based on the existing background literature, the knowledge gaps are identified. The major contributions of this thesis are then outlined and linked with the identified knowledge gaps. Finally, the chapter is concluded with a brief description of each thesis chapter.

Chapter 2

Literature Review

This chapter reviews the basic concept of microgrids, its associated benefits and challenges. The motivations behind the rapid adoption of this concept and potential benefits are discussed. Moreover, the existing inverter control techniques for microgrids are reviewed. The existing hierarchical control layers including primary, secondary and tertiary control loops are reviewed. Further, the existing techniques to analyse the local as well as global stability of the system are discussed. The literature on power flow analysis, and on the existence and uniqueness of power flow equations solution is also reviewed.

2.1 Microgrids

In remote locations, where electrical power is not available through conventional power grids, a localised grid concept is introduced known as microgrids. A microgrid utilises locally available renewable and conventional energy sources to produce electricity, and fulfil the load requirements. Like conventional power grids, a microgrid consists of energy generation sources, loads, energy storage elements and a distribution system. However, most of the sources and loads are in close proximity to each other. The concept of local energy generation encourages the use of renew-

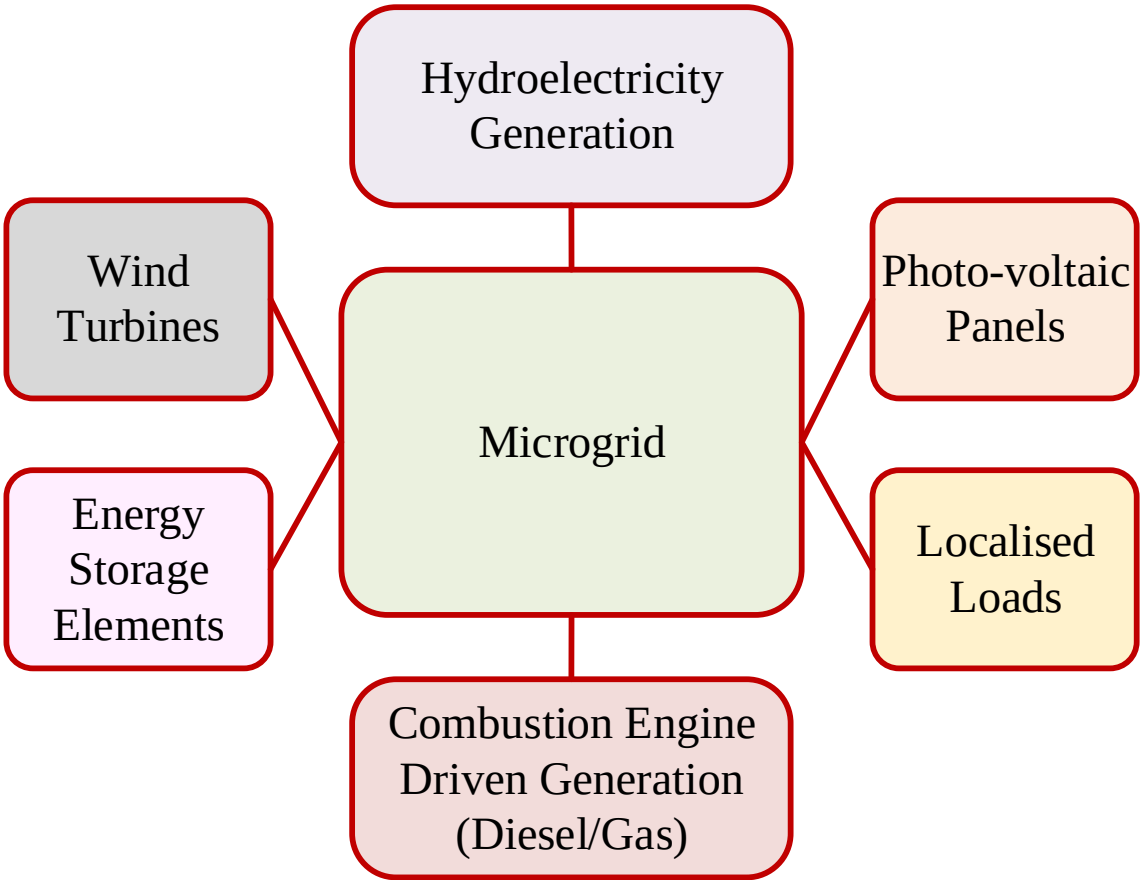

Figure 2.1: A typical microgrid representation consisting of locally available energy sources, energy storage units, household and commercial loads, and energy distribution system.

able energy sources (RESs) including photo-voltaic (PV) panels, wind turbines, tidal energy, geo-thermal energy, etc [6]. Fig. 2.1 shows a typical microgrid structure.

2.1.1 Modes of Operation

A microgrid can operate in two modes. The first mode is the islanding mode in which a microgrid operates independently of the conventional power grid, whereas in the second mode, the microgrid operates in parallel with the conventional power grid. The point of interconnection between the microgrid and conventional power system is called the point of common coupling (PCC) and is illustrated in Fig. 2.2. A microgrid can either absorb or deliver power while operating in parallel with the conventional power system, depending on the load requirements.

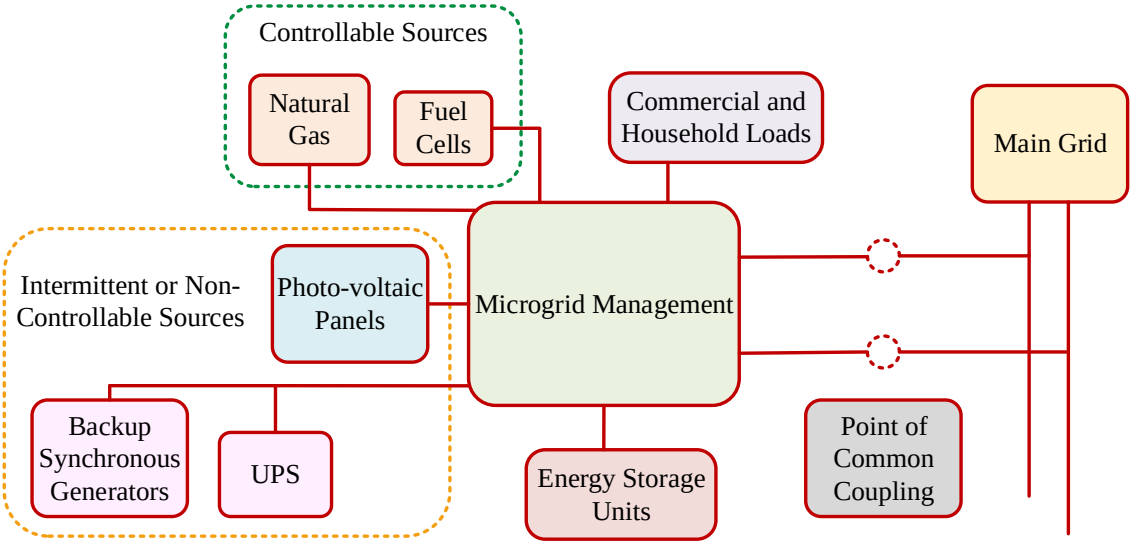

Figure 2.2: A microgrid can operate either in the islanding mode independently of the main power grid or in parallel with the main power grid with the point of interconnection known as the point of common coupling (PCC).

2.1.2 Main Features

A microgrid is an intelligent and autonomous grid concept. It can manage each available energy source efficiently and effectively. For example, during the day-time, it should draw maximum energy from PV panels whereas at night it should utilise other available energy sources. Further, a microgrid can isolate itself from faults autonomously, and continue supplying power in cases of main grid failure/blackout, etc. In addition to its self-healing property, a microgrid reduces greenhouse gas emissions, increases the system's reliability and modularity, reduces stress on the distribution network, and lowers energy losses [3, 35].

2.2 Microgrids: A Low Inertia Power System

Renewable energy sources are integrated into the power system using power electronic inverters as an interface. The inertia of these power electronic inverters is very low compared to conventional synchronous generators. Due to the high inertia associated with synchronous generators, they can resist sudden disturbances in the

power system using the kinetic energy stored in their rotors. However, this is not the case with inverters. Hence, special control techniques are required for low inertia power grids with a high penetration of distributed energy resources [28]. Some of the main stability issues associated with low inertia power grids are discussed in the following sections. A typical microgrid should:

- preserve the power quality of the overall system.
- fulfil the reactive power demand to avoid voltage sags.
- regulate the system's voltage and frequency.
- have the capability to rapidly supply the active and reactive power on mode transfer (from grid connected to islanded mode and vice-versa).

The energy storage elements in the microgrid should be fast enough to supply the required active and reactive power demand while ensuring the system's voltage and frequency stay within the desired limits when there is a sudden disturbance in the microgrid.

2.3 Challenges Associated with the Increased Integration of Distributed Energy Resources in a Power System

The dynamic behaviour of a microgrid with a high number of distributed energy resources is quite different from that of a conventional power system. This results in some advanced challenges outlined below [22, 30].

2.3.1 Power Flow Control

Distributed energy resources and their respective control techniques should be fast enough with capability to respond to sudden change in the load, line switching and loss of generation. The low inertia associated with microgrids (due to the high penetration of renewable energy sources) results in relatively large frequency and voltage deviations compared to conventional power systems [21].

2.3.2 Mode Transfer and Synchronisation

One of the main challenges is the smooth transition from grid connected mode to islanded mode. The operating points of the distributed energy resources change when a microgrid is isolated from the main grid. The control techniques should be advanced enough to stabilise the system, and keep the inverters synchronised corresponding to the new operating points [28]. Further, there must be enough supply of reactive power to avoid voltage sags, and energy storage in terms of spinning reserves, batteries, etc., to fulfil the load requirements.

2.3.3 Natural Uncertainties in Distributed Energy Resources

The renewable energy sources are intermittent in nature (e.g. solar photo-voltaic panel and wind turbines). The uncertainty in their generation can cause significant voltage/frequency stability issues. Therefore, these issues must be considered at the system planning stage.

2.3.4 Harmonic Distortion

Most of the distributed energy resources are integrated into the power system using some kind of power electronic converter as an interface. These power converters

have switching harmonics in their output. These harmonics can cause a resonance issue with cable capacitance and source inductance (line and transformer leakage inductance) [27]. Hence, the harmonic content in the inverter's output should be minimised, and care must be taken to avoid resonance while designing the system parameters. The harmonic content should be minimum near the critical loads, point of common coupling and at the output of distributed energy resources.

2.3.5 Dispatchable Generation

Existing inverter control techniques including droop control, proportional-resonant control, virtual oscillator control, etc., enable parallel-connected inverters to share the power proportional to their power ratings. With the increased integration of renewable energy sources into the power system, proportional power sharing is not always desirable. For example, the photo-voltaic panels should be utilised at maximum capacity when it is sunny. Similarly, the maximum power should be extracted from the wind turbines when it is windy. Moreover, the power demand should be supplied by the nearest generation source to avoid line losses and stress on the distribution network. All these factors necessitate the investigation of dispatchable inverter control techniques. The dispatch of output power for each energy source in the system enables better energy source utilisation, increased efficiency, and reduced line losses and stress on the distribution network. The recent literature on dispatchable virtual oscillator controller (dVOC) includes [36–40] and is compared with the proposed research work in this thesis in Section 2.7.3.4.

2.3.6 Heterogeneously Controlled Inverters

With the increased integration of distributed energy resources into the power system, the inverters used as an interface to connect these resources with the power system are not necessarily controlled using the same control technique. Most of the

existing inverter control literature assumes the parallel-connected inverters are controlled by the same control technique. Hence, a need arises to investigate a system of heterogeneously controlled parallel-connected inverters and to develop advanced control techniques to regulate the system's voltage and frequency within the desired limits while enabling optimal power sharing between these inverters.

2.4 Stability Issues in a Low Inertia Microgrid

The major stability issues associated with a low inertia power system are the following [21, 23, 24, 29]:

- Rotor angle stability
- Voltage stability
- Frequency stability

These three major stability issues are discussed in the following sections. Fig. 2.3 and Fig. 2.4 show a detailed description of stability issues and the corresponding methods to improve the system's stability, respectively [29].

2.4.1 Rotor Angle Stability

Rotor angle stability is defined as the ability of the power system to maintain synchronisation between parallel-connected machines while it is subjected to disturbances. A rotor angle stability problem can occur due to line switching, sudden change in load, loss of a generation unit or severe fault conditions in a power system. In case of small-signal stability analysis, the low inertia of the distributed generation resources results in a relatively large imaginary part of the eigenvalues

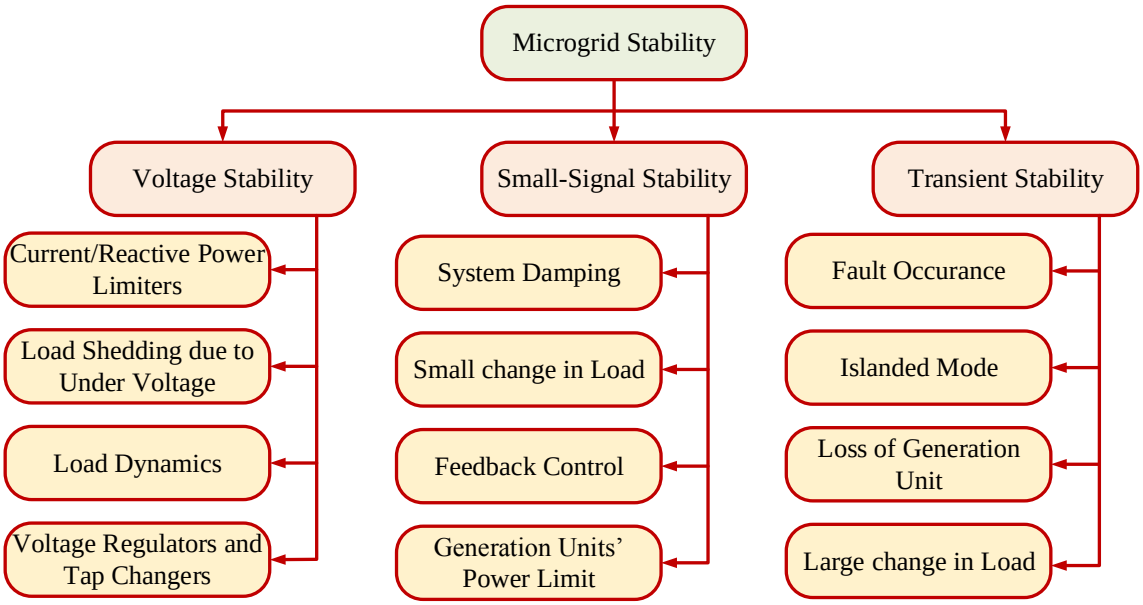

Figure 2.3: An overall description of possible stability issues in a low inertial power system [29].

which in turn results in reduced damping, and produces large oscillation in the system [21, 41].

2.4.2 Frequency Stability

Frequency stability corresponds to the ability of the system to maintain a steady frequency while there are significant disturbances in the generation or load [42]. Low inertia microgrids result in a high rate of change of frequency (ROCOF) and a lower nadir frequency compared to conventional power systems with synchronous generators as reported in [21]. A high ROCOF results in relatively large frequency deviations and can cause system instability. Further, in case of high ROCOF, a fast response time is required to restore the frequency [21].

2.4.2.1 Impact on Protective Relaying

A high ROCOF can trigger the protective relays with settings based on the conventional power system. Hence, in order to incorporate a high penetration of distributed

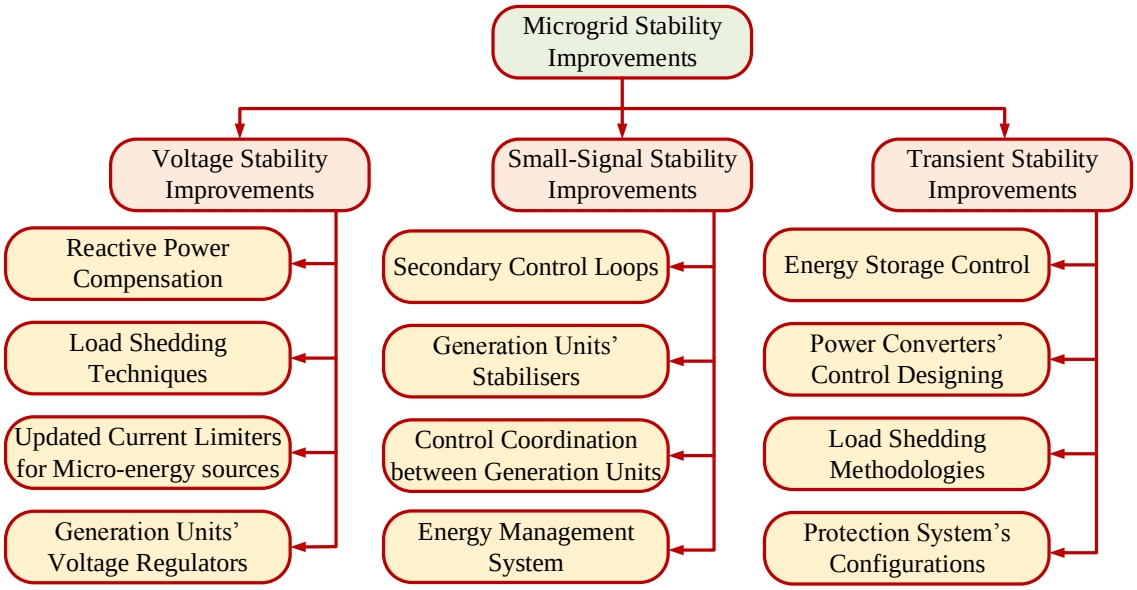

Figure 2.4: An overview of the methods to improve the stability of power systems with low inertia [29].

energy resources into the power system, the settings for ROCOF and the current protection relays need to be modified. Further, high speed tracking of the system's frequency is required to detect the disturbances.

2.4.2.2 Effect of High Rate of Change of Frequency

A relatively high ROCOF results in increased wear and tear of the generators and turbines. Hence, the life time of the generation units is significantly affected [43].

2.4.3 Voltage Stability

The intermittent nature of distributed energy resources can result in voltage flickering and sags. If a DER is connected to a lightly loaded feeder, its voltage level rises. Similarly, unavailability of sufficient reactive power can result in significant voltage sags. The different aspects that can result in voltage instability are discussed in [29].

There are several mitigation techniques to avoid instability in low inertia power systems and they are described in the following sections.

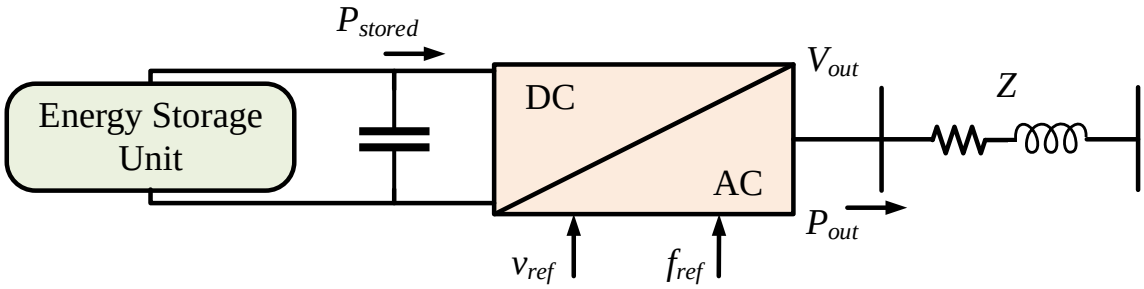

Figure 2.5: A typical energy storage unit in low inertia power system [24].

2.5 Mitigation Techniques to Improve the Stability of Low Inertia Power Systems

This section includes a number of mitigation techniques to avoid instability in low inertia power systems.

2.5.1 Spinning Reserves

In order to enhance the inertia of a power system with a large number of distributed energy resources, spinning reserves should be introduced into the power system. These spinning reserves can be in the form of intermediate energy storage units or individual battery banks at the DC link of each inverter. These reserves can be used to fulfil the power requirements in case of sudden loss of generation or change in loading conditions.

Another technique to incorporate the spinning reserves in a power system is to operate the photo-voltaic systems at lower output power than the maximum power point (MPP) so that the remaining energy can be stored and made available in case of disturbance [44]. The most commonly used energy storage elements are batteries, flywheels, ultra-capacitors, super conducting magnetic energy storage, pumped hydroelectric storage and compressed air energy storage. A typical energy storage distributed unit is shown in Fig. 2.5.

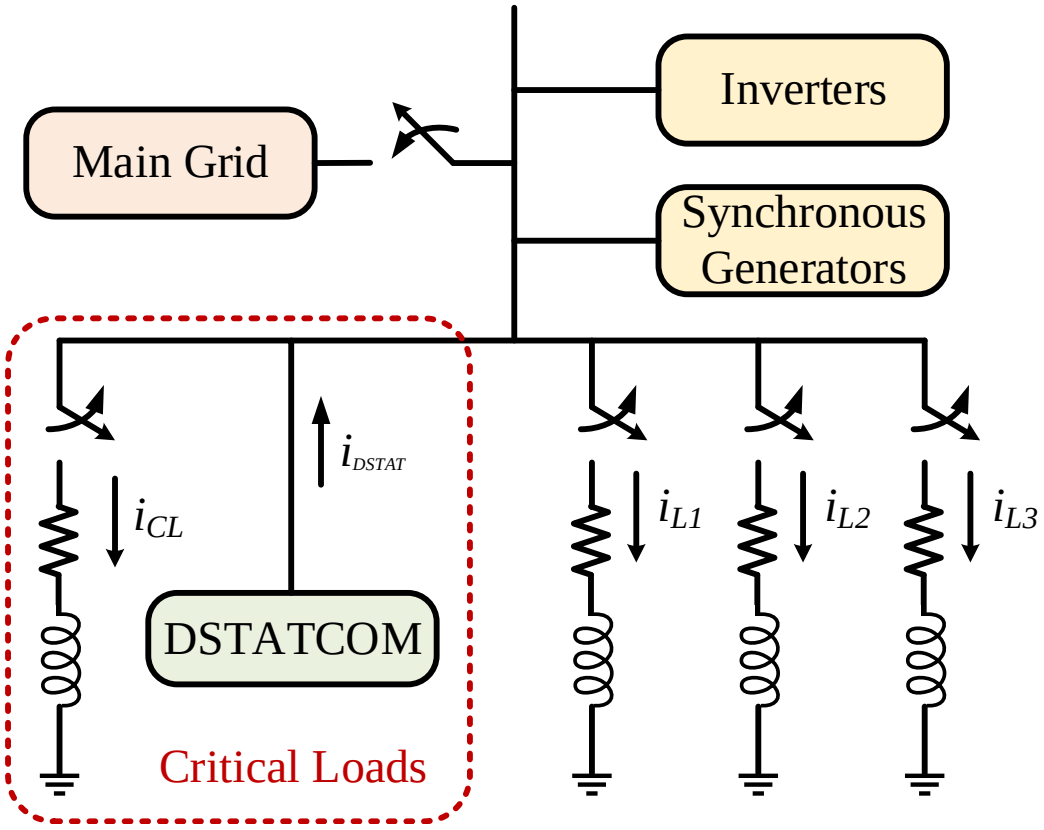

Figure 2.6: A block diagram representation of reactive power compensation using DSTATCOM [29].

2.5.2 Reactive Power Supply

In order to avoid voltage sags due to unavailability of reactive power, the distributed static reactive power compensator (DSTATCOM) can be used, as shown in Fig. 2.6. However, unlike conventional power systems, the choice of place to position these DSTATCOMs is still a point of research in low inertia power systems [26, 45].

Flywheels can also be used to store energy in MW range and supply back within $\frac{1}{4}$ of an ac-cycle to the grid in accordance with voltage and frequency conditions [29]. They consist of two back-to-back converters, as shown in Fig. 2.7.

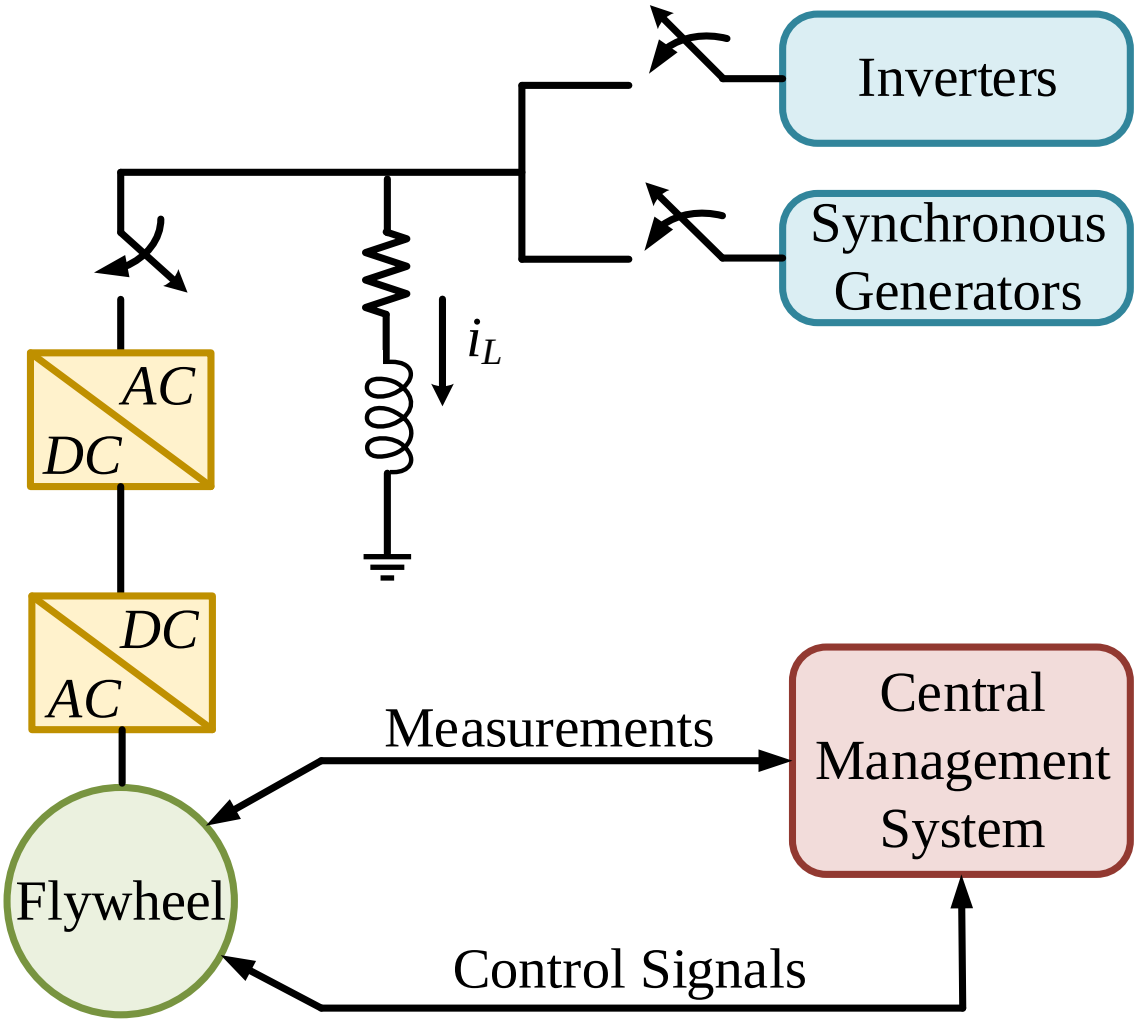

Figure 2.7: A representation of a flywheel energy storage system [29].

2.5.3 Supplementary Control Loops

Voltage stability of the microgrids can be improved by the addition of supplementary control loops in the closed-loop system, as shown in Fig. 2.8. A detailed hierarchical control structure for microgrids is reviewed in Section 2.6.

2.5.4 Microgrid Protection Schemes

Conventional protection schemes are not sufficient for low inertia microgrids with DERs and modifications are required in the configuration of protective relays. Syn-

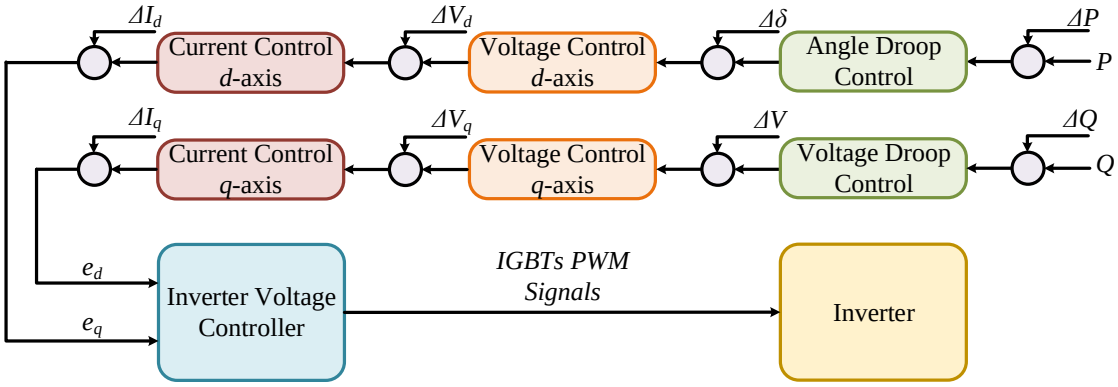

Figure 2.8: Supplementary control loops to improve the small-signal stability [29].

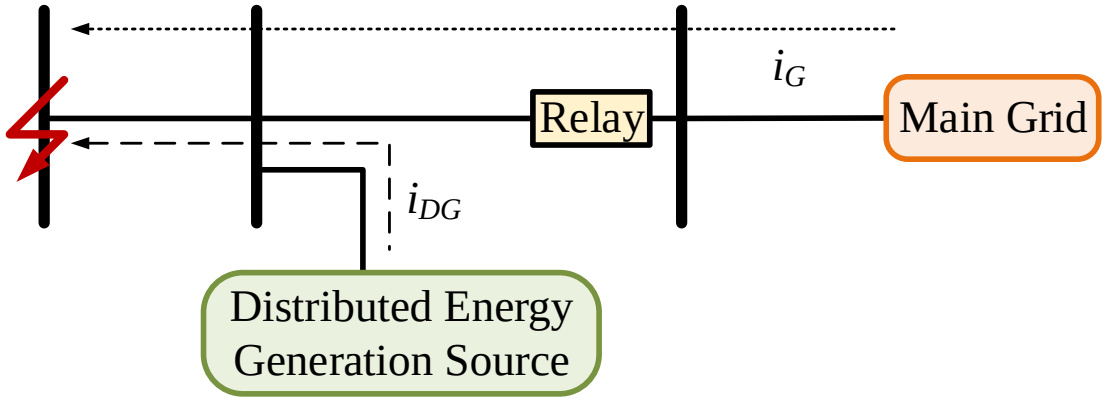

Figure 2.9: A representation of a blinding phenomenon for protective relays in power grids with high penetration of renewable energy sources [27].

chronous generators can withstand a high fault current for a considerable time. However, this is not the case with inverters. Another important phenomenon in the case of high DERs penetration (into the power system) is the blinding of protection, also known as protection under-reach [27]. In this case, if a fault occurs close to a DER, the fault current is shared by both the DER and main grid. There is a possibility that the current supplied by the main grid never reaches the relay pick-up current value and the fault remains undetected, as shown in Fig. 2.9. Hence, this demands new procedures for designing power system protection schemes with the possibility of increased distributed energy resource penetration.

The inverter control techniques should be fast enough to track the sudden disturbances in voltage and frequency, and adjust their operating points to maintain system stability [46]. The techniques should have fault ride-through capabilities [47] so that a high penetration of DERs can be achieved in the power system.

2.6 Hierarchical Control Structure in a Microgrid

A typical hierarchical control structure in a microgrid is shown in Fig. 2.10. The main objectives of these control layers are as follow [48].

- The regulation of system's voltage.
- The regulation of system's frequency.
- Cost optimisation of the microgrid.
- The optimal load sharing between distributed generation units.
- Stability, and control of steady-state and dynamic response.
- The transition from grid connected mode to islanding mode and vice-versa.

2.6.1 Primary Controllers

The most commonly used primary controllers include droop controllers, proportional-resonant controllers and virtual oscillator controllers. The main objectives of the primary controllers include system's voltage and frequency stability, and control. Moreover, primary controllers are used to reduce the interactions between the parallel-connected energy generation sources and to enable proportional power sharing between them.

2.6.1.1 Inner Voltage and Current Control Loops

The most common way to design inverter controls is by converting the *abc*-reference frame voltages and currents into *dq*-reference frame. This transformation converts the sinusoidal voltage and current signals to DC signals that can be controlled using conventional PI controllers. However, the conversion of signals from an *abc*-reference

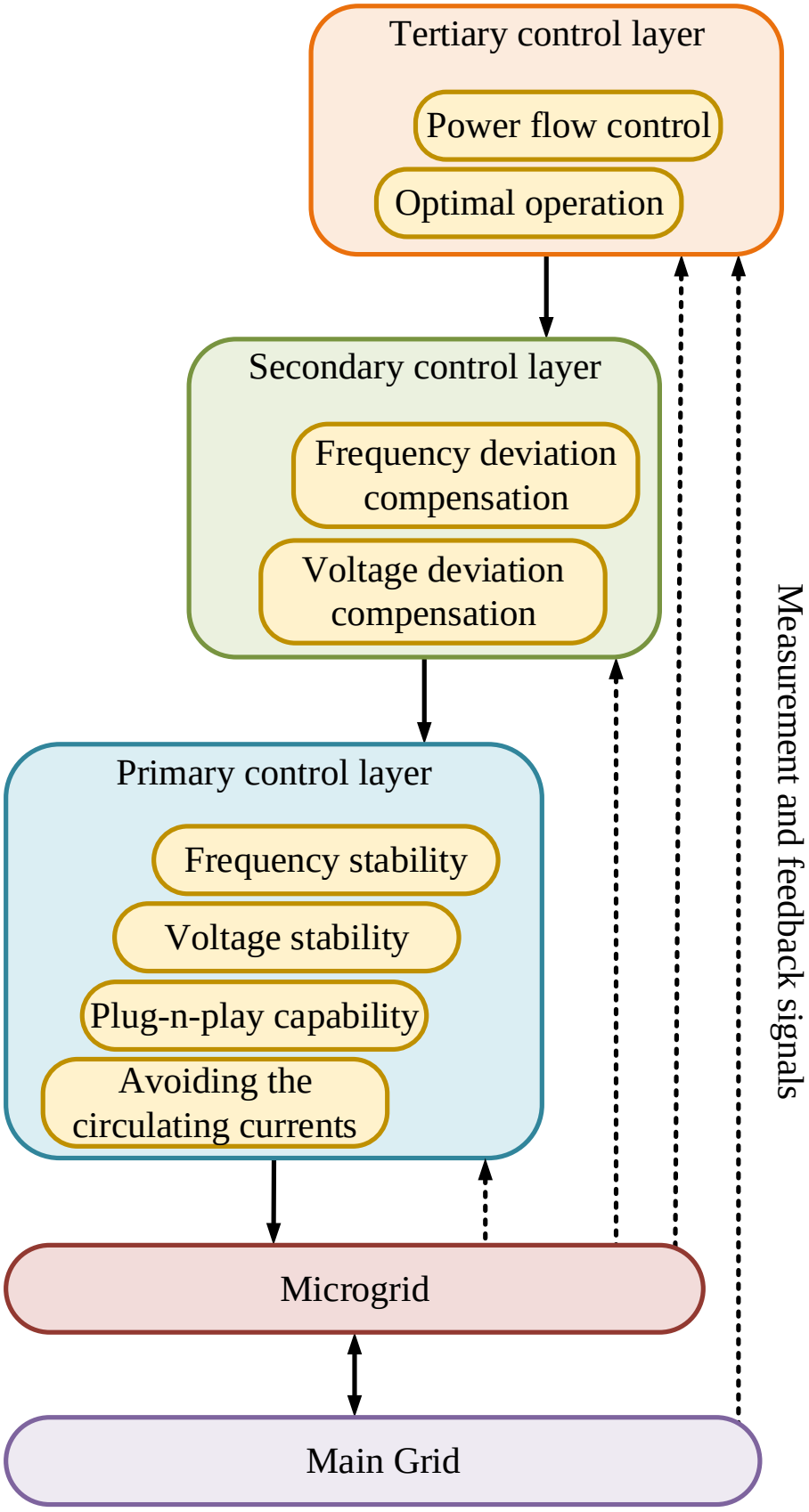

Figure 2.10: A hierarchical control structure in a microgrid [48].

frame to a dq-reference frame, results in the coupling terms appearing in both the d-axis and q-axis components of the voltage and current signals. In [49], the inner voltage and current control loops are proposed in the dq-reference frame to control the inverters. A graphical design approach is presented for the decoupling terms to avoid cross-coupling in the d-axis and q-axis components. Further, a detailed systematic procedure is presented for designing the PI controller gains, and bandwidth selection criteria for the voltage and current control loops. These voltage and current control loops are primarily designed to reject high frequency disturbances and avoid resonance with the external network by damping the output LC filters [7].

2.6.1.2 PLL Structure for Single-Phase Systems

A single-phase system contains less information than a three-phase system, and in order to convert single-phase voltage and current to the dq-reference frame, advanced techniques are required. Some of the techniques to generate orthogonal signals for single-phase systems include transport delay to introduce a phase shift of 90° in the signal, Hilbert transformation [50] and inverse Park transformation [50–53]. However, these techniques are frequency dependent, complex, non-linear, and provide low or no filtering [54].

A new phase-locked loop structure based on the second order generalised integrator (SOGI) is presented in [54] to generate the orthogonal voltage system and provide filtering without any delay due to its resonance at the fundamental frequency. This proposed structure is also frequency independent. Moreover, the filtering provided by this PLL structure can be enhanced by designing the parameters accordingly; however, at the cost of slower dynamic response of the system. Further, several ways to implement the PLL structure (to generate the orthogonal system) are discussed including the trapezoidal method, second order integrator and third order integrator [54].

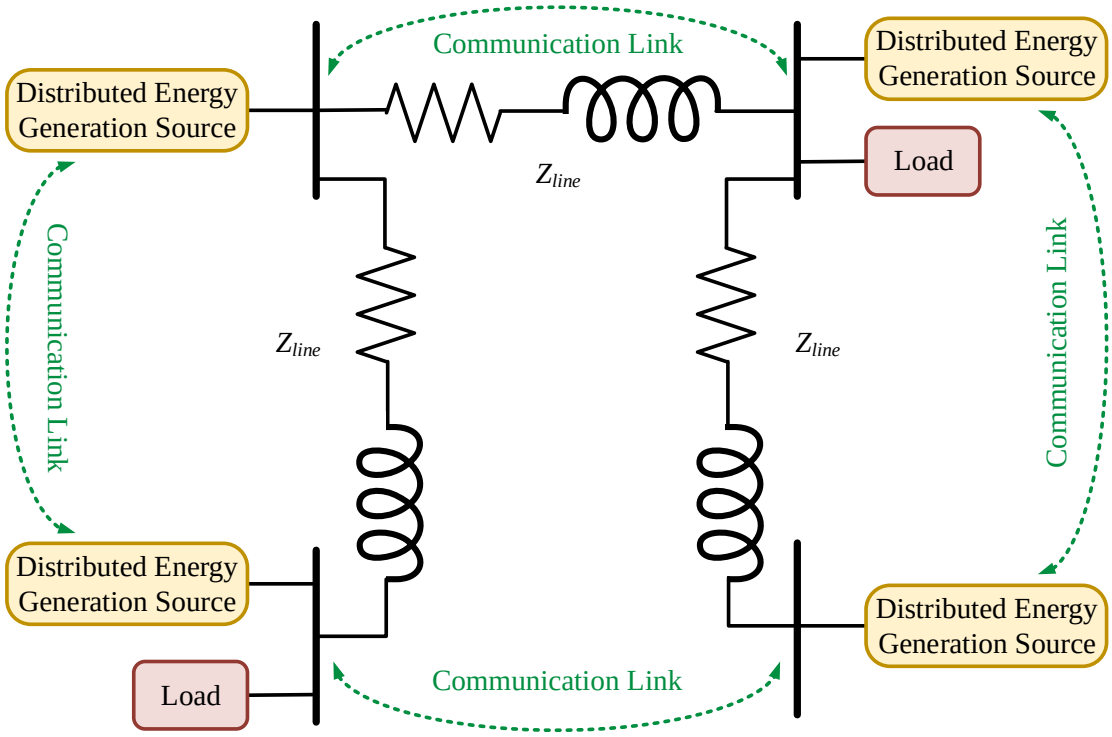

Figure 2.11: A representation of a secondary control layer to regulate the system's voltage and frequency back to the nominal values [58, 59]. The bidirectional (dotted) arrows represent the communication link between the neighbouring generation sources.

2.6.2 Secondary Controllers

In most inverter control techniques, inverters are made to follow the conventional $P-\omega$ and $Q-V$ droop-characteristics. While designing the controller for inverters, the terminal voltage and frequency variations must remain within the desired tolerance band as specified by the ac-performance metrics/standards. This results in inverters operating close to the nominal values for voltage and frequency. To restore the voltage and frequency to the nominal values, secondary control techniques are proposed in [55–59]. These techniques [58, 59] use a communication link between the neighbouring generation sources, and restore the terminal voltage and frequency to the nominal set points, as shown in Fig. 2.11.

2.6.3 Tertiary Controllers

The tertiary control is the highest level of control layers that is used to manage the optimal operation of distributed energy resources, and for the power flow control to achieve the planned grid operation [48].

2.7 Inverter Control Strategies

A microgrid consists of several renewable energy sources, each of which generates electrical power at different voltage levels and frequencies. To integrate these renewable energy sources into the power grid, a power electronic interface is required in the form of an inverter. The inverter generates regulated terminal voltage and frequency in order to satisfy the conventional power grid voltage/frequency standards. Further, the dynamic behaviour of conventional synchronous generators is quite different from that of power electronic inverters. Hence, in order to make these heterogeneous generation sources work in parallel, their dynamic and steady-state responses should be in agreement with each other or the control techniques should be advanced enough to address these challenges. There is a lot of literature [60] available on the control techniques developed so far for the control of inverters in a microgrid. Some of the promising techniques are discussed below.

2.7.1 Droop Control

In a conventional droop control strategy, inverters are made to imitate the dynamics of a synchronous generator. In the case of a synchronous generator with inductive lines, the increase in the active power demand results in a reduced rotational speed of the generator and in the system's frequency. Similarly, there exists a relationship between synchronous generator terminal voltage magnitude and output reactive

power [61–64].

In order to match their terminal characteristics with those of a synchronous generator, inverters are made to follow active power-frequency and reactive power-voltage droop-characteristics. This also helps in proportional power sharing among several parallel-connected distributed generators, in accordance with their power ratings, thereby improving the system's reliability, and avoiding the overloading of a particular generation source. A block diagram representation of a droop-controlled inverter is given in Fig. 2.12. The typical droop-control relationships [65] are given by the following equations:

$$f_{ref} = f_{nom} - m \times (P - P_{nom}), \tag{2.1}$$

$$V_{ref} = V_{nom} - n \times (Q - Q_{nom}), \tag{2.2}$$

where f_{nom} denotes the nominal grid frequency, and V_{nom} denotes the nominal grid voltage. The P_{nom} and Q_{nom} are the nominal set-points for the active and reactive power, respectively. The f_{ref} and V_{ref} are the reference values for the system's frequency and voltage magnitude, respectively, based on the inverter's output active and reactive power. The m and n denote the respective active and reactive power droop-coefficient.

2.7.1.1 Droop Control: A Decentralised Control Strategy

To enhance the modularity of the microgrid and its plug and play capability, most of the droop control strategies are designed as decentralised control strategies thus avoiding the need for direct communication between the inverters. In [66, 67], a virtual resistive output impedance technique is presented to overcome the synchronisation and power sharing issues resulting from the mismatches between filter and line impedance values for several droop-controlled inverters operating in a microgrid.

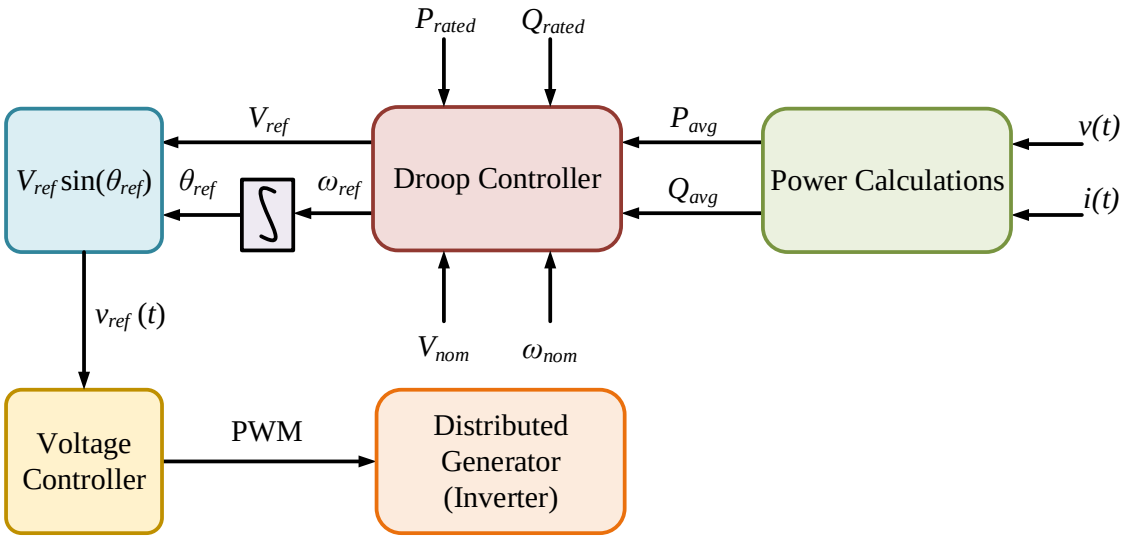

Figure 2.12: A block diagram representation of a droop-controlled inverter [65].

The use of a virtual feedback impedance loop results in proportional power sharing even with different filters and line impedance values. Similarly in [8], a current based droop control strategy is presented to reduce the harmonics in the output. A droop control technique for the smooth transition between grid connected and islanded modes is presented in [68].

2.7.1.2 Droop Control: Output Power Regulation

In [69], a droop control strategy is presented to control the active and reactive output power of an inverter. A second order generalised integrator (SOGI) is used to estimate the grid voltage, frequency and impedance values. Based on these values, droop control has been designed to regulate the active and reactive powers with negligible offset error.

2.7.1.3 Droop Control: Limitations

Despite several appealing features and promising results, there are several limitations associated with conventional droop control strategies and are presented below.

- A major limitation lies in the slow dynamics associated with the voltage control loop in the case of dual-loop control strategies. The bandwidth of the voltage controller has to be upper bounded by $1/10^{th}$ the bandwidth of the current controller [9].

- Power measurements and phasor calculations result in slower dynamic response of the overall system. The presence of low-pass filters in the loop, ac-cycle averaging and coordinate transformations to calculate the active and reactive power make the system's dynamic response slower.

- The difference in the response times of droop-controlled inverters results in the interactions between the distributed generation units. This causes circulating currents to flow between generation sources and can result in stability issues.

- Droop control strategies are highly sensitive to filter and line impedance values. The control designed for one particular system need not necessarily work in other situations. The line's X/R ratio must be taken into consideration while designing the controller.

2.7.2 Proportional-Resonant Control

Proportional-resonant (PR) control techniques are proposed in [12, 13, 70–73] for inverters operating in parallel in an islanded microgrid. PR control is a current regulation technique for voltage source inverters (VSIs) to regulate their terminal characteristics (voltage and frequency) within the desired tolerance band. Due to the intrinsic droop-characteristics of PR controllers, voltage/frequency regulation and proportional power sharing can be achieved without any communication between the parallel-connected VSIs in the islanded mode. Further, an improved transient response can be achieved as compared to that from conventional droop-control techniques. Fig. 2.13 shows a block diagram representation of PR controlled inverters.

A bode plot of the PR linear compensator's transfer function is presented in [74].

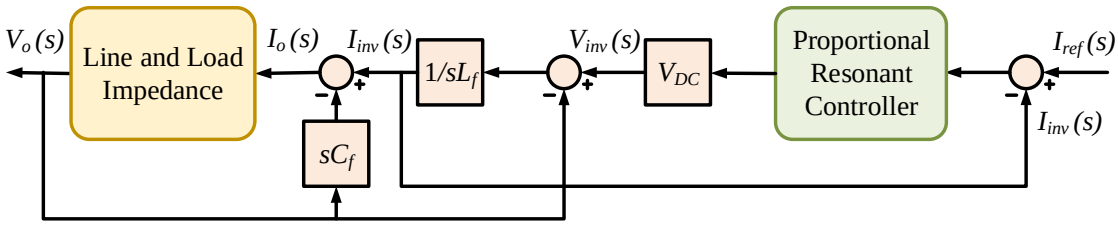

Figure 2.13: The block diagram representation of a proportional-resonant (PR) controller [70].

In the bode plot, the infinite gain at the resonant frequency results in the zero steady-state error. Moreover, looking at the phase plot, there exists a steep slope at the resonant frequency [74]. This results in small frequency deviations from the nominal value for a large change in phase angle, which is used to control the reactive power. By properly designing the PR controller gains, the frequency deviations can be limited within the desired tolerance band. The secondary/outer predictive control loops can be used to restore the system's voltage and frequency to the nominal values [74].

2.7.2.1 PR Controller: Design Procedure

In this section, the PR controller design rules are presented as proposed in [74, 75]. The continuous time transfer function of the PR controller is given by:

$$G_{PR}(s) = K_P \left(1 + \frac{K_i s}{s^2 + \omega_{PR}^2}\right), \tag{2.3}$$

where $\omega_{PR} = 2\pi f_{PR}$ is the PR controller resonant frequency. The f_{PR} is chosen to be equal to the nominal value of grid frequency ω^*. The gains K_p and K_i are designed to achieve the desired transient response and phase margin ϕ_m at the crossover frequency w_c. The gains are defined as follows:

$$K_p = \frac{w_{c,max} L_f}{V_{DC}}, \tag{2.4}$$

$$K_i = \frac{w_{c,max}}{10}, \tag{2.5}$$

where $w_{c,max} = \frac{\frac{\pi}{2}-\phi_m}{T_{std}}$ is the maximum crossover frequency that can be achieved corresponding to the desired phase margin ϕ_m, T_{std} is the sampling time plus transportation delay, L_f is the inverter output filter inductance and V_{DC} is the inverter DC bus voltage. The choice of $\omega_{c,max}$ results in the maximum possible values of PR controller gains K_p and K_i. The inverter output current i_{inv} is compared with the reference current signal i_{ref}, and the corresponding error signal $i_{err} = i_{ref} - i_{inv}$ is fed to the PR controller that in turn generates the modulation signal for the inverter, as shown in Fig. 2.13.

2.7.2.2 PR Controller: Limitations

The main limitations associated with the PR controller are as follow:

- The slower dynamic response due to the involvement of coordinate transformations and phase-locked loops (PLLs).
- The variations in phase angle causing considerable frequency deviations from the nominal value, resulting in the need for secondary/predictive frequency restoration loops to restore the frequency back to the admissible range [74].

2.7.3 Virtual Oscillator Control

Recently, an inverter control strategy, referred to as virtual oscillator controller (VOC) [16–18, 76–80], has been proposed to control islanded inverters operating in a microgrid. A virtual oscillator controller is a time-domain controller and exhibits nearly sinusoidal oscillations in steady-state [76]. Unlike other existing inverter control techniques, the virtual oscillator controller only needs the instantaneous inverter output current as a feedback and does not require coordinate transformations, trigonometric function evaluations, phase-locked loops, phasor computations and low-pass filters to calculate power. The non-linear oscillator dynamics (e.g. Van

der Pol oscillator, dead-zone oscillator, Andronov-Hopf oscillator, etc.) are used to control the inverters and regulate their terminal characteristics. To realise the non-linear oscillator, the mathematical model of a Van der Pol oscillator [81] is used in [76]. A block diagram representation of a Van der Pol oscillator is shown in Fig. 2.14. It consists of an LC harmonic oscillator with a resonant frequency $\omega^* = \frac{1}{\sqrt{LC}}$, where L and C denotes the virtual oscillator inductance and the capacitance, respectively. Moreover, the LC harmonic oscillator is in parallel with a negative resistance element $R = \frac{-1}{\sigma}$, and a non-linear voltage dependent current source with a positive parameter α. The inductor current and capacitor voltage are denoted by i_L and v_C, respectively. The inverter output current i is scaled by the current feedback gain k_i before entering the virtual oscillator. Inverters are made to follow the dynamics of a non-linear oscillator and converge to the stable limit-cycle. The self-synchronisation is an inherent property of the non-linear Van der Pol oscillators that can synchronise to a steady-state limit cycle starting from arbitrary initial conditions (except the origin). Synchronisation conditions for parallel-connected VOC inverters are presented in [16, 18]. The self-synchronisation property eliminates the need for any direct communication between the inverters. A dynamic model of the virtual oscillator's RMS terminal-voltage amplitude V and instantaneous phase angle $\phi = \omega t + \theta$ (where θ is the phase-offset with respect to ωt) is given by [76]:

$$\frac{dV}{dt} = \frac{\epsilon\omega^*}{\sqrt{2}}\left(\sigma g\left(\sqrt{2}V\cos(\phi)\right) - k_v k_i i\right)\cos(\phi), \tag{2.6}$$

$$\frac{d\phi}{dt} = \omega^* - \frac{\epsilon\omega^*}{\sqrt{2}V}\left(\sigma g\left(\sqrt{2}V\cos(\phi)\right) - k_v k_i i\right)\sin(\phi), \tag{2.7}$$

where k_v denotes the voltage scaling factor for the virtual oscillator's capacitor voltage v_C. The function $g(v) = v - \frac{\beta}{3}v^3$, where $\beta = \frac{3\alpha}{k_v^2\sigma}$ [76]. The VOC design parameters include α, σ and ϵ. The epsilon $\epsilon = \sqrt{\frac{L}{C}}$ is a key VOC design parameter that controls the dynamic response and extent of harmonic content in the non-linear oscillator's output. The non-linear oscillator is implemented on a digital signal microprocessor by discretising its dynamics using a trapezoidal rule of integration [76]

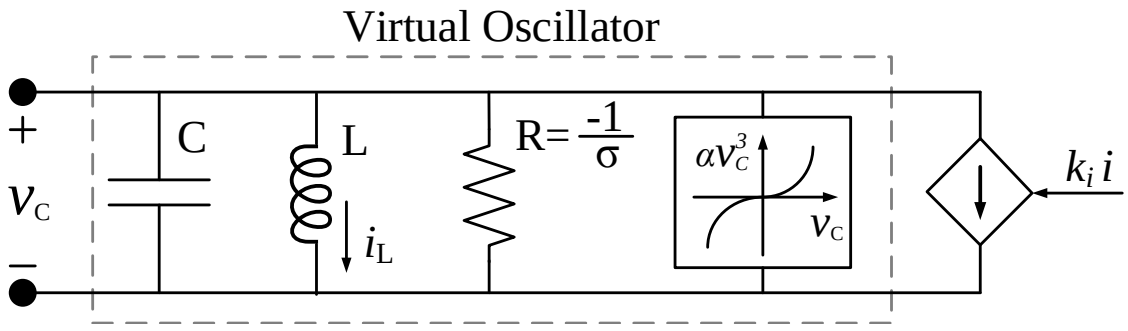

Figure 2.14: A block diagram representation of Van der Pol oscillator [76].

and this is the reason for the name,"virtual oscillator controller". The aforementioned discretised dynamics are given by [76]:

$$\begin{aligned} v[k] = &\left(1 - \frac{T_s\sigma}{2C} + \frac{T_s^2}{4LC}\right)^{-1} \left[\left(1 + \frac{T_s\sigma}{2C} - \frac{T_s^2}{4LC}\right) v[k-1] - \frac{T_s}{C} k_v i_L[k-1] \right. \\ &\left. - \frac{T_s}{2C} k_v k_i \left(i[k] + i[k-1]\right) - \frac{\alpha T_s}{C k_v^2} v^3[k-1]\right], \\ i_L[k] = &\, i_L[k-1] + \frac{T_s}{2Lk_v}\left(v[k] + v[k-1]\right), \end{aligned} \tag{2.8}$$

where T_s denotes the sampling time, $k \in \mathbb{Z}_{\geq 0}$ denotes the kth sampling instance, $v[k]$ denotes the sampled instantaneous inverter terminal-voltage, $i[k]$ denotes the sampled instantaneous inverter output current and $i_L[k]$ denotes the sampled instantaneous virtual oscillator inductor current.

A virtual oscillator control scheme for three-phase islanded inverters in a microgrid with high penetration of photo-voltaic panels is presented in [17]. In order to reduce the transients while connecting the virtual oscillator-controlled inverter with the rest of the system and to enhance the plug-n-play capability, a pre-synchronisation technique is used. This is discussed in [16]. In [82], a unified virtual oscillator control (uVOC) for both grid forming and grid following inverters is proposed based on the dispatchable virtual oscillator controller presented in [36, 37, 83, 84]. The proposed unified virtual oscillator controller enables the inverter synchronisation with low grid voltage, and its fast current limiting capability results in a fault ride-through operation. Further, during grid following mode, bidirectional

power flow and DC voltage regulation are achieved.

A hierarchical control structure for virtual oscillator-controlled inverters to either operate in islanded mode or grid connected mode is presented in [85]. In islanded mode, the control achieves voltage and frequency regulation whereas, in grid-tied mode, a notch filter is used to remove the harmonic content in the output of virtual oscillator-controlled inverters. In [86], a frequency-domain method is presented for virtual oscillator-controlled inverters to suppress the harmonic distortion in the output current. A selective harmonic current suppression method based on virtual impedance is proposed. Similarly, a voltage harmonics attenuation technique based on virtual impedance is proposed in [87]. A graphical approach to analyse the transient stability of dispatchable virtual oscillator controller (dVOC) using vector fields on the circle is presented in [88].

2.7.3.1 Averaged VOC Model

In order to simplify the analysis of non-linear virtual oscillator-controlled inverters, and to identify the embedded $P-V$ and $Q-\omega$ droop-characteristics within the dynamics of virtual oscillators, an averaged VOC model is derived in [76] by averaging the actual VOC dynamics (2.6)-(2.7) over an ac-cycle $\frac{2\pi}{\omega^*}$ and is given by:

$$\frac{d}{dt}\overline{V} = \frac{\sigma}{2C}\left(\overline{V} - \frac{\beta}{2}\overline{V}^3\right) - \frac{k_v k_i}{2C\overline{V}}\overline{P}, \tag{2.9}$$

$$\frac{d}{dt}\overline{\theta} = \omega^* - \omega + \frac{k_v k_i}{2C\overline{V}^2}\overline{Q}, \tag{2.10}$$

where $\overline{V}$ denotes the averaged terminal-voltage magnitude and $\overline{\theta}$ denotes the averaged phase-offset with respect to ωt. The $\overline{P}$ and $\overline{Q}$ denote the averaged active and reactive power, respectively. These resulting differential equations describe the relationship between inverter terminal characteristics including voltage, frequency, active and reactive power. By analysing these differential equations (decoupled in terms of active and reactive power), it can be observed that the $P-V$ and $Q-\omega$

droop-characteristics are embedded within the dynamics of a non-linear virtual oscillator. Hence, by using the simplified averaged VOC model, the behaviour of inverters can be observed under the desired steady-state operating conditions; and corresponding equilibrium solution can be determined using the following equations:

$$\overline{V}_{eq} = k_v \left(\frac{\sigma \pm \sqrt{\sigma^2 - 6\alpha(k_i/k_v)\overline{P}_{eq}}}{3\alpha} \right)^{\frac{1}{2}}, \tag{2.11}$$

$$\omega_{eq} = \omega^* + \frac{k_v k_i}{2C\overline{V}_{eq}^2}\overline{Q}_{eq}, \tag{2.12}$$

where $\overline{V}_{eq}$ denotes the equilibrium terminal-voltage magnitude and ω_{eq} denotes the equilibrium frequency. Similarly, the $\overline{P}_{eq}$ and $\overline{Q}_{eq}$ denote the equilibrium values of averaged active and reactive power, respectively. Fig. 2.15 shows a comparison between the limit-cycles for both the actual and averaged non-linear virtual oscillator dynamics as a function of VOC design parameter ϵ in steady-state. Note that the limit-cycle for the actual VOC dynamics contains harmonics and is not perfectly sinusoidal. The limit-cycle for the averaged VOC dynamics is described by a circle of radius $\sqrt{2\overline{V}}$, rotating at a fixed angular frequency ω_{eq}. Note that the harmonic content in the output of the virtual oscillator can be reduced by making ϵ smaller (i.e. $\epsilon \searrow 0$). However, this results in the system's slower dynamic response [76]. Hence, a design trade-off exists while designing the VOC parameters to achieve either a fast dynamic response or low harmonic distortion in the output.

2.7.3.2 Variants of Virtual Oscillator Controller

To realise the virtual oscillator controller [16, 36, 76, 84], several variants of the non-linear oscillator are proposed. The main idea is that each variant of the non-linear oscillator should posses a stable limit-cycle rotating at a constant angular frequency. Further, the limit-cycle should be nearly sinusoidal to avoid harmonic distortion in the output. A dead-zone oscillator is proposed in [16] for islanded microgrids. The

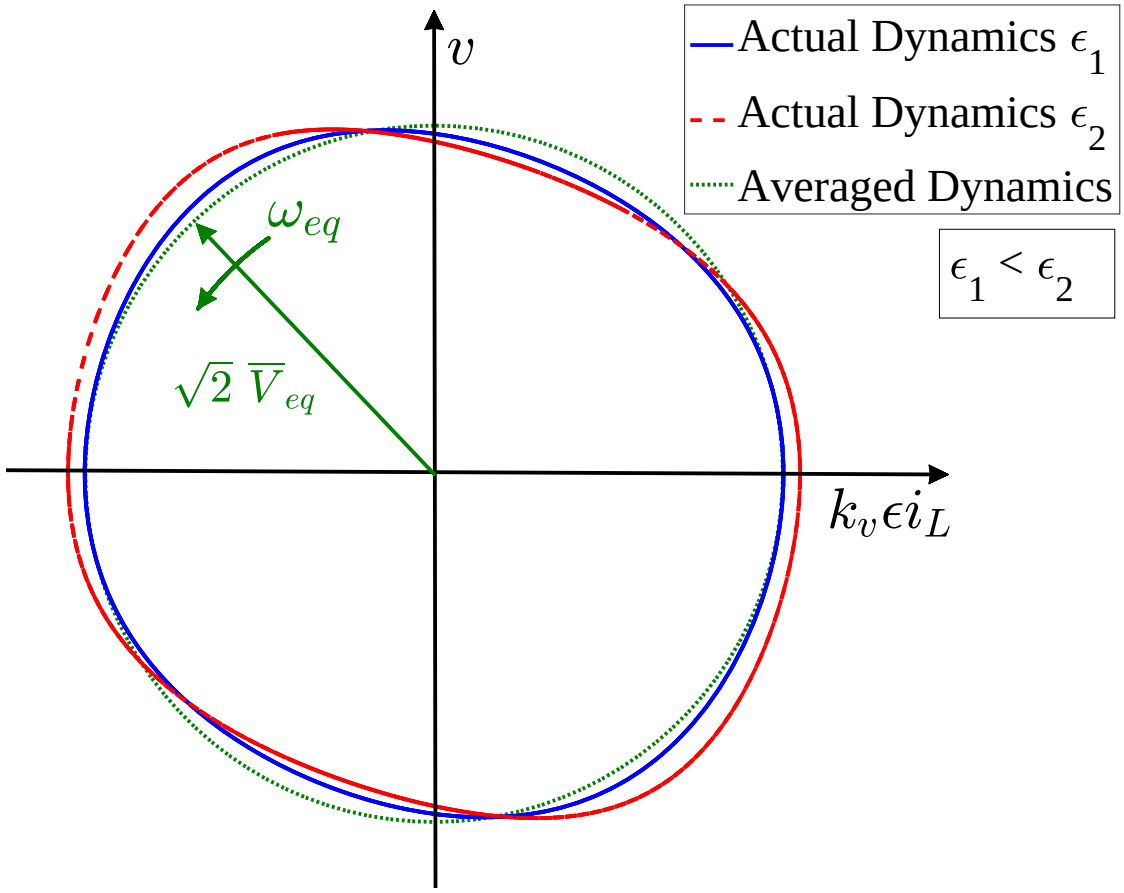

Figure 2.15: A comparison of steady-state limit cycles for both the actual and averaged non-linear oscillator dynamics. In quasi-stationary sinusoidal steady-state, the averaged VOC terminal-voltage is represented by a circle of radius $\sqrt{2}\,\overline{V}_{eq}$ rotating at an angular frequency of ω_{eq}. It can be seen that for the actual (unloaded) VOC model, a smaller value of ϵ results in reduced harmonics in the inverter terminal-voltage. On the other hand, a smaller ϵ results in slower dynamic response. The states $y = v$ (y-axis) and $x = k_v \epsilon i_L$ (x-axis) are the inverter-terminal voltage and scaled version of the inductor current, respectively [76].

limitation associated with a dead-zone oscillator is that it requires online tuning of the gains for designing the closed-loop control. However, in the case of the Van der Pol oscillator with cubic non-linearity [76], this type of gain tuning is not required. An electrical realisation of the dead-zone oscillator is presented in Fig. 2.16 and a phase-plot of the steady-state limit-cycles as a function of VOC design parameter ϵ is presented in [16]. Note that (similar to the Van der Pol oscillator) by decreasing the value of the VOC design parameter ϵ, the dead-zone virtual oscillator exhibits nearly sinusoidal oscillations. However, choosing a smaller of value of $\epsilon \searrow 0$ results in a slower dynamic response. Another variant of the non-linear oscillator with

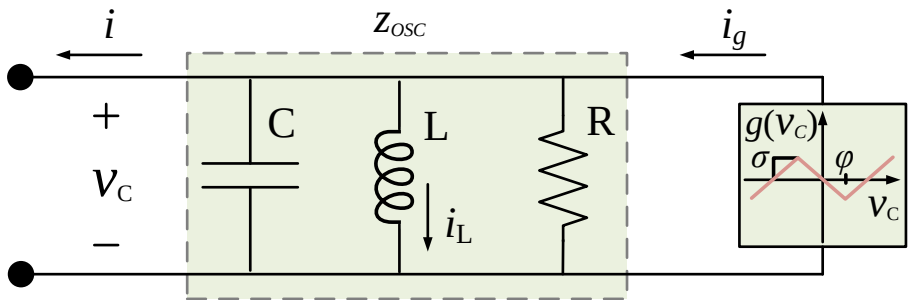

Figure 2.16: A block diagram representation of the dead-zone oscillator [16].

sinusoidal output voltage (i.e. without harmonic distortion) is presented in [84].

2.7.3.3 VOC Parameter Design Procedure

In an ac-power system, there are several constraints on the terminal characteristics of a power generation source. In order to meet the ac-performance specifications, the power grid voltage and frequency should be regulated to remain in the desired tolerance band (by designing the droop-characteristics accordingly). Hence, in order to ensure the inverter's operation in accordance with the strict ac-performance specifications, a detailed VOC parameter design procedure is presented in [76], and is described below. By properly designing the controller parameters, desired terminal characteristics, and proportional power sharing between multiple parallel-connected inverters, can be achieved.

In order to standardise the parameter design procedure, the VOC voltage scaling factor k_v is designed such that when the VOC capacitor RMS voltage $V_C = 1$ V, the inverter terminal-voltage magnitude should be equal to open circuit voltage $\overline{V}_{oc}$. Similarly, the current feedback gain k_i is designed such that the VOC input current is equal to 1 A when the inverter is supplying the rated active power $\overline{P}_{rated}$. According to these design rules, the current feedback gain and voltage scaling factor are given by the following equations:

$$k_v = \overline{V}_{oc}, \tag{2.13}$$

$$k_i = \frac{\overline{V}_{min}}{\overline{P}_{rated}}, \tag{2.14}$$

where $\overline{V}_{min}$ is the terminal-voltage corresponding to $\overline{P}_{rated}$. The open-circuit voltage $\overline{V}_{oc}$ corresponding to $\overline{P} = 0$ is given by:

$$\overline{V}_{oc} = k_v \sqrt{\frac{2\sigma}{3\alpha}}. \tag{2.15}$$

From (2.13)-(2.15), we have:

$$\alpha = \frac{2\sigma}{3}. \tag{2.16}$$

Now, substituting $\overline{P} = \overline{P}_{rated}$ and $\overline{V} = \overline{V}_{min}$ in (2.11), and using (2.13)-(2.16), we get:

$$\sigma = \frac{\overline{V}_{oc}}{\overline{V}_{min}} \frac{\overline{V}_{oc}^2}{\overline{V}_{oc}^2 - \overline{V}_{min}^2}. \tag{2.17}$$

The values for inductance L and capacitance C of the harmonic oscillator are also calculated while considering the ac-performance specifications. Considering the maximum allowable frequency deviation $|\Delta\omega|_{max}$ from the nominal grid frequency ω^*, the constraint on the minimum value of capacitance C is given by:

$$C \geq \frac{1}{2|\Delta\omega|_{max}} \frac{\overline{V}_{oc}}{\overline{V}_{min}} \frac{|\overline{Q}_{rated}|}{\overline{P}_{rated}} = C^{min}_{|\Delta\omega|_{max}}, \tag{2.18}$$

where $\overline{Q}_{rated}$ is the rated averaged reactive power supplied or absorbed by the VOC inverter. Similarly, the constraint on capacitance C due to the maximum allowable rise time t^{max}_{rise} for the open circuit voltage $\overline{V}_{oc}$ to rise from 10% to 90% of its steady-state value is given by:

$$C \leq \frac{t^{max}_{rise}}{6} \frac{\overline{V}_{oc}}{\overline{V}_{min}} \frac{\overline{V}_{oc}^2}{\overline{V}_{oc}^2 - \overline{V}_{min}^2} = C^{max}_{t_{rise}}. \tag{2.19}$$

The third constraint on the capacitance C corresponds to the maximum allowable third harmonic to first harmonic ratio $\delta^{max}_{3:1}$ for the inverter's terminal-voltage and

is given by:

$$C \geq \frac{1}{8\omega^{\star}\delta_{3:1}^{max}} \frac{\overline{V}_{oc}}{\overline{V}_{min}} \frac{\overline{V}_{oc}^{2}}{\overline{V}_{oc}^{2} - \overline{V}_{min}^{2}} = C_{\delta_{3:1}}^{min}. \tag{2.20}$$

Hence, in order to satisfy the desired ac-performance specifications, the capacitance C is chosen according to the above three constraints, as defined below:

$$max\{C_{|\Delta\omega|_{max}}^{min}, C_{\delta_{3:1}}^{min}\} \leq C \leq C_{t_{rise}}^{max}. \tag{2.21}$$

The corresponding value for oscillator's inductance L is given by:

$$L = \frac{1}{C(\omega^{*})^{2}}. \tag{2.22}$$

2.7.3.4 Existing Literature on Dispatchable Virtual Oscillator Control

The research work in this thesis is based on the Van der Pol oscillator version of the virtual oscillator controller [76] that cannot be used for power dispatch by itself. In order to dispatch the power, external PI power control loops are proposed in this thesis. On the other hand, the recent literature on the dispatchable virtual oscillator controller (dVOC) [36–40] is an improved version of virtual oscillator that can be dispatched by incorporating the power and voltage set-points in the controller itself.

The main differences between the reported research work in this thesis and the earlier literature on dispatchable virtual oscillator control (dVOC) [36–40] are as follow.

- The embedded droop-characteristics (2.9)-(2.10) within the averaged dynamics of the Van der Pol oscillator [76] are independent of the line's $\frac{X}{R}$ ratio and do not change with the line parameters. On the other hand, the embedded droop-characteristics within the dynamics of the recently proposed dVOC depend on

and change with the line's $\frac{X}{R}$ ratio, and are described as follows [36–40]:

$$\frac{d}{dt}v = \omega_o \mathcal{J} v + \eta e_\theta(v) + \alpha e_{||v||}(v), \tag{2.23}$$

where $v \in \mathbb{R}^2$ denotes the oscillator state variable, ω_o denotes the fundamental grid frequency, η denotes the synchronisation gain, α denotes the control gain, $e_\theta(v)$ denotes the phase error, and $e_{||v||}(v)$ denotes the voltage magnitude error. The $\mathcal{J} = I_n \otimes J$, where $\otimes$ denotes the Kronecker product, I_n denotes an identity matrix of order n, and J is the matrix defined below:

$$J = \begin{bmatrix} 0 & -1 \\ 1 & 0 \end{bmatrix}. \tag{2.24}$$

The matrix K used to derive the control laws is defined as [36–40]:

$$K = \frac{1}{v^{*2}} \begin{bmatrix} \cos(\kappa) & -\sin(\kappa) \\ \sin(\kappa) & \cos(\kappa) \end{bmatrix} \begin{bmatrix} p^* & q^* \\ -q^* & p^* \end{bmatrix}, \tag{2.25}$$

where

$$\kappa = \tan^{-1}\left(\frac{\omega_o L_{line}}{R_{line}}\right). \tag{2.26}$$

The v^* denotes the voltage magnitude set-point. Similarly, the p^* and q^* denote the active and reactive power set-points, respectively. The L_{line} and R_{line} denote the line inductance and resistance, respectively.

Note that the control matrix K defined in (2.25) depends on the line's $\frac{X}{R}$ ratio, whereas the control design for the Van der Pol oscillator (that is the main focus of the proposed dispatchable inverter control technique in this thesis) is independent of the line's $\frac{X}{R}$ ratio.

- In the recent literature on dVOC [36–40], an assumption is made that the line's $\frac{X}{R}$ ratio is the same/constant for all the lines in the network. This assumption

of same/constant $\frac{X}{R}$ ratio for all the lines in the network may not always be true. For instance, the $\frac{X}{R}$ ratio in case of the overhead lines and underground cables can be quite different. Similarly, two overhead lines with different cross-sectional area can have different $\frac{X}{R}$ ratios. The dependence of dVOC controller matrix K on the line's $\frac{X}{R}$ ratio makes it unclear how to determine this matrix if an inverter is connected to two or more lines with different $\frac{X}{R}$ ratios.

On the other hand, the Van der Pol oscillator used for the proposed dispatchable inverter control technique in this thesis does not require such an assumption on the line's $\frac{X}{R}$ ratio.

- In the existing literature on dVOC [36–40], all the inverters are considered to be dispatchable without any non-dispatched inverter acting like a slack bus to compensate for the remaining power demand. In this case, only those set-points can be achieved that are consistent with the power flow equations. If a set-point is inconsistent, power dispatch cannot be achieved, and the inverters start to share power proportional to the ratio of their individual power set-points [40].

  In contrast to the existing literature on dVOC, the reported research work in this thesis is for a system with at least one non-dispatched inverter acting like a slack bus to compensate for the remaining power demand. In the reported research work, the consistent set-points are those satisfying the power security constraints (4.26) and (5.55).

In [84], a new version of the virtual oscillator controller is presented based on the dynamics of the non-linear Andronov-Hopf oscillator. Unlike the Van der Pol oscillator, the Andronov-Hopf oscillator does not contain harmonics in the output. Moreover, the power dispatch results presented in [84, 89] are for the grid-connected mode only, whereas the proposed research work in this thesis is mainly on the power dispatch of islanded inverters.

2.7.3.5 Comparison between Inverter Control Techniques

The conventional droop control strategies [61–64] use phasor quantities to calculate the active and reactive output power of an inverter, and then follow the droop control laws to regulate the system's voltage and frequency, accordingly. The calculation of active and reactive power, coordinate transformations and trigonometric function evaluations, involve complex arithmetic computations and introduce delays in the closed-loop control. Moreover, low-pass filters used to calculate the active and reactive power usually have low cut-off frequencies and impede the controller bandwidth. As a result, the dynamic behaviour of droop-controlled inverters can be much slower than virtual oscillator-controlled inverters. A comparison in terms of synchronisation and power sharing properties of these two inverter control techniques is presented in [76]. In [76, Fig. 5], it is demonstrated that the parallel-connected VO-controlled inverters synchronise 6 times faster compared to parallel-connected droop-controlled inverters. Similarly, in [76, Fig. 6], it is shown that the parallel-connected VO-controlled inverters achieve identical active and reactive power sharing faster than the droop-controlled inverters. The VOC, being a time-domain controller, uses only the instantaneous value of inverter output current to regulate the terminal-voltage magnitude and frequency, and by choosing the parameters properly, it can be designed to have a faster dynamic response compared to the conventional droop controller [90–92].

Similarly, in the case of both the virtual synchronous generators (VSGs) and PR control, voltage and current measurements are required. Further, in the case of virtual synchronous generators, the power calculations require low-pass filters that result in a slower dynamic response. Unlike conventional PR controllers, a current regulated technique is presented in [70] that does not require the calculation of inverter output power.

2.8 Stability Analysis

The most commonly used techniques to determine local as well as global stability of inverters in a microgrid include the following.

2.8.1 System Linearisation and Eigenvalues Analysis

A small-signal stability analysis of a microgrid, considering the state-space model of parallel-connected inverters, distribution network and loads, is presented in [7]. The overall system model is linearised around the operating point and the system matrix is used to determine the eigenvalues. Moreover, a sensitivity analysis is considered to determine the origin of modes, and the control scheme is designed accordingly to improve the stability of system.

2.8.2 Systems with Manifold of Equilibria

In case of power systems, at a particular operating point, the phase angle of each inverter can take an arbitrary value, however, the phase difference between all the inverters remains the same that is referred as the “rotational invariance" of the system in [39]. This results in the system having a manifold of non-hyperbolic equilibria about which the Jacobian has at least one eigenvalue on the imaginary axis.

Local stability analysis for time-invariant ODEs with a manifold of equilibria ware developed in the context of formation control of multi-agent systems in [93] using center manifold theory [94–96]. More recently, such analysis was developed for time-varying ODEs in the context of local stability analysis of sinusoidal orbits of single-phase microgrids with proportional and resonant controllers in [97], using integral manifolds of time-varying ODEs [98].

2.8.3 Sum-of-Squares Technique

As is well-known, finding a Lyapunov function to ascertain the stability of non-linear systems is challenging in general, with no general method that is applicable to all systems. Fortunately, for systems with polynomial vector fields, one can seek sum-of-squares polynomials as candidate Lyapunov functions [99–101] using semidefinite programming and linear matrix inequalities [102]. Using semidefinite programming, the Lyapunov functions can be constructed at the polynomial level in a very efficient and effective way.

2.9 Power Flow Analysis

The power flow analysis is used to determine the power flows and voltages for the transmission and distribution networks in a power system under the pre-specified bus conditions. The power flow analysis is mainly used for the steady-state analysis of the power system but also to evaluate the dynamic performance [41]. The buses in a power system are classified into the following three main categories.

- Swing/Slack bus with voltage magnitude and phase angle specified.
- Voltage-controlled/PV bus with active power and voltage magnitude specified.
- Load/PQ bus with active and reactive power specified.

In order to solve for the power flow analysis, the network equations are usually written using the system's bus impedance matrix (Zbus) or nodal admittance matrix (Ybus). The primary methods used to solve for the non-linear power flow equations include the Guass-Seidel method, Newton-Raphson method and Fast Decoupled Load Flow methods [41, 103, 104].

2.9.1 Feasible Operating Regions

The existing literature on the existence and uniqueness of power flow solutions, and security regions (feasible operating regions in terms of active and reactive power) can be found in [105–110]. Similar work on the feasible operating points for droop-controlled inverters is presented in [111, 112].

2.10 Conclusion

In this chapter, the concept of microgrids was reviewed in detail. The major motivations behind the adoption of microgrids, their modes of operation, and associated benefits were discussed. The major challenges involved in the implementation of microgrids, associated stability issues and their mitigation techniques were reviewed. Further, a hierarchical control structure and its different control layers were discussed. Moreover, the existing inverter control techniques including the droop control, proportional-resonant control and virtual oscillator control were reviewed. A brief comparison between these existing control techniques was also presented.

The virtual oscillator controller that is the main focus of this thesis was analysed in detail. The existing literature on the virtual oscillator controller, including that on synthesising the averaged virtual oscillator controller dynamics, systematic parameter design procedure to satisfy the desired ac-performance specifications, and the synchronisation conditions for virtual oscillator-controlled inverters, was reviewed. The existing literature on dispatchable virtual oscillator control was also reviewed and compared with the research work presented in this thesis, while identifying the main differences.

The most commonly used techniques to determine both local and global stability of the system, including small-signal stability analysis (i.e. system linearisation and

eigenvalue analysis), and sum-of-squares (SOS) technique to construct polynomial Lyapunov functions, were discussed. The literature on power flow analysis including the type of buses, formulation of network equations, and iterative numerical methods to solve the power flow equations was reviewed. Moreover, the existing literature on the feasible operating regions and corresponding power security constraints was presented.

Chapter 3

Regulation of Active and Reactive Power of a Virtual Oscillator Controlled Inverter

Utilisation of variable distributed energy sources in a microgrid necessitates control of active power and is enhanced by the control of reactive power. A control technique to regulate the active and reactive power of a virtual oscillator-controlled inverter is proposed in this chapter. Current feedback gain of the virtual oscillator-controlled inverter is used to regulate either the active or reactive power. In order to achieve the desired power set-point, a PI controller is used to tune the current feedback gain. An approximate local stability analysis is presented using the system linearisation and eigenvalues analysis. The constraints (3.29)-(3.33) on the virtual oscillator controller and system parameters are identified in Section 3.3.1.4 to ensure the stability of the system. The global stability of the system is investigated by determining a polynomial Lyapunov function using the sum-of-squares (SOS) technique. Simulation and experimental results are presented for both the cases of active and reactive power control of a virtual oscillator-controlled inverter to verify the analytical analysis and to demonstrate the effectiveness of the proposed control scheme.

3.1 Introduction

In this chapter[1], an output power regulation technique is proposed for a VO-controlled inverter connected to an RL load. The current feedback gain of the VOC is used to control the output power. A PI controller is used to tune the current feedback gain according to the desired output power set-point. Further, the effects of IGBTs' ON-state resistance, series resistance of LCL filter components and stray losses on the practical implementation of a virtual oscillator controller, are discussed. Note that in an islanded inverter connected to an RL load, the output power can only be controlled through the terminal voltage magnitude. Hence, either active or reactive power regulation can be achieved in a particular scenario but not both simultaneously. The control of output power in case of renewable energy sources is of vital importance. This helps in better utilisation of each energy source present in the microgrid, and reduces the line losses and stress on the transmission/distribution lines. The photo-voltaic panels should be utilised at their maximum capacity during day-time. Similarly, maximum power should be drawn from the wind turbines when it is windy. Further, the reactive power should be supplied to the inductive loads by the nearest generation source in order to reduce the line losses and stress on the distribution network. In order to investigate the local stability of the system, a system linearisation and eigenvalues analysis is considered. Constraints on both the VOC and system parameters are identified to ensure local stability of the system. Further, the global stability analysis of the system is carried out using the sum-of-squares (SOS) technique [99–101] and a polynomial Lyapunov function is determined. A brief discussion is considered on the issues related to the practical implementation of a virtual oscillator controller. Simulation and experimental results are presented for the regulation of active and reactive power to demonstrate the effectiveness of

[1]This chapter is based on conference paper [31] and journal article [1]. The co-authors, Mr. Jiacheng Li and Dr. Leonardo Callegaro provided the technical assistance and helped in the development of the experimental microgrid prototype. The co-authors, Dr. Hendra I. Nurdin and Professor John E. Fletcher supervised the research work, they being the joint and primary supervisors, respectively.

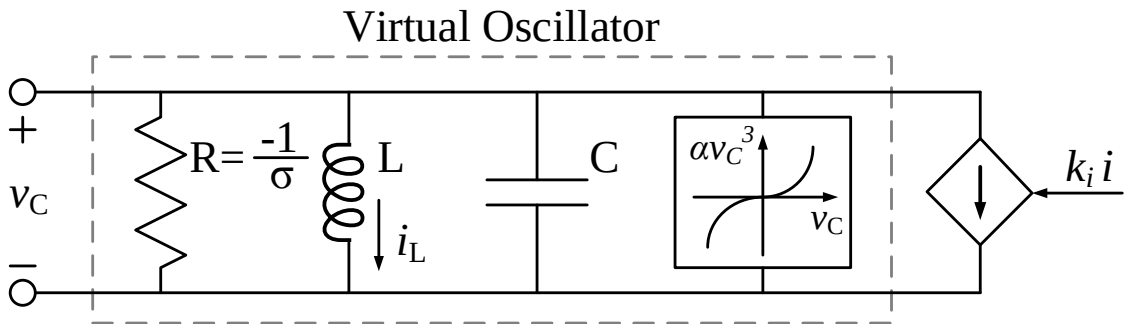

Figure 3.1: A virtual oscillator controller consists of an LC harmonic oscillator with resonant frequency ω^*. Inverter output current is denoted by i that is fed to the VOC after scaling by the current feedback gain k_i.

the proposed control scheme.

The chapter is organised as follows. In Section 3.2, the dynamics of the virtual oscillator controller and PI controller are presented. In Section 3.3, the stability analysis of the system is considered. In Section 3.4, an overall system description is presented. In Section 3.5, simulation results are presented. In Section 3.6, experimental results are discussed. In Section 3.7, the conclusion is drawn.

3.2 System Model Description

A detailed model description of both the virtual oscillator controller and PI controller is presented in this section.

3.2.1 Virtual Oscillator Controller

Recall from Chapter 2, the virtual oscillator controller is the non-linear Van der Pol oscillator with the block diagram represented in Fig. 3.1. The harmonic oscillator's capacitor voltage and inductor current are denoted by v_C and i_L, respectively. The dynamics of RMS terminal-voltage magnitude V and instantaneous phase angle ϕ are as follow, and a detailed derivation of these dynamics can be found in [19].

$$\frac{dV}{dt} = \frac{\epsilon\omega^*}{\sqrt{2}}\Big(\sigma g\big(\sqrt{2}V\cos(\phi)\big) - k_v k_i i\Big)\cos(\phi),$$
$$\frac{d\phi}{dt} = \omega^* - \frac{\epsilon\omega^*}{\sqrt{2}V}\Big(\sigma g\big(\sqrt{2}V\cos(\phi)\big) - k_v k_i i\Big)\sin(\phi), \tag{3.1}$$

where k_v denotes the voltage scaling factor, k_i denotes the current feedback gain and i denotes the inverter output current. It is hereby emphasised that the term 'virtual oscillator' means that a non-linear oscillator is implemented by programming the discretised VOC dynamic equations (as discussed earlier in Chapter 2) on the digital signal processor and an actual physical non-linear oscillator is not required for the real-world inverter control applications.

3.2.2 Averaged Model of a Virtual Oscillator Controller

Recall from Chapter 2, in order to simplfy the analysis and identify the $P-V$ and $Q-\omega$ droop-characteristics embedded within the averaged VOC dynamics, the actual VOC dynamics are averaged over an ac-cycle $\frac{2\pi}{\omega^*}$ [19]. The averaged VOC dynamics are given by:

$$\frac{d}{dt}\overline{V} = \frac{\sigma}{2C}\left(\overline{V} - \frac{\beta}{2}\overline{V}^3\right) - \frac{k_v k_i}{2C\overline{V}}\overline{P}, \tag{3.2}$$
$$\frac{d}{dt}\overline{\theta} = \omega^* - \omega + \frac{k_v k_i}{2C\overline{V}^2}\overline{Q}, \tag{3.3}$$

where $\overline{V}$ is the averaged RMS terminal-voltage magnitude, and $\overline{\theta}$ is the averaged phase-offset with respect to ωt. The $\overline{P}$ and $\overline{Q}$ are the averaged output active and reactive power, respectively. Recall from Chapter 2, the equilibrium points corresponding to the averaged VOC dynamics (3.2)-(3.3) are given by:

$$\overline{V}_{eq} = k_v\left(\frac{\sigma \pm \sqrt{\sigma^2 - 6\alpha(k_i/k_v)\overline{P}_{eq}}}{3\alpha}\right)^{\frac{1}{2}}, \tag{3.4}$$
$$\omega_{eq} = \omega^* + \frac{k_v k_i}{2C\overline{V}_{eq}^2}\overline{Q}_{eq}, \tag{3.5}$$

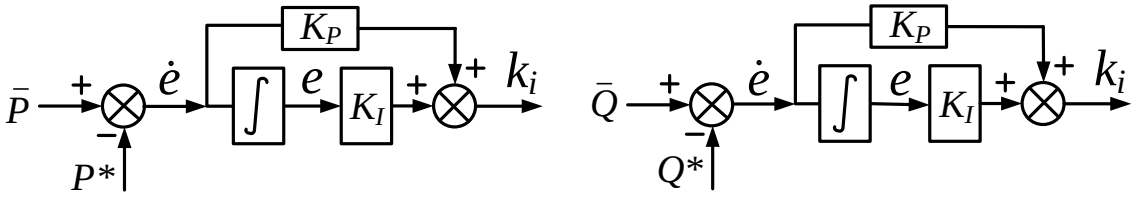

Figure 3.2: A block diagram representation of the PI controllers used to regulate either the active power $\overline{P}$ or reactive power $\overline{Q}$. The desired reference power set-points for active and reactive power are denoted by P^* and Q^*, respectively. K_I and K_P are the integral and proportional gains of the PI controller.

where $\overline{P}_{eq}$ and $\overline{Q}_{eq}$ are the equilibrium values of averaged output active and reactive power, respectively.

3.2.3 PI Controller Dynamics

The PI controllers used to regulate either the active or reactive power are shown in Fig. 3.2. Due to the dependence of terminal-voltage magnitude $\overline{V}$ on current feedback gain k_i as evident in (3.4), PI controllers are used to tune the current feedback gain k_i to regulate the inverter output power. In the case of an islanded inverter connected to an RL load, the only possible way to control the output power is through terminal-voltage magnitude. Hence, the simultaneous regulation of both the active and reactive power can not be achieved in the case of an islanded inverter. However, the simultaneous regulation of both the active and reactive power can be achieved in the case of multiple parallel-connected inverters by controlling both the magnitude and phase of the terminal-voltage, which will be considered in subsequent chapters. The dynamics of the PI controller used to regulate the active power are given by the following equations:

$$\dot{e} = \overline{P} - P^*, \tag{3.6}$$

$$k_i = K_P(\overline{P} - P^*) + K_I e, \tag{3.7}$$

where P^* is the desired active power set-point. Similarly, the dynamics of the PI controller used to regulate the reactive power are given by:

$$\dot{e} = \overline{Q} - Q^*, \tag{3.8}$$

$$k_i = K_P(\overline{Q} - Q^*) + K_I e, \tag{3.9}$$

where Q^* is the desired reactive power set-point. K_P and K_I are the proportional and integral gains of the PI controller, respectively. Let us denote the active and reactive power set-points for single-phase and three-phase power systems by $(P^*_{1\phi}, Q^*_{1\phi})$ and $(P^*_{3\phi}, Q^*_{3\phi})$, respectively.

3.3 Approximate Stability Analysis

In order to investigate the stability of the closed-loop system consisting of a VO-controlled inverter, a PI controller to regulate the output power and an RL load, both local and global stability analysis are considered. The proposed stability analysis is approximate as it is based on the averaged approximate model of the VOC instead of the actual VOC dynamics (3.1). Further, constraints are identified on the system and VOC parameters to ensure local stability of the system under parametric variations.

3.3.1 Local Approximate Stability Analysis

A local approximate stability analysis is presented in this section. A system linearisation and eigenvalues analysis are considered.

3.3.1.1 Equilibrium Points

Under the assumption $\omega_{eq} = \omega^*$, the active power $\overline{P}$ can be expressed in terms of load impedance z_L with magnitude Z and angle θ_z as follows:

$$\overline{P} = \frac{\overline{V}^2}{Z}\cos(\theta_z). \tag{3.10}$$

The closed-loop equilibrium points for the PI controller and averaged VOC dynamics can be determined using (3.2), (3.6), and (3.10). The equilibrium points are as follow:

$$\overline{V}_{eq} = \sqrt{\frac{ZP^*}{\cos(\theta_z)}}, \tag{3.11}$$

$$\overline{V}_{eq} = \sqrt{\frac{2}{\beta}\left(1 - \frac{k_v k_{i,eq}\cos(\theta_z)}{\sigma Z}\right)}. \tag{3.12}$$

Equating (3.11) and (3.12), we have:

$$k_{i,eq} = \left(\frac{\sigma\overline{V}_{eq}^2}{k_v} - \frac{3\alpha\overline{V}_{eq}^4}{2k_v^3}\right)\frac{1}{P^*}. \tag{3.13}$$

At equilibrium we have $\overline{P} = P^*$ and from (3.7) we get:

$$e_{eq} = \frac{k_{i,eq}}{K_I} = \left(\frac{\sigma\overline{V}_{eq}^2}{k_v} - \frac{3\alpha\overline{V}_{eq}^4}{2k_v^3}\right)\frac{1}{K_I P^*}. \tag{3.14}$$

In addition to the above equilibrium points (3.11) and (3.14), there is another equilibrium point i.e. $\overline{V}_{eq} = 0$. This equilibrium point corresponds to zero stored energy in the harmonic oscillator capacitor C and inductor L. This state is only achievable when there is no energy present in the LC harmonic oscillator. However, if the harmonic oscillator is once energised and oscillating, this equilibrium point is not achievable. Further from (3.2), (3.7), and (3.10), it can be seen that the system dynamics do not depend on the averaged phase-offset $\overline{\theta}$. Thus, $\overline{\theta}$ is not considered for the stability analysis of the system. As discussed earlier, in the case of an islanded

inverter connected to an RL load, the output power only depends on the terminal voltage magnitude $\overline{V}$.

3.3.1.2 Linearised System

The approximate non-linear averaged VOC dynamics in state-space form are given by:

$$\dot{x} = \begin{pmatrix} \dot{\overline{V}} \\ \dot{e} \end{pmatrix} = f(x), \tag{3.15}$$

$$f(x) = \begin{pmatrix} \left(\frac{\sigma}{2C} - \frac{k_v\left(K_P(\overline{P}-P^*)+K_I e\right)\cos(\theta_z)}{2CZ}\right)\overline{V} - \frac{\sigma\beta}{4C}\overline{V}^3 \\ \left(\frac{\overline{V}^2}{Z}\cos(\theta_z) - P^*\right) \end{pmatrix}, \tag{3.16}$$

where $x = [\overline{V},\, e]^T$. The linearised system is as follows:

$$A = \left.\frac{\partial f}{\partial x^T}\right|_{x=x^*} = \left.\begin{bmatrix} \frac{\partial f_1}{\partial \overline{V}} & \frac{\partial f_1}{\partial e} \\ \frac{\partial f_2}{\partial \overline{V}} & \frac{\partial f_2}{\partial e} \end{bmatrix}\right|_{x=x^*}, \tag{3.17}$$

where

$$A_{11} = \frac{\partial f_1}{\partial \overline{V}} = \left(\frac{\sigma}{2C} + \frac{k_v(K_P P^* - K_I e_{eq})\cos(\theta_z)}{2CZ}\right) - \left(\frac{3k_v K_P \cos^2(\theta_z)}{2CZ^2} + \frac{3\sigma\beta}{4C}\right)\overline{V}_{eq}^2, \tag{3.18}$$

$$A_{12} = \frac{\partial f_1}{\partial e} = -\frac{k_v K_I \cos(\theta_z)}{2CZ}\overline{V}_{eq}, \tag{3.19}$$

$$A_{21} = \frac{\partial f_2}{\partial \overline{V}} = \frac{2\cos(\theta_z)}{Z}\overline{V}_{eq}, \tag{3.20}$$

$$A_{22} = \frac{\partial f_2}{\partial e} = 0. \tag{3.21}$$

3.3.1.3 Eigenvalues Analysis

The eigenvalues of a system can be calculated using the linearised system equations and equilibrium points. The eigenvalues are:

$$|A - \lambda I| = \lambda^2 - \lambda A_{11} - A_{12}A_{21} = 0, \tag{3.22}$$

$$\lambda = \frac{A_{11} \pm \sqrt{A_{11}^2 + 4A_{12}A_{21}}}{2}. \tag{3.23}$$

3.3.1.4 Stability Constraints

For a system to be asymptotically stable around the equilibrium points (3.11) and (3.14), the real part of the eigenvalues (that are the roots of the characteristic equation (3.22)) must be negative. Hence, the constraints on the system parameters can be identified as follows:

$$A_{11} < 0, \tag{3.24}$$

$$4A_{12}A_{21} < 0. \tag{3.25}$$

The condition $A_{11} < 0$ implies,

$$\overline{V}_{eq} > \sqrt{\frac{2Z\left(\sigma Z + kv\left(K_P P^* - K_I e_{eq}\right)\cos(\theta_z)\right)}{6k_v K_P \cos^2(\theta_z) + 3\sigma\beta Z^2}}. \tag{3.26}$$

For a non-negative value of proportional gain $K_P \geq 0$, the denominator on the right hand side of (3.26) is always positive. For the right hand side of (3.26) to be real valued, we have the following constraint:

$$K_I e_{eq} \leq K_P P^* + \frac{\sigma Z}{k_v \cos(\theta_z)}. \tag{3.27}$$

Similarly, for $4A_{12}A_{21} < 0$, we have:

$$-\frac{K_I k_v \cos^2(\theta_z)}{CZ^2}\overline{V}_{eq}^2 < 0, \tag{3.28}$$

which implies:

$$k_v > 0, \tag{3.29}$$

$$K_I > 0, \tag{3.30}$$

$$\overline{V}_{eq} \neq 0, \tag{3.31}$$

$$-90^\circ < \theta_z < 90^\circ, \tag{3.32}$$

$$0 < Z < \infty. \tag{3.33}$$

Hence, these stability constraints ensure local stability of the closed-loop system under the variations in system parameters as long as none of these is violated. Fig. 3.3 shows the plot of system eigenvalues as a function of $P^*_{1\phi} : 0.1 \rightarrow 666$ W (or equivalently $P^*_{3\phi} : 0.3 \rightarrow 2000$ W) for the system parameters in Table 3.2 and PI controller gains as in Section 3.5. Note that the real part of eigenvalues is always negative in Fig. 3.3.

3.3.1.5 Root Locus Analysis

A detailed analysis of the root locus in Fig. 3.3 is considered. The system's states (i.e. $\overline{V}$ and e) are perturbed around the equilibrium point and the corresponding behaviour of the system is observed under the disturbance. The perturbations (i.e. $\delta\overline{V}$ and δe) in the system's states are chosen to be 10% of the corresponding steady-state values (i.e. V_{eq} and e_{eq}). In order to perturb the state $\overline{V}$, the VOC output voltage v_C is transformed to the $dq-$reference frame (with $v_C^q = 0$) and v_C^d is perturbed around the equilibrium point v_{Ceq}^d by a 10% perturbation δv_C^d. Five different cases are considered corresponding to the power set-points and eigenvalues as in Table

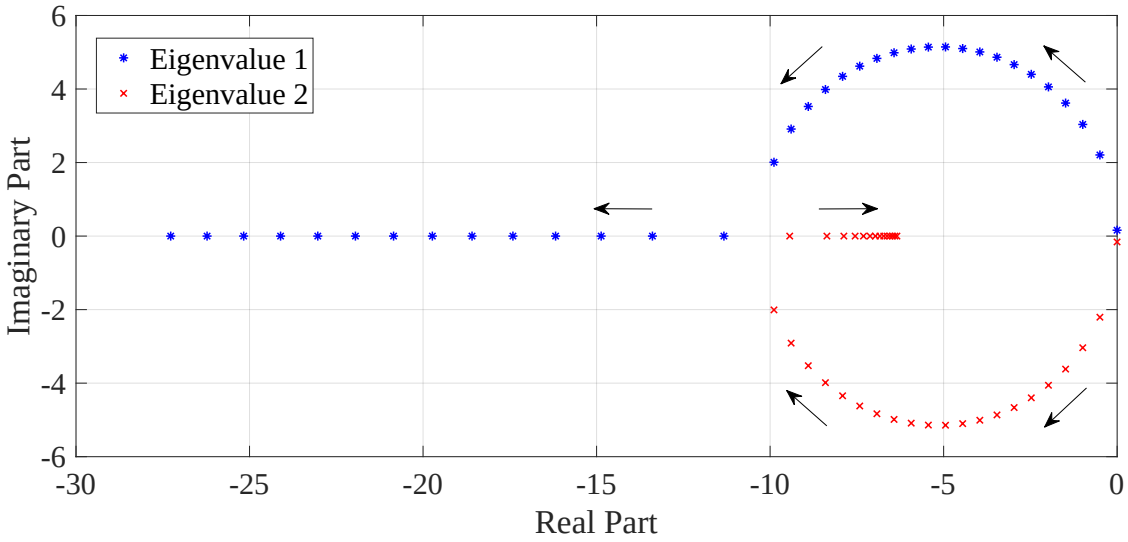

Figure 3.3: A plot of system eigenvalues as a function of $P^*_{1\phi}$: 0.1 $\rightarrow$ 666 W (or equivalently $P^*_{3\phi}$: 0.3 $\rightarrow$ 2000 W). The real part of both the eigenvalues remains negative through-out the range of P^*.

3.1. Fig. 3.4 shows the response of the system when perturbed in steady-state for different power set-points. The system is perturbed at $t = 5$ s for Case 1 and at $t = 1$ s for rest of the cases. It can be seen that the settling time ($t_s = 8$ s) is highest for Case 1 with the eigenvalues nearest to the imaginary axis as compared to the other power set-points. Similarly, the settling time ($t_s = 0.3$ s) is lowest for Case 5 with eigenvalues away from the imaginary axis as compared to the other power set-points. Hence, the simulation results in Fig. 3.4 corresponding to different power set-points validate the analytical findings.

Further, it is demonstrated that other than on the power set-point P^*, the shape of root locus also depends on the proportional gain K_P and integral gain K_I of the PI controller for a fixed impedance RL load. Fig. 3.5 shows the variations in the trajectory of the root locus for different values of proportional and integral gains of the PI controller with system parameters as in Table 3.2. Hence, using the aforementioned root locus analysis, the PI controller gains can be designed to get an adequate system response as a function of output power set-point P^*.

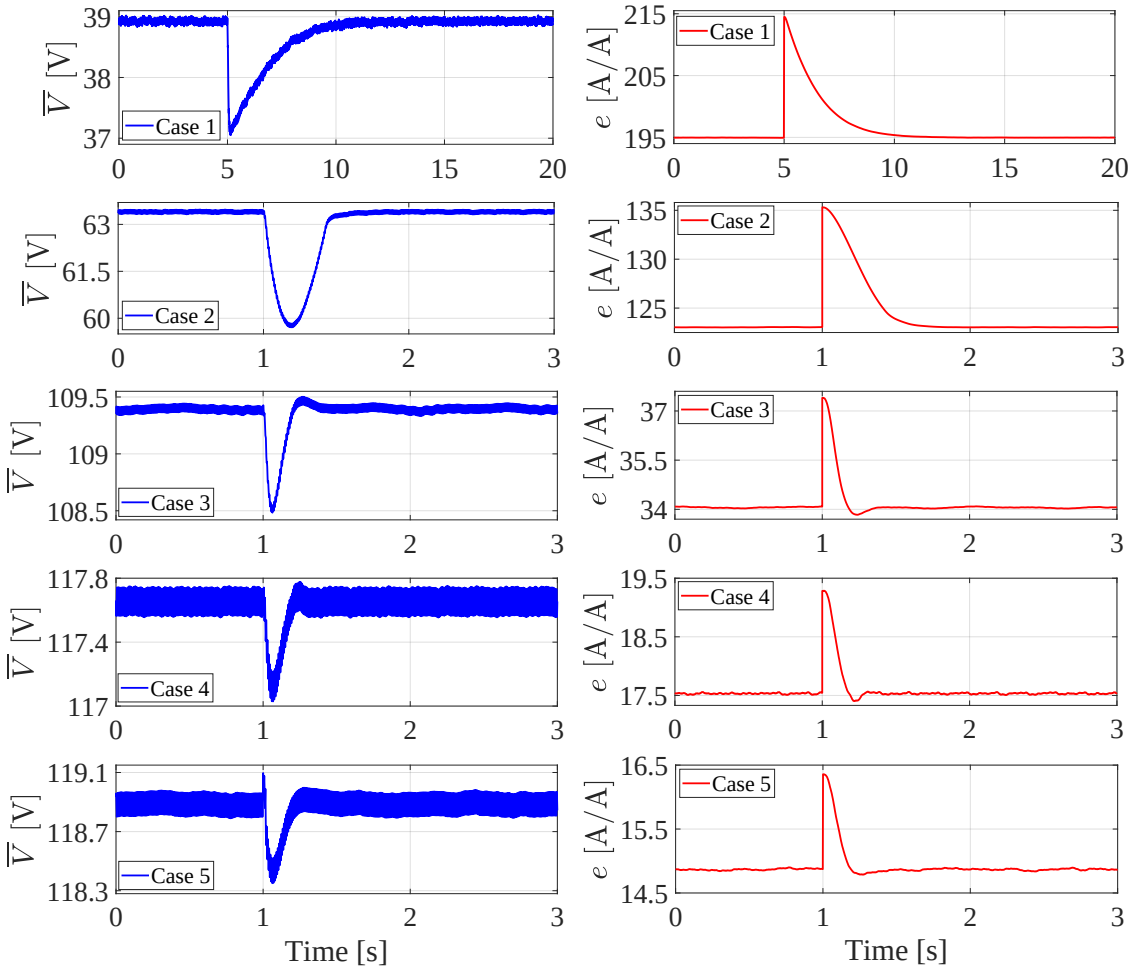

Figure 3.4: The system's response is presented for perturbations in the system's states (i.e. $\overline{V}$ and e) around the equilibrium point corresponding to the five different cases described in Table 3.1.

3.3.2 Global Approximate Stability Analysis

In order to investigate the global stability of the system, a polynomial Lyapunov function is constructed using the sum-of-squares (SOS) technique. Recall from Section 2.8.3, the stability of non-linear dynamical equations with polynomial vector fields can be analysed using the sum-of-squares approach.

3.3.2.1 Sum-of-Squares Technique

Considering the averaged VOC dynamics with parameters as in Table 3.2, the following polynomial Lyapunov function is constructed using the SOS technique for a

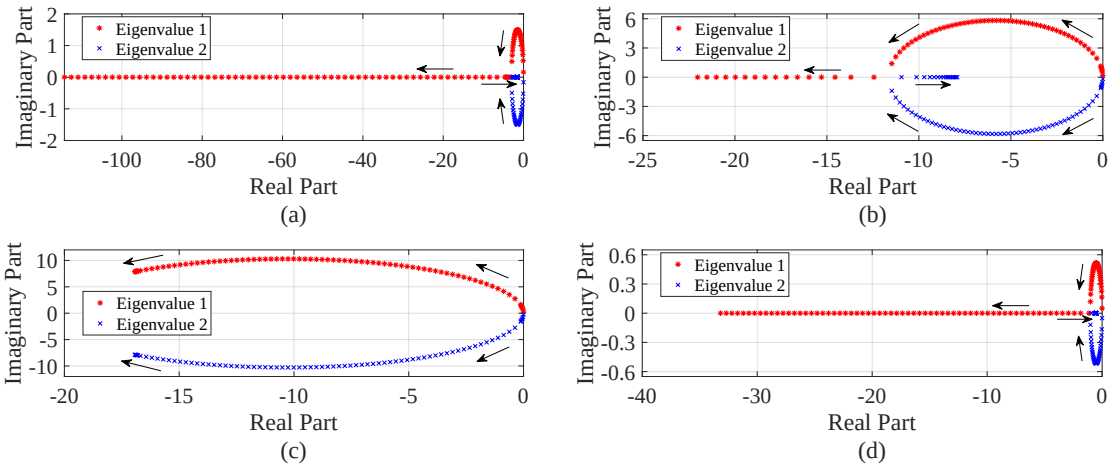

Figure 3.5: A plot of system's eigenvalues as a function of $P^*_{1\phi} : 0.1 \rightarrow 666$ W (or equivalently $P^*_{3\phi} : 0.3 \rightarrow 2000$ W) for different values of PI controller gains (i.e. K^ι_P and K^ι_I): (a) $K^\iota_P = 20K_P$ and $K^\iota_I = K_I$, (b) $K^\iota_P = K_P/10$ and $K^\iota_I = K_I$, (c) $K^\iota_P = K_P$ and $K^\iota_I = 2K_I$, (d) $K^\iota_P = K_P$ and $K^\iota_I = K_I/10$. The K_P and K_I are defined in Section 3.5.

Table 3.1: Root Locus Analysis – Power Set-points and Eigenvalues

Case	Power Set-point [W]	Eigenvalue 1	Eigenvalue 2
1	$P^*_{1\phi} = 017.0$	$-0.4 + 2.0i$	$-0.4 - 2.0i$
2	$P^*_{1\phi} = 077.0$	$-1.9 + 4.0i$	$-1.9 - 4.0i$
3	$P^*_{1\phi} = 339.0$	$-8.4 + 4.0i$	$-8.4 - 4.0i$
4	$P^*_{1\phi} = 400.0$	$-9.9 + 2.0i$	$-9.9 - 2.0i$
5	$P^*_{1\phi} = 416.5$	-10.3	-10.3

reference power set-point $P^*_{1\phi} = 500$ W (or equivalently $P^*_{3\phi} = 1500$ W):

$$\begin{aligned}\mathcal{V} &= 3.092 \times 10^{-5}x_1^4 + 3.592 \times 10^{-5}x_1^3x_2 + 0.01327x_1^3 + 6.121 \times 10^{-5}x_1^2x_2^2 \\ &+ 0.02618x_1^2x_2 + 2.941x_1^2 + 7.768 \times 10^{-6}x_1x_2^3 + 0.004259x_1x_2^2 + 0.9725x_1x_2 \\ &+ 3.033 \times 10^{-5}x_2^4 + 0.01196x_2^3 + 1.872x_2^2, \end{aligned} \tag{3.34}$$

where $x_1 = \overline{V}$ and $x_2 = e$.

Table 3.2: System Parameters

Symbol	Parameter	Value	Unit
k_i	Current feedback gain	[variable]	A/A
k_v	Voltage scaling factor	126	V/V
σ	Conductance	6.09	Ω^{-1}
α	Cubic-current source coefficient	4.06	A/V^3
L	Virtual oscillator inductance	3.35×10^{-5}	H
C	Virtual oscillator capacitance	0.21	F
R_L	Resistance - series RL load	22.3	Ω
L_L	Inductance - series RL load	12.2	mH

3.4 System Description

A three-phase system is considered as shown in Fig. 3.6. It consists of a three-phase inverter with an output LCL filter connected to a load impedance z_L. The three-phase currents are measured and a coordinate transformation $i_{abc} \rightarrow i_{\alpha\beta}$ is used. The current i_α is fed back to the VOC after scaling by the current feedback gain k_i. Similarly, a coordinate transformation $v_{\alpha\beta} \rightarrow v_{abc}$ is used to generate the modulation signals m_{abc} for the three-phase inverter. The current feedback gain k_i is generated by the PI controller according to the desired reference power set-point P^* or Q^*. The coordinate transformations for a signal h from $h_{abc} \rightarrow h_{\alpha\beta}$ or $h_{\alpha\beta} \rightarrow h_{abc}$ are given by the following equations:

$$\begin{bmatrix} h_\alpha \\ h_\beta \end{bmatrix} = \frac{2}{3} \begin{bmatrix} 1 & -\frac{1}{2} & -\frac{1}{2} \\ 0 & \frac{\sqrt{3}}{2} & -\frac{\sqrt{3}}{2} \end{bmatrix} \begin{bmatrix} h_a \\ h_b \\ h_c \end{bmatrix}, \tag{3.35}$$

$$\begin{bmatrix} h_a \\ h_b \\ h_c \end{bmatrix} = \begin{bmatrix} 1 & -\frac{1}{2} & -\frac{1}{2} \\ 0 & \frac{\sqrt{3}}{2} & -\frac{\sqrt{3}}{2} \end{bmatrix}^T \begin{bmatrix} h_\alpha \\ h_\beta \end{bmatrix}. \tag{3.36}$$

3.4.1 Tuning the Current Feedback Gain

In the case of an islanded inverter connected to an RL load, the output power can be regulated through the terminal-voltage magnitude. Based on the dependence of terminal-voltage magnitude $\overline{V}$ on current feedback gain k_i, PI controllers are used that tune the current feedback gain k_i to achieve the desired power set-point. Further, as there is only one control parameter $\overline{V}$, simultaneous regulation of both active and reactive power cannot be achieved in this case.

3.4.2 Designing PI Controller Gains

The non-linear dynamics of the VOC result in a non-linear relation between current feedback gain k_i and terminal-voltage magnitude $\overline{V}$. In order to achieve the desired dynamic performance and avoid the power oscillations around the equilibrium point, the PI controller gains (K_P and K_I) should be designed as a function of load impedance. The PI controller gains designed for a particular load impedance do not necessarily give the same dynamic performance for a different load. In order to systematically design the PI controller gains, the pole assignment technique [113] can be used for a known fixed impedance load. Using the linearised system model along with the PI controller dynamics, the characteristic equation parameters i.e. damping ratio ζ and natural frequency ω_n for the second order system can be designed to get the desired dynamic performance with terminal-voltage magnitude as a state-feedback. The PI controller gains (K_P and K_I) are then calculated based on the designed values of damping ratio ζ and natural frequency ω_n. However, in this chapter, we are interested in regulating the output power of the inverter.

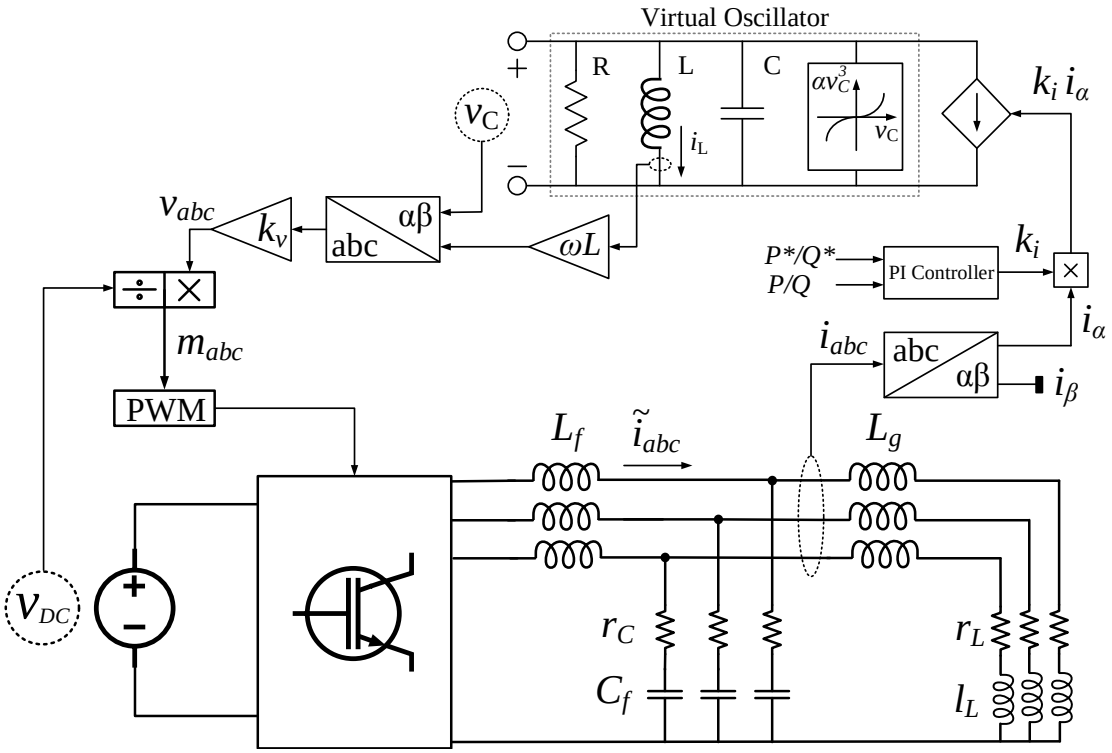

Figure 3.6: An overall system representation consisting of a three-phase inverter with an output LCL filter, a virtual oscillator controller and a PI controller. A series RL load z_L is used with parameters R_L and L_L. The $\tilde{i}_{abc}$ and i_{abc} denote the inverter filter and output currents, respectively.

Therefore, the output power is used as a feedback (instead of the state-variable i.e. terminal-voltage magnitude) to the PI controller with proportional and integral gains determined through trial and error to get an adequate dynamic response. Due to the presence of an external power control loop instead of the state-feedback loop, the pole assignment technique to systematically design the PI controller gains cannot be used directly in this case. A systematic procedure to design the PI controller gains is not considered in this thesis and is a possible topic future work.

3.5 Simulation Results

The simulation results are presented for both the active and reactive power regulation. MATLAB is used to perform the simulations. The system parameter values and ac-performance specifications are provided in Table 3.2 and Table 3.3, respec-

Table 3.3: AC Performance Specifications

Symbol	Parameter	Value	Unit
$\overline{V}_{oc}$	RMS open-circuit voltage	126	V
$\overline{V}_{min}$	RMS rated power voltage	114	V
$\overline{P}_{rated}$	Rated active power	2000	W
$\lvert\overline{Q}_{rated}\rvert$	Rated reactive power	2000	VAr
ω^*	Nominal oscillator frequency	$2\pi 60$	rad/s
$\lvert\Delta\omega\rvert_{max}$	Maximum frequency offset	$2\pi 0.5$	rad/s
t_{rise}^{max}	Maximum rise time	0.3	s
$\delta_{3:1}^{max}$	3^{rd} to 1^{st} harmonic ratio	1	%

tively. The values for output LCL filter parameters are $L_f = 1.8$ mH, $C_f = 4.7\,\mu$F with $r_C = 3.3\,\Omega$, and $L_g = 0.5$ mH.

3.5.1 Active Power Regulation

The response of a VO-controlled inverter for step changes in active power set-point $P_{3\phi}^*$ is shown in Fig. 3.7. The PI controller gains are $K_I = 0.01$ and $K_P = 0.00025$. Initially at $t = 0$ s, the inverter is operating at $P_{3\phi}^* = 1600$ W. A step-up change in $P_{3\phi}^* : 1600 \rightarrow 2000$ W is applied at $t = 1$ s. In the same way, a step-down change is applied in $P_{3\phi}^* : 2000 \rightarrow 1400$ W at $t = 2$ s. The inverter tracks the desired active power set-points effectively and reaches the new steady-state operating points in less than 200 ms. The output voltage variations to achieve the desired power set-points are also shown in Fig. 3.7.

3.5.2 Reactive Power Regulation

The response of a VO-controlled inverter for step changes in reactive power set-point $Q_{3\phi}^*$ is presented in Fig. 3.8. The PI controller gains are $K_I = 0.065$ and

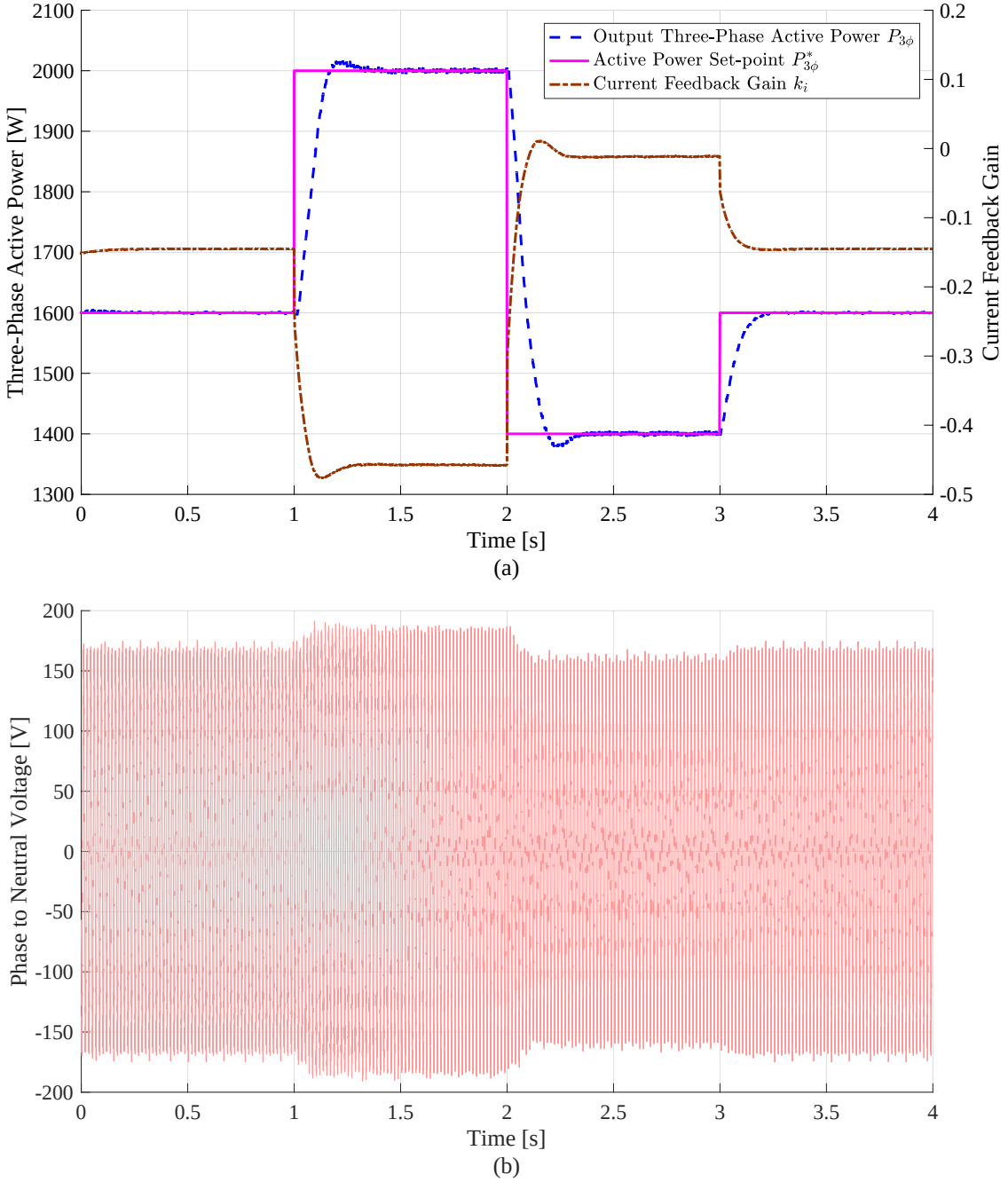

Figure 3.7: The response of a VO-controlled inverter for step changes in $P^*_{3\phi}$: (a) active power, active power set-point and current feedback gain, (b) output phase to neutral voltage. The PI controller tunes the current feedback gain (dash-dotted line) to adjust the output voltage magnitude. The active power (dashed line) tracks the reference power set-points (solid line) effectively.

$K_P = 0.0025$. Initially at $t = 0$ s, the inverter is operating at $Q^*_{3\phi} = 300$ VAr. At $t = 1$ s, a step-up change in reactive power set-point $Q^*_{3\phi} : 300 \rightarrow 400$ VAr is applied. In order to observe the response of the inverter for a step-down change, at $t = 2$ s, a step-down change is applied in $Q^*_{3\phi} : 400 \rightarrow 250$ VAr. The PI controller tunes the current feedback gain and effectively tracks the desired power set-points. The inverter reaches the new steady-state operating points in approximately 200 ms.

Remark 3.1. *While regulating the output power, the output voltage magnitude may drop below the threshold $\overline{V}_{min}$. This is because in the case of an islanded inverter connected to a fixed impedance load, the only way to regulate the output power is through terminal-voltage magnitude. Further, for a higher value of current feedback gain and a reduced output voltage magnitude corresponding to a significantly lower value of output power set-point (mainly for highly inductive loads), the frequency deviation from the nominal value ω^* may be higher then the threshold $|\Delta\omega|_{max}$. This deviation in frequency from the nominal value is evident from* (3.5).

3.6 Experimental Results

In this section, experimental results are presented for both the cases of active and reactive power control. The non-linear dynamics of VOC are discretised using the trapezoidal rule of integration (as discussed earlier in Chapter 2) at the sampling time T_s and implemented on a Texas Instruments TMS320F28379D digital signal processor. A three-phase inverter with an output LCL filter is used. The LCL filter parameters are the same as for simulation results. The inverter switching frequency $f_{sw} = 10\,\text{kHz}$ and a space vector PWM are used. The sampling time $T_s = 100\,\mu\text{s}$ and the dead-time $T_D = 2\,\mu\text{s}$. A series RL load with resistance $R_L = 22.3\,\Omega$ and inductance $L_L = 12.2$ mH is used for the experimental results.

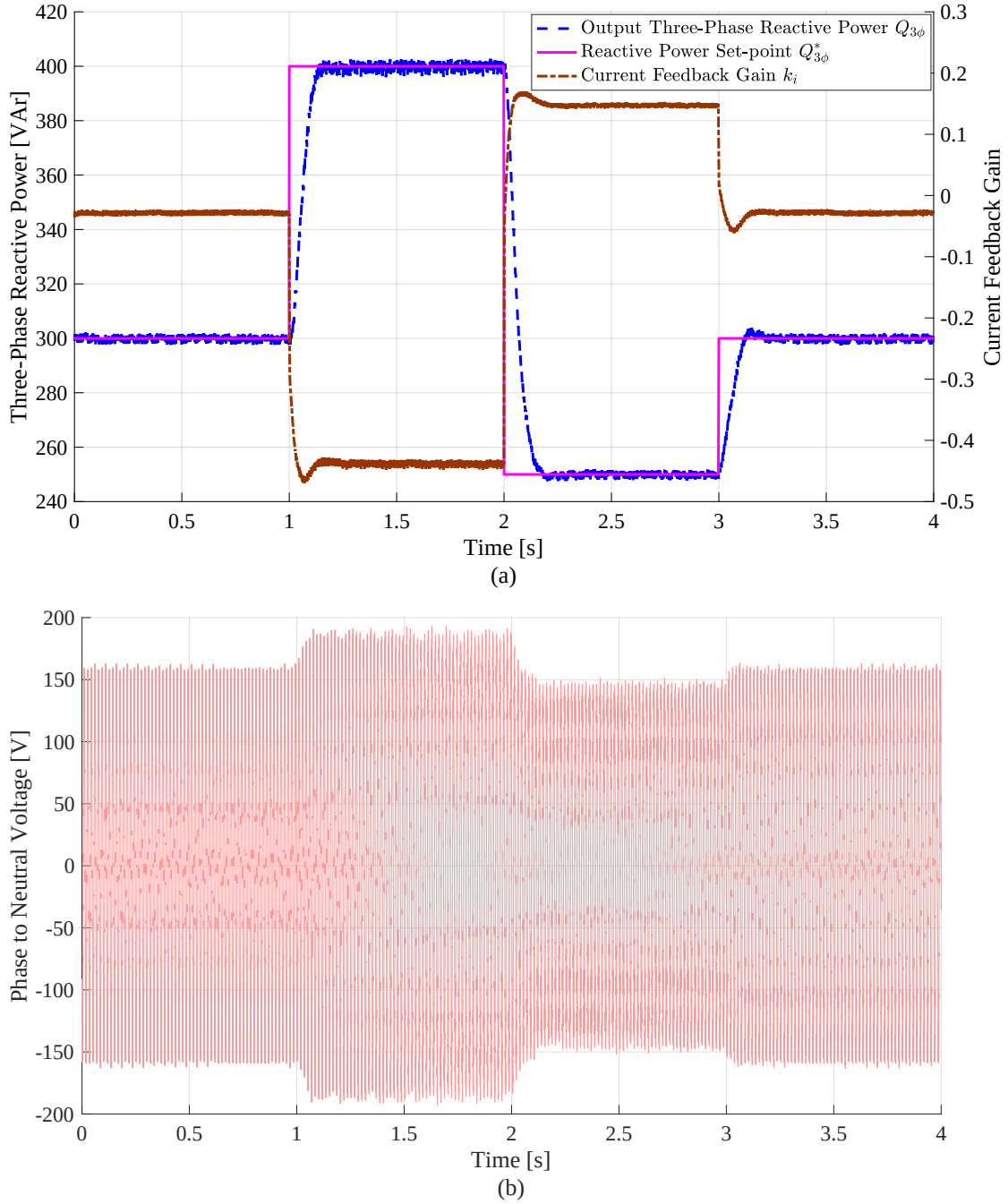

Figure 3.8: The response of a VO-controlled inverter for step changes in $Q^*_{3\phi}$: (a) reactive power, reactive power set-point and current feedback gain, (b) output phase to neutral voltage. The inverter tracks the reference set-points (solid line) effectively and reaches the new equilibrium points in approximately 200 ms. The variations in current feedback gain (dash-dotted line) to adjust the output voltage magnitude corresponding to the desired reactive power set-points can be seen in the figure.

3.6.1 Active Power Regulation

Fig. 3.9 shows the dynamic behaviour of a VO-controlled inverter for step changes in active power set-point $P^*_{3\phi}$. The PI controller gains are the same as in the simulation results. Initially at $t = 0$ s, the inverter is operating at $P^*_{3\phi} = 1600$ W. A step-up change is applied in $P^*_{3\phi} : 1600 \rightarrow 2000$ W at $t = 1$ s. At $t = 2$ s, a step-down change is applied in $P^*_{3\phi} : 2000 \rightarrow 1400$ W. At $t = 3$ s, the set-point is changed back to the initial value $P^*_{3\phi} = 1600$ W. The inverter follows the desired active power set-points effectively and reaches the new equilibrium points in less than 200 ms. The output voltage magnitude varies in order to achieve the desired power set-points.

3.6.2 Reactive Power Regulation

In Fig. 3.10, the response of a VO-controlled inverter for step-changes in reactive power set-point $Q^*_{3\phi}$ is presented. The PI controller gains are the same as for simulation results. Initially, at $t = 0$ s, the inverter is operating at $Q^*_{3\phi} = 300$ VAr. At $t = 1$ s, a step-up change is applied in $Q^*_{3\phi} : 300 \rightarrow 400$ VAr. In the same way, at $t = 2$ s, a step-down change is applied in $Q^*_{3\phi} : 400 \rightarrow 250$ VAr. At $t = 3$ s, the set-point is changed back to the initial value $Q^*_{3\phi} = 300$. The response time of the inverter is approximately 200 ms and it tracks the desired set-points effectively.

Remark 3.2. *Comparing the simulation and experimental results, it can be seen that the response time of inverter is nearly the same and the inverter tracks the desired power set-points effectively in both cases. However, a difference in the values of current feedback gain k_i can be observed between the simulation and experimental results. This difference in the current feedback gains is due to the ON-state resistance of IGBTs in an actual physical inverter, the series resistance of LCL filter inductors and voltage loss/gain at each switching cycle due to the dead-time (as there is no voltage feedback loop in the case of a virtual oscillator-controlled inverter). As these losses are not considered in the simulation results, the same desired power set-points*

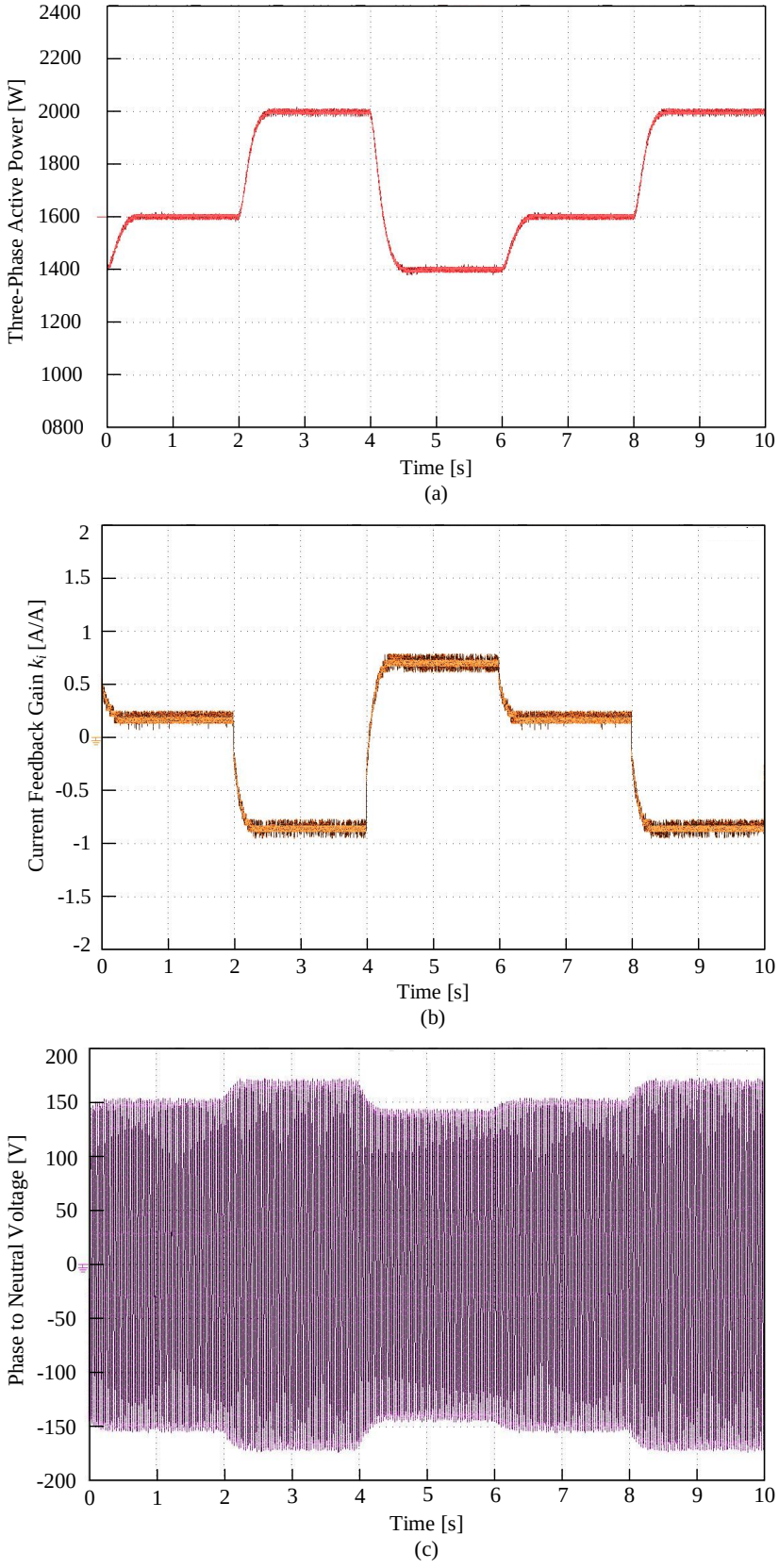

Figure 3.9: The response of a VO-controlled inverter for step changes in $P^*_{3\phi}$: (a) active power, (b) current feedback gain, (c) output phase to neutral voltage. The inverter tracks the desired power set-points effectively. The variations in current feedback gain to achieve the desired power set-points can be seen in the figure.

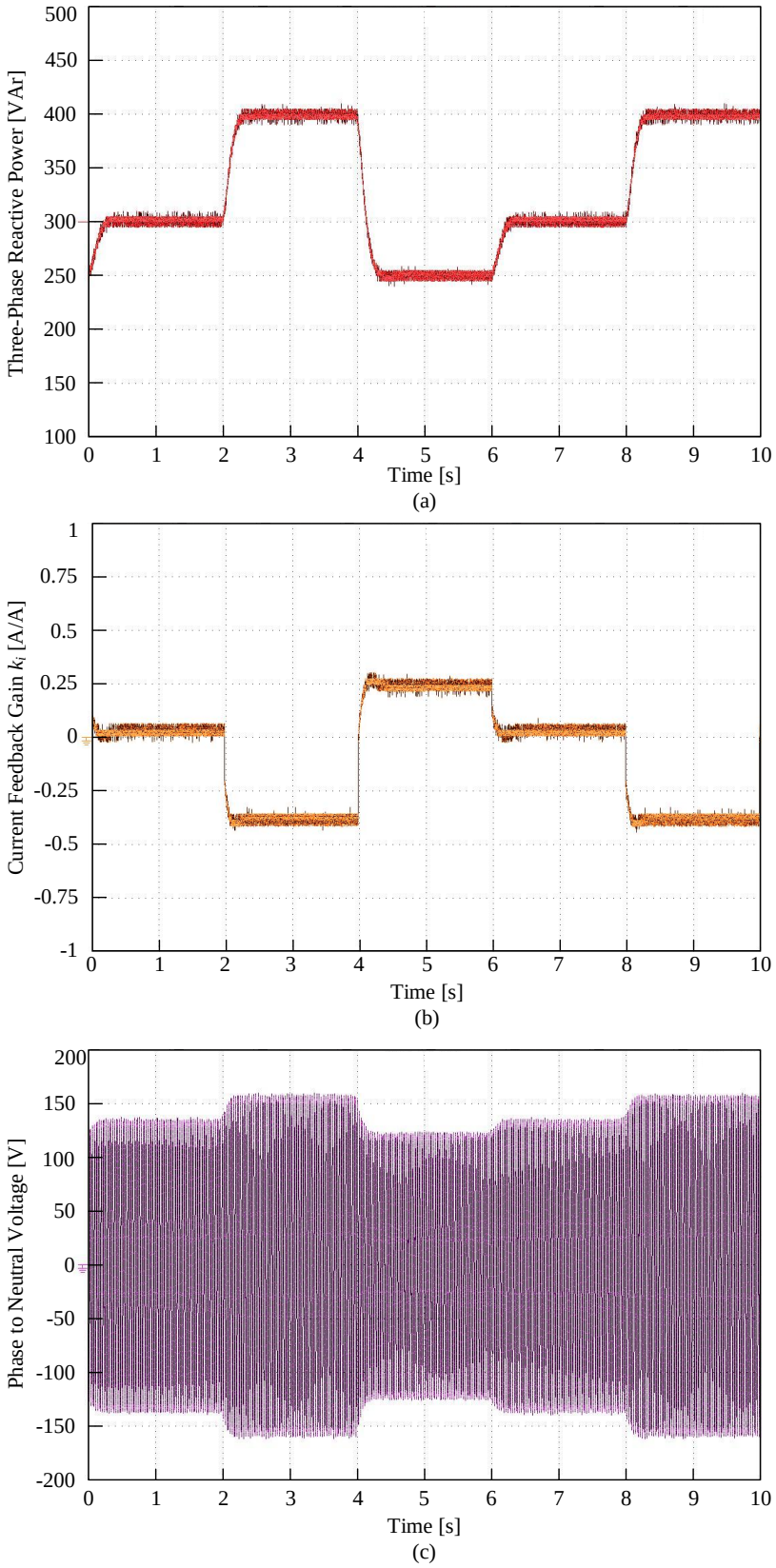

Figure 3.10: The response of a VO-controlled inverter for step changes in $Q^*_{3\phi}$: (a) reactive power, (b) current feedback gain, (c) output phase to neutral voltage. Inverter tracks the desired set-points effectively and settles at the new operating points in approximately 200 ms. The PI controller tunes the current feedback gain to achieve the desired power set-points.

are achieved in both simulation and experimental results with relatively different values of current feedback gain. In order to compensate for these inverter non-linearities, inner control loops are proposed in Chapter 6.

3.7 Conclusion

A control technique to regulate the active and reactive power of a virtual oscillator-controlled inverter is presented. The current feedback gain of the VOC is used to regulate the output power. It is demonstrated that using a PI controller that tunes the current feedback gain, output power regulation can be achieved. The closed-loop system is linearised and eigenvalues analysis is presented to investigate the local stability of the system. Constraints are derived on the system and VOC parameters that ensure local stability. A polynomial Lyapunov function is constructed using the sum-of-squares technique to demonstrate the global stability of the system for a particular reference power set-point. The stability analysis considered is approximate as it is based on the averaged VOC model rather than the actual Van der Pol oscillator model. In order to verify the analytical treatment, simulation and experimental results are presented. It is shown that with the proposed control strategy, the inverter follows the desired power set-points effectively.

Chapter 4

Dispatchable Virtual Oscillator Control for Single Phase Islanded Inverters: Analysis and Experiments

The increased penetration of renewable energy sources into the power system has resulted in a need for dispatchable control for the inverters. Dispatchable generation enables intelligent use of power sources thus enhancing the system's efficiency, reliability and reducing the stress on the distribution lines. In this chapter, a dispatchable control for virtual oscillator-controlled inverters is proposed to achieve simultaneous regulation of both the active and reactive power in a single-phase system of m-controlled and n-uncontrolled inverters. Further, a set of security constraints is derived to determine the achievable power set-points for each controlled inverter present in the system. The dispatchable controller parameters corresponding to the desired power set-point can be determined using the proposed control laws. A technique to design the control parameters and line impedance for the uncontrolled inverters is presented to enable optimal power sharing proportional to their power ratings. Simulation and experimental results are presented for the power regulation of multiple virtual oscillator-controlled inverters connected to a load through respective line impedances. The proposed dispatchable control strategy effectively

regulates both the active and reactive power of the controlled inverters for a number of cases and in a wide operating range[1].

4.1 Introduction

Dispatchable power generation has gained a lot of attention with the increased penetration of renewable energy sources (RESs) into the power system. Power dispatch is a smart and intelligent way to utilise the power sources resulting in increased efficiency as well as reduced distribution lines losses and stress. Due to the intermittent nature of renewable energy sources, a power regulation technique is of vital importance. This necessitates a dispatchable control technique for the inverters used as interfaces to connect these renewable energy sources with the power system. The recent work on the dispatchable control of inverters can be found in [1, 31, 32, 36–40, 84, 89].

This chapter is an extension of the work presented in Chapter 3 and and is unlike the existing literature on VOC oscillators (dead-zone and Van der Pol), that does not include discussion on dispatchable generation [2, 16, 18, 20, 76]. A dispatchable control technique is proposed to simultaneously regulate both the active and reactive power of parallel-connected virtual oscillator-controlled inverters in a system consisting of m-controlled and n-uncontrolled inverters connected to a common constant power or / and a fixed impedance load through respective line impedances. Unlike the recent literature on dispatchable virtual oscillator control (dVOC) [36–40], the work presented in this chapter is based on the Van der Pol oscillator for which the steady-state droop-characteristics embedded within the averaged dynamics are independent of the line's $\frac{X}{R}$ ratio. Further in contrast to the existing literature [36–40], the system considered in this chapter consists of a mix of

[1]This chapter is based on conference paper [32] and journal article [33]. The co-authors, Dr. Hendra I. Nurdin and Professor John E. Fletcher supervised the research work, they being the joint and primary supervisors, respectively.

both the dispatchable inverters and uncontrolled (non-dispatchable) inverters acting as slack bus to compensate for the remaining load demand. The output power is regulated for the m-controlled inverters, whereas the n-uncontrolled inverters share the remaining load power proportionally. The active and reactive power regulation is achieved by continuously tuning the voltage and current gains, respectively, of the m-controlled inverters. PI controllers are used to tune the voltage and current gains according to the desired power set-point. The current and voltage gains are fixed for the n-uncontrolled inverters and are designed to satisfy the desired ac-performance specifications while sharing the power proportionally. In order to determine the feasible power set-points, security constraints are presented for a system consisting of m-controlled and n-uncontrolled inverters. Using these security constraints, achievability of a desired power set-point can be approximately determined a-priori. Further, control laws are presented to determine the values of voltage and current gains for each controlled inverter corresponding to a particular power set-point. An iterative numerical method to solve the power flow equations with the virtual oscillator dynamics included is proposed. The design of virtual oscillator control parameters and line impedances for the n-uncontrolled inverters is also discussed [16]. By designing these parameters correctly, optimal power sharing between uncontrolled inverters can be achieved.

The chapter is organised as follows. In Section 4.2, an overall system description is presented. In Section 4.3, the actual and averaged dynamics of the virtual oscillator are presented. Further, the dynamics of the PI controllers are also considered. In Section 4.4, security constraints for the feasible power set-points are derived and control laws are proposed. In Section 4.5, detailed stability analysis is presented. In Section 4.6, simulation results for power dispatch and security constraint violation are presented. In Section 4.7, experimental results are verified against the simulation results. In Section 4.8, a discussion on the experimental and simulation results is considered. In Section 4.9, the conclusion is drawn.

4.2 System Description

The dispatchable control is presented for a system of m-controlled and n-uncontrolled inverters, where the total number of inverters is $n_T = m + n$. The output power is regulated for the m-controlled inverters corresponding to the desired reference power set-points, whereas the n-uncontrolled inverters share the remaining power demand proportional to their power ratings. The controlled inverters can be used for any energy source that needs to be dispatched. This includes renewable energy sources (i.e. photo-voltaic panels, wind turbines, etc.) or energy storage systems. Let $\mathbb{I} = \{1, ..., m, m+1, ..., m+n\}$ denotes the set of all the inverters present in the system, $\mathbb{M} = \{1, ..., m\}$ denotes the set of m-controlled inverters and $\overline{\mathbb{M}} = \{m+1, ..., m+n\}$ denotes the set of n-uncontrolled inverters. The j^{th} virtual oscillator-controlled inverter in the system is connected to the load bus through line impedance $z_{l,j} = r_{l,j} + \jmath x_{l,j}$, where $j \in \mathbb{I}$. The load considered in this system can be a fixed impedance load z_L or a constant power load S_L. The active and reactive output power of the g^{th} controlled inverter is denoted respectively by P_g and Q_g, where $g \in \mathbb{M}$. The output power of the m-controlled inverters is regulated based on the desired power set-points $\{(P_1^*, Q_1^*), ..., (P_m^*, Q_m^*)\}$, while the remaining load power is shared optimally by the n-uncontrolled inverters proportional to their power ratings. Let $b_T = \{1, ..., m+n+1\}$ be the set of all the buses present in the system, where the $(m+n+1)^{th}$ bus is the load bus. The total number of buses in the system is denoted by $\Gamma_b = m + n + 1$. In the rest of the chapter, $g \in \mathbb{M}$ denotes the g^{th} controlled inverter, $\overline{g} \in \overline{\mathbb{M}}$ denotes the $\overline{g}^{th}$ uncontrolled inverter and $j \in \mathbb{I}$ denotes the j^{th} inverter in the system. In Fig. 4.1, an overview of the complete system is presented.

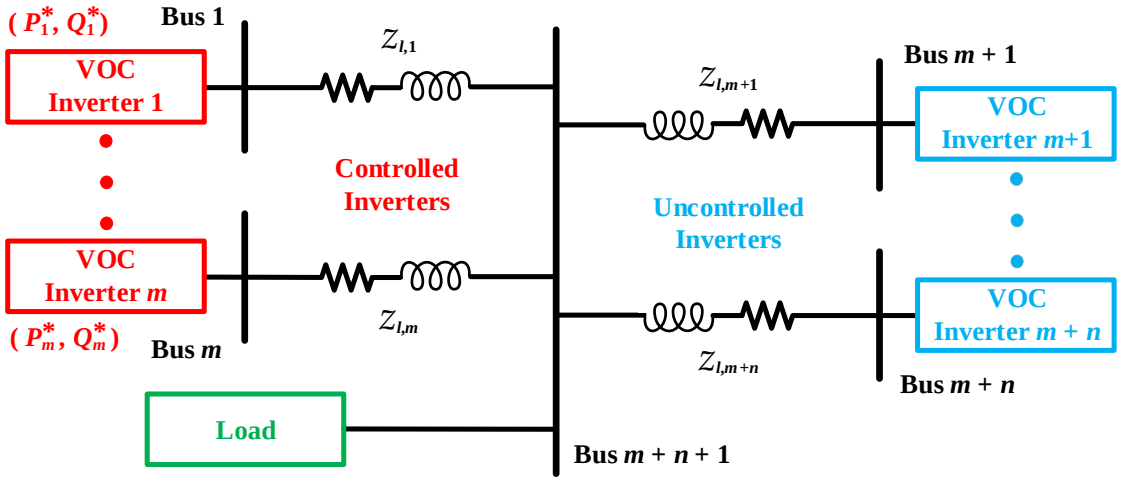

Figure 4.1: An overview of the overall system consisting of m-controlled and n-uncontrolled inverters. The j^{th} inverter is connected to the load bus through the line impedance $z_{l,j}$, where $j \in \mathbb{I}$. The (P_g^*, Q_g^*) denotes the desired power set-point for the g^{th} controlled inverter, where $g \in \mathbb{M}$.

4.3 System Modelling

A detailed modelling of both the actual and averaged dynamics of virtual oscillator controllers and PI controllers used to dispatch the power of m-controlled inverters, is presented.

4.3.1 Virtual Oscillator Controller

Recall from Chapter 2, based on the ac-performance specifications, a virtual oscillator controller can be designed to oscillate at the frequency $\omega = \omega^* \pm \Delta\omega$ and generate output voltage $v = v_{rated} \pm \Delta v$ within the desired range, where ω^* is the fundamental grid frequency and v_{rated} is the nominal grid voltage. A block diagram representation of a virtual oscillator controller is shown in Fig. 4.2. The capacitor voltage and inductor current are denoted by v_C and i_L, respectively. The parameter i denotes the inverter output current that is fedback to the virtual oscillator controller after being scaled by current feedback gain k_i. The virtual oscillator controller for the j^{th} inverter is described by the following dynamic equations [76]:

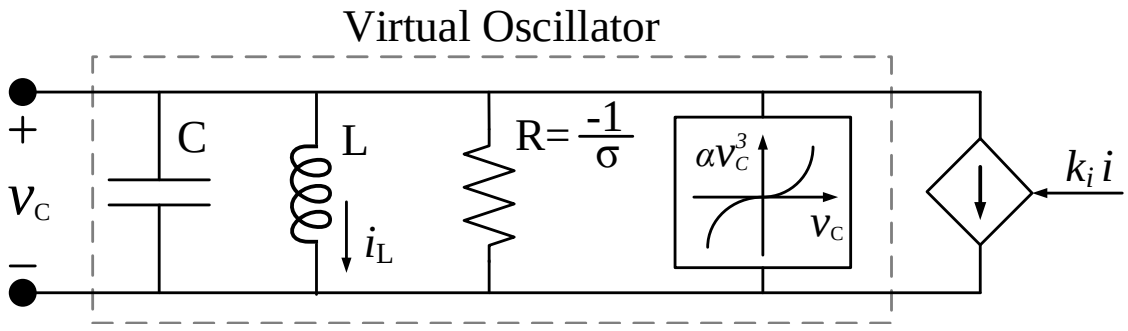

Figure 4.2: A virtual oscillator controller consists of a parallel combination of an LC harmonic oscillator, a non-linear voltage-dependent current source, a resistive element R and a current-controlled current source with a scaled version of inverter output current i (i.e. $k_i i$) as the input. The parameter k_i denotes the current feedback gain.

$$\begin{aligned}\frac{dV_j}{dt} &= \frac{\epsilon_j \omega^*}{\sqrt{2}}\left(\sigma_j \tilde{g}\big(\sqrt{2}V_j\cos(\phi_j)\big) - k_{v,j}k_{i,j}i_j\right)\cos(\phi_j),\\ \frac{d\phi_j}{dt} &= \omega^* - \frac{\epsilon_j \omega^*}{\sqrt{2}V_j}\left(\sigma_j \tilde{g}\big(\sqrt{2}V_j\cos(\phi_j)\big) - k_{v,j}k_{i,j}i_j\right)\sin(\phi_j),\end{aligned} \tag{4.1}$$

where V_j denotes the RMS terminal-voltage magnitude of the j^{th} virtual oscillator controller, $\phi_j = \omega_j t + \theta_j$ is the instantaneous phase angle and θ_j denotes the phase-offset with respect to $\omega_j t$. The parameter i_j denotes the inverter output current. The function $\tilde{g}$ is defined by $\tilde{g}(v_j) = v_j - \frac{\beta_j}{3}v_j^3$, where $\beta_j = \frac{3\alpha_j}{k_{v,j}^2\sigma_j}$. The parameters $k_{v,j}$ and $k_{i,j}$ denote the voltage scaling factor and current feedback gain, respectively. The VOC design parameters include σ_j, α_j and ϵ_j. Recall from Chapter 2, the VOC design parameter $\epsilon_j = \sqrt{\frac{L_j}{C_j}}$ that controls the extent of harmonic content present in the output of VOC is of vital importance. A detailed model derivation and parameter description of the virtual oscillator controller can be found in [76].

4.3.2 Averaged Dynamics of VOC Inverter

Recall from Chapter 2, the averaged VOC dynamics for the j^{th} inverter are given by the following non-linear dynamic equations [76]:

$$\frac{d}{dt}\overline{V}_j = \frac{\sigma_j}{2C_j}\left(\overline{V}_j - \frac{\beta_j}{2}\overline{V}_j^3\right) - \frac{k_{v,j}k_{i,j}}{2C_j\overline{V}_j}\overline{P}_j, \tag{4.2}$$

$$\frac{d}{dt}\overline{\theta}_j = \omega^* - \omega_j + \frac{k_{v,j}k_{i,j}}{2C_j\overline{V}_j^2}\overline{Q}_j, \tag{4.3}$$

where $\overline{V}_j$ denotes the averaged terminal-voltage magnitude and $\overline{\theta}_j$ denotes the averaged phase-offset with respect to $\omega_j t$. For the averaged VOC dynamics (4.2)-(4.3), the corresponding equilibrium points are:

$$\overline{V}_{eq,j} = k_{v,j}\left(\frac{\sigma_j \pm \sqrt{\sigma_j^2 - 6\alpha_j(k_{i,j}/k_{v,j})\overline{P}_{eq,j}}}{3\alpha_j}\right)^{\frac{1}{2}}, \tag{4.4}$$

$$\omega_{eq,j} = \omega^* + \frac{k_{v,j}k_{i,j}}{2C_j\overline{V}_{eq,j}^2}\overline{Q}_{eq,j}, \tag{4.5}$$

where $\overline{P}_{eq,j}$ and $\overline{Q}_{eq,j}$ are the equilibrium steady-state values of averaged active and reactive output power for the j^{th} inverter, respectively.

4.3.3 PI Controller Dynamics

The simultaneous regulation of both the active and reactive output power of the g^{th} inverter, where $g \in \mathbb{M}$, is achieved by continuously tuning two VOC parameters, the voltage scaling factor $k_{v,g}$ and current feedback gain $k_{i,g}$, respectively. For each controlled inverter g, two PI controllers continuously tune both the VOC parameters ($k_{v,g}$ and $k_{i,g}$), based on the desired power set-point (P_g^*, Q_g^*), as shown in Fig. 4.3. The PI controller that regulates the active power $\overline{P}_g$ is described by the following dynamic equations:

$$\dot{e}_{p,g} = K_{I,g}^p(\overline{P}_g - P_g^*), \tag{4.6}$$

$$k_{v,g} = K_{P,g}^p(\overline{P}_g - P_g^*) + e_{p,g}, \tag{4.7}$$

where $K_{P,g}^p$ and $K_{I,g}^p$ denote the proportional and integral gains, respectively. P_g^* is the reference active power set-point. Similarly, the PI controller that regulates the

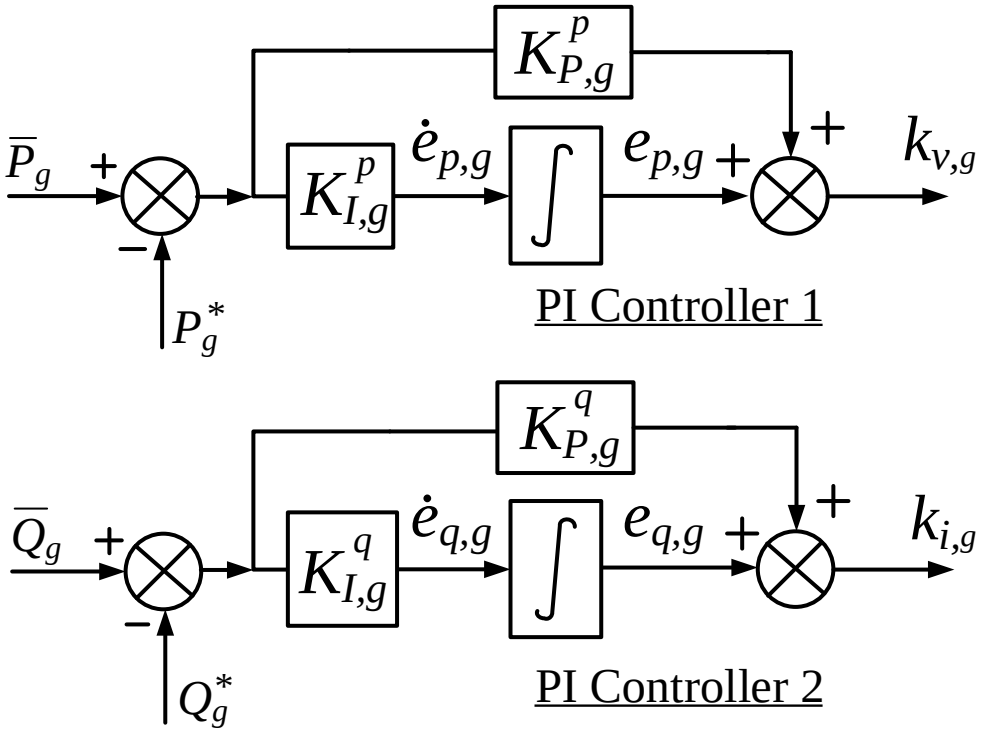

Figure 4.3: PI controllers are used to continuously tune the current feedback gain $k_{i,g}$ and voltage scaling factor $k_{v,g}$ for the g^{th} inverter to regulate the active and reactive power simultaneously according to the desired power set-point (P^*_g, Q^*_g), where $g \in \mathbb{M}$. PI controller 1 regulates the active power P_g and PI controller 2 regulates the reactive power Q_g.

reactive power $\overline{Q}_g$ is described by the following dynamic equations:

$$\dot{e}_{q,g} = K^q_{I,g}(\overline{Q}_g - Q^*_g), \tag{4.8}$$

$$k_{i,g} = K^q_{P,g}(\overline{Q}_g - Q^*_g) + e_{q,g}, \tag{4.9}$$

where $K^q_{P,g}$ and $K^q_{I,g}$ are the proportional and integral gains, respectively. Q^*_g is the reference reactive power set-point.

4.4 Security Constraints for Achievable Power Set-points

Considering the dispatchable generation, the determination of achievable power set-points is crucial for planning the optimal power dispatch and control of a power system. A set of security constraints is derived that approximately guarantees the achievability of desired reference power set-point (P_g^*, Q_g^*) and the existence of a real-valued solution for the corresponding control variables i.e. current feedback gain $k_{i,g}$ and voltage scaling factor $k_{v,g}$ for the m-controlled inverters, where $g \in \mathbb{M}$. For the applicability of this technique to determine the feasible power set-points, knowledge of line impedances and load is required as in conventional power system load flow analysis. Hence, using these security constraints and the proposed load flow analysis in Section 4.4.1 with the VOC dynamics included, the achievability of a particular power set-point can be determined.

4.4.1 Power Flow Analysis with VOC Dynamics

In order to perform power flow analysis for the system of m-controlled and n-uncontrolled inverters, an iterative numerical method is proposed. The algorithm solves for the b^{th} bus voltage magnitude V_b and angle θ_b, where $b \in b_T$, corresponding to the power set-points (P_g^*, Q_g^*), where $g \in \mathbb{M}$, considering the VOC dynamics of n-uncontrolled inverters. Once the power flow analysis is performed, the VOC dynamics of the m-controlled inverters are considered in Theorem 4.1 to determine the achievability of the desired power set-points and corresponding VOC parameters (i.e. current feedback gain and voltage scaling factor). This algorithm can be used for both a constant impedance load z_L or / and a constant power load $S_L = P_L + jQ_L$ attached at the load bus. The state vector $\mathbf{x}$ and non-linear equation $\mathbf{F(x)}$ to be

solved for the power flow analysis, including the VOC dynamics, are as follow:

$$\mathbf{x} = \begin{bmatrix} \theta_1 \\ . \\ . \\ . \\ \theta_m \\ \theta_{m+1} \\ \theta_{m+2} \\ . \\ . \\ . \\ \theta_{m+n} \\ \theta_{m+n+1} \\ V_1 \\ . \\ . \\ . \\ V_m \\ V_{m+1} \\ . \\ . \\ . \\ V_{m+n} \\ V_{m+n+1} \end{bmatrix}, \qquad \mathbf{F(x)} = \begin{bmatrix} P_1^* - P_1(x) \\ . \\ . \\ . \\ P_m^* - P_m(x) \\ 0 \\ \omega_{m+2}(x) - \omega_{m+1}(x) \\ . \\ . \\ . \\ \omega_{m+n}(x) - \omega_{m+1}(x) \\ P_L^* - P_L(x) \\ Q_1^* - Q_1(x) \\ . \\ . \\ . \\ Q_m^* - Q_m(x) \\ V_{m+1} - \overline{V}_{m+1}(P_{m+1}) \\ . \\ . \\ . \\ V_{m+n} - \overline{V}_{m+n}(P_{m+n}) \\ Q_L^* - Q_L(x) \end{bmatrix}, \tag{4.10}$$

where V_{m+n+1} and θ_{m+n+1} denote the load bus voltage magnitude V_L and angle θ_L, respectively. The active and reactive power flow at the b^{th} bus is described as follows

[114]:

$$P_b(x) = V_b \sum_{k=1}^{m+n+1} Y_{b,k} V_k \cos\left(\theta_b - \theta_k - \delta_{b,k}\right) \quad \forall b \in b_T, \tag{4.11}$$

$$Q_b(x) = V_b \sum_{k=1}^{m+n+1} Y_{b,k} V_k \sin\left(\theta_b - \theta_k - \delta_{b,k}\right) \quad \forall b \in b_T, \tag{4.12}$$

where $y_{b,k} = Y_{b,k}\angle\delta_{b,k}$ is the line admittance between bus b and bus k. The Y_{bus} formulation technique can be found in [114]. The bus angle $\theta_{m+1} = 0°$ is taken as reference for solving the power flow equation $\mathbf{F(x)} = 0$. VOC dynamics are included in the power flow analysis, using $\omega_{\overline{g}}(x)$ and $\overline{V}_{\overline{g}}(P_{\overline{g}})$ representing the angular frequency and averaged RMS terminal-voltage magnitude, respectively, of the $\overline{g}^{th}$ uncontrolled inverter according to equations (4.4)-(4.5), where $\overline{g} \in \overline{\mathbb{M}}$.

Assumption 4.1. *If there exists a solution for the load flow equation* (4.10) *corresponding to the desired power set-points* (P_g^*, Q_g^*)*, where* $g \in \mathbb{M}$*, such that* $\omega_{\overline{g}}$*,* $V_{\overline{g}}$*,* $P_{\overline{g}}$ *and* $Q_{\overline{g}}$ *satisfy the equations* (4.4)-(4.5)*, where* $\overline{g} \in \overline{\mathbb{M}}$*, then this solution is unique.*

Theorem 4.1. *Under Assumption 4.1, assuming the averaged model of the* $m+n$ *VOC inverters that synchronise to a common frequency, and the VOC inverters are connected to a common constant power load* S_L *or / and a fixed impedance load* z_L *through line impedance values* $z_{l,j}$*, where* $j \in \mathbb{I}$*, the desired output power set-point* $(\overline{P}_g^*, \overline{Q}_g^*)$ *for the* g^{th} *controlled inverter, where* $g \in \mathbb{M}$*, can be achieved; and there exists corresponding real-valued voltage scaling factor* $k_{v,g}^{\iota}$ *and current feedback gain* $k_{i,g}^{\iota}$*, if, for the averaged VOC dynamics, the following security constraints are satisfied:*

$$\overline{P}_g^* \frac{\overline{Q}_j^{\iota}}{\overline{Q}_g^*} < \gamma_{g,j} \overline{V}_j^{\iota\,2} \qquad \forall\ j \underset{j \neq g}{\in} \mathbb{I}, \tag{4.13}$$

where,

$$\gamma_{g,j} = \frac{\sigma_g}{k_{v,j} k_{i,j}} > 0. \tag{4.14}$$

The parameters $\overline{Q}_j^{\iota}$ and $\overline{V}_j^{\iota}$ denote the steady-state averaged output reactive power and terminal-voltage magnitude for the j^{th} inverter, corresponding to the desired output power set-point $(\overline{P}_g^*, \overline{Q}_g^*)$.

Proof. The iterative method in Section 4.4.1 to numerically solve the non-linear power flow equations including the VOC dynamics can be used to determine the bus voltage magnitudes and angles corresponding to the power set-point $(\overline{P}_g^*, \overline{Q}_g^*)$, where $g \in \mathbb{M}$, for the g^{th} controlled inverter. Using the solution of power flow equations, the corresponding values for $k_{i,g}^{\iota}$ and $k_{v,g}^{\iota}$ can be determined as follow:

$$\overline{V}_g^{\iota} = k_{v,g}^{\iota} \left(\frac{\sigma_g \pm \sqrt{\sigma_g^2 - 6\alpha_g (k_{i,g}^{\iota}/k_{v,g}^{\iota}) \overline{P}_g^*}}{3\alpha_g} \right)^{\frac{1}{2}}. \tag{4.15}$$

From the frequency synchronisation condition, we have:

$$\omega_g = \omega_j \qquad \forall g \in \mathbb{M}, j \in \mathbb{I}, \tag{4.16}$$

$$\frac{k_{i,g}^{\iota} k_{v,g}^{\iota}}{\overline{V}_g^{\iota\,2}} \overline{Q}_g^* = \frac{k_{i,j} k_{v,j}}{\overline{V}_j^{\iota\,2}} \overline{Q}_j^{\iota}, \tag{4.17}$$

$$k_{i,g}^{\iota} k_{v,g}^{\iota} = k_{i,j} k_{v,j} \frac{\overline{Q}_j^{\iota} \overline{V}_g^{\iota\,2}}{\overline{Q}_g^* \overline{V}_j^{\iota\,2}} = \mu_{g,j}. \tag{4.18}$$

Simplifying (4.15) and substituting $\alpha_g = \frac{2\sigma_g}{3}$ (according to the design procedure in [76]), we get:

$$\frac{\sigma_g \overline{V}_g^{\iota\,4}}{k_{v,g}^{\iota\,4}} - \frac{\sigma_g \overline{V}_g^{\iota\,2}}{k_{v,g}^{\iota\,2}} + \frac{k_{i,g}^{\iota}}{k_{v,g}^{\iota}} \overline{P}_g^* = 0. \tag{4.19}$$

Replacing $k^{\iota}_{v,g} = \frac{\mu_{g,j}}{k^{\iota}_{i,g}}$ in (4.19), we get:

$$\frac{k^{\iota}_{i,g}}{k^{\iota}_{v,g}} \left(\frac{\sigma_g \overline{V}^{\iota\,4}_{g} {k^{\iota}_{i,g}}^{2}}{\mu^3_{g,j}} - \frac{\sigma_g \overline{V}^{\iota\,2}_{g}}{\mu_{g,j}} + \overline{P}^{*}_{g} \right) = 0. \tag{4.20}$$

There are two possible solutions for (4.20) for a positive voltage scaling factor k_v and they are as follows:

$$\left(\frac{\sigma_g \overline{V}^{\iota\,4}_{g} {k^{\iota}_{i,g}}^{2}}{\mu^3_{g,j}} - \frac{\sigma_g \overline{V}^{\iota\,2}_{g}}{\mu_{g,j}} + \overline{P}^{*}_{g} \right) = 0, \tag{4.21}$$

and

$$k^{\iota}_{i,g} = 0. \tag{4.22}$$

Continuing with the solution in (4.21), we have:

$$k^{\iota}_{i,g} = \pm \frac{\mu_{g,j}}{\overline{V}^{\iota}_{g}} \sqrt{1 - \frac{\mu_{g,j} \overline{P}^{*}_{g}}{\sigma_g \overline{V}^{\iota\,2}_{g}}}, \tag{4.23}$$

$$k^{\iota}_{v,g} = \frac{\mu_{g,j}}{k^{\iota}_{i,g}}. \tag{4.24}$$

Hence, (4.23) and (4.24) represent the control laws to determine $k^{\iota}_{i,g}$ and $k^{\iota}_{v,g}$, respectively.

The frequency synchronisation condition (4.17) and the solution (4.22) (i.e. $k^{\iota}_{i,g} = 0$), imply that the reactive power $\overline{Q}^{\iota}_{j}$ must be zero. For the solution (4.22), the terminal-voltage magnitude $\overline{V}^{\iota}_{g}$ becomes independent of active power $\overline{P}^{\iota}_{g}$ and remains constant for a fixed value of $k^{\iota}_{v,g}$. This results in the embedded droop-characteristics within the averaged VOC dynamics disappearing. This special case corresponds to the solution (4.22) with $\overline{V}^{\iota}_{g}$ independent of $\overline{P}^{\iota}_{g}$ and $\overline{Q}^{\iota}_{j} = 0$ already embedded in (4.23). Thus, the solution (4.22) does not require separate consideration. From (4.18), $\overline{Q}^{\iota}_{j} = 0$ implies $\mu_{g,j} = 0$ and according to (4.24), this results in an indeterminate form for $k^{\iota}_{v,g} = \frac{0}{0}$.

For the existence of a real-valued solution to the control laws (4.23)-(4.24) ($k_i \in \mathbb{R}$ and $k_v \in \mathbb{R}_+$), we require:

$$1 - \frac{\mu_{g,j}\overline{P}_g^*}{\sigma_g \overline{V}_g^{\iota\,2}} > 0. \tag{4.25}$$

Replacing $\mu_{g,j}$ and $\gamma_{g,j}$ in (4.25), we obtain (4.13). For the case where $\overline{Q}_g^* > 0$ and $\overline{Q}_j^\iota > 0$, the constraint (4.13) can be written as:

$$\overline{P}_g^* < \gamma_{g,j} \frac{\overline{Q}_g^*}{\overline{Q}_j^\iota} \overline{V}_j^{\iota\,2}. \tag{4.26}$$

This completes the proof. ■

Remark 4.1. *In order to ensure all the VOC inverters present in the system synchronise to a common frequency, the frequency synchronisation conditions are considered in* (4.10) *and* (4.16)*. In Sections 4.6-4.7, simulation and experimental results demonstrate that the VOC inverters remain synchronised under all possible extreme power sharing scenarios. Further discussion on a stronger type of synchronisation (i.e. phase synchronisation) between parallel-connected VOC inverters with a dead-zone non-linearity can be found in [16, 18].*

Remark 4.2. *For the desired output power set-points* $(\overline{P}_g^*, \overline{Q}_g^*)$*, where* $g \in \mathbb{M}$*, the corresponding steady-state values for* $\overline{P}_{\overline{g}}^\iota$*,* $\overline{Q}_{\overline{g}}^\iota$ *and* $\overline{V}_{\overline{g}}^\iota$*, where* $\overline{g} \in \overline{\mathbb{M}}$*, can be determined by solving the non-linear equation* (4.10) *iteratively. Using the known values of line and load impedances, the iterations can be performed starting with an initial guess of the state vector* $\boldsymbol{x_o}$ *in order to determine the* $\overline{P}_{\overline{g}}^\iota$ *and* $\overline{Q}_{\overline{g}}^\iota$ *that result in the desired* $\overline{P}_g^*$ *and* $\overline{Q}_g^*$*. Once having the solution for* (4.10)*, the achievability of a particular output power set-point can be determined a-priori using the constraint* (4.13)*.*

Remark 4.3. *The security constraint* (4.13) *in Theorem 4.1 is a necessary and sufficient condition for the averaged VOC dynamics. However, it is emphasised that the security constraint* (4.13) *only provides an approximation in practice and is a useful approximate tool for analysing the actual VOC dynamics whose effectiveness*

is supported by simulation and experimental results. This is due to the fact that the averaged VOC model is derived under the assumption $\epsilon_j \searrow 0$ *and is an approximation of Van der Pol oscillator, where* $j \in \mathbb{I}$. *For a non-zero positive value of* ϵ_j, *the control variables obtained through the control laws* (4.23)-(4.24) *result in a steady-state offset error in the output power for the actual VOC dynamics (without external PI power control loops). In [32], for a fixed value of* ϵ_j, *the steady-state offset error in the output power for several power set-points, which is quite small, has been presented. The steady-state offset error can be improved by making* $\epsilon_j \searrow 0$ *for actual VOC dynamics at the cost of slower dynamic response [76]. Hence, a design trade-off exists between the steady-state offset error in the output power and the inverter dynamic response. It is worth noting that the use of PI controllers for power dispatch removes the steady-state offset error in the output power, as can be seen in the simulation and experimental results.*

4.4.2 Designing the Line and Filter Impedances for Uncontrolled VOC Inverters

The remaining power $S_R = S_L - S_M$ can be shared optimally between the n-uncontrolled inverters, where S_L denotes the load complex power and $S_M = S_1 + ... + S_m$ denotes the sum of complex power supplied by the m-controlled inverters. As presented in [16], power sharing proportional to the rated power between VOC inverters can be achieved if the filter and line impedances of the inverters are designed properly. The base impedance for the n-uncontrolled inverters can be defined as $z_{base,\overline{g}} = V_{rated}^2/P_{\overline{g}}$, where V_{rated} is the rated RMS voltage magnitude of the system and $P_{\overline{g}}$ denotes the active power output of $\overline{g}^{th}$ inverter, where $\overline{g} \in \overline{\mathbb{M}}$. Defining the net line and filter impedance for $\overline{g}^{th}$ inverter $z_{\overline{g}} = z_f/\varkappa_{\overline{g}}$, where z_f is the reference impedance and $\varkappa_{\overline{g}}$ is a scalar, the per-unitised impedance can be written as $z_f/(\varkappa_{\overline{g}} z_{base,\overline{g}})$. By designing the per-unit line and filter impedance of each inverter to be the same, proportional power sharing between the inverters can be achieved.

Using the above definition of per-unitised impedance, the ratio can be written as:

$$\frac{P_{\overline{g}}}{\varkappa_{\overline{g}}} = \frac{P_k}{\varkappa_k} \qquad \forall \overline{g}, k \in \overline{\mathbb{M}}. \tag{4.27}$$

Further, the proposed filter design strategy [16] also enables identical relative contributions of distortion from each inverter's output current such that the THD of each individual inverter is reasonably the same as that of the overall system [115–117].

4.5 Stability Analysis

In order to investigate the system's stability, a system consisting of one controlled inverter and one uncontrolled inverter (with $m = n = 1$) is considered, as in Section 4.6.1. The system's states include $\chi = [\overline{\theta}_1, \overline{\theta}_2, \overline{V}_1, \overline{V}_2, e_{p,1}, e_{q,1}]$. The system dynamics are given by the averaged VOC model (4.2)-(4.3) and PI controller dynamics (4.6)-(4.9). An equilibrium point $\chi^* = [\overline{\theta}^*_1, \overline{\theta}^*_2, \overline{V}^*_1, \overline{V}^*_2, e^*_{p,1}, e^*_{q,1}]$ corresponding to the power set-point (P^*_1, Q^*_1) can be determined using the iterative numerical method presented in Section 4.4.1, the control laws (4.23)-(4.24) and PI controller dynamics (4.6)-(4.9). For a fixed impedance RL load, the inverter's active and reactive output power can be expressed as a function of state variables given by:

$$\overline{P}_j = \frac{\overline{V}_j^2 \cos\left(\theta_{z_{f,j}}\right)}{Z_{f,j}} - \frac{\overline{V}_j V_{o,j} \cos\left(\theta_j - \theta_{v_{o,j}} + \theta_{z_{f,j}}\right)}{Z_{f,j}}, \tag{4.28}$$

$$\overline{Q}_j = \frac{\overline{V}_j^2 \sin\left(\theta_{z_{f,j}}\right)}{Z_{f,j}} - \frac{\overline{V}_j V_{o,j} \sin\left(\theta_j - \theta_{v_{o,j}} + \theta_{z_{f,j}}\right)}{Z_{f,j}}, \tag{4.29}$$

where $z_{f,j} = R_{L_{f,j}} + \jmath\omega^* L_{f,j} = Z_{f,j}\angle\theta_{z_{f,j}}$ denotes the inverter side inductor's impedance, $\jmath = \sqrt{-1}$ and $v_{o,j} = V_{o,j}\angle\theta_{v_{o,j}} = \mathbb{m}_{o,j} + \jmath\,\mathbb{n}_{o,j}$ is the capacitor voltage

phasor for the j^{th} inverter. The $V_{o,j}$ and $\theta_{v_{o,j}}$ are defined as:

$$\begin{aligned} V_{o,j} &= \sqrt{\mathbb{m}_{o,j}^2 + \mathbb{n}_{o,j}^2}, \\ \theta_{v_{o,j}} &= \tan^{-1}\left(\frac{\mathbb{n}_{o,j}}{\mathbb{m}_{o,j}}\right). \end{aligned} \tag{4.30}$$

In the case of a system consisting of two inverters (i.e. $j \in \{1, 2\}$), the capacitor voltage $v_{o,j}$ phasor can be expressed in terms of the state variables as follows:

$$\begin{aligned} v_{o,1} &= Z_{\alpha,1}\overline{V}_1 \cos\left(\theta_1 + \theta_{z_{\alpha,1}}\right) + \jmath\, Z_{\beta,1}\overline{V}_2 \cos\left(\theta_2 + \theta_{z_{\beta,1}}\right), \\ v_{o,1} &= \mathbb{m}_{o,1} + \jmath\, \mathbb{n}_{o,1}, \end{aligned} \tag{4.31}$$

$$\begin{aligned} v_{o,2} &= Z_{\alpha,2}\overline{V}_1 \cos\left(\theta_1 + \theta_{z_{\alpha,2}}\right) + \jmath\, Z_{\beta,2}\overline{V}_2 \cos\left(\theta_2 + \theta_{z_{\beta,2}}\right), \\ v_{o,2} &= \mathbb{m}_{o,2} + \jmath\, \mathbb{n}_{o,2}, \end{aligned} \tag{4.32}$$

where $z_{\alpha,j} = Z_{\alpha,j}\angle\theta_{z_{\alpha,j}}$ and $z_{\beta,j} = Z_{\beta,j}\angle\theta_{z_{\beta,j}}$ are the impedance constants that can be determined through solving the network equations. In order to define the system dynamics as a function of state variables χ, the real power $\overline{P}_j$ and reactive power $\overline{Q}_j$ can be replaced by (4.28)-(4.32) in the averaged VOC dynamics (4.2)-(4.3) and PI controller dynamics (4.6)-(4.9).

Recall from Section 2.8.2, the system under consideration has a 1-D manifold of non-hyperbolic equilibria (i.e., equlibria about which the Jacobian has at least one eigenvalue on the imaginary axis). This is because for a particular power set-point (P_1^*, Q_1^*), the Inverter 1 phase-offset $\overline{\theta}_1$ and Inverter 2 phase-offset $\overline{\theta}_2$ can have arbitrary values, but the phase difference $\overline{\theta}_1 - \overline{\theta}_2$ between the two inverters remains the same at equilibrium (referred to as the "rotational invariance" of the system in [39]). For this system, we will be interested in its local stability. That is, if a small perturbation is given to the system state around an operating point on the manifold of equilibria, then the system should converge back to the manifold. The following

subsections present local stability analysis of the system (sufficiently close to the 1-D manifold of equilibria) using the results presented in [93, 97]. Further, a system linearisation and eigenvalue analysis is developed. In order to validate the analysis, the system's states are perturbed around an equilibrium point on the 1-D manifold and a simulation comparison is made between the linearised averaged VOC dynamics and actual VOC dynamics. Note that the proposed stability analysis presented in this section is approximate, as the averaged VOC dynamics are an approximation of actual VOC dynamics under the assumption $\epsilon \searrow 0$.

4.5.1 Stability Analysis with a 1-D Manifold of Equilibria

The system of interest is a non-linear system with six state variables given by:

$$\dot{\chi} = f(\chi), \tag{4.33}$$

where $\chi \in \mathbb{R}^6$. The 1-D manifold of equilibria $\mathcal{M}$ is given by:

$$\mathcal{M} = \{\chi \in \mathbb{R}^6 \mid \chi_1 - \chi_2 = \theta_d^*, \chi_3 = \chi_3^*, \ldots, \chi_6 = \chi_6^*\}, \tag{4.34}$$

where $\theta_d^* = \chi_1^* - \chi_2^*$ is the steady-state phase difference between the two inverters, such that $f(\chi^*) = 0$ for any $\chi^* \in \mathcal{M}$. Let us make a change of basis as follows [97, pp. 46-47]. Set $v_1 = [\ 1 \quad 1 \quad 0 \quad 0 \quad 0 \quad 0\ ]^T$ and choose $v_2, ..., v_6$ arbitrary such that $v_1, v_2, ..., v_6$ form a basis for $\mathbb{R}^6$. Define a 6×6 invertible matrix $V = [\ v_1 \quad v_2 \quad v_3 \quad v_4 \quad v_5 \quad v_6\ ]$. Considering an equilibrium point χ^* on the 1-D manifold $\mathcal{M}$ corresponding to a power set-point (P_1^*, Q_1^*), define a new variable z through the relation $\chi = \chi^* + Vz$ or equivalently $z = V^{-1}(\chi - \chi^*)$. In this new variable z, the linear manifold of equilibria is given by:

$$\mathcal{M} = \{\chi^* + Vz \in \mathbb{R}^6 \mid z \in \mathbb{R}^6,\ z_2 = z_3 = \ldots = z_6 = 0\}, \tag{4.35}$$

which is the same 1-D manifold of equilibria as in (4.34) such that for every point on the 1-D manifold $\mathcal{M}$, z_1 can take arbitrarily values while all other components of z are zero. Notice that an equilibrium point χ^* corresponds to z at the origin. In the new variable z, the non-linear system dynamics indexed by an equilibrium point χ^* are given by:

$$\dot{z} = \tilde{f}_{\chi^*}(z) = V^{-1} f(\chi^* + Vz). \tag{4.36}$$

Note that $\tilde{f}_{\chi^*}(z_1, 0, 0, 0, 0, 0) = 0$ for all z_1 as the vector field vanishes on the linear manifold $\mathcal{M}$. This implies that $\frac{\partial}{\partial z_1}\tilde{f}_{\chi^*}(z) = 0$ for any z in $\mathcal{M}$. It follows that the Jacobian of $\tilde{f}_{\chi^*}$ at the origin, denoted by $J\tilde{f}_{\chi^*}(0)$, has a first column which is zero. The dynamical system can then be written as:

$$\dot{z} = J\tilde{f}_{\chi^*}(0)z + \left[\tilde{f}_{\chi^*}(z) - J\tilde{f}_{\chi^*}(0)z\right]. \tag{4.37}$$

Considering that the first column of $J\tilde{f}_{\chi^*}(0)$ is zero, (4.37) can be written as:

$$\begin{aligned} \dot{z}_1 &= g_1(z), \\ \dot{\mathbf{z}}_2 &= A_s \mathbf{z}_2 + g_2(z), \end{aligned} \tag{4.38}$$

where $\mathbf{z}_2 = [\ z_2 \quad z_3 \quad ... \quad z_6\ ]^T$, $g_1(z)$ is the first element of $\tilde{f}_{\chi^*}(z)$, A_s denotes the lower right 5×5 block of $J\tilde{f}_{\chi^*}(0)$ and $g_2(z)$ is given by:

$$g_2(z) = \left[\tilde{f}_{\chi^*,2}(z), \tilde{f}_{\chi^*,3}(z), ..., \tilde{f}_{\chi^*,6}(z)\right]^T - A_s \mathbf{z}_2, \tag{4.39}$$

where $\tilde{f}_{\chi^*,\rho}(z)$ denotes the ρ-th element of vector field $\tilde{f}_{\chi^*}(z)$. According to [93, Theorem 5], for the transformed system's local stability about $z = 0$, the matrix A_s must have all its eigenvalues in the left half plane. Considering (4.36), the Jacobian

$J\tilde{f}_{\chi^*}(0)$ can be calculated as:

$$J\tilde{f}_{\chi^*}(0) = V^{-1} Jf(\chi^*) V, \tag{4.40}$$

where $Jf(\chi^*)$ denotes the Jacobian of the original vector field f at $\chi = \chi^*$. Let v_1 be an eigenvector that corresponds to the zero eigenvalue of $Jf(\chi^*)$ and that spans a 1-D invariant subspace under $Jf(\chi^*)$, then $v_2, v_3, ..., v_6$ can be chosen such that:

$$J\tilde{f}_{\chi^*}(0) = V^{-1} Jf(\chi^*) V = \begin{bmatrix} 0 & 0_{1\times 5} \\ 0_{5\times 1} & J_s \end{bmatrix}, \tag{4.41}$$

where the 5×5 matrix J_s consists of the Jordan blocks corresponding to the remaining eigenvalues of $Jf(\chi^*)$. According to (4.41), with this choice of matrix V, the matrix $A_s = J_s$ and the system is stable if J_s has all of its eigenvalues in the left half plane. In order to demonstrate the original system's stability around $\chi = \chi^*$, the eigenvalues of the Jacobian $Jf(\chi^*)$ of the original vector field at $\chi = \chi^*$ have been evaluated in the following subsections for a number of power dispatch cases throughout the feasible operating region, as given by power security constraint (4.26). It has been shown that all eigenvalues, except one single zero eigenvalue of $Jf(\chi^*)$, are in the left half plane for all the cases, thus confirming the system's stability.

4.5.2 System Linearisation and Eigenvalues Analysis

A system linearisation and eigenvalues analysis approach is considered based on the discussion in Section 4.5.1. The averaged VOC model (4.2)-(4.3) and PI controller dynamics (4.6)-(4.9) are linearised around an equilibrium point $\chi^* = [\overline{\theta}_1^*, \overline{\theta}_2^*, \overline{V}_1^*, \overline{V}_2^*, e_{p,1}^*, e_{q,1}^*]$ corresponding to the power set-point (P_1^*, Q_1^*) and an eigenvalues analysis has been performed. In Fig. 4.4, the eigenvalues are plotted for all the five power dispatch cases considered in Section 4.6.1. It can be seen that for each case, the real part of all the eigenvalues is negative except for one eigenvalue that lies at zero.

Table 4.1: System Parameters

Symbol	Parameter	Inverter 1 & 2	Inverter 3	Unit
k_i	Current feedback gain	[control variable]	0.152	A/A
k_v	Voltage scaling factor	[control variable]	126	V/V
σ	Conductance	6.09	6.09	Ω^{-1}
α	Cubic-current source coefficient	4.06	4.06	A/V^3
L	Virtual oscillator inductance	39.09	39.09	μH
C	Virtual oscillator capacitance	0.18	0.18	F
R_l	Line resistance	0.3	0.3	Ω
L_l	Line inductance	3.7	3.7	mH

Further, to better illustrate the system's stability throughout the feasible region given by power security constraint (4.26), ζ_{min} is defined as:

$$\zeta_{min} = \min_{\kappa \in \{1,\ldots,5\}} -\Re\{\lambda_\kappa\}, \tag{4.42}$$

where $\Re\{\lambda_\kappa\}$ denotes the real part of the κ-th eigenvalue of the linearised system and $\lambda_1, \ldots, \lambda_5$ are the eigenvalues of J_s. A surface plot for ζ_{min} is presented in Fig. 4.5 for the system parameters and ac-performance specifications as in Table 4.1 and Table 4.2, respectively. It can be seen that for all the feasible power set-points, the ζ_{min} stays positive, thus confirming the system's stability.

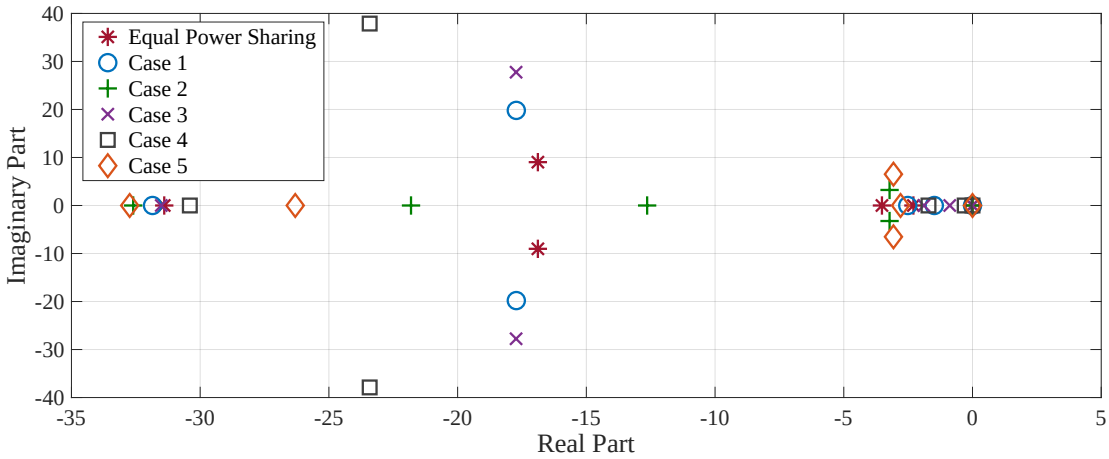

Figure 4.4: The plot of linearised system's eigenvalues for all the five power dispatch cases considered in Section 4.6.1.

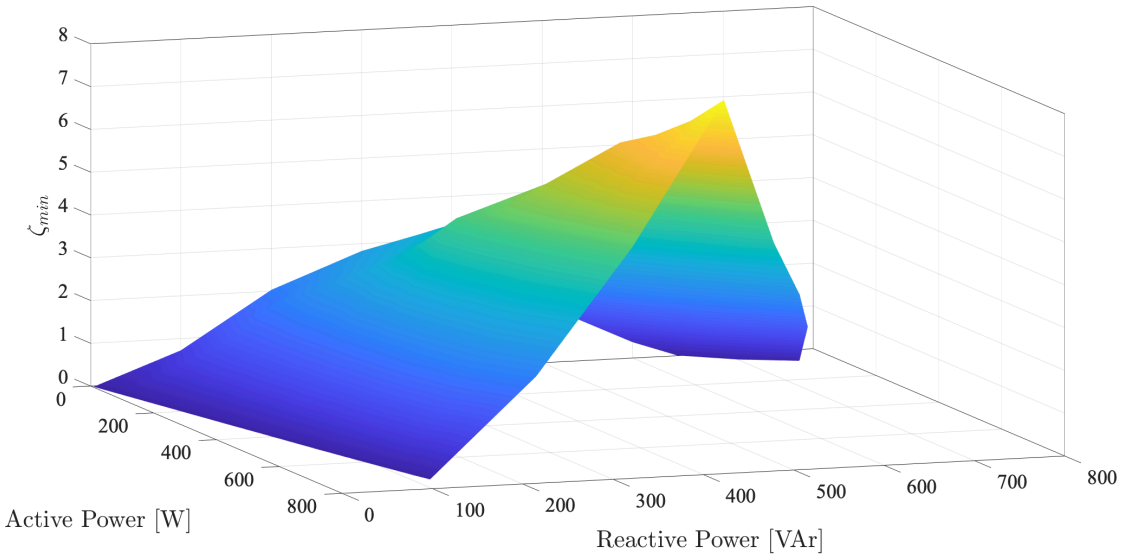

Figure 4.5: The surface plot of ζ_{min} for all the feasible power set-points given by power security constraint (4.26). The ζ_{min} stays positive throughout the feasible region, thus confirming the system's stability.

Table 4.2: AC Performance Specifications

Symbol	Parameter	Value	Unit
$\overline{V}_{oc}$	RMS open-circuit voltage	126	V
$\overline{V}_{rated}$	RMS rated grid voltage	120	V
$\overline{V}_{min}$	RMS rated power voltage	114	V
$\overline{P}_{rated}$	Rated active power	750	W
$\lvert\overline{Q}_{rated}\rvert$	Rated reactive power	750	VAr
ω^*	Nominal oscillator frequency	$2\pi 60$	rad/s
$\lvert\Delta\omega\rvert_{max}$	Maximum frequency offset	$2\pi 0.5$	rad/s
t_{rise}^{max}	Maximum rise time	0.2	s
$\delta_{3:1}^{max}$	3^{rd} to 1^{st} harmonic ratio	1.5	%

4.5.3 Validation by Simulation

In order to validate the system linearisation and eigenvalues analysis, a perturbation approach has been considered. The system's states are perturbed around an equilibrium point on the 1-D manifold of equilibria by 10% of their steady-state values and a simulation comparison is made in between the linearised averaged VOC dynamics and actual VOC (Van der Pol oscillator) dynamics. In order to perform the comparison, Case 5 in Section 4.6.1 has been considered. In Fig. 4.6, it can be seen that the linearised averaged VOC dynamics are close to the actual VOC dy-

namics. A small steady-state offset error in the PI controller states can be observed in Fig. 4.6(d) and Fig. 4.6(e). This offset error is due to the non-zero value of ϵ for the actual VOC dynamics, whereas the averaged VOC dynamics are derived under the assumption $\epsilon \searrow 0$. Further, due to the harmonics present in the actual VOC dynamics, a ripple in the steady-state values can be observed in Fig. 4.6(a)-4.6(c).

4.6 Simulation Results

In order to demonstrate the power regulation of virtual oscillator-controlled inverters, two types of scenarios are presented. In Scenario 1, a system consisting of two inverters with $m = n = 1$ is considered. In Scenario 2, a system consisting of three inverters with $m = 1$ and $n = 2$ is considered. The overall system's description is similar to the one presented in Fig. 4.7 but now with one controlled and two uncontrolled inverters. Inverter 1 is used as a controlled inverter, whereas Inverter 2 and Inverter 3 supply the remaining power to the load, acting more like a slack bus in conventional power systems. The system parameters and ac-performance specifications are as in Table 4.1 and Table 4.2, respectively. The PI controllers' gains used for the power regulation are $K_P^p = -0.001$, $K_I^p = -0.15$, $K_P^q = 0.0001$ and $K_I^q = 0.0075$. An LCL filter is used at the output of each inverter with inverter side inductor $L_f = 3.7\,\text{mH}$ with a series resistance $R_{L_f} = 0.3\,\Omega$, filter capacitor $C_f = 4.7\,\mu\text{F}$ with series resistance $R_{C_f} = 3.3\,\Omega$ and grid side inductor $L_g = 0.5\,\text{mH}$ with a series resistance $R_{L_g} = 80.3\,\text{m}\Omega$. A series RL load is used with $R_L = 22.12\,\Omega$ and $L_L = 14.4\,\text{mH}$. Simulations are performed in MATLAB/Simulink.

4.6.1 One Controlled and One Uncontrolled Inverter

In Fig. 4.8, simulation results are presented for the five possible cases of Inverter 1 output power regulation. Inverter 1 tracks the reference output power set-points

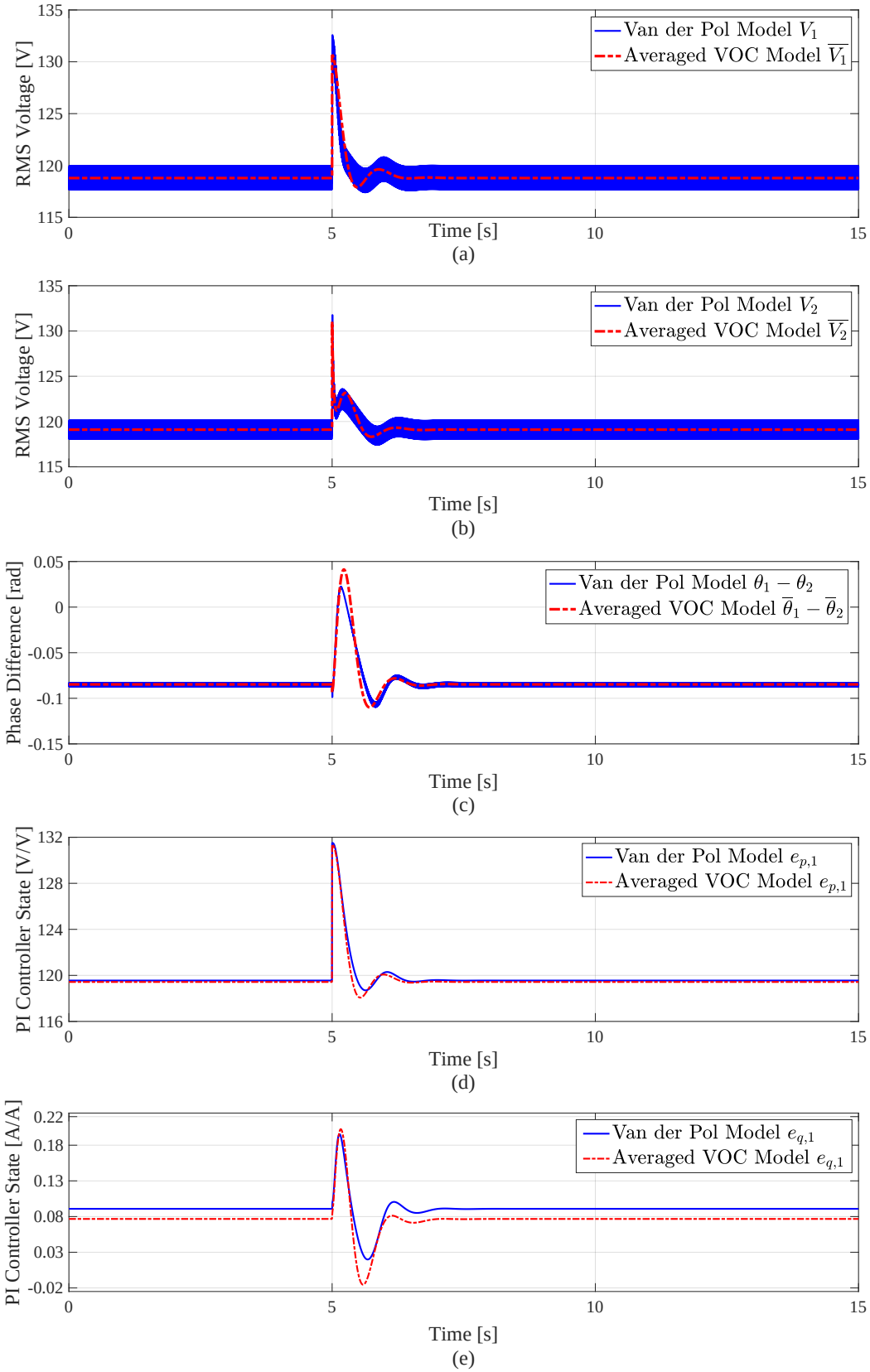

Figure 4.6: A comparison is presented between the linearised averaged VOC dynamics and actual VOC dynamics. The system's states are perturbed around an equilibrium point χ^* corresponding to the power set-point (P_1^*, Q_1^*) by 10% of their steady-state values. It can be seen that the two systems' behaviours are close to each other under disturbance.

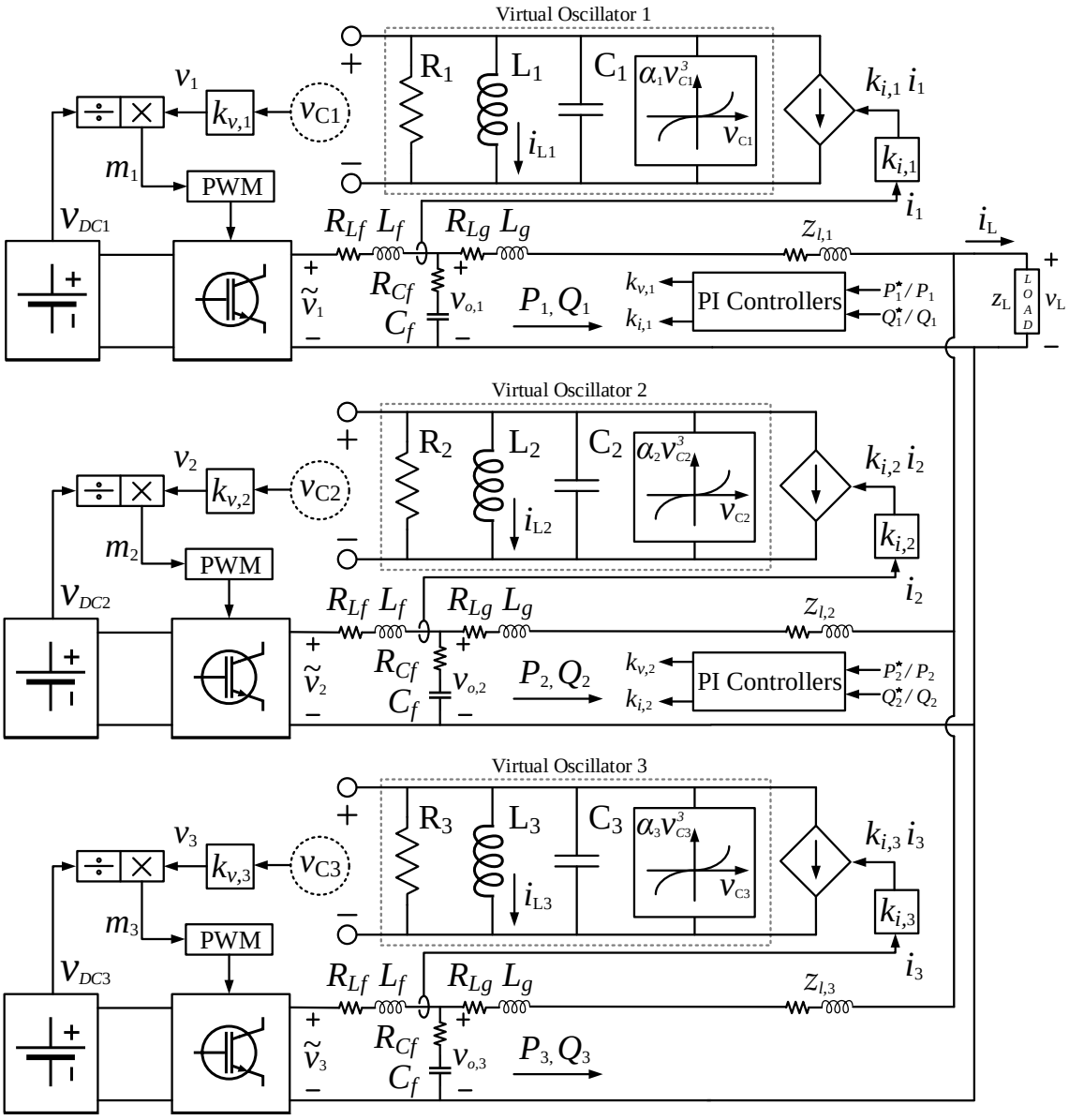

Figure 4.7: An overview of the system consisting of three parallel-connected VOC inverters with $m = 2$ and $n = 1$. Output power is controlled for Inverter 1 and Inverter 2 corresponding to the desired power set-points (P_1^*, Q_1^*) and (P_2^*, Q_2^*), respectively. The role of Inverter 3 is that of a conventional slack bus supplying the remaining power to the load z_L. The three inverters are connected to the load bus through line impedances $z_{l,1}$, $z_{l,2}$ and $z_{l,3}$, respectively.

Table 4.3: Total Harmonic Distortion in Inverter's Output Voltage

Case No.	Inverter 1	Inverter 2	Load Voltage
1	2.10 %	2.50 %	1.75 %
2	2.10 %	2.00 %	1.80 %
3	2.20 %	2.80 %	1.80 %
4	1.85 %	2.25 %	2.05 %
5	2.70 %	2.30 %	2.10 %

effectively while Inverter 2 supplies the remaining power to the load. The detailed descriptions of the power regulation cases considered are presented in Section 4.7.1. In order to quantify the inverter's output voltage quality without an inner voltage control loop, the total harmonic distortion (THD) is presented in Table 4.3.

4.6.2 One Controlled and Two Uncontrolled Inverters

In Fig. 4.9, simulation results are presented for the output power regulation of Inverter 1 while Inverter 2 and Inverter 3 share the remaining load power proportionally. It can be seen that the Inverter 1 tracks the reference output power set-points effectively. The detailed descriptions of the power regulation cases considered are presented in the following subsections.

4.6.2.1 Case 1

Initially, the three inverters are sharing equal active and reactive power at $t = 0$ s and have the same values of control variables (i.e. k_i and k_v) as in Fig. 4.9. At $t = 5$ s, a step-up change is applied in the active power set-point $P_1^* : 173 \rightarrow 350$ W while the reactive power set-point is the same $Q_1^* = 44$ VAr. The PI controllers tune the control variables and Inverter 1 reaches the desired set-point at $t = 5.8$ s. This is the case when Inverter 1 is supplying a major portion of load active power demand while Inverter 2 and Inverter 3 are supplying the remaining load power proportionally.

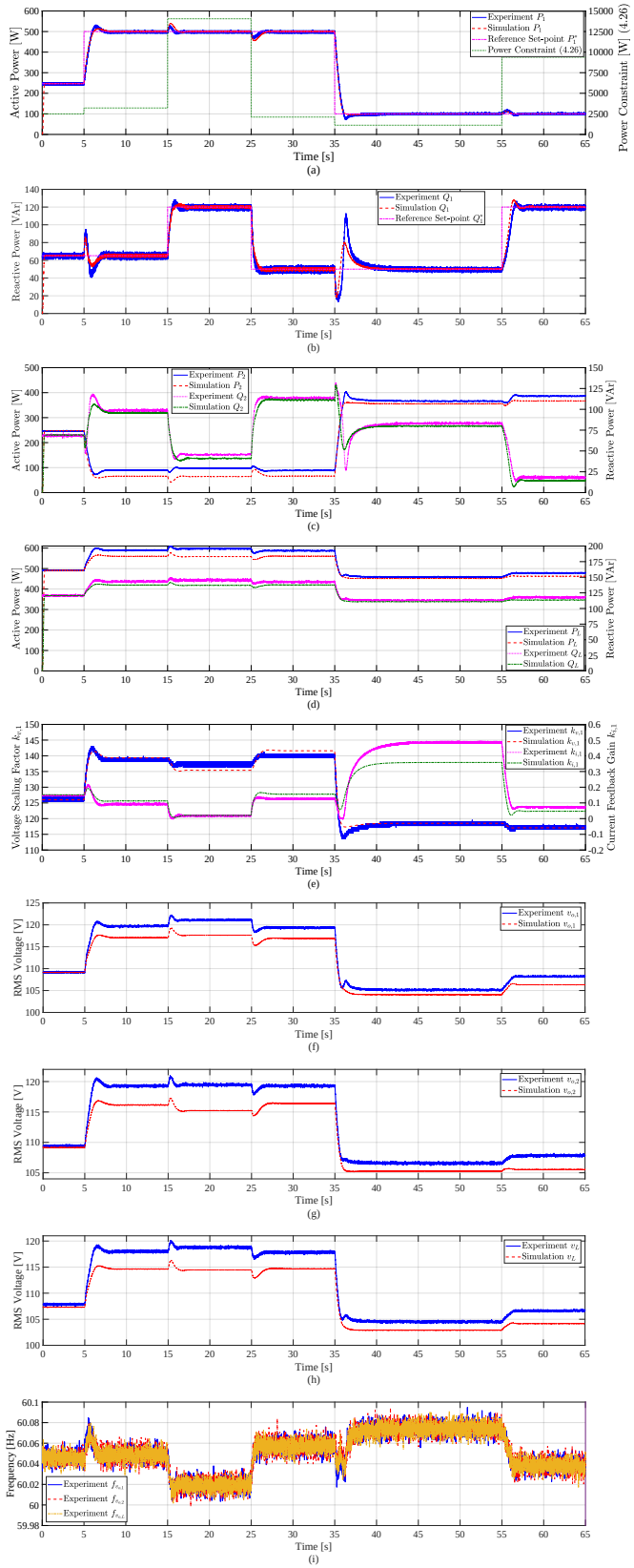

Figure 4.8: Experimental and simulation results for power dispatch in case of two parallel-connected VOC inverters: (a) reference set-point P_1^*, active power P_1 and power constraint (4.26), (b) reference set-point Q_1^* and reactive power Q_1, (c) Inverter 2 active power P_2 and reactive power Q_2, (d) load active power P_L and reactive power Q_L, (e) control variables $k_{v,1}$ and $k_{i,1}$, (f) Inverter 1 RMS voltage, (g) Inverter 2 RMS voltage, (h) load RMS voltage, (i) variations in fundamental frequency.

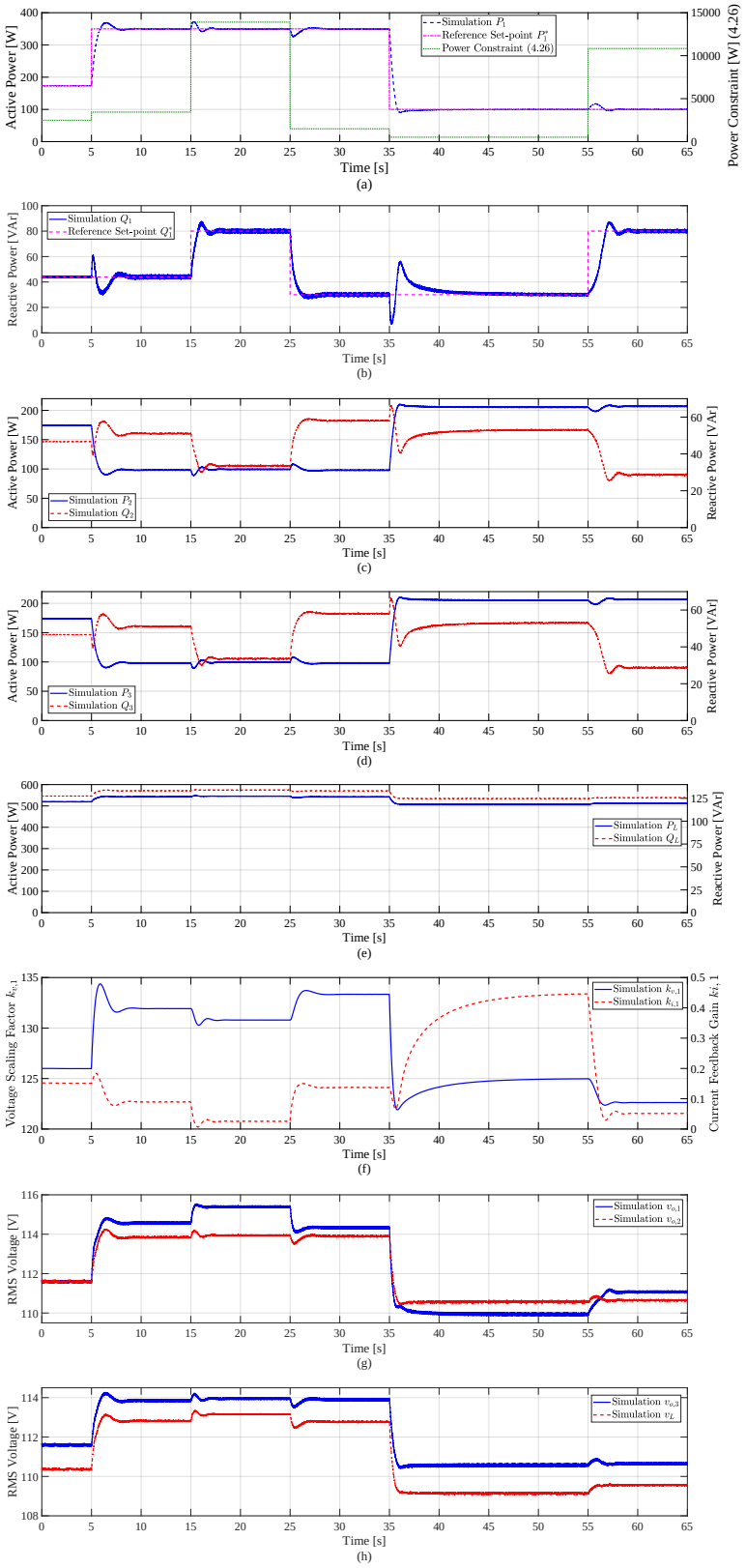

Figure 4.9: Simulation results for power dispatch in case of three parallel-connected VOC inverters: (a) reference set-point P_1^*, active power P_1 and power constraint (4.26), (b) reference set-point Q_1^* and reactive power Q_1, (c) Inverter 2 active power P_2 and reactive power Q_2, (d) Inverter 3 active power P_3 and reactive power Q_3 (e) load active power P_L and reactive power Q_L, (f) control variables $k_{v,1}$ and $k_{i,1}$, (g) Inverter 1 and Inverter 2 RMS voltage, (h) Inverter 3 and load RMS voltage.

4.6.2.2 Case 2

In this case Inverter 1 is supplying a major portion of both the active and reactive load power demand, while Inverter 2 and Inverter 3 supply a relatively small portion. At $t = 15$ s, a step-up change is applied in the reactive power set-point $Q_1^* : 44 \rightarrow 80$ VAr. The active power set-point $P_1^* = 350$ W is the same as in Case 4.6.2.1. Inverter 1 reaches the steady-state at $t = 15.8$ s. In Fig. 4.9, it can be seen that the step-change in the reference set-point for one of the controlled variables (i.e. P_1 and Q_1) also results in a disturbance in the other controlled variable due to the coupling effect between them, as discussed in Section 4.8.

4.6.2.3 Case 3

A step-down change in the reactive power set-point $Q_1^* : 80 \rightarrow 30$ VAr is applied at $t = 25$ s while the active power set-point is fixed at $P_1^* = 350$ W. Inverter 1 tracks the reference set-point effectively and reaches the new set-point at $t = 26.2$ s. An undershoot occurs in the active power P_1 for the step-down change in Q_1^*. As in Fig. 4.9, P_1 recovers back to the desired set point $P_1^* = 350$ W after the step-change in Q_1^*. In this case, Inverter 1 is supply most of the active power and a small portion of reactive power demand.

4.6.2.4 Case 4

Inverter 1 is made to deliver a small portion of both the active and reactive power demand while Inverter 2 and Inverter 3 are supplying a major portion of load power demand. At $t = 35$ s, a step-down change is applied in active power set-point $P_1^* : 350 \rightarrow 100$ W while the reactive power set-point is the same $Q_1^* = 30$ VAr. In Fig. 4.9, it can be seen that Inverter 1 reaches the new set-point at $t = 35.8$ s.

4.6.2.5 Case 5

At $t = 55$ s, a step-up change in the reactive power set-point is applied $Q_1^* : 30 \rightarrow 80$ VAr while the active power set-point is unchanged at $P_1^* = 100$ W. Inverter 1 settles at the new steady-state at $t = 56.8$ s. In this scenario, Inverter 1 is supplying a small portion of active power and a relatively major portion of reactive power demand. The corresponding changes in the current feedback gain $k_{i,1}$ and voltage scaling factor $k_{v,1}$ can be seen in Fig. 4.9.

4.6.3 Security Constraint Violation

In order to verify the security constraint (4.26), simulation results are presented in Fig. 4.10 for a non-feasible power set-point violating the security constraint. For the purpose of security constraint verification, the inverters are modelled as ideal ac-voltage sources because neither the actual nor average VOC dynamics take the dead-time and semiconductor voltage-drop present in an actual physical inverter, into account. The system under consideration consists of one controlled inverter and one uncontrolled inverter with $m = n = 1$. Initially at $t = 0$ s, the active and reactive power set-points for Inverter 1 are $P_1^* = 600$ W and $Q_1^* = 20$ VAr, respectively. According to the power security constraint (4.26), for an active power set-point $P_1^* = 600$ W, the reactive power set-point $Q_1^* > 12.7$ VAr must pertain for an operating point to be feasible. At $t = 20$ s, a step-down change in reactive power set-point $Q_1^* : 20 \rightarrow 11.5$ VAr is applied that violates the security constraint. In Fig. 4.10, it can be seen that the PI controllers try to achieve the desired power set-point. However, as the security constraint is not satisfied, neither real valued current feedback gain $k_{i,1}$ nor voltage scaling factor $k_{v,1}$ exists. We can see that the system starts to oscillate while trying to achieve the desired power set-point and becomes unstable at $t = 108$ s.

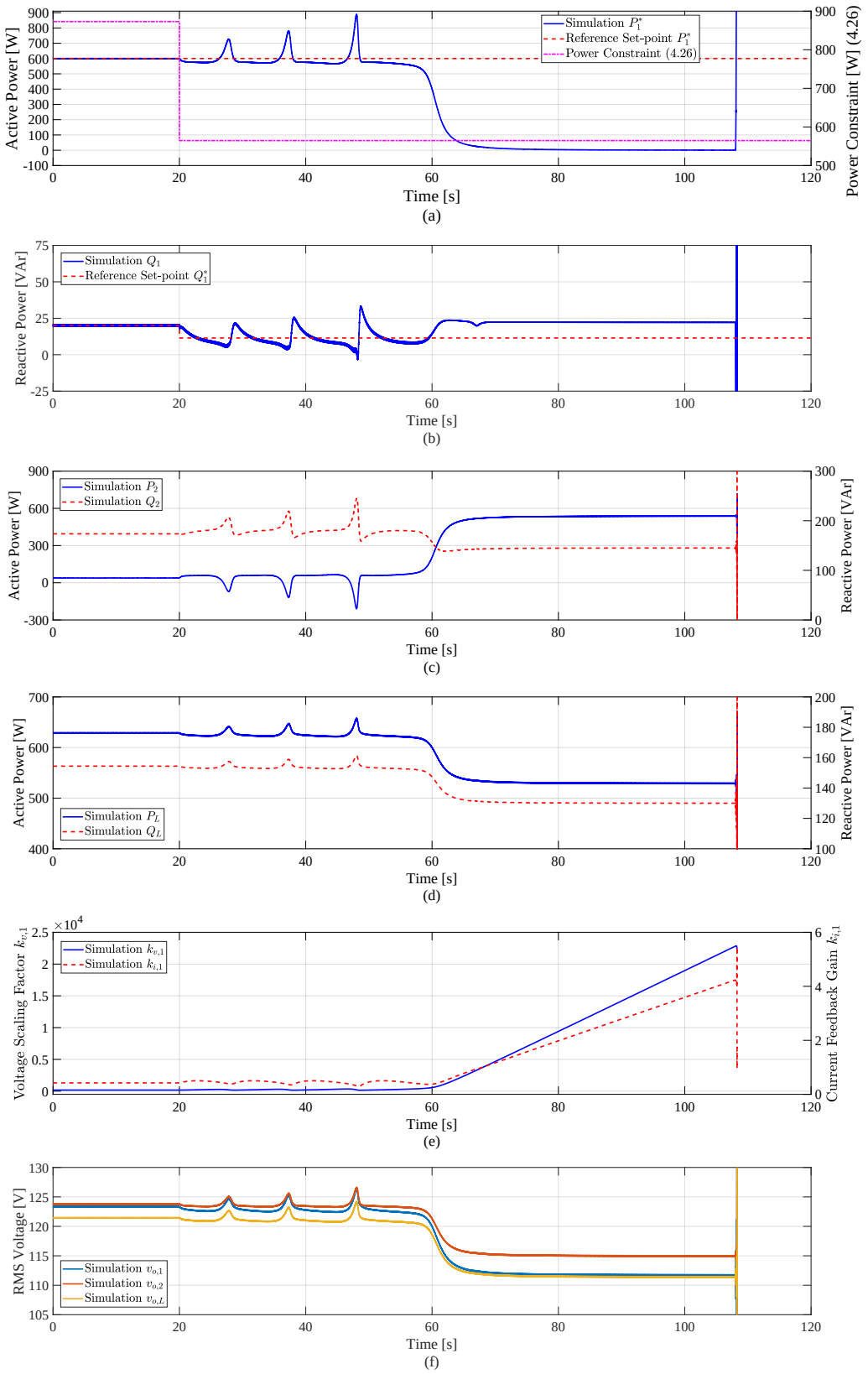

Figure 4.10: Simulation results for the security constraint (4.26) violation in case of two parallel-connected VOC inverters: (a) reference set-point P_1^*, active power P_1 and power constraint (4.26), (b) reference set-point Q_1^* and reactive power Q_1, (c) Inverter 2 active power P_2 and reactive power Q_2, (d) load active power P_L and reactive power Q_L, (e) control variables $k_{v,1}$ and $k_{i,1}$, (f) Inverter 1, Inverter 2 and load RMS voltage.

4.7 Experimental Results

The experimental setup consists of three single-phase inverters with IGBTs operating at a switching frequency of 10 kHz and a dead-time of 2μs. Two types of scenarios are considered for the experimental results. In Scenario 1, a system consisting of two inverters with $m = n = 1$ is considered. In Scenario 2, a system consisting of three inverters with $m = 2$ and $n = 1$ is considered, as shown in Fig. 4.7. The virtual oscillator controller is implemented on a Texas Instrument TMSC2000 digital signal processor by discretising the VOC dynamic equations adopting the trapezoidal rule of integration at a sampling time of 100μs [76]. Fig. 4.11 shows the experimental prototype used to demonstrate the power sharing in the case of a series RL load. In order to validate the simulation results in Section 4.6.1, all possible five combinations of active and reactive output power regulation are considered for the experimental results as well and are discussed in the following sections. In Fig. 4.8, it can be seen that the experimental results for the output power regulation are nearly the same as the simulation results. Further, the security constraint is satisfied for all the cases considered and is lowest for Section 4.7.1.4. From (4.26), it can be inferred that the only way the security constraint can be hit is by increasing the active power set-point P_1^* and decreasing the reactive power set-point Q_1^*. Hence, the proposed control approach can achieve a wide range of output power set-points.

4.7.1 One Controlled and One Uncontrolled Inverter

4.7.1.1 Case 1

Initially, the two inverters are sharing equal active and reactive power at $t = 0$ s and have the same control variable values (i.e. k_i and k_v) as in Fig. 4.8. At $t = 5$ s, a step-up change is applied in the active power set-point $P_1^* : 246 \rightarrow 500$ W while the reactive power set-point is the same $Q_1^* = 65$ VAr. PI controllers tune the control

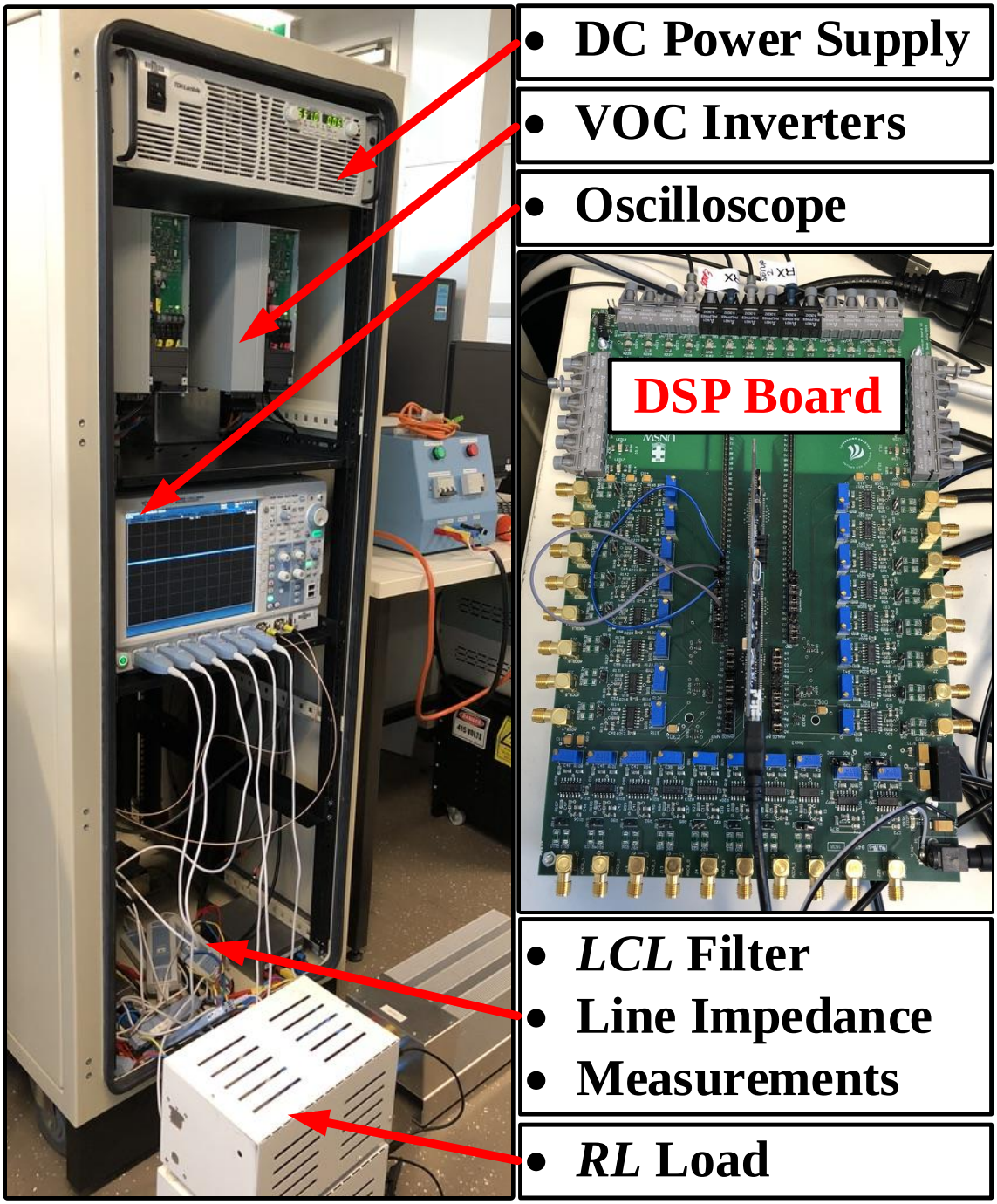

Figure 4.11: Experimental setup consisting of three parallel-connected VOC inverters, each with an output LCL filter. The inverters are connected to a common RL load through respective line impedances.

variables and Inverter 1 reaches the desired set-point at $t = 6.2$ s. In this case, Inverter 1 is supplying a major portion of active power while Inverter 2 is supplying the remaining load power.

4.7.1.2 Case 2

In this case, Inverter 1 is supplying a major portion of both the active and reactive load power demand while Inverter 2 is supplying a relatively small portion. At $t = 15$ s, a step-up change is applied in the reactive power set-point $Q_1^* : 65 \rightarrow 120$ VAr. The active power set-point $P_1^* = 500$ W is the same as in Case 4.7.1.1. Inverter 1 reaches the steady-state at $t = 15.7$ s. In Fig. 4.8, it can be seen that the step-change in the reference set-point for one of the controlled variables (i.e. P_1 and Q_1) also results in a disturbance in the other controlled variable due to the coupling effect between them, as discussed in Section 4.8.

4.7.1.3 Case 3

A step-down change in the reactive power set-point $Q_1^* : 120 \rightarrow 50$ VAr is applied at $t = 25$ s while the active power set-point is fixed at $P_1^* = 500$ W. Inverter 1 tracks the reference set-point effectively and reaches the new set-point at $t = 26$ s. An undershoot occurs in the active power P_1 for the step-down change in Q_1^*. As in Fig. 4.8, the P_1 recovers back to the desired set point $P_1^* = 500$ W after the step-change in Q_1^*. In this case, Inverter 1 is supplying most of the active power and a small portion of reactive power demand.

4.7.1.4 Case 4

In this case, Inverter 1 is made to deliver a small portion of both the active and reactive power demand, while Inverter 2 is supplying a major portion of load power

demand. At $t = 35$ s, a step-down change is applied in active power set-point $P_1^* : 500 \rightarrow 100$ W while the reactive power set-point is the same $Q_1^* = 50$ VAr. In Fig. 4.8, it can be seen that Inverter 1 reaches the new set-point at $t = 36.2$ s.

4.7.1.5 Case 5

At $t = 55$ s, a step-up change in the reactive power set-point is applied $Q_1^* : 50 \rightarrow 120$ VAr while the active power set-point is unchanged at $P_1^* = 100$ W. Inverter 1 settles at the new steady-state at $t = 56.5$ s. In this scenario, Inverter 1 is supplying a small portion of active power and a relatively major portion of reactive power demand. The corresponding change in the current feedback gain $k_{i,1}$ and voltage scaling factor $k_{v,1}$ can be seen in Fig. 4.8.

4.7.2 Two Controlled and One Uncontrolled Inverter

In order to better illustrate the phenomenon of dispatchability, experimental results with two controlled inverters and one uncontrolled inverter are presented. Inverter 1 and Inverter 2 are the controlled inverters and follow the desired power set-points, whereas Inverter 3 supplies the remaining power to the load, acting more like a slack bus. A series RL load is used with $R_L = 11.06\,\Omega$ and $L_L = 7.2\,\text{mH}$. A number of power dispatch scenarios are considered, with detailed descriptions presented in the following subsections.

4.7.2.1 Case 1

Initially, the three inverters are sharing nearly equal active and reactive power at $t = 0$ s and have approximately the same control variable values (i.e. k_i and k_v) as in Fig. 4.12. At $t = 5$ s, a step-up change is applied in the active power set-point $P_1^* : 307 \rightarrow 500$ W while the reactive power set-point is the same $Q_1^* = 86.5$ VAr.

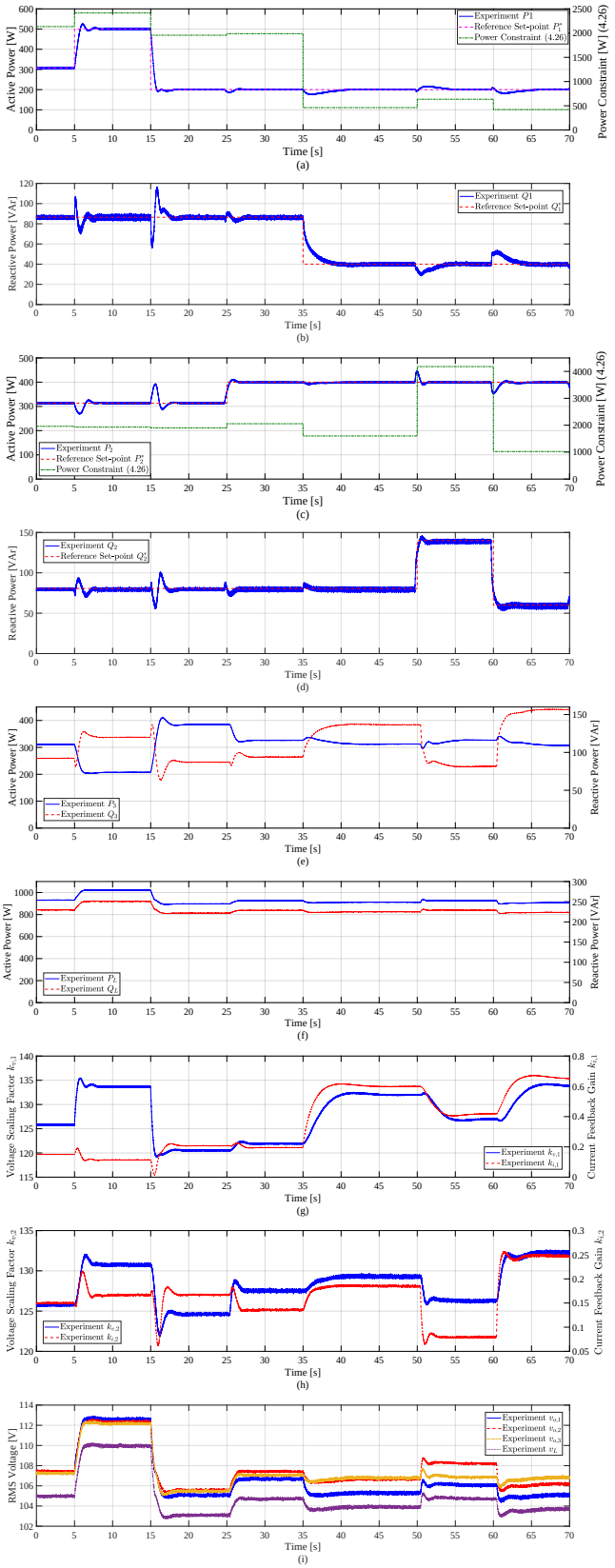

Figure 4.12: Experimental results for three parallel-connected VOC inverters: (a) set-point P_1^*, active power P_1 and constraint (4.26), (b) set-point Q_1^* and reactive power Q_1, (c) set-point P_2^*, active power P_2 and constraint (4.26), (d) set-point Q_2^* and reactive power Q_2, (e) Inverter 3 active power P_3 and reactive power Q_3, (f) load active power P_L and reactive power Q_L, (g) control variables $k_{v,1}$ and $k_{i,1}$, (h) control variables $k_{v,2}$ and $k_{i,2}$, (i) RMS voltages.

The PI controllers tune the control variables and Inverter 1 reaches the desired set-point at $t = 5.8$ s. This is the case when Inverter 1 is supplying a major portion of load active power demand. Inverter 2 also regulates its output power at the desired set-points $P_2^* = 313$ W and $Q_2^* = 80.6$ VAr while Inverter 3 supplies the remaining load demand.

4.7.2.2 Case 2

At $t = 15$ s, a step-down change is applied in the active power set-point $P_1^* : 500 \rightarrow 200$ W. The reactive power set-point $Q_1^* = 86.5$ VAr is unchanged. Inverter 1 reaches the new set-point at $t = 15.8$ s. Inverter 2 continues on regulating the active and reactive power at the desired set-points, which are the same as in Case 4.7.2.1. In Fig. 4.12, it can be seen that the step-change in the reference set-point for one of the controlled variables (i.e. P^* and Q^*) results in a disturbance in the other controlled variable due to the coupling effect between them, as discussed in Section 4.8.

4.7.2.3 Case 3

A step-up change in the active power set-point $P_2^* : 313 \rightarrow 400$ W is applied at $t = 25$ s while the reactive power set-point is fixed at $Q_2^* = 80.6$ VAr. Inverter 2 tracks the reference set-point effectively and reaches the new set-point at $t = 25.7$ s. The set-points $P_1^* = 200$ W and $Q_1^* = 86.5$ VAr for Inverter 1 are unchanged, as in Case 4.7.2.2.

4.7.2.4 Case 4

At $t = 35$ s, a step-down change is applied in reactive power set-point $Q_1^* : 86.5 \rightarrow 40$ VAr while the active power set-point is constant at $P_1^* = 200$ W. In Fig. 4.12, it can be seen that Inverter 1 reaches the new set-point at $t = 38.6$ s. The set-points

for Inverter 2 are unchanged, as in Case 4.7.2.3 and it continues on regulating the power at desired set-points.

4.7.2.5 Case 5

At $t = 50$ s, a step-up change in the reactive power set-point is applied $Q_2^* : 80.6 \rightarrow 140$ VAr while the active power set-point is unchanged at $P_2^* = 400$ W. Inverter 2 reaches the new set-point at $t = 50.6$ s. In this scenario, Inverter 2 is supplying a major portion of reactive power demand, relatively. The set-points $P_1^* = 200$ W and $Q_1^* = 40$ VAr for Inverter 1 are unchanged, as in Case 4.7.2.4. The corresponding changes in control variables for Inverter 1 and Inverter 2 can be seen in Fig. 4.12.

4.7.2.6 Case 6

A step-down change in the reactive power set-point $Q_2^* : 140 \rightarrow 60$ VAr is applied at $t = 60$ s while the active power set-point is fixed at $P_2^* = 400$ W. Inverter 2 tracks the reference set-point effectively and reaches the new set-point at $t = 60.8$ s. The set-points $P_1^* = 200$ W and $Q_1^* = 40$ VAr for Inverter 1 are unchanged, as in Case 4.7.2.5.

4.7.3 Dispatchability under Load Transients

In order to demonstrate the power dispatch in the case of load transients, a system of three parallel-connected inverters is considered. Inverter 1 and Inverter 2 are regulating the output power according to the desired power set-points, as shown in Fig. 4.13. The set-points for Inverter 1 are $P_1^* = 250$ W and $Q_1^* = 60$ VAr. Similarly, the set-points for Inverter 2 are $P_2^* = 200$ W and $Q_2^* = 40$ VAr. Inverter 3 is uncontrolled and supplies the remaining power to the load. In Fig. 4.13 at $t = 15$ s, a step-up change in RL load is applied. It can be seen that both Inverter 1 and

Inverter 2 continue on regulating their output power according to the desired power set-points, while the output power of Inverter 3 increases to supply the additional load demand. The active and reactive output power of Inverter 3 increases from $P_3 : 102 \rightarrow 210$ W and $Q_3 : 42 \rightarrow 75$ VAr, respectively. Similarly, a step-down change in the RL load is applied at $t = 30$ s. As a result, the output power of uncontrolled Inverter 3 decreases while the controlled inverters (Inverter 1 and Inverter 2) continue supplying the desired power according to their set-points.

4.8 Discussion

From Fig. 4.8, it can be seen that whenever there is a step-change in the reference power set-point for one of the controlled variables (P_1, Q_1), there is a disturbance in the other controlled variable. This is due to the fact that the relation between control variables $k_{v,1}$ and $k_{i,1}$ and the controlled variables P_1 and Q_1, respectively, is not decoupled. Further, an abrupt change in the control variables may result in un-synchronised inverters and high circulating current to flow between them. This coupling effect between the controlled variables can be avoided by using a ramp-change instead of a step-change in the reference power set-point or by making the PI controller's response slow. A systematic design approach for the PI controller gains to achieve the desired dynamic response and minimise the coupling effect between the controlled variables, is potential future work (as discussed in Chapter 8).

In Fig. 4.8, comparing the simulation and experimental results, it can be seen that Inverter 1 tracks the reference power set-points effectively. However, comparing the control variables $k_{v,1}$ and $k_{i,1}$ for both the simulation and experimental results, indicates that a steady-state offset error exists. In the case of the VOC inverter control system, the only feedback to the controller is the filter current. As there is no voltage feedback loop and the VOC model does not take into account the dead-

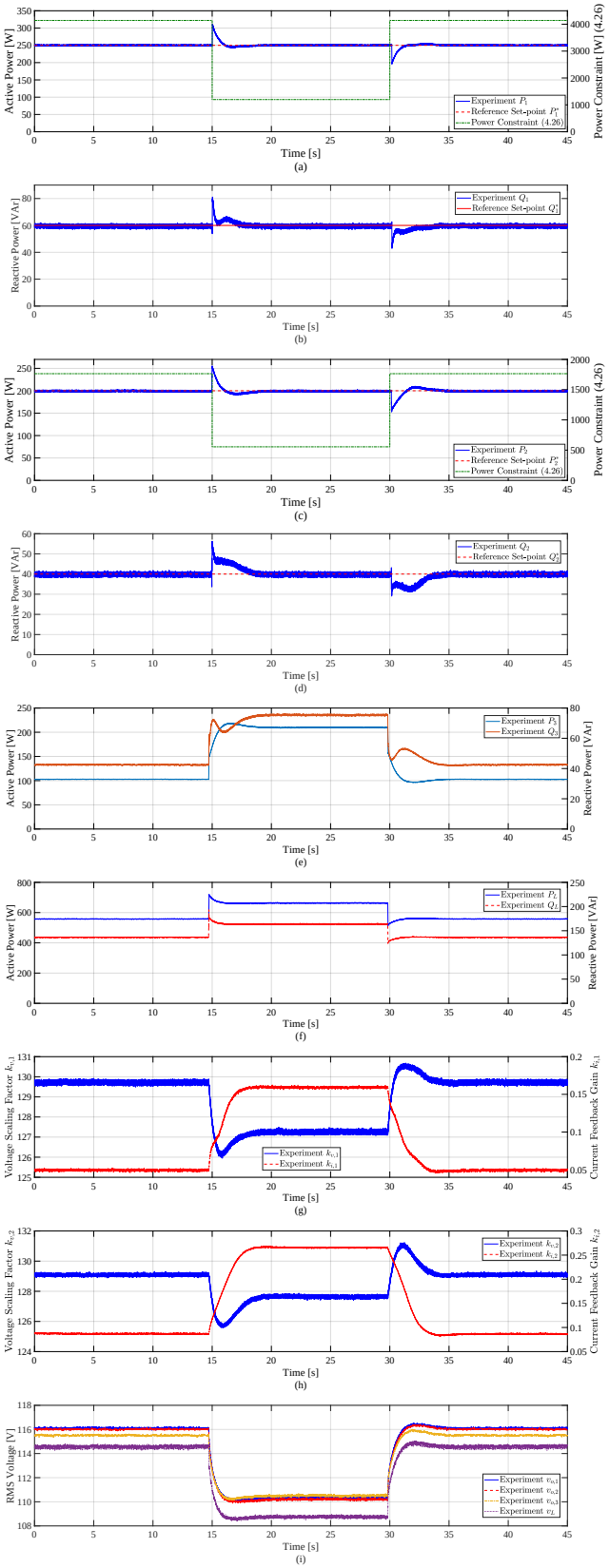

Figure 4.13: Experimental results for load transients in case of three parallel-connected VOC inverters: (a) set-point P_1^*, active power P_1 and constraint (4.26), (b) set-point Q_1^* and reactive power Q_1, (c) set-point P_2^*, active power P_2 and constraint (4.26), (d) set-point Q_2^* and reactive power Q_2, (e) Inverter 3 active power P_3 and reactive power Q_3, (f) load active power P_L and reactive power Q_L, (g) control variables $k_{v,1}$ and $k_{i,1}$, (h) control variables $k_{v,2}$ and $k_{i,2}$, (i) RMS voltages.

time and switching losses (voltage drop across the IGBTs), the voltage that appears at the output of the VOC inverter is not exactly the same as that generated by the virtual oscillator controller. In SIMULINK, we tuned the IGBTs forward voltage drop to match the simulation results to the experimental results for the nominal instance of when both the inverters are supplying equal power for $t = 0$ s to $t = 5$ s. In Fig. 4.8, it can be seen that for the first 5 seconds, the simulation results are almost the same as the experimental results, including the Inverter 1 output power, Inverter 2 output power, load power and the control inputs $(k_{i,1}, k_{v,1})$. The ON-state voltage drop across the IGBT is a function of the conduction current. The current flowing through the IGBTs depends on the output power set-point. The change in output power set-point from the nominal case results in a mismatch between the IGBT forward voltage drop (which is tuned/matched for the nominal case) for the simulation and experimental results. This mismatch in the forward voltage drop contributes to the mismatch between the simulation and experimental results. A compensation technique to avoid the effects of dead-time, switching and conduction losses is proposed in Chapter 6.

4.9 Conclusion

In the case of multiple parallel-connected virtual oscillator-controlled inverters, simultaneous regulation of both the active and reactive output power can be achieved using the proposed dispatchable control strategy. PI controllers are used to continuously tune the voltage scaling factor and current feedback gain of each controlled inverter to achieve the desired power set-point. The achievability of a particular power set-point can be determined a-priori using the derived security constraints. The desired output power set-points can be achieved as long as the security constraints are not violated. Further, using the derived control laws, the values of virtual oscillator control parameters can be determined to achieve the desired power set-

points. Experimental and simulation results demonstrate the merits of the proposed dispatchable control technique for a system of m-controlled and n-uncontrolled inverters, where $n_T = m + n$ denotes the total number of virtual oscillator-controlled inverters present in the system.

Chapter 5

Synthesising Averaged Virtual Oscillator Dynamics to Control Islanded Inverters with an Output *LCL* Filter

In commercial inverters, an LCL (or LC) filter is always considered an integral part for filtering out the switching harmonics and generating a sinusoidal output voltage. Considering the existing literature on virtual oscillator control (VOC), averaged VOC dynamics have been presented for inverters with current feedback before the output LCL filter that contains the switching harmonics or for inductive filters ignoring the effect of filter capacitance. In this chapter, a new version of averaged VOC dynamics is presented for islanded inverters with an output LCL (or LC) output filter. In the proposed approach, the current feedback is after the output LCL filter, thus avoiding the switching harmonics going into the virtual oscillator controller. Embedded droop-characteristics within the averaged VOC dynamics are identified and a parameter design procedure is presented to regulate the output voltage magnitude and frequency according to the desired ac-performance specifications. Further, a power dispatch technique is presented based on the proposed newer

version of averaged VOC dynamics simultaneously regulating both the active and reactive output power of two parallel-connected islanded inverters. The control laws are derived to determine the control inputs corresponding to the particular power set-point. A power security constraint is presented to check a-priori if a particular power set-point is achievable. Simulation results validate the proposed version of averaged VOC dynamics for a number of scenarios including load transients, proportional power sharing and power dispatch[1].

5.1 Introduction

Recall from Chapter 2, the averaged VOC model presented in [20, 76] is derived to explicitly identify the $P-V$ and $\omega-Q$ droop-characteristics embedded within the averaged dynamics of the virtual oscillator controller. The averaged VOC model presented in [76] is derived for the case where current feedback to the controller is before the output filter. However, this model is not an accurate representation when there is a current feedback after the output LCL filter. In the case of commercial inverters, an output LCL (or LC) filter is always considered an essential part for filtering out the switching harmonics and improving the quality of the output voltage. Section 5.3 presents the proposed new version of averaged VOC dynamics that takes into account the LCL filter at the output of an inverter. In the proposed control scheme, the current is fedback after the output LCL filter, thus avoiding the switching harmonics going into the virtual oscillator controller. The contributions of this chapter are twofold. First, an averaged VOC model is derived for an inverter with current feedback after the output LCL filter. The updated embedded droop-characteristics within the proposed averaged VOC dynamics are presented and corresponding equilibrium points are derived. In Section 5.4, a system's parameter design procedure is

[1]This chapter is based on conference paper [34]. The co-authors, Dr. Hendra I. Nurdin and Professor John E. Fletcher supervised the research work, they being the joint and primary supervisors, respectively.

presented to regulate the inverter's output voltage magnitude and frequency according to the desired ac-performance specifications. In order to validate the proposed averaged VOC dynamics, Section 5.6 presents the simulation results for a number of scenarios including rise time, harmonics analysis, droop-characteristics and load transients. It is shown that for all the scenarios, the proposed averaged VOC model predicts the actual VOC (Van der Pol) dynamics accurately. A comparison with the previously reported averaged VOC model [76] is also presented. The previously derived averaged VOC dynamics [76] start to differ more from the actual VOC dynamics (with current feedback after the output LCL filter) for a large value of filter capacitance. This is due to the fact that a higher value of filter capacitance draws more current and results in a significant difference between the current before and after the filter.

The second contribution of this chapter is the extension of the power dispatch technique (presented in Chapter 4) to this new version of averaged VOC dynamics. In Section 5.5, the updated control laws are derived based on this new model to determine the control inputs corresponding to a particular power set-point. Further, an updated power security constraint is derived to determine the feasible power set-points. Using this constraint, it can be checked a-priori if a particular power set-point is achievable or not. Simulation results are presented in Section 5.6 for a number of power dispatch scenarios to validate the proposed power dispatch technique.

The chapter is organised as follows. In Section 5.2, an overall system description is presented. In Section 5.3, an averaged VOC model is derived for inverters with current feedback after the output LCL filter. In Section 5.4, a VOC parameter design procedure is discussed. In Section 5.5, a power dispatch technique is presented. In Section 5.6, simulation results are presented for a number of scenarios, including load transients and power dispatch. In Section 5.7, the conclusion is drawn.

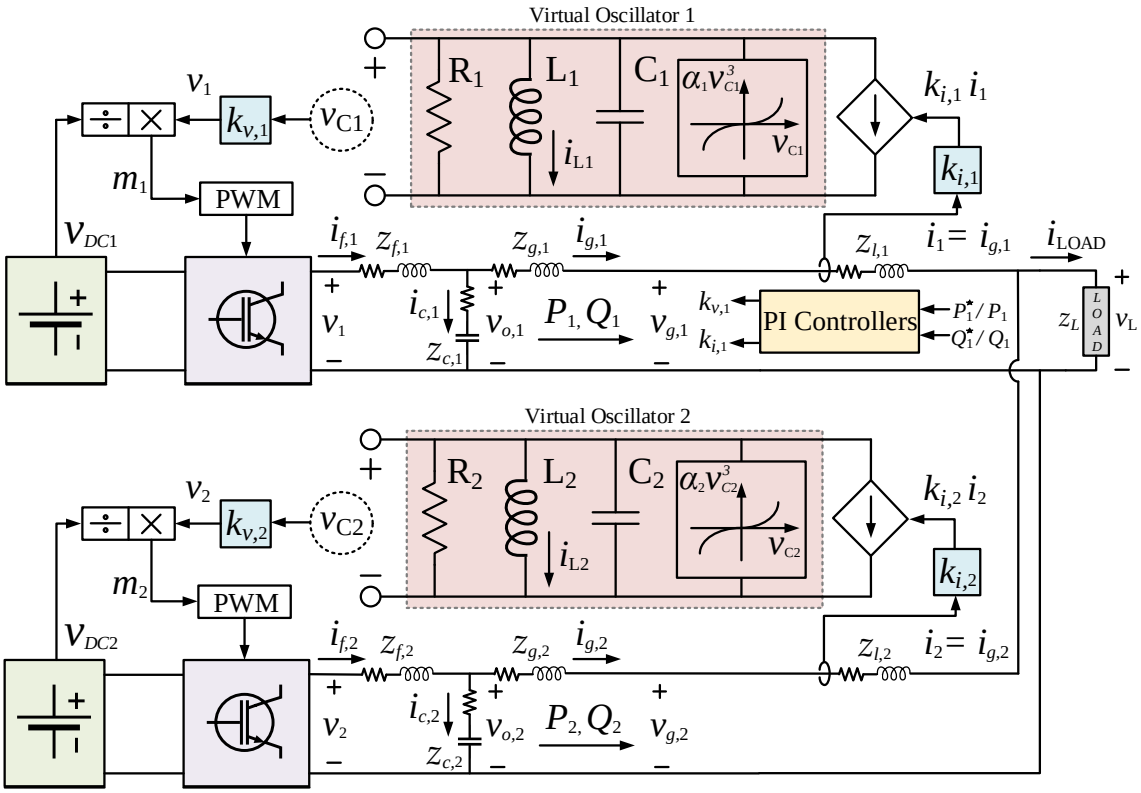

Figure 5.1: An overview of the overall system consisting of two parallel-connected virtual oscillator-controlled inverters. Inverter 1 can dispatch power using the PI controllers while Inverter 2 supplies the remaining load power.

5.2 System Description

The system considered in this chapter consists of two virtual oscillator-controlled inverters with current feedback after the output LCL filter. A complete system overview is shown in Fig. 5.1. The filter impedances are $z_f = R_f + \jmath\omega^* L_f$, $z_c = R_c + \frac{1}{\jmath\omega^* C_f}$ and $z_g = R_g + \jmath\omega^* L_g$. The line impedance is represented as $z_l = R_l + \jmath\omega^* L_l$. The inverters are connected to a common RL load $z_L = R_L + \jmath\omega^* L_L$ through the point of common coupling (PCC). Moreover, Inverter 1 can dispatch power by the use of two additional PI controllers.

5.3 System Modelling

In this section, the dynamics of the virtual oscillator controller are presented. Further, the proposed averaged VOC model is derived for inverters with current feedback after the output LCL filter. The dynamics of the PI controllers used for power dispatch (similar to Chapter 4) are also presented.

5.3.1 Virtual Oscillator Controller

Recall from Chapter 2, the actual VOC dynamics are given by the following dynamic equations for an nth virtual oscillator-controlled inverter [76]:

$$\begin{aligned}\frac{dV_n}{dt} &= \frac{\epsilon_n \omega^*}{\sqrt{2}}\Big(\sigma_n g\big(\sqrt{2}V_n\cos(\phi_n)\big) - k_{v,n}k_{i,n}i_n\Big)\cos(\phi_n),\\ \frac{d\phi_n}{dt} &= \omega^* - \frac{\epsilon_n \omega^*}{\sqrt{2}V_n}\Big(\sigma_n g\big(\sqrt{2}V_n\cos(\phi_n)\big) - k_{v,n}k_{i,n}i_n\Big)\sin(\phi_n).\end{aligned} \tag{5.1}$$

A detailed derivation and parametric description of the dynamic model for the inverter RMS output voltage magnitude V and instantaneous phase angle $\phi = \omega t + \theta$ where θ is the phase offset with respect to ωt, can be found in [76] and are reviewed in Chapter 2.

5.3.2 Proposed Averaged VOC Model for Inverters with an Output *LCL* Filter

In this section, a new version of averaged VOC dynamics is presented for inverters with current feedback after the output LCL filter. The averaged VOC model is derived by averaging the actual VOC dynamics (5.1) over an ac-cycle $\frac{2\pi}{\omega^*}$. A brief derivation of the new averaged VOC model is presented in Appendix A. The averaged VOC model helps to explicitly identify the embedded droop-characteristics within

the averaged dynamics of the Van der Pol oscillator and simplifies the analysis. The proposed averaged VOC model is given by the following dynamics equations:

$$\frac{d}{dt}\overline{V} = \frac{\sigma}{2C}\left(\overline{V} - \frac{\beta}{2}\overline{V}^3\right) - \frac{k_v k_i}{2C}\left(\frac{C_\alpha \overline{P}}{\overline{V}} + \frac{S_\alpha \overline{Q}}{\overline{V}} + C_\beta \overline{V}\right), \tag{5.2}$$

$$\frac{d}{dt}\overline{\theta} = \omega^* - \omega + \frac{k_v k_i}{2C}\left(\frac{C_\alpha \overline{Q}}{\overline{V}^2} - \frac{S_\alpha \overline{P}}{\overline{V}^2} - S_\beta\right), \tag{5.3}$$

where $\beta = \frac{3\alpha}{k_v^2 \sigma}$, $\overline{V}$ denotes the averaged RMS output voltage magnitude and $\overline{\theta}$ denotes the averaged phase offset with respect to ωt. The averaged active and reactive power are denoted by $\overline{P}$ and $\overline{Q}$, respectively. The $C_\alpha = Z_\alpha \cos\theta_\alpha$, $C_\beta = Z_\beta \cos\theta_\beta$, $S_\alpha = Z_\alpha \sin\theta_\alpha$ and $S_\beta = Z_\beta \sin\theta_\beta$ are the impedance constants (defined in Appendix A) where $z_\alpha = R_\alpha + \jmath X_\alpha = Z_\alpha \angle\theta_\alpha = \frac{z_c + z_f}{z_c}$ and $z_\beta = R_\beta + \jmath X_\beta = Z_\beta \angle\theta_\beta = \frac{-1}{z_c}$.

5.3.2.1 Voltage Regulation Characteristics

The equilibrium value for the averaged RMS voltage magnitude $\overline{V}$ can be determined by the solution to the following equation:

$$0 = \frac{\sigma}{2C}\left(\overline{V}_{eq} - \frac{\beta}{2}\overline{V}_{eq}^3\right) - \frac{k_v k_i}{2C}\left(\frac{C_\alpha \overline{P}_{eq}}{\overline{V}_{eq}} + \frac{S_\alpha \overline{Q}_{eq}}{\overline{V}_{eq}} + C_\beta \overline{V}_{eq}\right), \tag{5.4}$$

where $\overline{V}_{eq}$ denotes the equilibrium value for the averaged RMS voltage magnitude, and $\overline{P}_{eq}$ and $\overline{Q}_{eq}$ denote the active and reactive power values at the equilibrium. Solving the Eq. (5.4), the equilibrium value $\overline{V}_{eq}$ can be determined as follows:

$$\overline{V}_{eq} = k_v \sqrt{\frac{\sigma_\beta \pm \sqrt{\sigma_\beta^2 - 6\alpha\left(k_i/k_v\right)\left(C_\alpha \overline{P}_{eq} + S_\alpha \overline{Q}_{eq}\right)}}{3\alpha}}, \tag{5.5}$$

where $\sigma_\beta = (\sigma - k_v k_i C_\beta)$. Note that both the roots of (5.5) are real valued if the following inequality holds:

$$\left(C_\alpha \overline{P} + S_\alpha \overline{Q}\right) < S_{cr} := \frac{\sigma_\beta^2}{6\alpha \left(k_i/k_v\right)}, \tag{5.6}$$

where $k_i > 0$ and $k_v > 0$. S_{cr} denotes the critical power constant with the corresponding critical value of the inverter RMS output voltage as follows:

$$\overline{V}_{cr} = k_v \sqrt{\frac{\sigma_\beta}{3\alpha}}. \tag{5.7}$$

A local asymptotic stability analysis of the high voltage solution of (5.5) (similar to [76]) is presented in Appendix B and in the subsequent analysis, with a slight abuse of notation, we denote it by $\overline{V}_{eq}$. Using (5.5), the open circuit voltage $\overline{V}_{oc}$ for the virtual oscillator-controlled inverter (i.e. $\overline{P}_{eq} = \overline{Q}_{eq} = 0$) is as follows:

$$\overline{V}_{oc} = k_v \sqrt{\frac{2\sigma_\beta}{3\alpha}}. \tag{5.8}$$

5.3.2.2 Frequency Regulation Characteristics

Solving the phase angle dynamics (5.3) for the equilibrium point gives the system's frequency ω_{eq} in steady-state as follows:

$$\omega_{eq} = \omega^* + \frac{k_v k_i}{2C} \left(\frac{C_\alpha \overline{Q}_{eq}}{\overline{V}_{eq}^2} - \frac{S_\alpha \overline{P}_{eq}}{\overline{V}_{eq}^2} - S_\beta \right), \tag{5.9}$$

where $\overline{V}_{eq}$ is the high voltage solution for (5.5).

5.3.2.3 Dynamic Response

In order to quantify the dynamic response of the virtual oscillator-controlled inverter, the time taken by the inverter to reach its open circuit voltage $\overline{V}_{oc}$ is considered.

The voltage dynamics of interest in a variable-separable ODE form are obtained from (5.2) by setting $\overline{P} = \overline{Q} = 0$:

$$\frac{d}{dt}\overline{V} = \frac{\sigma}{2C}\left(\overline{V} - \frac{\beta}{2}\overline{V}^3\right) - \frac{k_v k_i C_\beta}{2C}\overline{V}. \tag{5.10}$$

The rise time t_{rise} is defined as the time taken by the inverter to build-up output voltage from $0.1\overline{V}_{oc}$ to $0.9\overline{V}_{oc}$. The t_{rise} can be determined by separating the variables in (5.10) and integrating them between the limits of $0.1\overline{V}_{oc}$ and $0.9\overline{V}_{oc}$. The t_{rise} is given by the solution of:

$$t_{rise} = \frac{2}{\omega^*\epsilon\sigma_\beta}\left[\log|\overline{V}| - \frac{1}{2}\log\left|\frac{\omega^*\epsilon\sigma_\beta}{2}\left(1 - \frac{\overline{V}^2}{k_v^2}\right)\right|\right]_{0.9\overline{V}_{oc}}^{0.1\overline{V}_{oc}}. \tag{5.11}$$

Evaluating the limits in (5.11), we get:

$$t_{rise} \approx \frac{6}{\omega^*\epsilon\sigma_\beta}. \tag{5.12}$$

Note that in (5.12), the t_{rise} depends on the VOC design parameter ϵ. The significance of this dependence will be explored in Section 5.4.3 while designing the capacitance value for the virtual oscillator.

5.3.2.4 Embedded Droop Characteristics

The previously reported averaged VOC model [76] uncovers the embedded $V-P$ and $\omega-Q$ droop-characteristics within the averaged VOC dynamics. However, this is not the case for the proposed averaged VOC dynamics. The equilibrium RMS voltage magnitude $\overline{V}_{eq}$ and frequency ω_{eq} depend on both the active and reactive power, as in (5.5),(5.9). For the system parameters and ac-performance specifications as in Table 5.1 and Table 5.2, respectively, the variations in equilibrium RMS voltage magnitude $\overline{V}_{eq}$ as a function of active and reactive power, are shown in Fig. 5.4. Similarly, the variations in the equilibrium frequency ω_{eq} as a function of active

and reactive power, are shown in Fig. 5.5. Note that the equilibrium RMS voltage magnitude $\overline{V}_{eq}$ mainly depends on the active power, and the variations with respect to the reactive power are not significant. Similarly, the equilibrium frequency ω_{eq} mainly depends on the reactive power and does not vary much with the change in active power. In fact, the dependence of the equilibrium RMS voltage magnitude $\overline{V}_{eq}$ and the equilibrium frequency ω_{eq} on the active and reactive power is defined by the weighing factors C_α and S_α which are determined based on the LCL filter parameters as in Appendix A.

In order to develop a better understanding of the droop-characteristics embedded within the proposed averaged VOC dynamics, an approach presented in [8] is adopted. Let us denote a phasor associated with a time-domain signal (.) by $\overrightarrow{(.)}$. Similarly, the complex conjugate of a complex number (.) is denoted by $\bar{(.)}$. Let us define a scaled version of phasor $\overrightarrow{V}$ (the phasor associated with the voltage v before the output LCL filter) as follows:

$$\overrightarrow{V_\gamma} = \bar{z}_\alpha \overrightarrow{V}, \tag{5.13}$$

where $\bar{z}_\alpha = R_\alpha - \jmath X_\alpha = Z_\alpha \angle -\theta_\alpha$, $\overrightarrow{V} = V\angle\theta$ and $\overrightarrow{V_\gamma} = V_\gamma\angle\theta_\gamma$. Simplifying (5.13), we get:

$$\overrightarrow{V_\gamma} = V_\gamma\angle\theta_\gamma = Z_\alpha V\angle(\theta - \theta_\alpha). \tag{5.14}$$

The power flow and phasor diagrams are given in Fig. 5.2 where $\overrightarrow{I_f} = I_f\angle\theta_f$ denotes the phasor associated with the inverter side inductor current i_f. Note that $\theta_f = 0^\circ$ is taken as the reference angle. The $\overrightarrow{S} = S\angle\theta = P + \jmath Q$ denotes the complex power inflow at point A while $\overrightarrow{S_\gamma} = S_\gamma\angle\theta_\gamma = P_\gamma + \jmath Q_\gamma$ denotes the complex power outflow at point B where $\theta_\gamma = \theta - \theta_\alpha$. The active and reactive power outflow at point B is

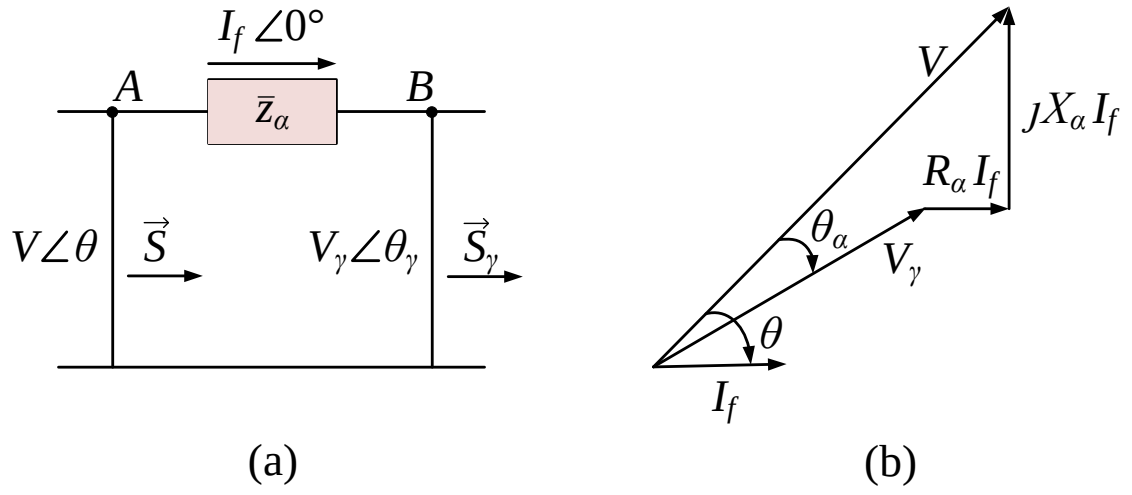

Figure 5.2: A schematic representation of: (a) power flow between the points A and B, (b) phasor diagram.

given by:

$$\begin{aligned} P_\gamma &= V_\gamma I_f \cos(\theta - \theta_\alpha), \\ Q_\gamma &= V_\gamma I_f \sin(\theta - \theta_\alpha). \end{aligned} \tag{5.15}$$

Using the trigonometric identities and substituting (5.14) in (5.15), we get:

$$\begin{aligned} P_\gamma &= Z_\alpha \cos\theta_\alpha V I_f \cos\theta + Z_\alpha \sin\theta_\alpha V I_f \sin\theta, \\ P_\gamma &= C_\alpha P + S_\alpha Q, \\ Q_\gamma &= Z_\alpha \cos\theta_\alpha V I_f \sin\theta - Z_\alpha \sin\theta_\alpha V I_f \cos\theta, \\ Q_\gamma &= C_\alpha Q - S_\alpha P. \end{aligned} \tag{5.16}$$

Using the orthogonal linear transformation matrix $\mathbf{T}$, (5.16) can be written as follows:

$$\begin{aligned} \begin{bmatrix} P_\gamma \\ Q_\gamma \end{bmatrix} &= \begin{bmatrix} C_\alpha & S_\alpha \\ -S_\alpha & C_\alpha \end{bmatrix} \begin{bmatrix} P \\ Q \end{bmatrix} = \begin{bmatrix} Z_\alpha \cos\theta_\alpha & Z_\alpha \sin\theta_\alpha \\ -Z_\alpha \sin\theta_\alpha & Z_\alpha \cos\theta_\alpha \end{bmatrix} \begin{bmatrix} P \\ Q \end{bmatrix}, \\ &= Z_\alpha \begin{bmatrix} \cos\theta_\alpha & \sin\theta_\alpha \\ -\sin\theta_\alpha & \cos\theta_\alpha \end{bmatrix} \begin{bmatrix} P \\ Q \end{bmatrix} = Z_\alpha \mathbf{T} \begin{bmatrix} P \\ Q \end{bmatrix}. \end{aligned} \tag{5.17}$$

The constants C_α and S_α can be written as follows:

$$\begin{aligned} C_\alpha &= Z_\alpha \cos\theta_\alpha = Z_\alpha \frac{R_\alpha}{Z_\alpha} = R_\alpha, \\ S_\alpha &= Z_\alpha \sin\theta_\alpha = Z_\alpha \frac{X_\alpha}{Z_\alpha} = X_\alpha. \end{aligned} \tag{5.18}$$

Substituting (5.18) in (5.17), we get:

$$\begin{bmatrix} P_\gamma \\ Q_\gamma \end{bmatrix} = \begin{bmatrix} R_\alpha & X_\alpha \\ -X_\alpha & R_\alpha \end{bmatrix} \begin{bmatrix} P \\ Q \end{bmatrix}. \tag{5.19}$$

In order to further simplify the analysis, let us define a scaled version of active and reactive power outflow at point B as follows:

$$\begin{bmatrix} P_\gamma \\ Q_\gamma \end{bmatrix} = Z_\alpha \begin{bmatrix} P^\iota_\gamma \\ Q^\iota_\gamma \end{bmatrix}, \tag{5.20}$$

where,

$$\begin{bmatrix} P^\iota_\gamma \\ Q^\iota_\gamma \end{bmatrix} = \begin{bmatrix} \frac{R_\alpha}{Z_\alpha} & \frac{X_\alpha}{Z_\alpha} \\ -\frac{X_\alpha}{Z_\alpha} & \frac{R_\alpha}{Z_\alpha} \end{bmatrix} \begin{bmatrix} P \\ Q \end{bmatrix} = \begin{bmatrix} \cos\theta_\alpha & \sin\theta_\alpha \\ -\sin\theta_\alpha & \cos\theta_\alpha \end{bmatrix} \begin{bmatrix} P \\ Q \end{bmatrix} = \mathbf{T} \begin{bmatrix} P \\ Q \end{bmatrix}. \tag{5.21}$$

Using (5.19)-(5.21), the proposed averaged VOC dynamics (5.2)-(5.3) can be re-written as follows:

$$\frac{d}{dt}\overline{V} = \frac{\sigma}{2C}\left(\overline{V} - \frac{\beta}{2}\overline{V}^3\right) - \frac{k_v k_i}{2C}\left(\frac{\overline{P}_\gamma}{\overline{V}} + C_\beta \overline{V}\right), \tag{5.22}$$

$$\frac{d}{dt}\overline{\theta} = \omega^* - \omega + \frac{k_v k_i}{2C}\left(\frac{\overline{Q}_\gamma}{\overline{V}^2} - S_\beta\right). \tag{5.23}$$

Similarly, by substituting (5.20) in (5.22)-(5.23), we get:

$$\frac{d}{dt}\overline{V} = \frac{\sigma}{2C}\left(\overline{V} - \frac{\beta}{2}\overline{V}^3\right) - \frac{k_v k_i}{2C}\left(\frac{Z_\alpha \overline{P}^{\iota}_{\gamma}}{\overline{V}} + C_\beta \overline{V}\right), \tag{5.24}$$

$$\frac{d}{dt}\overline{\theta} = \omega^* - \omega + \frac{k_v k_i}{2C}\left(\frac{Z_\alpha \overline{Q}^{\iota}_{\gamma}}{\overline{V}^2} - S_\beta\right). \tag{5.25}$$

The corresponding equilibrium values are as follows:

$$\overline{V}_{eq} = k_v\sqrt{\frac{\sigma_\beta \pm \sqrt{\sigma_\beta^2 - 6\alpha\left(k_i/k_v\right)\overline{P}_{\gamma,eq}}}{3\alpha}} = k_v\sqrt{\frac{\sigma_\beta \pm \sqrt{\sigma_\beta^2 - 6\alpha\left(k_i/k_v\right)Z_\alpha\overline{P}^{\iota}_{\gamma,eq}}}{3\alpha}}, \tag{5.26}$$

$$\omega_{eq} = \omega^* + \frac{k_v k_i}{2C}\left(\frac{\overline{Q}_{\gamma,eq}}{\overline{V}^2_{eq}} - S_\beta\right) = \omega^* + \frac{k_v k_i}{2C}\left(\frac{Z_\alpha \overline{Q}^{\iota}_{\gamma,eq}}{\overline{V}^2_{eq}} - S_\beta\right), \tag{5.27}$$

where $\overline{P}^{\iota}_{\gamma,eq}$ and $\overline{Q}^{\iota}_{\gamma,eq}$ denote the equilibrium values of the scaled version (5.20) of averaged active and reactive power outflow $\left(\overline{P}_\gamma, \overline{Q}_\gamma\right)$ at point B in Fig. 5.2. A detailed comparison between the modified embedded droop-characteristics (5.26),(5.27) (defined in terms of the scaled version $\left(\overline{P}^{\iota}_{\gamma}, \overline{Q}^{\iota}_{\gamma}\right)$ of averaged active and reactive power outflow at point B) and actual embedded droop-characteristics (5.5),(5.9) is presented in Fig. 5.3 for a number of scenarios based on the impedance ratio $\frac{X_\alpha}{R_\alpha}$.

A simplified version of $V-P$ and $\omega-Q$ droop-characteristics can be recovered from the proposed averaged VOC dynamics for an ideal LCL filter (i.e. $R_f = R_c = R_g = 0$) resulting in $S_\alpha = 0$. A comparison between the droop-characteristics of actual VOC dynamics and proposed averaged VOC dynamics for an ideal LCL filter is presented in Section 5.6.1.

5.3.3 PI Controller Dynamics

In order to continuously tune the current feedback gain $k_{i,1}$ and voltage scaling factor $k_{v,1}$ to achieve the desired reference power set-points, two PI controllers are used as

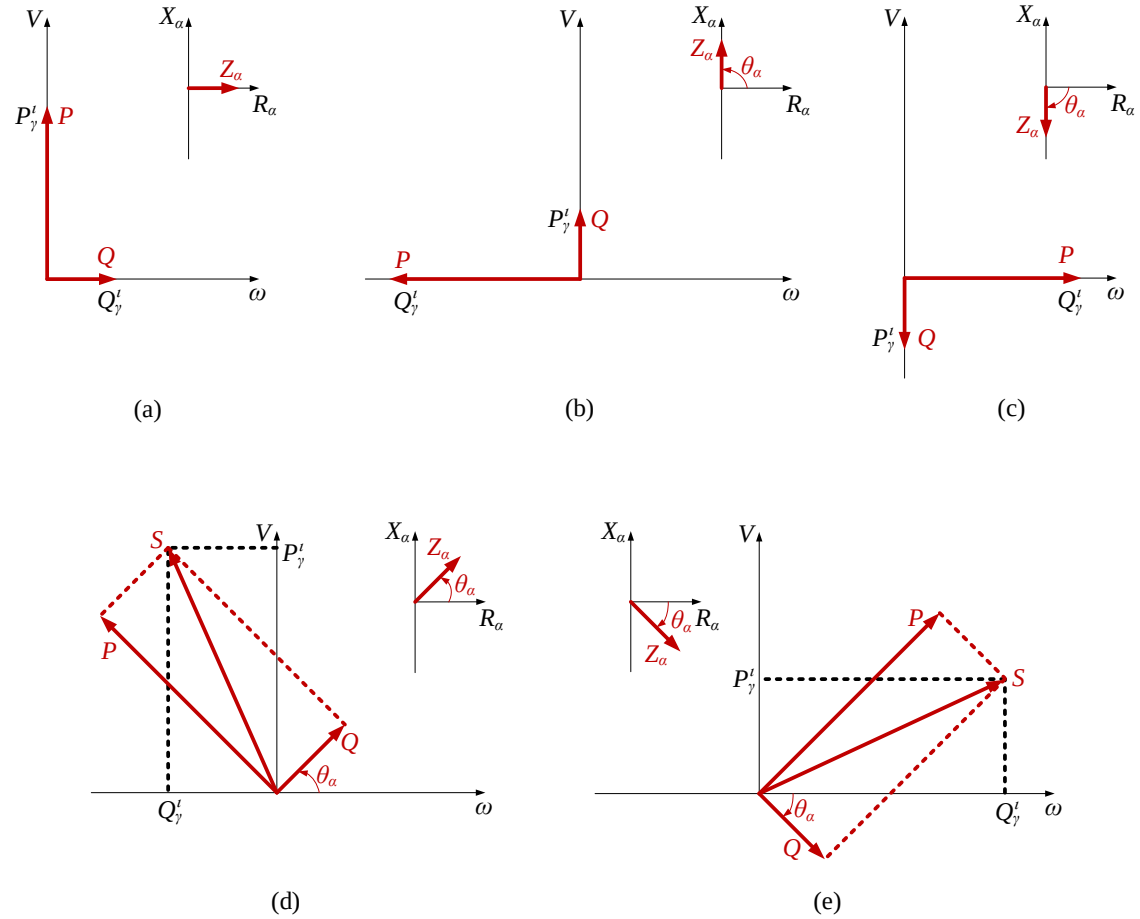

Figure 5.3: The variations in actual and modified embedded droop-characteristics as a function of impedance ratio $\frac{X_\alpha}{R_\alpha}$: (a) $\frac{X_\alpha}{R_\alpha} = 0$, (b) $\frac{X_\alpha}{R_\alpha} = \infty$, (c) $\frac{X_\alpha}{R_\alpha} = -\infty$, (d) $\frac{X_\alpha}{R_\alpha} = 1$, (e) $\frac{X_\alpha}{R_\alpha} = -1$.

in Fig. 5.6. PI controller 1 tunes the voltage scaling factor $k_{v,1}$ to regulate the active power $\overline{P}_1$. Similarly, PI controller 2 tunes the current feedback gain $k_{i,1}$ to regulate the reactive power $\overline{Q}_1$. The dynamics of the PI controller used to regulate the active power $\overline{P}_1$ are given by the following equations:

$$\dot{e}_p = K_I^p \left(\overline{P}_1 - P_1^*\right), \tag{5.28}$$

$$k_{v,1} = K_P^p \left(\overline{P}_1 - P_1^*\right) + e_p, \tag{5.29}$$

where P_1^* is the reference active power set-point. K_P^p and K_I^p are the proportional and integral gains, respectively, for the PI controller 1. Similarly, the dynamics of

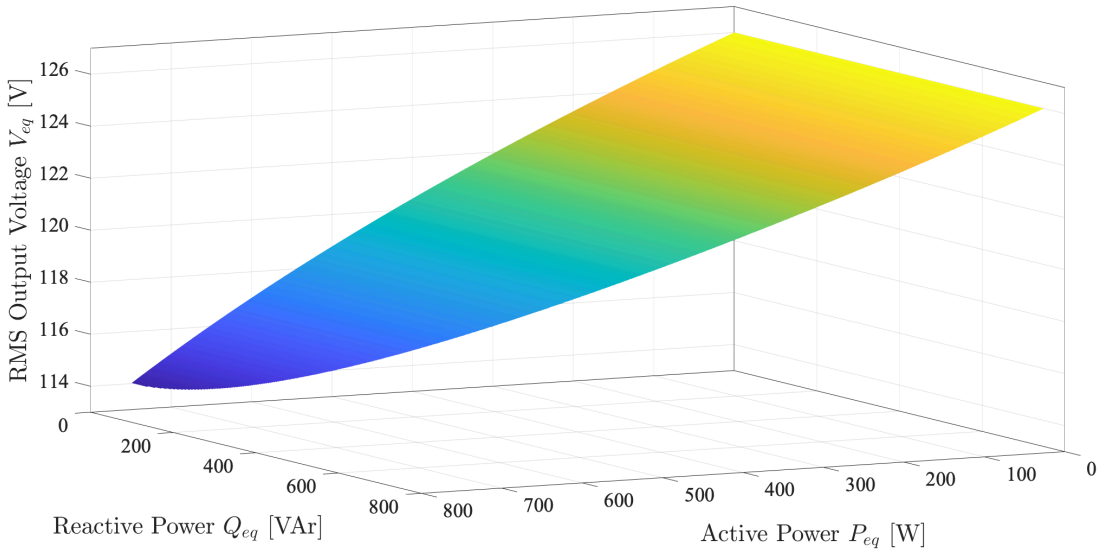

Figure 5.4: A surface plot demonstrating the variations in equilibrium RMS voltage magnitude $\overline{V}_{eq}$ as a function of active and reactive power for the proposed averaged VOC dynamics.

PI controller 2 used to regulate the reactive power $\overline{Q}_1$ are as follows:

$$\dot{e}_q = K_I^q \left(\overline{Q}_1 - Q_1^*\right), \tag{5.30}$$

$$k_{i,1} = K_P^q \left(\overline{Q}_1 - Q_1^*\right) + e_q, \tag{5.31}$$

where Q_1^* is the reference reactive power set-point. K_P^q and K_I^q are the proportional and integral gains, respectively, for the PI controller 2.

5.4 VOC Parameter Design Procedure

In this section, a parameter design procedure is presented for virtual oscillator-controlled inverters with current feedback after the output LCL filter. The parameters are selected such that the virtual oscillator-controlled inverter satisfies the desired ac-performance specifications. The parameters are classified into three categories: i) scaling factors k_v and k_i, ii) voltage regulation parameters σ and α, and iii) the harmonic oscillator parameters L and C.

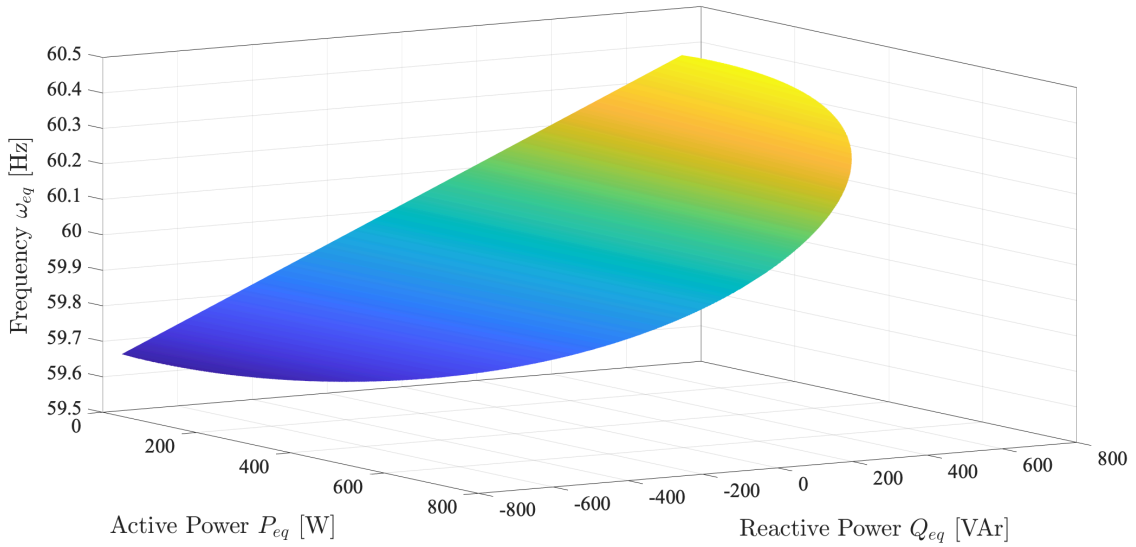

Figure 5.5: A surface plot demonstrating the variations in equilibrium frequency ω_{eq} as a function of active and reactive power for the proposed averaged VOC dynamics.

5.4.1 Designing the Scaling Factors

The scaling factors scale the voltage and current between the actual physical inverter and virtual oscillator controller. The voltage scaling factor k_v is chosen equal to the open circuit voltage $\overline{V}_{oc}$. This choice standardises the design procedure such that the virtual oscillator capacitor voltage is equal to 1 V RMS when the inverter's output voltage is equal to $\overline{V}_{oc}$. The current feedback gain k_i is chosen as the ratio of $\overline{V}_{min}$ to $\overline{S}_{max}$. The $\overline{V}_{min}$ corresponds to the constant $\overline{S}_{max}$ defined by:

$$\overline{S}_{max} = \max_{\overline{P}^2+\overline{Q}^2 \leq |\overline{S}_{rated}|^2} \left(C_\alpha \overline{P} + S_\alpha \overline{Q} \right). \tag{5.32}$$

By choosing the gains as:

$$k_v := \overline{V}_{oc}, \qquad k_i := \frac{\overline{V}_{min}}{\overline{S}_{max}}, \tag{5.33}$$

the parallel-connected virtual oscillator-controlled inverters share the power proportional to their power ratings [16, 20, 76] and this is demonstrated through the simulation results in Section 5.6.

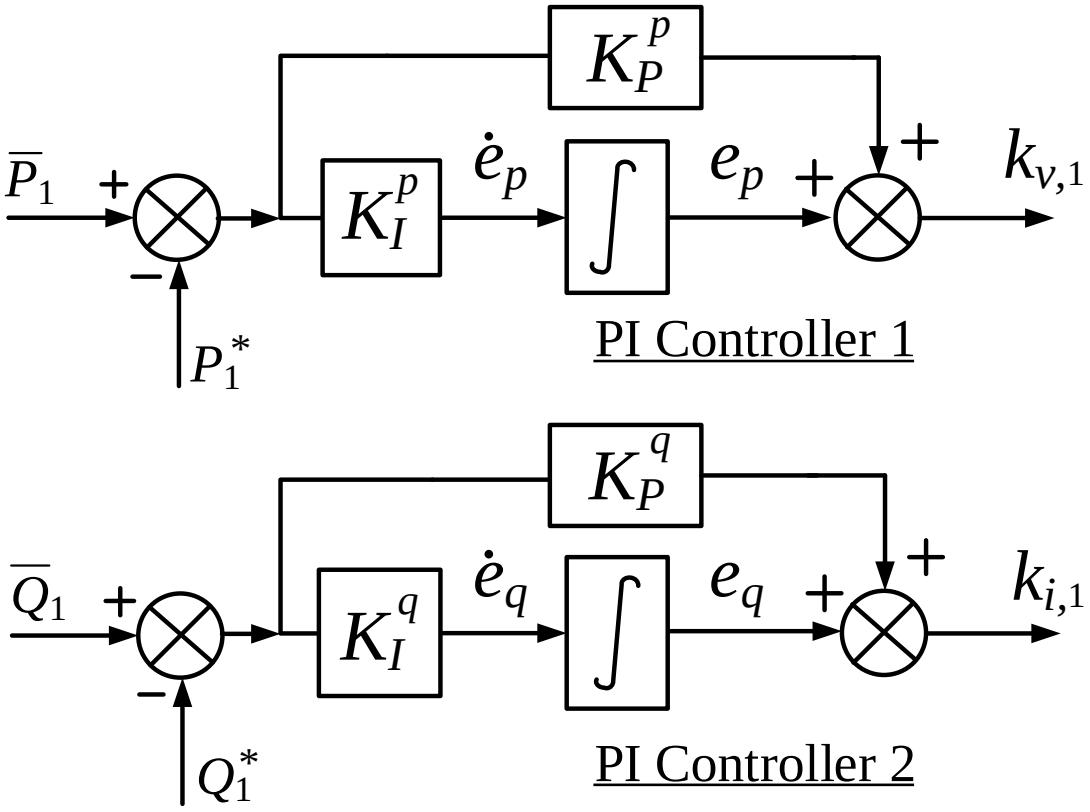

Figure 5.6: Block diagram representation of the PI controllers used to tune the current feedback gain $k_{i,1}$ and voltage scaling factor $k_{v,1}$. PI controller 1 is used to regulate the active power and PI controller 2 is used to regulate the reactive power.

5.4.2 Designing the Voltage Regulation Parameters

In this section, a design procedure for the virtual oscillator negative resistance element $R = \frac{-1}{\sigma}$ and the coefficient of non-linear current source α is presented. The proposed design procedure ensures the RMS output voltage stays within the range: $\overline{V}_{min} \leq \overline{V}_{eq} \leq \overline{V}_{oc}$ for $\overline{S}_{max} \geq C_\alpha \overline{P}_{eq} + S_\alpha \overline{Q}_{eq} \geq 0$. Notice that from (5.8) the choice of k_v in (5.33) results in the following relation between σ and α:

$$\sigma = \frac{3\alpha}{2} + k_i k_v C_\beta. \tag{5.34}$$

Substituting $C_\alpha \overline{P}_{eq} + S_\alpha \overline{Q}_{eq} = \overline{S}_{max}$ and $\overline{V}_{eq} = \overline{V}_{min}$ in the high voltage solution of (5.5) gives:

$$\overline{V}_{min} = k_v \sqrt{\frac{\sigma_\beta + \sqrt{\sigma_\beta^2 - 6\alpha \left(k_i/k_v\right) \overline{S}_{max}}}{3\alpha}}. \tag{5.35}$$

Replacing the scaling factors k_v and k_i as in (5.33) and α from (5.34) in (5.35), we get:

$$\overline{V}_{min} = k_v \sqrt{\frac{\sigma_\beta + \sqrt{\sigma_\beta^2 - 4\sigma_\beta \left(\overline{V}_{min}/\overline{V}_{oc}\right)}}{2\sigma_\beta}}. \tag{5.36}$$

From (5.36), we get:

$$\sigma_\beta = \frac{\overline{V}_{oc}}{\overline{V}_{min}} \frac{\overline{V}_{oc}^2}{\overline{V}_{oc}^2 - \overline{V}_{min}^2}. \tag{5.37}$$

Substituting $\sigma_\beta = \sigma - k_v k_i C_\beta$, we get:

$$\sigma = \frac{\overline{V}_{oc}}{\overline{V}_{min}} \frac{\overline{V}_{oc}^2}{\overline{V}_{oc}^2 - \overline{V}_{min}^2} + \frac{\overline{V}_{min}\overline{V}_{oc} C_\beta}{\overline{S}_{max}}. \tag{5.38}$$

Hence, using the design inputs $\overline{V}_{oc}$ and $\overline{V}_{min}$ (based on the desired ac-performance specifications), the VOC parameters σ and α can be determined through (5.34),(5.38).

5.4.3 Designing the Harmonic Oscillator Parameters

A set of constraints is derived to determine the harmonic oscillator parameters L and C. In order to determine the constraints, the frequency regulation characteristics (5.9), the rise time (5.12) and the ratio of the amplitude of the third harmonic to the fundamental $\delta_{3:1} = \frac{\epsilon\sigma}{8}$ as defined in [76, Eq. 41] are considered.

In order to design the harmonic oscillator parameters, one of the design inputs is the maximum permissible frequency deviation $|\Delta\omega|_{max}$. Let us start with the

frequency regulation characteristics in (5.9) and define the following constant:

$$\overline{S}_{|\Delta\omega|_{max}} = \max_{\overline{P}^2+\overline{Q}^2 \leq |\overline{S}_{rated}|^2} C_\alpha \overline{Q} - S_\alpha \overline{P}. \tag{5.39}$$

Using the worst-case operating condition for the output voltage (corresponding to $\overline{S}_{max}$ that results in the minimum permissible voltage $\overline{V}_{min}$) as in (5.36) and substituting the scaling factors from (5.33) into (5.9), the lower bound on capacitance C is given by:

$$C \geq \frac{1}{2|\Delta\omega|_{max}} \left(\frac{\overline{S}_{|\Delta\omega|_{max}} \overline{V}_{oc}}{\overline{V}_{min} \overline{S}_{max}} - \frac{S_\beta \overline{V}_{oc} \overline{V}_{min}}{\overline{S}_{max}} \right) =: C^{min}_{|\Delta\omega|_{max}}. \tag{5.40}$$

Let us define the maximum permissible rise time t^{max}_{rise} as one of the design inputs. Now, considering the expression (5.12) for the rise time t_{rise} of an unloaded inverter and (5.37), the upper bound on the capacitance C is defined as:

$$C \leq \frac{t^{max}_{rise}}{6} \frac{\overline{V}_{oc}}{\overline{V}_{min}} \frac{\overline{V}^2_{oc}}{\overline{V}^2_{oc} - \overline{V}^2_{min}} =: C_{t^{max}_{rise}}. \tag{5.41}$$

Finally, the third design input is the maximum-permissible ratio of the amplitude of the third harmonic to the fundamental $\delta^{max}_{3:1}$ where $\delta_{3:1} = \frac{\epsilon\sigma}{8}$ as defined in [76, Eq. 41]. Replacing (5.38) in the expression for $\delta_{3:1}$, we get another lower bound on the capacitance C given by:

$$C \geq \left(\frac{1}{8\omega^* \delta^{max}_{3:1}} \right) \left(\frac{\overline{V}_{oc}}{\overline{V}_{min}} \frac{\overline{V}^2_{oc}}{\overline{V}^2_{oc} - \overline{V}^2_{min}} + \frac{\overline{V}_{min} \overline{V}_{oc} C_\beta}{\overline{S}_{max}} \right) =: C^{min}_{\delta_{3:1}}. \tag{5.42}$$

The set of constraints (5.40)-(5.42) defines a permissible range for the capacitance to satisfy the desired frequency regulation, rise time and harmonic distortion specifications. Based on the set of constraints, the permissible range of capacitance C can be written as:

$$max\{C^{min}_{|\Delta\omega|_{max}}, C^{min}_{\delta_{3:1}}\} \leq C \leq C_{t^{max}_{rise}}. \tag{5.43}$$

Once the value is chosen for the capacitance C, the inductance L can be determined as follows:

$$L = \frac{1}{C(\omega^*)^2}. \tag{5.44}$$

Note that it may be possible (5.43) does not hold for the set of design inputs $\{|\Delta\omega|_{max}, t_{rise}^{max}, \delta_{3:1}^{max}\}$. As a result, we have to make a design trade-off between an inverter with short rise time (having higher frequency deviation from the nominal value ω^* and harmonic content) and an inverter with longer rise time (having smaller frequency deviation from the nominal value and reduced harmonic content).

5.5 Power Dispatch

In this section, the power dispatch technique presented in Chapter 4 is extended to the proposed averaged VOC model with current feedback after the output LCL filter. Inverter 1 simultaneously regulates both the active and reactive power according to the desired power set-point (P_1^*, Q_1^*) while Inverter 2 supplies the remaining load power acting like a conventional slack bus. In order to regulate the power, two PI controllers are used to continuously tune the VOC parameters $k_{v,1}$ and $k_{i,1}$, as in Chapter 4.

5.5.1 Power Flow Analysis with VOC Dynamics

In order to perform the power flow analysis, the iterative numerical method presented in Chapter 4 is used. The algorithm solves for the bus voltage magnitudes (i.e. $\overline{V}_1, \overline{V}_2$ and V_L) and angles (i.e. $\overline{\theta}_1, \overline{\theta}_2$ and θ_L) corresponding to the power set-point (P_1^*, Q_1^*) and considering the VOC dynamics of the uncontrolled inverters 2. Once the power flow analysis is performed, the VOC dynamics of the controlled Inverter

1 are considered in Theorem 5.1 to determine the achievability of the desired power set-point and corresponding VOC parameters (i.e. current feedback gain and voltage scaling factor). This algorithm can be used for both a constant impedance load z_L or / and a constant power load $S_L = P_L + \jmath Q_L$ attached at the load bus. The state vector $\mathbf{x}$ and non-linear equation $\mathbf{F(x)}$ to be solved for the power flow analysis including the VOC dynamics are as follows:

$$\mathbf{x} = \begin{bmatrix} \theta_1 \\ \theta_L \\ V_1 \\ V_2 \\ V_L \end{bmatrix}, \quad \mathbf{F(x)} = \begin{bmatrix} P_1^* - P_1(x) \\ P_L^* - P_L(x) \\ Q_1^* - Q_1(x) \\ V_2 - \overline{V}_2(P_2, Q_2) \\ Q_L^* - Q_L(x) \end{bmatrix}. \tag{5.45}$$

The bus angle $\theta_2 = 0^\circ$ is taken as reference for solving the power flow equation $\mathbf{F(x)} = 0$. VOC dynamics are included in the power flow analysis using the term $\overline{V}_2(P_2, Q_2)$, representing the averaged RMS terminal-voltage magnitude of the uncontrolled Inverter 2 according to equation (5.5).

5.5.2 Power Security Constraint

An updated power security constraint is derived based on the proposed averaged VOC model to determine the achievable power set-points and guarantee the existence of real valued control inputs to achieve these feasible power set-points. Recall from Chapter 4, a set of power security constrains for the previously reported averaged VOC model [76] was presented in Theorem 4.1.

Theorem 5.1. *Assuming the averaged model of two VOC inverters that synchronise to a common frequency, have feedback after the output LCL filter, and are connected to a common fixed impedance load z_L through line impedance values $z_{l,1}$ and $z_{l,2}$, respectively, the desired output power set-point $\overline{P}_1^*$ and $\overline{Q}_1^*$ for Inverter 1 can be*

achieved, and there exists corresponding real-valued current feedback gain $k_{i,1}^{\iota}$ *and voltage scaling factor* $k_{v,1}^{\iota}$*, if the following security constraint is satisfied for the averaged VOC dynamics:*

$$\sigma_1 \overline{V}_1^{\iota\,2} - \mu \left(C_{\alpha,1} \overline{P}_1^{*} + S_{\alpha,1} \overline{Q}_1^{*} + C_{\beta,1} \overline{V}_1^{\iota\,2} \right) > 0, \tag{5.46}$$

where,

$$\mu = k_{v,1}^{\iota} k_{i,1}^{\iota} = k_{v,2} k_{i,2} \frac{\left(\frac{C_{\alpha,2} \overline{Q}_2^{\iota} - S_{\alpha,2} \overline{P}_2^{\iota}}{\overline{V}_2^{\iota\,2}} - S_{\beta,2} \right)}{\left(\frac{C_{\alpha,1} \overline{Q}_1^{*} - S_{\alpha,1} \overline{P}_1^{*}}{\overline{V}_1^{\iota\,2}} - S_{\beta,1} \right)}. \tag{5.47}$$

The $\overline{V}_2^{\iota}$ *and* $\overline{Q}_2^{\iota}$ *denote the steady-state averaged output voltage magnitude and reactive power supplied by Inverter* 2*, respectively, corresponding to the desired output power set-point* $(\overline{P}_1^{*}, \overline{Q}_1^{*})$*.*

Proof. The iterative method in Section 5.5.1 to numerically solve the non-linear power flow equations including the VOC dynamics can be used to determine the bus voltage magnitudes and angles corresponding to the power set-point $(\overline{P}_1^{*}, \overline{Q}_1^{*})$ for the controlled Inverter 1. Using the solution of power flow equations, the corresponding values for $k_{i,1}^{\iota}$ and $k_{v,1}^{\iota}$ can be determined as follow:

$$\overline{V}_1^{\iota} = k_{v,1}^{\iota} \left(\frac{\left(\sigma_1 - k_{v,1}^{\iota} k_{i,1}^{\iota} C_{\beta,1} \right) \pm \sqrt{\left(\sigma_1 - k_{v,1}^{\iota} k_{i,1}^{\iota} C_{\beta,1} \right)^2 - 6\alpha_1 (k_{i,1}^{\iota} / k_{v,1}^{\iota}) \left(C_{\alpha,1} \overline{P}_1^{*} + S_{\alpha,1} \overline{Q}_1^{*} \right)}}{3\alpha_1} \right)^{\frac{1}{2}}. \tag{5.48}$$

From the frequency synchronisation condition, we have:

$$\omega_1 = \omega_2, \tag{5.49}$$

$$k_{v,1}^{\iota} k_{i,1}^{\iota} \left(\frac{C_{\alpha,1}}{\overline{V}_1^{\iota\,2}} \overline{Q}_1^{*} - \frac{S_{\alpha,1}}{\overline{V}_1^{\iota\,2}} \overline{P}_1^{*} - S_{\beta,1} \right) = k_{v,2} k_{i,2} \left(\frac{C_{\alpha,2}}{\overline{V}_2^{\iota\,2}} \overline{Q}_2^{\iota} - \frac{S_{\alpha,2}}{\overline{V}_2^{\iota\,2}} \overline{P}_2^{\iota} - S_{\beta,2} \right), \tag{5.50}$$

$$k_{v,1}^{\iota}k_{i,1}^{\iota} = k_{v,2}k_{i,2}\frac{\left(\frac{C_{\alpha,2}}{\overline{V}_2^{\iota\,2}}\overline{Q}_2^{\iota} - \frac{S_{\alpha,2}}{\overline{V}_2^{\iota\,2}}\overline{P}_2^{\iota} - S_{\beta,2}\right)}{\left(\frac{C_{\alpha,1}}{\overline{V}_1^{\iota\,2}}\overline{Q}_1^{*} - \frac{S_{\alpha,1}}{\overline{V}_1^{\iota\,2}}\overline{P}_1^{*} - S_{\beta,1}\right)} = \mu. \tag{5.51}$$

Simplifying (5.48), substituting α_1 from (5.34) and $k_{i,1}^{\iota} = \frac{\mu}{k_{v,1}^{\iota}}$ from (5.51), we get:

$$\frac{(\sigma_1 - \mu C_{\beta,1})}{{k_{v,1}^{\iota}}^2}\overline{V}_1^{\iota\,4} - (\sigma_1 - \mu C_{\beta,1})\,\overline{V}_1^{\iota\,2} + \mu\left(C_{\alpha,1}\overline{P}_1^{*} + S_{\alpha,1}\overline{Q}_1^{*}\right) = 0. \tag{5.52}$$

Solving for $k_{v,1}^{\iota}$, we have:

$$k_{v,1}^{\iota} = \pm\sqrt{\frac{(\sigma_1 - \mu C_{\beta,1})\,\overline{V}_1^{\iota\,4}}{(\sigma_1 - \mu C_{\beta,1})\,\overline{V}_1^{\iota\,2} - \mu\left(C_{\alpha,1}\overline{P}_1^{*} + S_{\alpha,1}\overline{Q}_1^{*}\right)}}, \tag{5.53}$$

$$k_{i,1}^{\iota} = \frac{\mu}{k_{v,1}^{\iota}}. \tag{5.54}$$

Hence, (5.53) and (5.54) represent the control laws to determine $k_{v,1}^{\iota}$ and $k_{i,1}^{\iota}$, respectively. For the existence of a real-valued solution of the control laws (5.53)-(5.54) ($k_i \in \mathbb{R}$ and $k_v \in \mathbb{R}_+$), we require:

$$(\sigma_1 - \mu C_{\beta,1})\,\overline{V}_1^{\iota\,2} - \mu\left(C_{\alpha,1}\overline{P}_1^{*} + S_{\alpha,1}\overline{Q}_1^{*}\right) > 0, \tag{5.55}$$

This completes the proof. ■

Remark 5.1. *The frequency synchronisation condition is considered in the above results. The details on frequency synchronisation condition can be found in Remark 4.1.*

Remark 5.2. *The details on the application of iterative numerical method to solve the power flow equations including the VOC dynamics* (5.45) *are given in Remark 4.2.*

Remark 5.3. *It should be noted that the proposed averaged VOC model is an approximation of the Van der Pol oscillator under the assumption* $\epsilon \searrow 0$ *and the security*

constraint (5.46) *in Theorem 5.1 only provides an approximation in practice. The details of this approximate analysis are presented in Remark 4.3.*

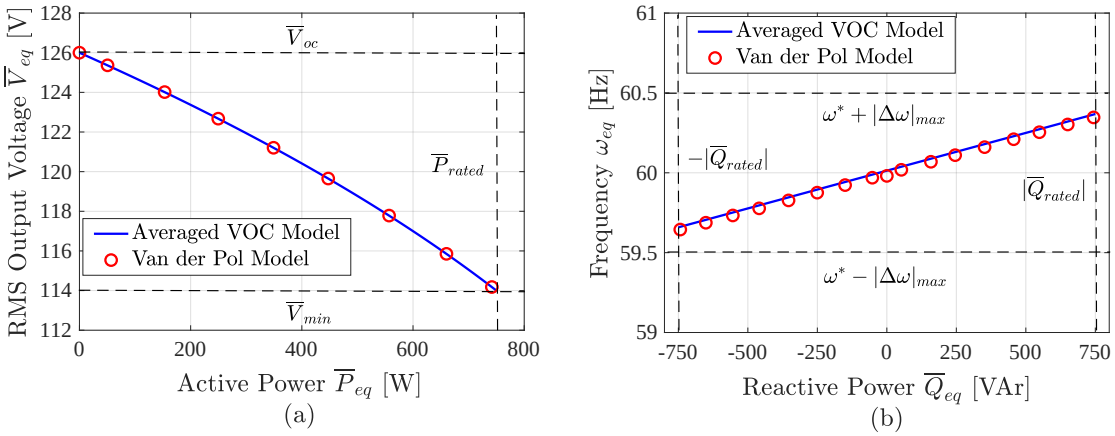

Figure 5.7: A comparison between the embedded droop-characteristics within the averaged VOC model and actual VOC dynamics with current feedback after the output LCL filter.

5.6 Simulation Results

The simulation results are presented to validate the proposed theoretical averaged VOC model and make a comparison with the previously reported averaged VOC model and actual VOC dynamics for a number of scenarios. Note that these VOC models do not take into account the dead-time and switching characteristics of the inverter. Hence, the inverters are modelled as ideal voltage sources for the simulation purpose. The line, load and filter parameters are $R_f = R_l = 0.15\,\Omega$, $L_f = L_l = 2.48$ mH, $R_c = 3.3\,\Omega$, $C_f = 4.7\,\mu$F, $R_g = 0.13\,\Omega$, $L_g = 0.97$ mH, $R_L = 22.1\,\Omega$ and $L_L = 14.4$ mH. The simulations are performed in MATLAB. The system parameters and ac-performance specifications are as in Table 5.1 and Table 5.2, respectively.

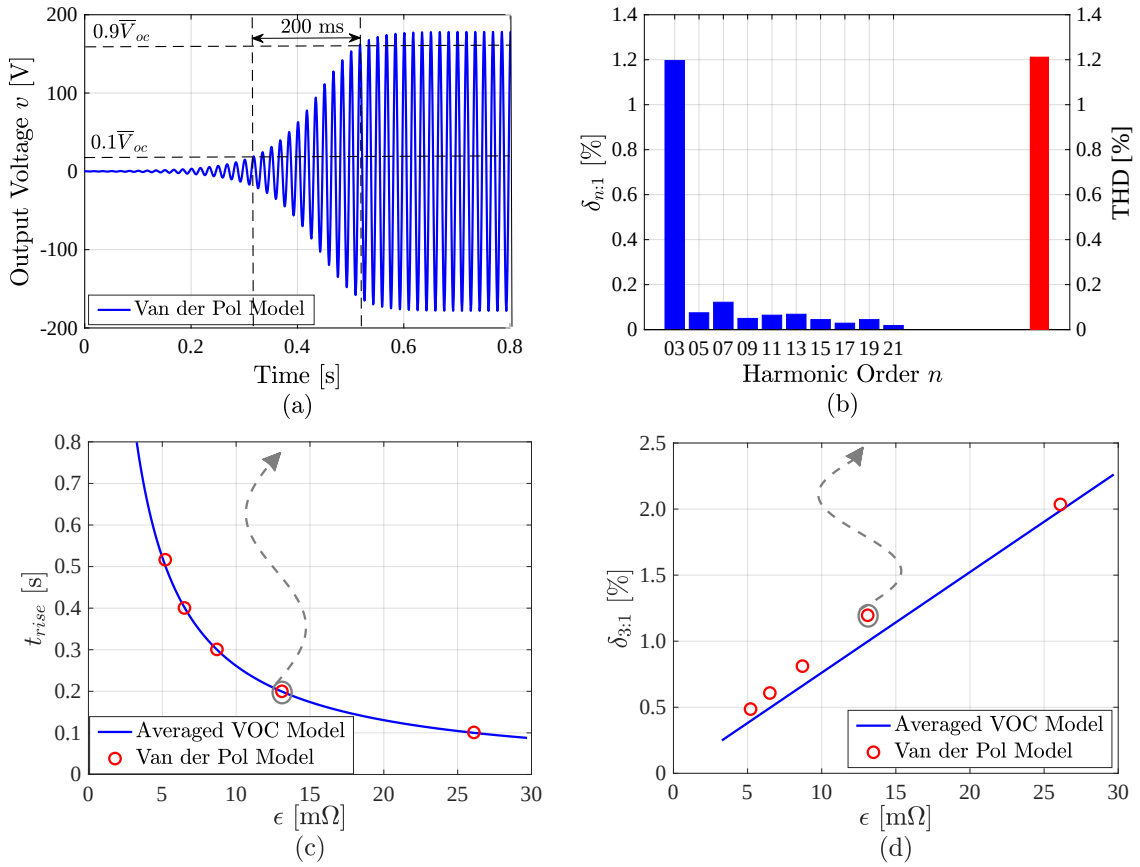

Figure 5.8: The rise time and harmonic analysis show that the virtual oscillator-controlled inverter closely follows the desired design inputs t_{rise}^{max} and $\delta_{3:1}^{max}$. The dashed-arrows represent the simulation results for a particular encircled value of the design inputs t_{rise}^{max} and $\delta_{3:1}^{max}$.

5.6.1 Embedded Droop Characteristics

In order to validate the embedded droop-characteristics (5.5), (5.9) within the averaged VOC dynamics, a comparison is made with the actual VOC (Van der Pol oscillator) dynamics (5.1) with current feedback after the output LCL filter. In Fig. 5.7, it can be seen that the embedded droop-characteristics are close to the actual VOC dynamics. In order to obtain the $\overline{V} - \overline{P}$ and $\omega - \overline{Q}$ droop-characteristics, the LCL filter is assumed to be ideal (i.e. $R_f = R_c = R_g = 0$) resulting in $S_\alpha = 0$ and the parameters in Table 5.1 are re-derived according to the design procedure in Section 5.4.

Table 5.1: System Parameters

Symbol	Parameter	Inverter 1	Inverter 2	Unit
k_i	Current feedback gain	0.15225	0.15225	A/A
k_v	Voltage scaling factor	126	126	V/V
σ	Conductance	6.09256	6.09256	Ω^{-1}
α	Cubic-current source coefficient	4.06184	4.06184	A/V^3
L	Virtual oscillator inductance	34.66	34.66	μH
C	Virtual oscillator capacitance	0.203	0.203	F

Table 5.2: AC Performance Specifications

Symbol	Parameter	Value	Unit
$\overline{V}_{oc}$	RMS open-circuit voltage	126	V
$\overline{V}_{min}$	RMS rated power voltage	114	V
$\overline{P}_{rated}$	Rated real power	750	W
$\lvert\overline{Q}_{rated}\rvert$	Rated reactive power	750	VAr
ω^*	Nominal oscillator frequency	$2\pi 60$	rad/s
$\lvert\Delta\omega\rvert_{max}$	Maximum frequency offset	$2\pi 0.5$	rad/s
t_{rise}^{max}	Maximum rise time	0.2	s
$\delta_{3:1}^{max}$	3^{rd} to 1^{st} harmonic ratio	1	%

5.6.2 Rise Time and Harmonic Analysis

In Fig. 5.8, the rise time and harmonic analysis are presented for an unloaded inverter. It can be seen that the virtual oscillator-controlled inverter closely follows the design inputs t_{rise}^{max} and $\delta_{3:1}^{max}$, thus validating the VOC parameter design procedure in Section 5.4. The corresponding values of the VOC design parameter $\epsilon = \sqrt{L/C}$ (defined in Chapter 2) are also presented.

5.6.3 Model Comparison

In this section, a comparison is made between the previously reported averaged VOC model [76], the proposed averaged VOC model (5.2)-(5.3) and actual VOC dynamics (5.1). In order to make an accurate comparison between these theoretical models, the simulations are performed using a small time-step size $T_{sim} = 1\,\mu$s and a high sampling frequency $f_{sam} = 1$ MHz. Such a high sampling frequency may seem inappropriate from a practical point of view but in this chapter we are mainly interested in validating the theoretical findings. A moving average window is used to compute the output RMS voltage, active and reactive power. The moving average window's implementation is the same that in Chapter 6. The moving average window's length and the quarter ac-cycle delay in the instantaneous output voltage v_o (required to compute the reactive power) are adjusted at each time-step according to the load dependent system's frequency ω, which is obtained for each VOC model using its respective dynamic equations. The load dependent system's frequency ω for the actual VOC dynamics (Van der Pol oscillator) is averaged using the moving average window to attenuate the inherent harmonic component present in it, which otherwise results in a harmonic ripple in the computed active and reactive power.

In order to make a comparison, three different LCL filters are used with an increasing value for filter capacitance C_f and the VOC design parameter ϵ is chosen to be $\epsilon^{\iota} = \frac{\epsilon}{8} = \frac{\sqrt{L/C}}{8}$. Further, a step-up change at $t = 10$ s and a step-down change at $t = 15$ s are applied in the load to make a comparison between the models during transients. Note that the difference between the previously reported averaged VOC model and actual VOC dynamics increases for a higher value of filter capacitance. A large filter capacitor draws relatively high current and results in a significant difference between the currents before and after the output LCL filter. In the first case, the LCL filter parameters are chosen as described in Section 5.6. The $z_L = 44.24 + \jmath 10.85\,\Omega$ with $z_{step} = z_L$ in-parallel, to implement the step-up and step-down load changes. In Fig. 5.9 for a relatively small value of filter capacitance, it can

be seen that the difference between the three models is not significant. However, in the following two cases with increased value of filter capacitance, the models start to differ with the proposed averaged VOC dynamics following the actual VOC dynamics more closely as compared to the previously reported averaged VOC model. In the second case, an LCL filter is chosen with higher values of filter parameters ($L_f^{\iota} = 10L_f, C_f^{\iota} = 19.75C_f$) and the system parameters in Table 5.1 are re-derived according to the design procedure in Section 5.4. The $z_L = 6.9 + \jmath 16.6\,\Omega$ with $z_{step} = 44.24 + \jmath 10.85\,\Omega$ in-parallel, to implement the step-up and step-down load changes. In Fig. 5.10, it can be noted that the proposed averaged VOC model follows the actual VOC dynamics more closely as compared to the previously reported averaged VOC model both in the steady-state and during transients. In the third case, an LCL filter is chosen with an even higher value of filter parameters ($L_f^{\iota} = 50L_f, C_f^{\iota} = 160.2C_f$) and similarly the system parameters in Table 5.1 are re-derived according to the design procedure in Section 5.4. The $z_L = 0.49 + \jmath 3.65\,\Omega$ with $z_{step} = 1.11 + \jmath 5.43\,\Omega$ in-parallel to implement the step-up and step-down load changes. In Fig. 5.11, the proposed averaged VOC model more closely predicts the actual VOC dynamics both in the steady-state and during transients as compared to the previously reported averaged VOC model.

5.6.4 *LCL* Filter and Line Parameter Design Procedure

In this section, an LCL filter and line parameter design procedure is presented for the proposed averaged VOC model with current feedback after the output LCL filter. The proposed design procedure is an extended version of the design procedure presented in [16]. The proportional power sharing results are presented for two inverters with rated complex power $S_{1,rated} = 750$ VA and $S_{2,rated} = 1500$ VA, respectively. The ratio $\eta_S = \frac{S_{1,rated}}{S_{2,rated}} = 0.5$. In order for the two inverters to share power proportionally (i.e. in a ratio $S_{1,rated} : S_{2,rated} = 1 : 2$), the LCL filter and line parameters for Inverter 2 are scaled by the factor η_S i.e. $R_{f,2} = \eta_S R_{f,1}$, $R_{l,2} = \eta_S R_{l,1}$,

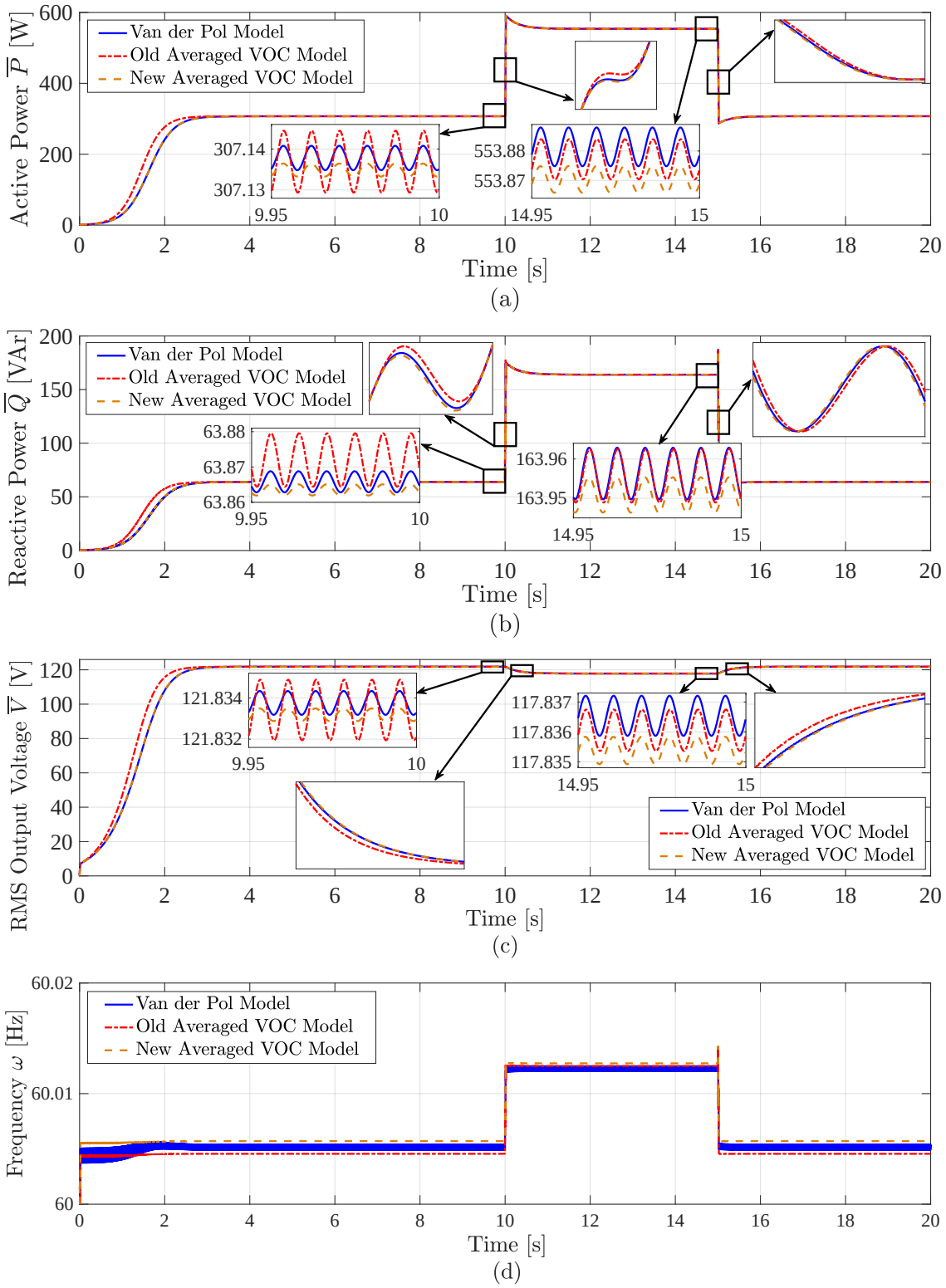

Figure 5.9: Comparison between previously reported averaged VOC model [76], the proposed averaged VOC model (5.2)-(5.3) and actual VOC dynamics (5.1) for $(L_f^\iota = L_f, C_f^\iota = C_f)$: (a) active power, (b) reactive power, (c) voltages, (d) frequency.

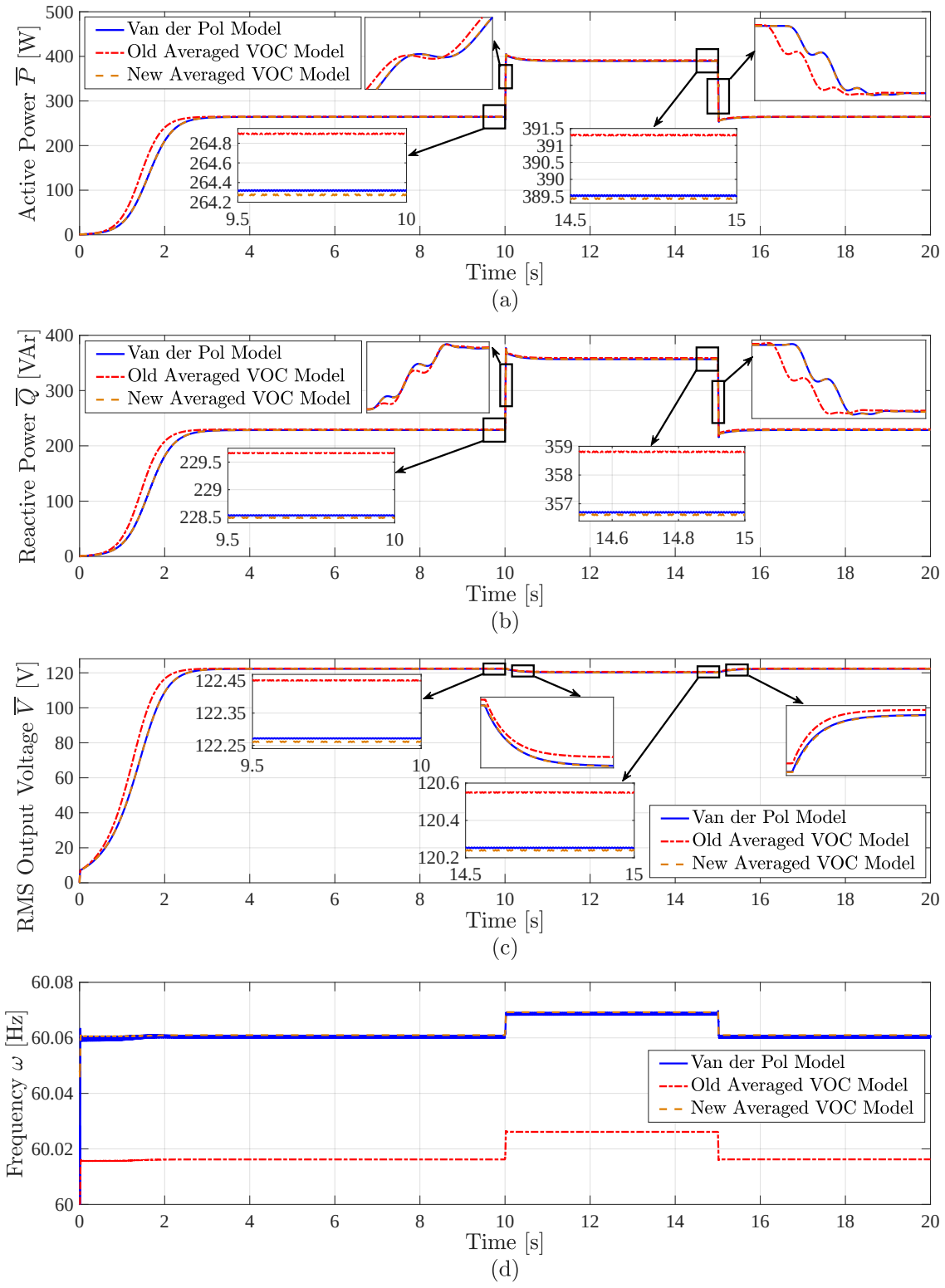

Figure 5.10: Comparison between previously reported averaged VOC model [76], the proposed averaged VOC model (5.2)-(5.3) and actual VOC dynamics (5.1) for $(L_f^\iota = 10L_f, C_f^\iota = 19.75C_f)$: (a) active power, (b) reactive power, (c) voltages, (d) frequency.

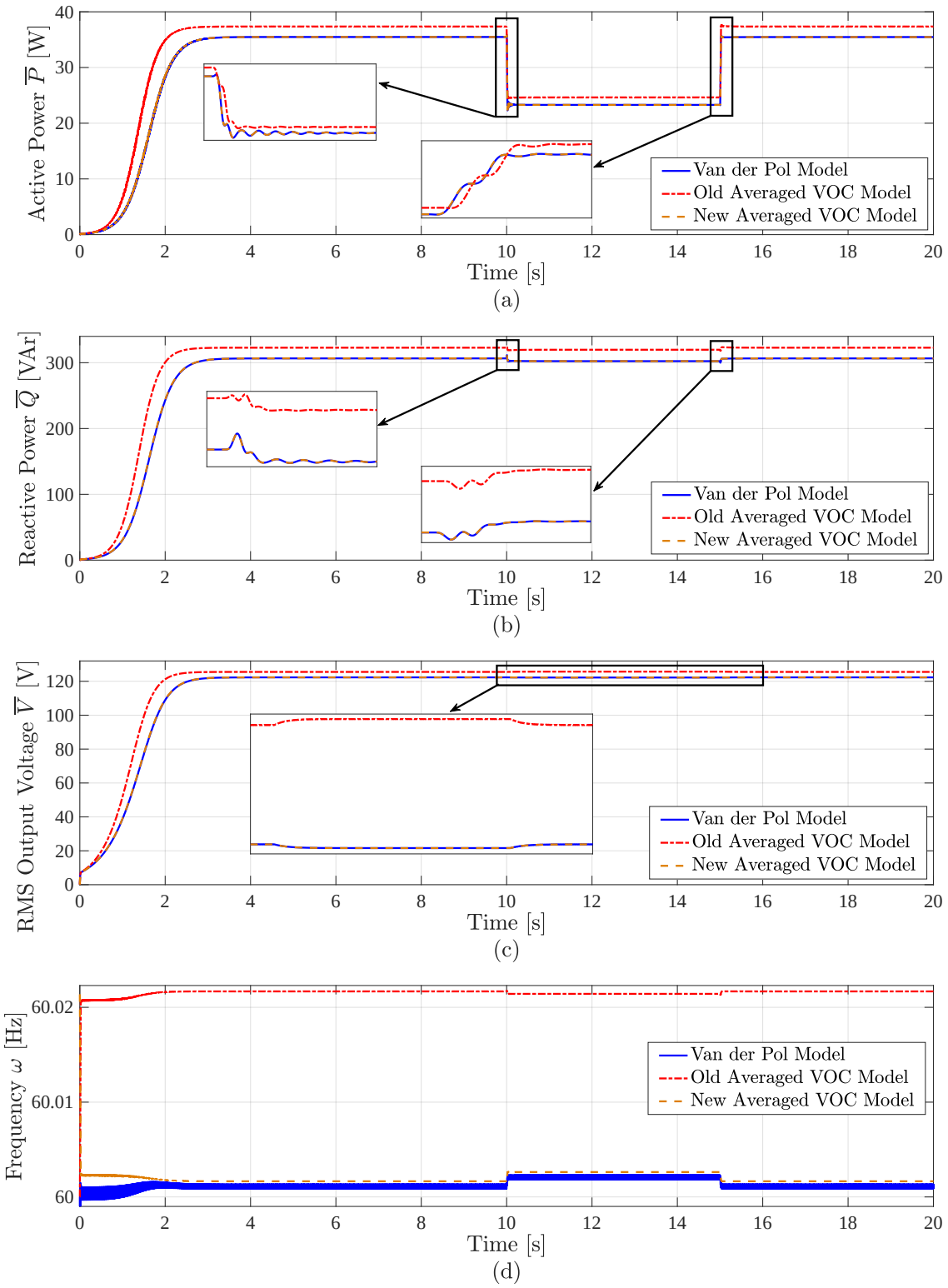

Figure 5.11: Comparison between previously reported averaged VOC model [76], the proposed averaged VOC model (5.2)-(5.3) and actual VOC dynamics (5.1) for $(L_f^\iota = 50L_f, C_f^\iota = 160.2C_f)$: (a) active power, (b) reactive power, (c) voltages, (d) frequency.

$L_{f,2} = \eta_S L_{f,1}$, $L_{l,2} = \eta_S L_{l,1}$, $R_{c,2} = \eta_S R_{c,1}$, $C_{f,2} = C_{f,1}/\eta_S$, $R_{g,2} = \eta_S R_{g,1}$ and $L_{g,2} = \eta_S L_{g,1}$. The LCL filter and line parameters for Inverter 1 are the same as those defined at the start of Section 5.6. Further, the system parameters in Table 5.1 are re-derived for Inverter 2 according to the design procedure in Section 5.4. The system parameters for Inverter 1 are the same as in Table 5.1. In Fig. 5.12, it can be seen that Inverter 1 and Inverter 2 share both the active and reactive power proportionally (i.e. in a ratio 1 : 2) verifying the proposed LCL filter and line parameter design procedure.

5.6.5 Power Dispatch

In Fig. 5.13, the power dispatch results are presented for a number of scenarios as listed in Table 5.3. Inverter 1 simultaneously regulates both the active and reactive power using the two PI controllers that continuously tune the voltage scaling factor $k_{v,1}$ and current feedback gain $k_{i,1}$. Inverter 2 supplies the remaining power to the load, acting like a slack bus. The PI controller gains are $K_P^p = -0.001$, $K_I^p = -0.15$, $K_P^q = 0.0001$ and $K_I^q = 0.01$. In Fig. 5.13, Inverter 1 tracks the desired power set-points effectively while satisfying the security constraint (5.46). The corresponding changes in Inverter 2 power, load power, control inputs and voltages are also presented. A detailed description of each power dispatch scenario is presented in the following subsections.

5.6.5.1 Case 1

In this scenario, both inverters are sharing equal active and reactive power demand. Further, the control inputs ($k_{v,1}$ and $k_{i,1}$) for Inverter 1 are the same as the fixed gains ($k_{v,2}$ and $k_{i,2}$) for Inverter 2.

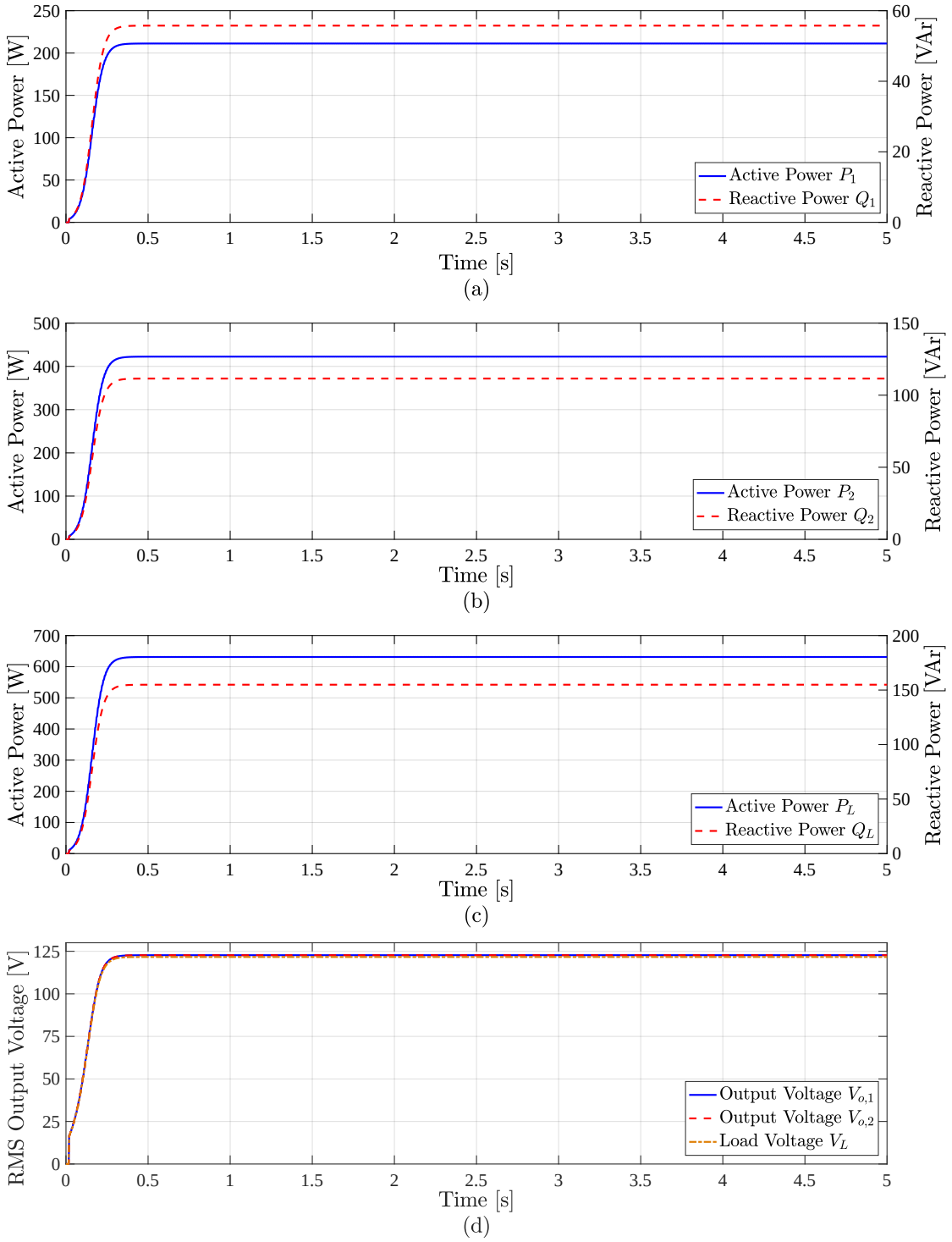

Figure 5.12: Proportional power sharing between Inverter 1 and Inverter 2 verifying the proposed LCL filter and line parameter design procedure: (a) Inverter 1 output power, (b) Inverter 2 output power, (c) load power, (d) voltages.

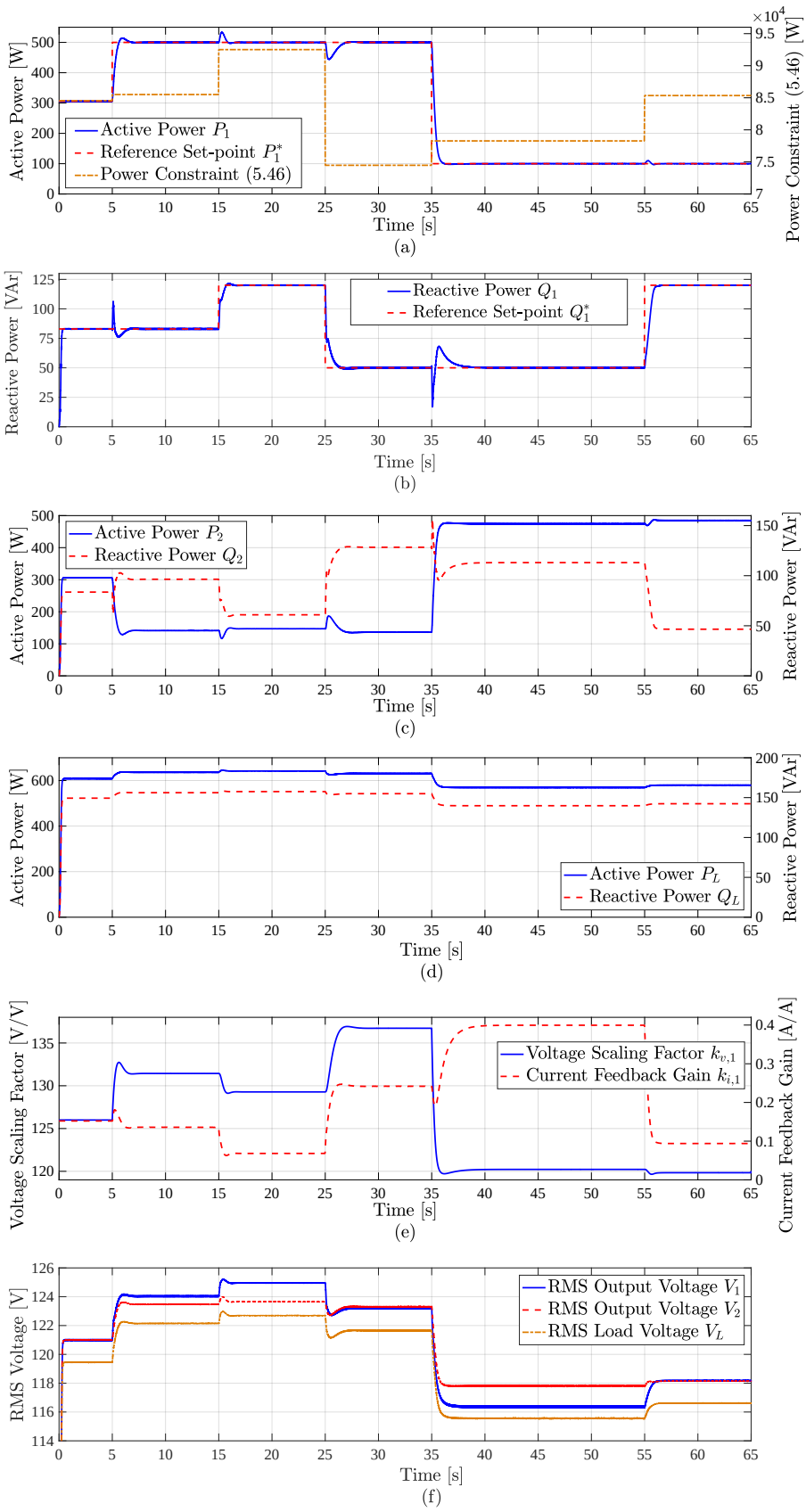

Figure 5.13: Power dispatch results are presented for Inverter 1 while Inverter 2 supplies the remaining load power: (a) Inverter 1 active power, power security constraint and reference set-point, (b) Inverter 1 reactive power and reference set-point, (c) Inverter 2 output power, (d) load power, (e) control inputs, (f) voltages.

5.6.5.2 Case 2

At $t = 5$ s, a step-up change is applied in $P_1^* = 306 \rightarrow 500$ W while the set-point for reactive power is kept constant $Q_1^* = 83$ VAr. Inverter 1 tracks the reference set-point effectively and reaches the new set-point at $t = 6$ s. The corresponding changes in the control inputs can be seen in Fig. 5.13. In this scenario, Inverter 1 supplies most of the active power demand.

5.6.5.3 Case 3

A step-up change in the reactive power set-point $Q_1^* = 83 \rightarrow 120$ VAr is applied at $t = 15$ s while the active power set-point is fixed at $P_1^* = 500$ W. Inverter 1 reaches the new set-point at $t = 16$ s. In this scenario, Inverter 1 supplies a major portion of both the active and reactive power demand.

5.6.5.4 Case 4

In this scenario, a step-down change in the reactive power set-point $Q_1^* = 120 \rightarrow 50$ VAr is applied while the active power set-point is still the same $P_1^* = 500$ W. Inverter 1 follows and reaches the desired reference set-point at $t = 26$ s. Inverter 1 supplies a major portion of active power demand while Inverter 2 supplies most of the reactive power.

5.6.5.5 Case 5

A step-down change is applied in the active power set-point $P_1^* = 500 \rightarrow 100$ W while the reactive power set-point is fixed at $Q_1^* = 50$ VAr. Inverter 1 tracks and reaches the desired reference set-point at $t = 36$ s. In this scenario, Inverter 1 is suppling a small portion of both the load active and reactive power demand.

Table 5.3: Power Dispatch Set-points

Case No.	P_1^* [W]	Q_1^* [VAr]	Time [s]
1	–	–	$0-5$
2	500	83	$5-15$
3	500	120	$15-25$
4	500	50	$25-35$
5	100	50	$35-55$
6	100	120	$55-65$

5.6.5.6 Case 6

Finally, a step-up change is applied in the reactive power set-point $Q_1^* = 50 \rightarrow 120$ VAr while the active power set-point is the same $P_1^* = 100$ W. The Inverter 1 reaches the new set-point at $t = 56$ s. In this scenario, Inverter 1 supplies most of the reactive power while Inverter 2 fulfils a major portion of active power demand.

5.6.6 Power Security Constraint Violation

In this section, the simulation results are presented for the power security constraint violation. In Fig. 5.14, initially at $t = 0$ s, Inverter 1 is following the desired power set-point $P_1^* = 600$ W and $Q_1^* = 10$ VAr, satisfying the power security constraint (5.46). At $t = 20$ s, a step-down change in reactive power set-point $Q_1^* = 10 \rightarrow 0.5$ VAr is applied while the active power set-point is kept the same at $P_1^* = 600$ W. According to the power security constraint (5.46), for an active power set-point $P_1^* = 600$ W, the reactive power set-point must be $Q_1^* \geq 0.76$ VAr for a power set-point to be feasible. Hence, this new power set-point does not satisfy the power security constraint and there do not exist real valued control inputs $(k_{v,1}, k_{i,1})$ to achieve the desired power set-point. The PI controllers (tuning the control inputs) are unable to achieve the desired power set-point (being infeasible) even after $t = 200$ s, as in Fig. 5.14.

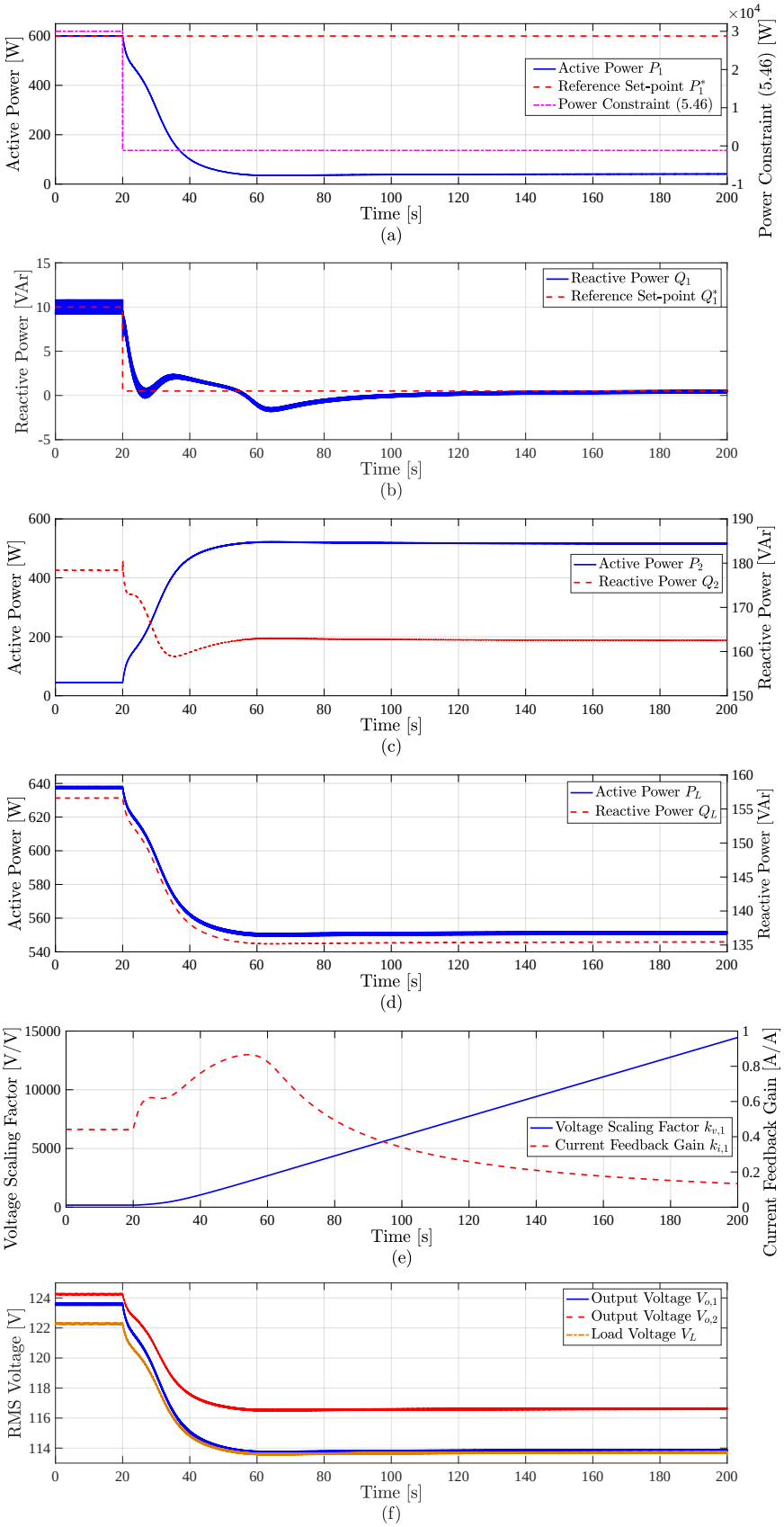

Figure 5.14: Power security constraint (5.46) violation results: (a) Inverter 1 active power, power security constraint and reference set-point, (b) Inverter 1 reactive power and reference set-point, (c) Inverter 2 output power, (d) load power, (e) control inputs, (f) voltages.

5.7 Conclusion

The LCL filter is considered an essential part of commercial inverters to filter out the switching harmonics and improve the output voltage. Keeping this in mind, an averaged VOC model is derived for inverters with current feedback after the output LC/LCL filter. The averaged model uncovers the embedded droop-characteristics within the averaged VOC dynamics and simplifies the analysis. The voltage and frequency regulation characteristics are determined. Further, to enable the virtual oscillator-controlled inverter to satisfy the desired ac-performance specifications, a parameter design procedure is presented. Moreover, the proposed power dispatch technique in Chapter 4 is extended to the proposed averaged VOC model with current feedback after the output LC/LCL filter. The updated control laws are derived to determine the control inputs corresponding to a particular power set-point. An updated power security constraint is derived to determine the feasible operating region. The power security constraint is helpful in planning the optimal power flow in an electric grid. The simulation results validate the proposed averaged VOC model and power dispatch technique. The simulation results also demonstrate that the inverter closely follows the desired design inputs, including the maximum-permissible rise time t_{rise}^{max} and the maximum-permissible ratio of the amplitude of the third harmonic to the fundamental $\delta_{3:1}^{max}$.

Chapter 6

Inner Control Loops to Compensate for Inverter Non-linearities Occurring in Virtual Oscillator Controlled Inverters

Virtual oscillator controllers regulate an inverter's output voltage and frequency according to the desired $V - P$ and $\omega - Q$ droop-characteristics embedded within their averaged dynamics. However, the existing literature on virtual oscillator control does not consider explicitly the effects of dead-time, semiconductor voltage-drop, and inverter side filter inductor voltage-drop on the inverter's intrinsic droop-characteristics. As a result, the inverter does not follow the desired droop-characteristics. Further, recall from Chapter 4, in the case of dispatchable virtual oscillator control, these factors result in steady-state offset-error in the control inputs. In this chapter, the effects of dead-time, semiconductor voltage-drop and inverter side filter inductor voltage-drop on the inverter's intrinsic droop-characteristics are analysed in detail. Moreover, inner voltage and current control loops are proposed to compensate for the voltage loss/gain at each switching cycle due to the dead-time, and voltage drops across the switching devices and inverter side filter inductor. The proposed tech-

nique does not require phase-locked loops and therefore can retain the fast dynamics of the virtual oscillator controller. Experimental and simulation results demonstrate the effectiveness of the proposed inner control loops in enabling the inverter to follow the desired droop-characteristics. Further, power dispatch results demonstrate that the proposed control loops avoid the steady-state offset-error in the control inputs apparent in Chapter 4 for the dispatchable virtual oscillator-controlled inverters.

6.1 Introduction

The existing literature on VOC does not specifically take into account the dead-time, semiconductor voltage-drop, and inverter side filter inductor voltage-drop present in a practical inverter. Beside the voltage drops across the switching devices and inverter side filter inductor, the dead-time results in a voltage loss/gain at each switching cycle [118]. These losses are not modelled or taken care of in the existing virtual oscillator models. As a result, virtual oscillator-controlled inverters do not follow the desired droop-characteristics and do not satisfy the desired ac-performance specifications. Recall from Chapter 4 that due to the dead-time, semiconductor voltage-drop, and inverter side filter inductor voltage-drop, there exists a steady-state offset-error between the control inputs when comparing the simulation and the experimental results for the power dispatch.

In this chapter, inner voltage and current control loops in a dq-reference frame are proposed to compensate the effects of unmodelled dead-time, semiconductor voltage-drop and inverter side filter inductor voltage-drop for virtual oscillator-controlled inverters. The proposed inner voltage and current control loops enable the virtual oscillator-controlled inverter to follow the desired intrinsic droop-characteristics effectively. Further, it is shown that using the proposed voltage and current control loops, the offset-error in the control inputs reported earlier in Chapter 4 is minimised for the dispatchable virtual oscillator control. This results in the experimental and

simulation results being in close agreement with each other.

Later, after addressing the offset-error issue in the control inputs using the proposed inner voltage and current control loops, we discovered a similar work for regulating the voltage at the output filter capacitor [119]. In contrast to our proposed inner control loops minimising the offset-error in the control inputs (discussed earlier in Chapter 4), the work in [119] is presented from a different perspective and reprograms the commercial current controlled inverters to behave as voltage source inverters in islanded mode with output voltage regulation capability. Moreover, [119] proposed a proportional-resonant (PR) controller in $\alpha\beta$-reference frame, whereas our proposed inner control loops are in a dq-reference frame. Note that both proposed techniques achieve the same objective of output voltage regulation while compensating for the inverter non-linearities, including the dead-time, semiconductor voltage-drop, and inverter side filter inductor voltage-drop. However, [119] does not explicitly consider and analyse the effects of dead-time, semiconductor voltage-drop and inverter side filter inductor voltage-drop on the inverter's droop-characteristics. In this chapter, the effects of dead-time, semiconductor voltage-drop and inverter side filter inductor voltage-drop on the inverter's droop-characteristics are analysed in detail. Recall from Chapter 2, other than the Van der Pol oscillator (that is the main focus of this thesis), a new version of virtual oscillator controller (i.e. dVOC [36–40]) can also achieve the set-point tracking for voltage, active power and reactive power.

The chapter is organised as follows. In Section 6.2, a detailed system description is presented. In Section 6.3, the actual and averaged VOC dynamics are presented. The dynamics of the PI controllers used for power dispatch are also discussed. Moreover, the dynamics of the proposed inner voltage and current control loops are presented. In Section 6.4, the description of our experimental prototype is presented. Moreover, the experimental results are presented for the black-start operation, synchronisation and power sharing capability, and load transients. In Section

6.5, a detailed discussion is considered on the effects of dead-time, semiconductor voltage-drop and inverter side filter inductor voltage-drop on the inverter's intrinsic droop-characteristics. The effectiveness of the proposed control loops is established through experimental and simulation results. In Section 6.6, experimental and simulation results are presented for the power dispatch of Inverter 1, while Inverter 2 supplies the remaining load power. It is shown that the proposed control loops minimise the steady-state offset-error in the control inputs due to the dead-time, semiconductor voltage-drop, and inverter side filter inductor voltage-drop reported earlier in Chapter 4. In Section 6.7, a conclusion is drawn.

6.2 System Description

A system consisting of two parallel-connected single-phase virtual oscillator-controlled inverters is considered. The inverters are connected to a common fixed impedance load $z_L = R_L + \jmath\omega^* L_L$ at the point of common coupling (PCC) through line impedance $z_{l,n} = R_{l,n} + \jmath\omega^* L_{l,n}$, where $n \in \{1, 2\}$. The ω^* denotes the fundamental grid frequency. There is an LCL filter at the output of each inverter with parameters $z_{f,n} = R_{f,n} + \jmath\omega^* L_{f,n}$, $z_{g,n} = R_{g,n} + \jmath\omega^* L_{g,n}$ and $z_{c,n} = R_{c,n} + \frac{1}{\jmath\omega^* C_{f,n}}$. A detailed system description is given in Fig. 6.1. The $i_{f,n}$ denotes the inverter side filter current, $i_{g,n}$ denotes the grid side inductor current and $i_{c,n}$ denotes the filter capacitor current. The v_n denotes the voltage before the LCL filter, $v_{o,n}$ denotes the filter capacitor voltage and v_L denotes the load voltage. The inner voltage and current control loops are used to compensate for the effects of dead-time, semiconductor voltage-drop and inverter side filter inductor voltage-drop. In the case of power dispatch, Inverter 1 regulates the output power according to the desired power set-point (P_1^*, Q_1^*), while Inverter 2 supplies the remaining load power demand. In order to regulate both the active and reactive power simultaneously, two PI controllers are used for Inverter 1 to continuously tune the voltage scaling factor $k_{v,1}$ and current

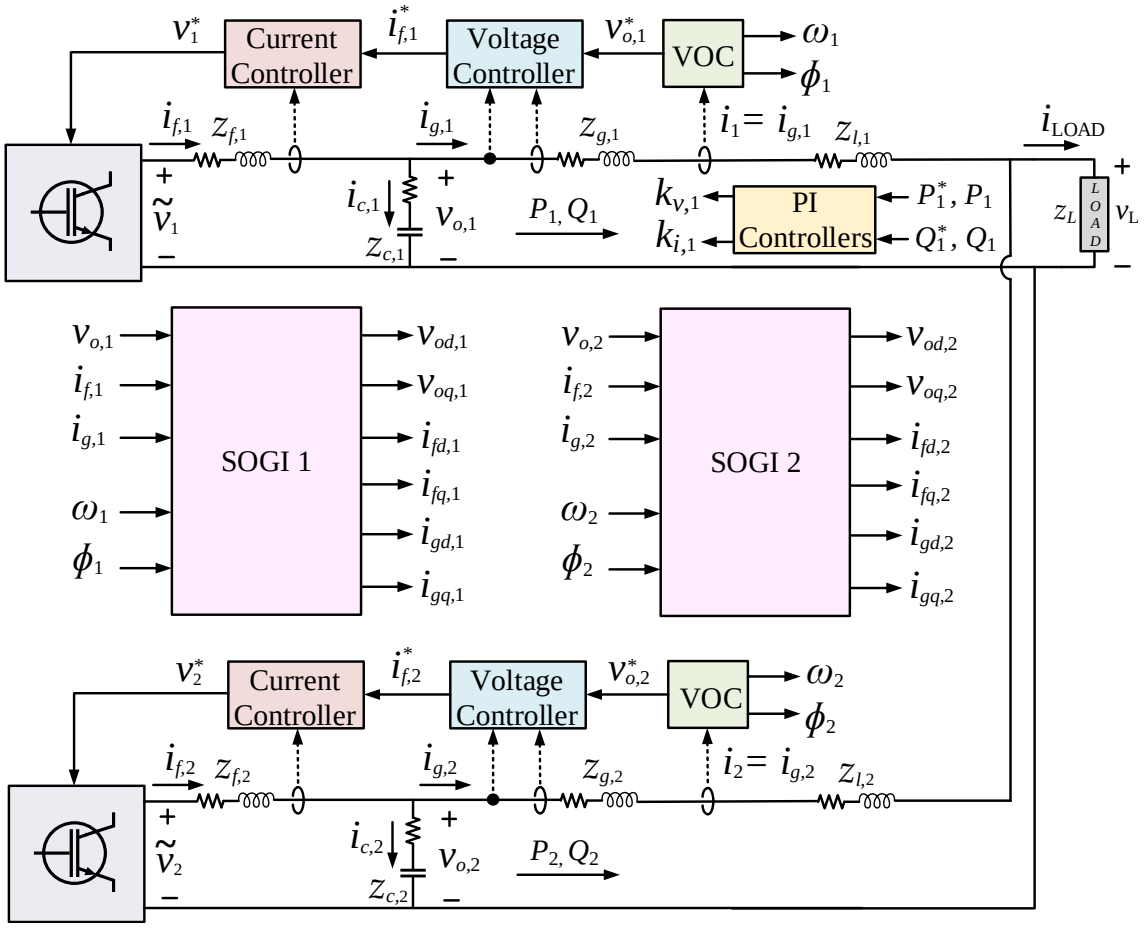

Figure 6.1: An overview of the system consisting of two parallel-connected single-phase virtual oscillator-controlled inverters with inner voltage and current control loops to compensate for the effects of dead-time, semiconductor voltage-drop and inverter side filter inductor voltage-drop. Inverter 1 can dispatch power using the PI controllers, while Inverter 2 supplies the remaining load demand. Moreover, the virtual oscillator controller also generates the instantaneous phase angle (and frequency) information and a phase-locked loop is not required.

feedback gain $k_{i,1}$.

6.3 System Modelling

In this section, the dynamics of a virtual (Van der Pol) oscillator are presented. Moreover, an averaged virtual oscillator model is presented that uncovers the embedded droop-characteristics within the averaged VOC dynamics. The PI controller dynamics used for power dispatch are also discussed. Further, the dynamics of the

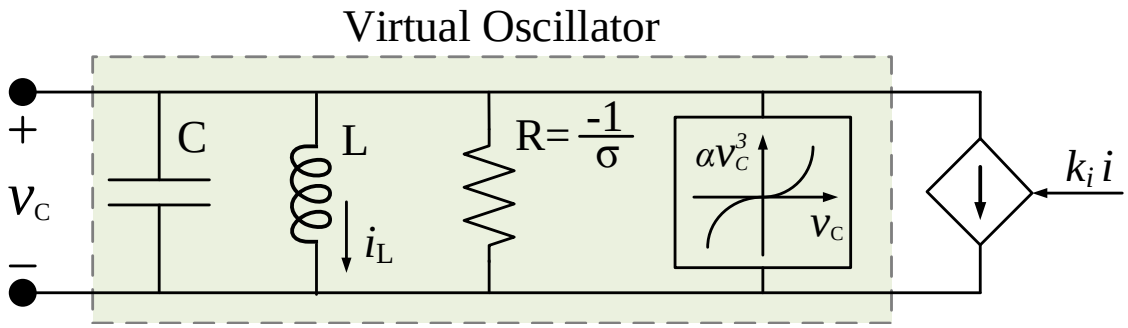

Figure 6.2: A schematic diagram of the virtual oscillator controller. The current feedback i is scaled by the current feedback gain k_i before entering the controller.

inner voltage and current control loops are presented.

6.3.1 Virtual Oscillator Controller

A block diagram representation of the VOC is given in Fig. 6.2. Note that the subscript n does not appear in Fig. 6.2 and is used in the text to denote the parameters of possibly distinct virtual oscillator-controlled inverters. The capacitor voltage $v_{C,n}$ is scaled by the voltage scaling factor $k_{v,n}$ to generate the reference voltage $v^*_{o,n}$ that should appear at the inverter's output filter capacitor. Recall from Chapter 2, the actual VOC dynamics are given by the following equations [76]:

$$\begin{aligned}\frac{dV_n}{dt} &= \frac{\epsilon_n \omega^*}{\sqrt{2}}\Big(\sigma_n g\big(\sqrt{2}V_n\cos(\phi_n)\big) - k_{v,n}k_{i,n}i_n\Big)\cos(\phi_n),\\ \frac{d\phi_n}{dt} &= \omega^* - \frac{\epsilon_n \omega^*}{\sqrt{2}V_n}\Big(\sigma_n g\big(\sqrt{2}V_n\cos(\phi_n)\big) - k_{v,n}k_{i,n}i_n\Big)\sin(\phi_n).\end{aligned} \tag{6.1}$$

6.3.2 Averaged Dynamics of VOC Inverter

Recall from Chapter 2, the averaged VOC model uncovering the $V-P$ and $\omega-Q$ droop-characteristics embedded within the dynamics of a virtual oscillator-controlled

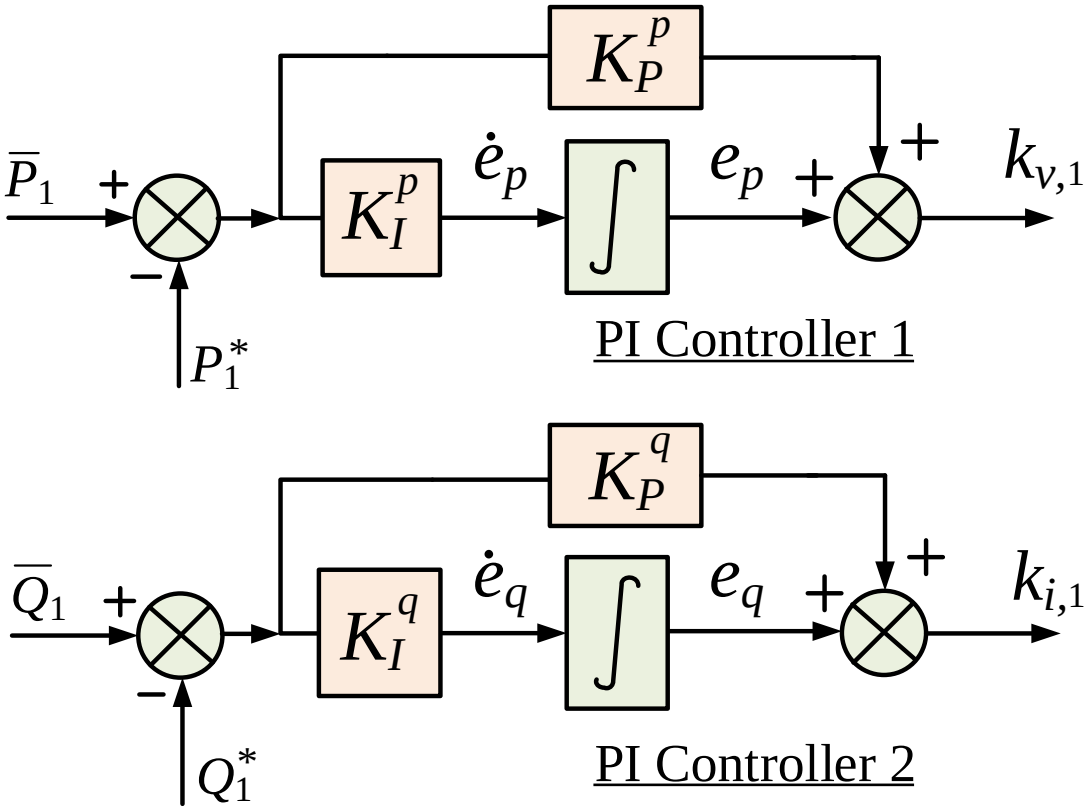

Figure 6.3: A block diagram representation of the PI controllers used to regulate Inverter 1 active and reactive power.

inverter is as follows:

$$\frac{d}{dt}\overline{V}_n = \frac{\sigma_n}{2C_n}\left(\overline{V}_n - \frac{\beta_n}{2}\overline{V}_n^3\right) - \frac{k_{v,n}k_{i,n}}{2C_n\overline{V}_n}\overline{P}_n, \tag{6.2}$$

$$\frac{d}{dt}\overline{\theta}_n = \omega^* - \omega_n + \frac{k_{v,n}k_{i,n}}{2C_n\overline{V}_n^2}\overline{Q}_n. \tag{6.3}$$

The equilibrium points corresponding to the averaged VOC dynamics are given by the following equations:

$$\overline{V}_{eq,n} = k_{v,n}\left(\frac{\sigma_n \pm \sqrt{\sigma_n^2 - 6\alpha_n(k_{i,n}/k_{v,n})\overline{P}_{eq,n}}}{3\alpha_n}\right)^{\frac{1}{2}}, \tag{6.4}$$

$$\omega_{eq,n} = \omega^* + \frac{k_{v,n}k_{i,n}}{2C_n\overline{V}_{eq,n}^2}\overline{Q}_{eq,n}. \tag{6.5}$$

6.3.3 PI Controller Dynamics

In order to dispatch the output power of Inverter 1, two PI controllers are used. A block diagram representation of the PI controllers is given in Fig. 6.3. Inverter 2 supplies the remaining load power, acting like a slack bus. The first PI controller regulates the active power $\overline{P}_1$ by tuning the voltage scaling factor $k_{v,1}$. Similarly, the second PI controller regulates the reactive power $\overline{Q}_1$ by tuning the current feedback gain $k_{i,1}$. The dynamics of PI controller 1 used to regulate the active power $\overline{P}_1$, are given by the following equations:

$$\dot{e}_p = K_I^p(\overline{P}_1 - P_1^*), \tag{6.6}$$

$$k_{v,1} = K_P^p(\overline{P}_1 - P_1^*) + e_p, \tag{6.7}$$

where P_1^* denotes the active power reference set-point and e_p is the PI controller state. The K_P^p and K_I^p denote the proportional and integral gains of PI controller 1. Similarly, the dynamics of PI controller 2 used to regulate the reactive power $\overline{Q}_1$ are given by the following equations:

$$\dot{e}_q = K_I^q(\overline{Q}_1 - Q_1^*), \tag{6.8}$$

$$k_{i,1} = K_P^q(\overline{Q}_1 - Q_1^*) + e_q, \tag{6.9}$$

where Q_1^* denotes the reactive power reference set-point and e_q is the PI controller state. The K_P^q and K_I^q denote the proportional and integral gains of PI controller 2.

6.3.4 Inner Control Loops

In order to compensate for the effects of dead-time, semiconductor voltage-drop and inverter side filter inductor voltage-drop, an inner current control loop and an outer voltage control loop are proposed in the *dq*-reference frame, as shown in

Fig. 6.1. Note that the inverter's frequency and instantaneous phase angle can be recovered from the original VOC dynamics (6.1). This avoids the time delays and complexities associated with the phase-locked loops. The current and voltage controllers bandwidth selection criteria depends on a number of factors including the closed-loop system's transient response, stability margin and disturbance rejection capability [49]. The PI controller gains K_{pi} and K_{ii}, for the current control loop are designed such that the bandwidth of the current controller is in-between $\frac{1}{20}$ and $\frac{1}{10}$ of the inverter's switching frequency [49]. Moreover, the PI controller gains K_{pv} and K_{iv} for the voltage control loop are designed so as to obtain a bandwidth in-between 25% and 75% of the current controller [49]. This results in a slower transient response of the outer voltage control loop compared to the innermost current control loop. The dynamics of the voltage and current control loops are presented in the following sections.

In the case of conventional droop-controlled inverters, the outer power-droop control loop is usually designed with a lower bandwidth ranging from a few Hz to tens of Hz to provide a time separation with respect to inner voltage and current control loops that are usually designed with a higher bandwidth ranging from hundreds of Hz to kHz. However, in the case of virtual oscillator-controlled inverters, the VOC being a time domain controller, has a higher bandwidth in hundreds of Hz as compared to the slower dynamics of conventional outer power-droop control loop. Moreover, the non-linear nature of the VOC makes the inner voltage and current loop design procedure complex, and hinders the adoption of VOC [85]. This gives rise to a need to investigate the inner control loops' design techniques for virtual oscillator-controlled inverters. In this chapter, due to the unavailability of standardised inner control loops design procedure for the virtual oscillator-controlled inverters, the PI controller gains are determined through trial and error to implement the inner control loops while achieving an adequate dynamic response. A systematic procedure to design the PI controller gains for the inner control loops is not considered in this thesis and is a possible direction for future work to take.

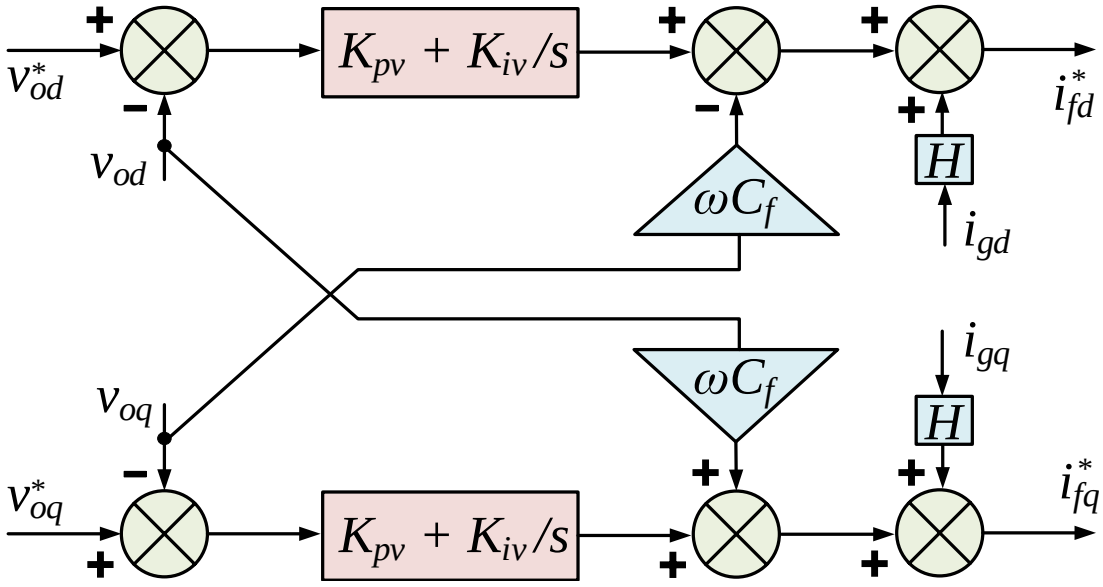

Figure 6.4: A block diagram representation of the inner voltage control loop with the decoupling, feedback and feedforward terms.

6.3.4.1 Voltage Control Loop

An outer voltage control loop is used to regulate the voltage $v_{o,n}$ at the filter capacitor and track the desired reference voltage signal $v^*_{o,n}$ generated by the virtual oscillator controller. A block diagram representation of the voltage controller is given in Fig. 6.4. In order to achieve the voltage regulation, a PI controller is used. The dynamics of the voltage controller are described by the following state and algebraic equations [7]:

$$\frac{de^d_v}{dt} = v^*_{od} - v_{od}, \quad \frac{de^q_v}{dt} = v^*_{oq} - v_{oq}, \tag{6.10}$$

$$i^*_{fd} = Hi_{od} - \omega^* C_f v_{oq} + K_{pv}\left(v^*_{od} - v_{od}\right) + K_{iv}e^d_v, \tag{6.11}$$

$$i^*_{fq} = Hi_{oq} + \omega^* C_f v_{od} + K_{pv}\left(v^*_{oq} - v_{oq}\right) + K_{iv}e^q_v, \tag{6.12}$$

where $\omega^* C_f v_{od}$ and $\omega^* C_f v_{oq}$ are the decoupling terms. The H is the feedforward gain. The K_{pv} and K_{iv} are the proportional and integral gains of the PI controller.

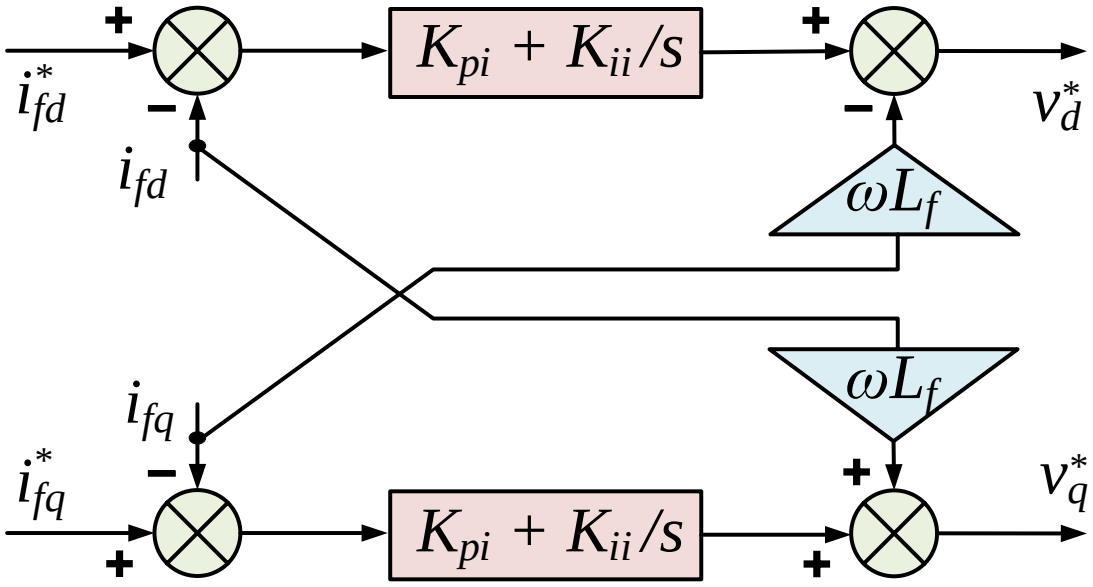

Figure 6.5: A block diagram representation of the inner current control loop with the decoupling and feedback terms.

6.3.4.2 Current Control Loop

An inner current control loop is used to regulate the filter current $i_{f,n}$. A block diagram representation of the current controller is given in Fig. 6.5. A PI controller is used to regulate the filter current. The current controller's state equations along with the algebraic equations are as follows [7]:

$$\frac{de_i^d}{dt} = i^*_{fd} - i_{fd}, \quad \frac{de_i^q}{dt} = i^*_{fq} - i_{fq}, \tag{6.13}$$

$$v^*_d = -\omega^* L_f i_{fq} + K_{pi}\left(i^*_{fd} - i_{fd}\right) + K_{ii} e_i^d, \tag{6.14}$$

$$v^*_q = \omega^* L_f i_{fd} + K_{pi}\left(i^*_{fq} - i_{fq}\right) + K_{ii} e_i^q, \tag{6.15}$$

where $\omega^* L_f i_{fd}$ and $\omega^* L_f i_{fq}$ are the decoupling terms. The K_{pi} and K_{ii} are the proportional and integral gains of the PI controller.

6.3.4.3 Second Order Generalised Integrator

Recall from Chapter 2, in contrast to three-phase power systems, the transformation of system variables into the $\alpha\beta$-reference frame cannot be achieved directly for single-

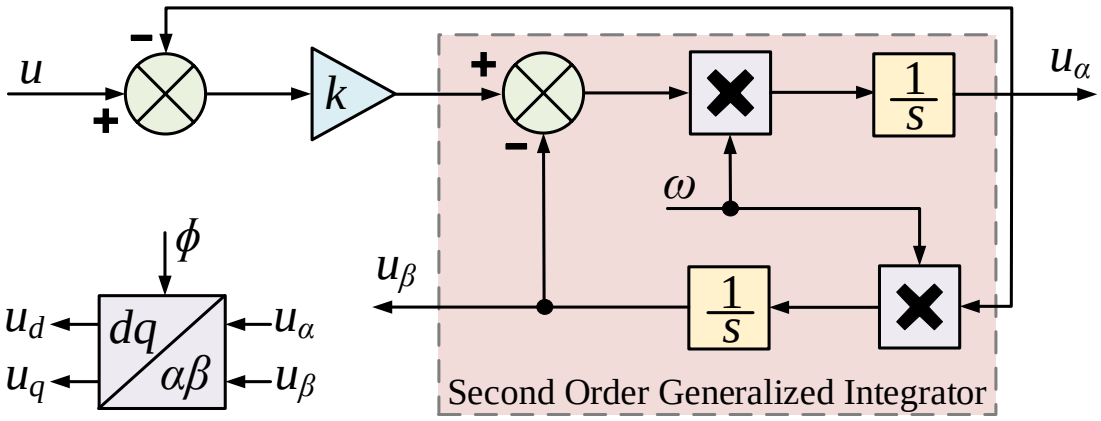

Figure 6.6: Second order generalised integrator (SOGI) used to transform the system variables into $\alpha\beta$-reference frame [54].

phase power systems. Hence, in order to transform the single-phase system variables into the $\alpha\beta$-reference frame, a second order generalised integrator (SOGI) is used [54]. A block diagram representation of the second order generalised integrator is shown in Fig. 6.6. The $\alpha\beta$-reference frame and dq-reference frame transformations are achieved by utilising the system frequency ω and instantaneous phase angle ϕ information generated by the virtual oscillator controller. A SOGI is used for each virtual oscillator-controlled inverter to generate the quadrature signals for the filter capacitor voltage v_o (i.e. v_{od} and v_{oq}), inverter side filter current i_f (i.e. i_{fd} and i_{fq}) and grid side inductor current i_g (i.e. i_{gd} and i_{gq}).

6.4 Experimental Setup

The experimental setup consisting of two parallel-connected single-phase virtual oscillator-controlled inverters with a common RL load is shown in Fig. 6.7. The IGBTs have a switching frequency $f_{sw} = \frac{1}{T_{sw}} = 10\,\text{kHz}$. The dead-time T_D can be adjusted to either $2\,\mu$s or $4\,\mu$s. A Texas Instruments TMSC2000 digital signal processor is used to implement the discretised dynamics of the virtual oscillator controller. As discussed earlier in Chapter 2, the virtual oscillator controller dynamic equations are discretised at a sampling time of $100\,\mu$s using the trapezoidal rule of

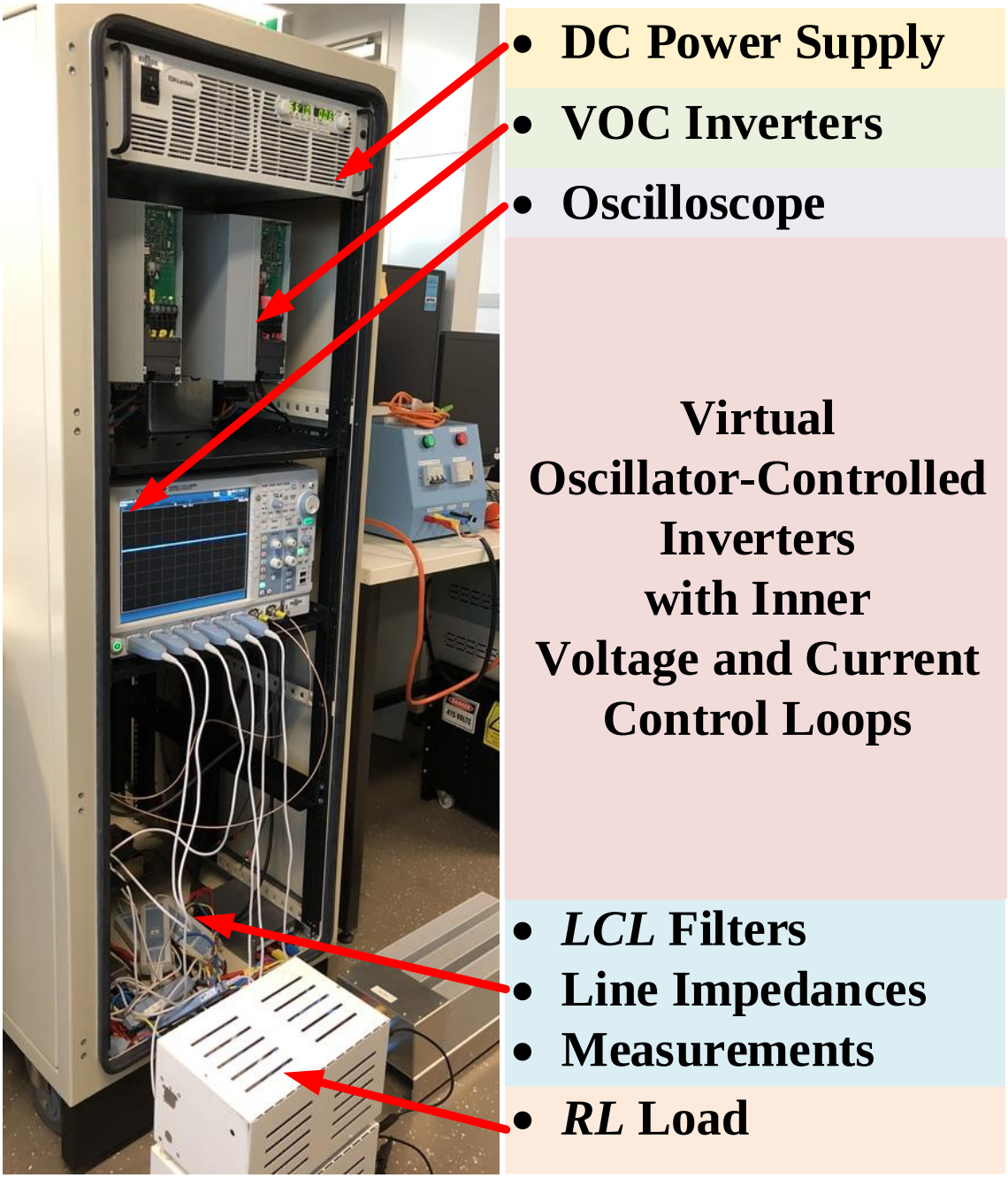

Figure 6.7: Experimental prototype consisting of two parallel-connected single-phase virtual oscillator-controlled inverters. The inverters are connected to a common RL load through respective line impedances.

integration [76]. The system parameters and ac-performance specifications are as in Table 6.1 and Table 6.2, respectively. The LCL filter, line and load parameters are $R_{f,n} = R_{l,n} = 0.15\,\Omega$, $L_{f,n} = L_{l,n} = 2.48$ mH, $R_{c,n} = 3.3\,\Omega$, $C_{f,n} = 4.7\,\mu$F, $R_{g,n} = 0.13\,\Omega$, $L_{g,n} = 0.97$ mH, $R_L = 22.3\,\Omega$ and $L_L = 14.4$ mH. The proportional and integral gains of the PI controllers used for the power dispatch of Inverter 1 are $K_P^p = -0.001$, $K_I^p = -0.08$, $K_P^q = 0.0001$ and $K_I^q = 0.003$. Recall from Section 4.8, a systematic design procedure for the PI controllers' gains to achieve the desired dynamic response and minimise the coupling effect between the controlled variables, is potential future work. A detailed PI controllers' gains design procedure for the secondary voltage and current control loops is presented in [49]. However, as discussed earlier in Section 6.3.4, the non-linear nature of the virtual oscillator controller and its relatively higher bandwidth as compared to the conventional outer power-droop control loop, necessitates an investigation into the revised inner control loops design techniques for virtual oscillator-controlled inverters. In this chapter, we have used the following proportional and integral gains (determined through trial and error while achieving an adequate dynamic response) for the PI controllers used to implement the inner voltage and current control loops: $K_{pv} = 1$, $K_{iv} = 10$, $K_{pi} = 1$ and $K_{ii} = 50$. The feedforward gain is $H = 0.65$. The SOGI gain is $k = 1.4$ [54]. In order to compute the ac-cycle averaged active and reactive power, a moving average window is used at the fundamental grid frequency ω^*. The moving average window's length is $T^* = \frac{2\pi}{\omega^*}$. The number of current and voltage samples taken in this window's length are $m^* = f_{sw}T^*$. The m^* (being not an integer in general) is rounded to the nearest integer. The instantaneous active and reactive power of an inverter in terms of output voltage v_o and current i_g at the m^{th} sampling instance is given by:

$$p_m = p(mT_{sw}) = v_o(mT_{sw})i_g(mT_{sw}), \tag{6.16}$$

$$q_m = q(mT_{sw}) = v_o\left(mT_{sw} - \frac{m^*T_{sw}}{4}\right)i_g(mT_{sw}). \tag{6.17}$$

The averaged active and reactive power over an ac-cycle $\frac{2\pi}{\omega^*}$ using the moving average window is determined as follows:

$$P_m = \frac{1}{m^*}\sum_{\gamma=0}^{m^*-1} p_{m-\gamma}, \quad Q_m = \frac{1}{m^*}\sum_{\gamma=0}^{m^*-1} q_{m-\gamma}. \tag{6.18}$$

For successive sampling instances, the moving average values can be determined as follows:

$$P_m = P_{m-1} + \frac{1}{m^*}\left(p_m - p_{m-m^*}\right), \tag{6.19}$$

$$Q_m = Q_{m-1} + \frac{1}{m^*}\left(q_m - q_{m-m^*}\right). \tag{6.20}$$

The RMS voltage is computed using the RMS block in MATLAB/Simulink and is given by the following equation:

$$V(t) = \sqrt{\frac{\omega^*}{2\pi}\int_{s=t}^{t+2\pi/\omega^*} v(s)^2 ds}. \tag{6.21}$$

Experimental results for the black-start operation, synchronisation and power sharing capability, and load transients are presented in the following sections.

6.4.1 Black-start Operation

The experimental results are presented for the black-start operation of a virtual oscillator-controlled inverter with inner control loops. The inverter is feeding an RL load defined in Section 6.4. In Fig. 6.8, the inverter follows the design parameter $t_{rise}^{max} = 0.2\,\text{s}$ (that is defined in Chapter 2 as the time to build-up the output voltage from 10 % to 90 % of the open-circuit output voltage V_{oc}). The inverter is turned ON at $t = 0.1\,\text{s}$. These results establish the grid forming capability of the virtual oscillator-controlled inverter with the proposed inner control loops.

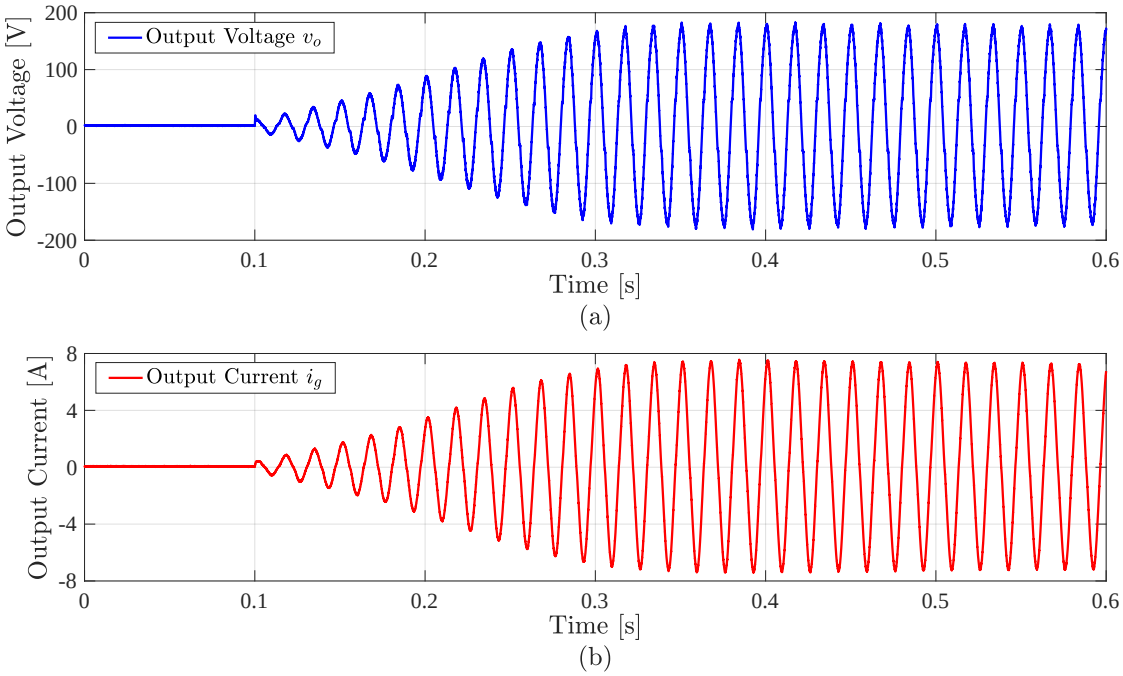

Figure 6.8: Experimental results for black-start operation: (a) output voltage v_o, (b) output current i_g.

6.4.2 Synchronisation and Power Sharing Capability

The synchronisation and power sharing capability of the virtual oscillator-controlled inverters with the proposed inner control loops is demonstrated in Fig. 6.9. Initially at $t = 0\,\text{s}$, Inverter 1 (forming the power grid) is supplying power to the load while Inverter 2 is OFF. In order to achieve a smooth addition of another inverter, Inverter 2 is turned ON at the instant ($t = 1\,\text{s}$) when the zero-crossings of both the modulation signal (for Inverter 2) and grid voltage overlap. An alternative way to connect an inverter with the power grid can be the utilisation of a pre-synchronisation circuit, proposed in [120] and reviewed in this thesis in Chapter 2. The experimental results demonstrate that the two inverters start to share the power proportionally. Similarly at $t = 5\,\text{s}$, Inverter 2 is disconnected from the grid. The corresponding changes in the load voltage and current can be seen in Fig. 6.9.

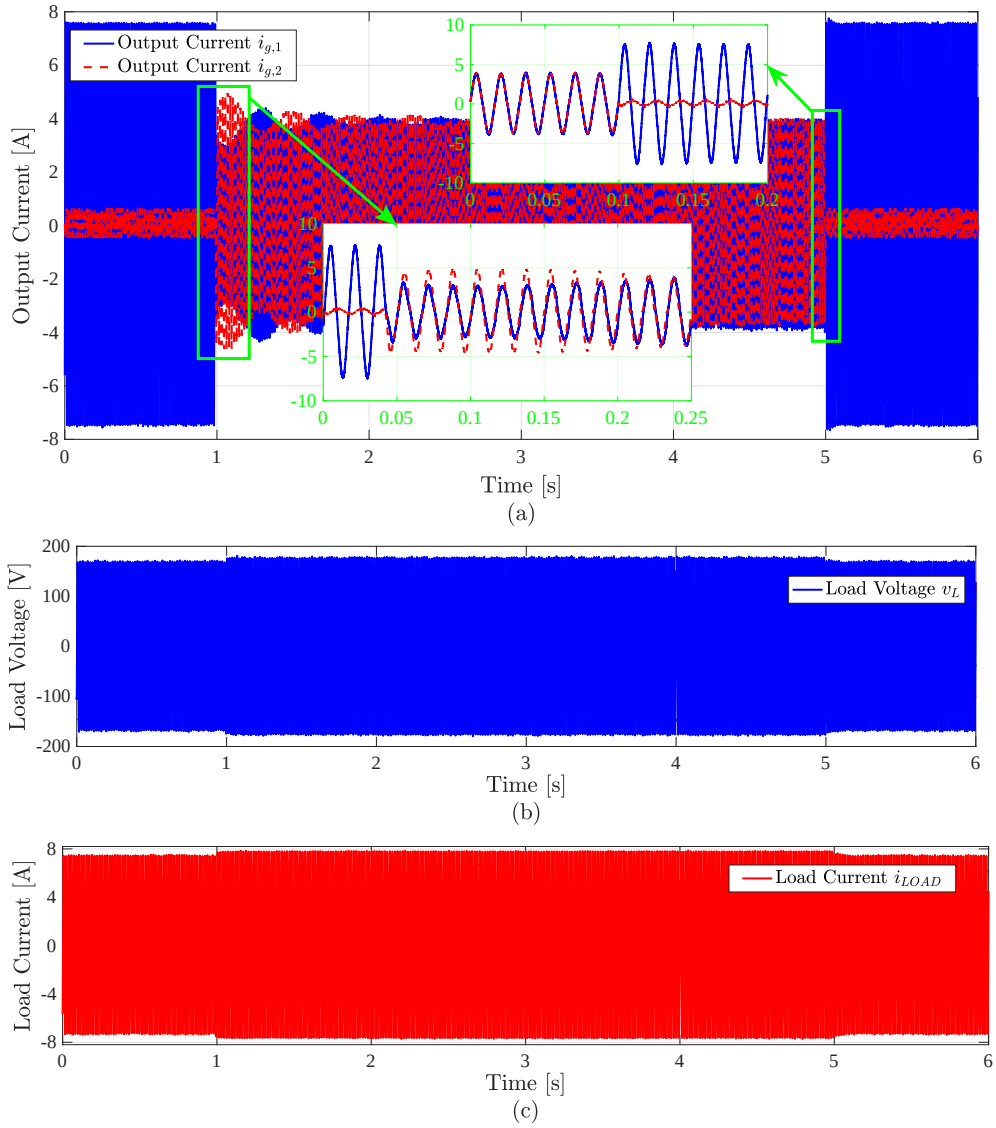

Figure 6.9: Experimental results demonstrating the synchronisation and power sharing capability of virtual oscillator-controlled inverters with proposed inner control loops: (a) output current $i_{g,1}$ and $i_{g,2}$, (b) load voltage v_L, (c) load current i_{LOAD}.

6.4.3 Load Transients

The experimental results for load transients are given in Fig. 6.10 for a system of two parallel-connected virtual oscillator-controlled inverters feeding an RL load with the proposed inner control loops. Initially at $t = 0\,\text{s}$, the two inverters are sharing both the active and reactive power demand proportionally. At $t = 4\,\text{s}$, a step-up change in the load is applied by connecting another similar RL load in-parallel with the existing RL load. Note that both the inverters adapt to the change and increase

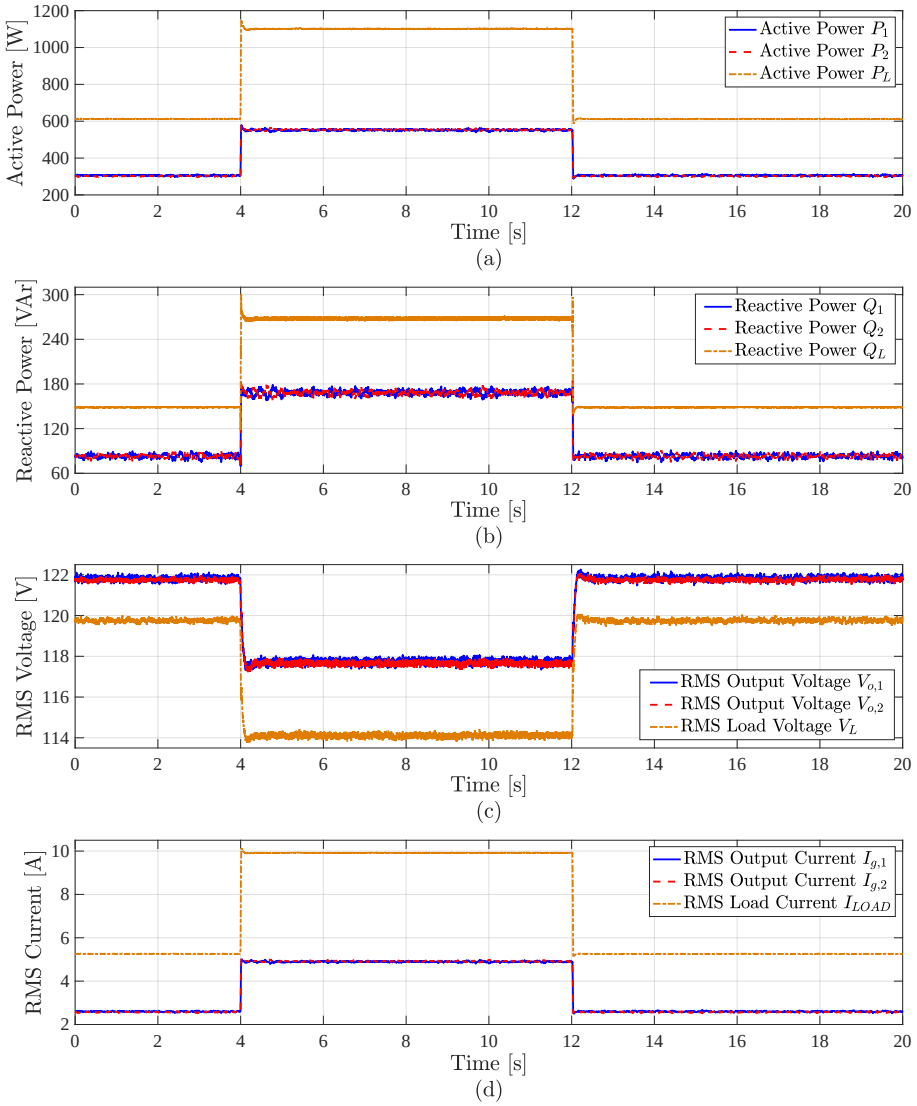

Figure 6.10: Experimental results for load transients in the case of two parallel-connected virtual oscillator-controlled inverters with the proposed inner control loops: (a) inverter and load active power, (b) inverter and load reactive power, (c) RMS voltages, (d) RMS currents.

their output power while sharing the load demand proportionally. Similarly, a step-down change in the load is applied at $t = 12\,\mathrm{s}$ by disconnecting one of the two parallel-connected RL loads from the system. The inverters reduce their output power according to the load demand. The corresponding changes in the system's voltages and currents are shown in Fig. 6.10.

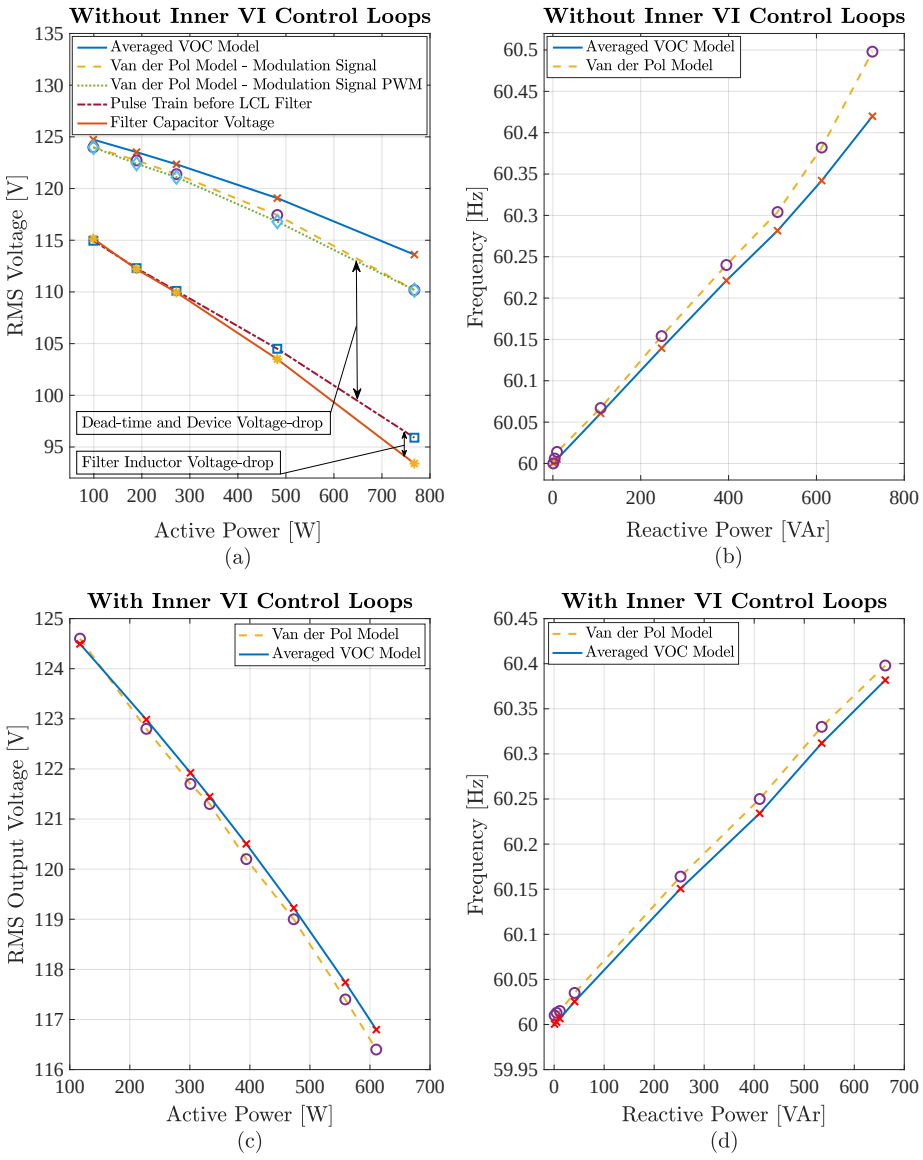

Figure 6.11: A comparison of experimentally determined droop-characteristics of an inverter with and without inner control loops. The results are for a dead-time $T_D = 2\,\mu$s and $\epsilon' = \epsilon = \sqrt{L/C}$: (a) $V - P$ droop-characteristics without inner control loops, (b) $\omega - Q$ droop-characteristics without inner control loops, (c) $V - P$ droop-characteristics with inner control loops, (d) $\omega - Q$ droop-characteristics with inner control loops.

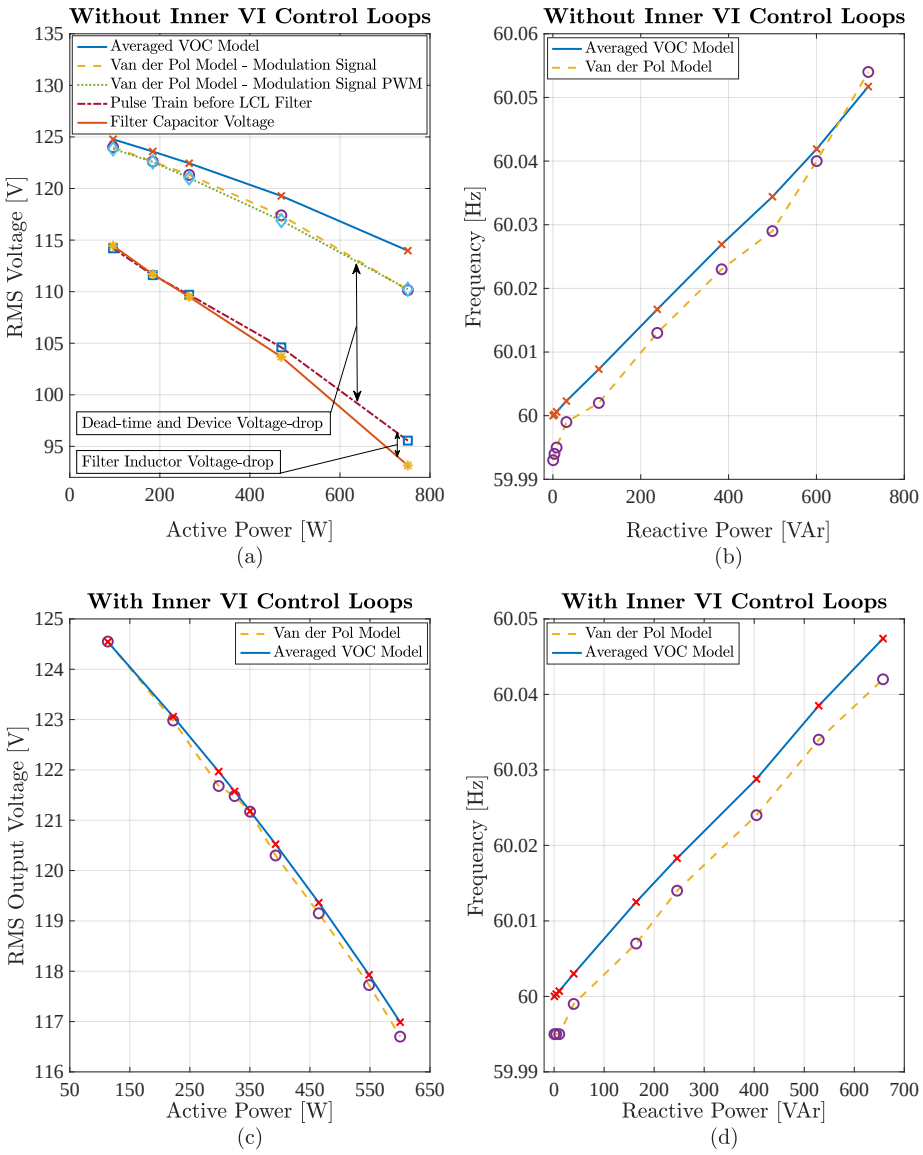

Figure 6.12: A comparison of experimentally determined droop-characteristics of an inverter with and without inner control loops. The results are for a dead-time $T_D = 2\,\mu$s and $\epsilon' = \epsilon/8 = \frac{\sqrt{L/C}}{8}$: (a) $V - P$ droop-characteristics without inner control loops, (b) $\omega - Q$ droop-characteristics without inner control loops, (c) $V - P$ droop-characteristics with inner control loops, (d) $\omega - Q$ droop-characteristics with inner control loops.

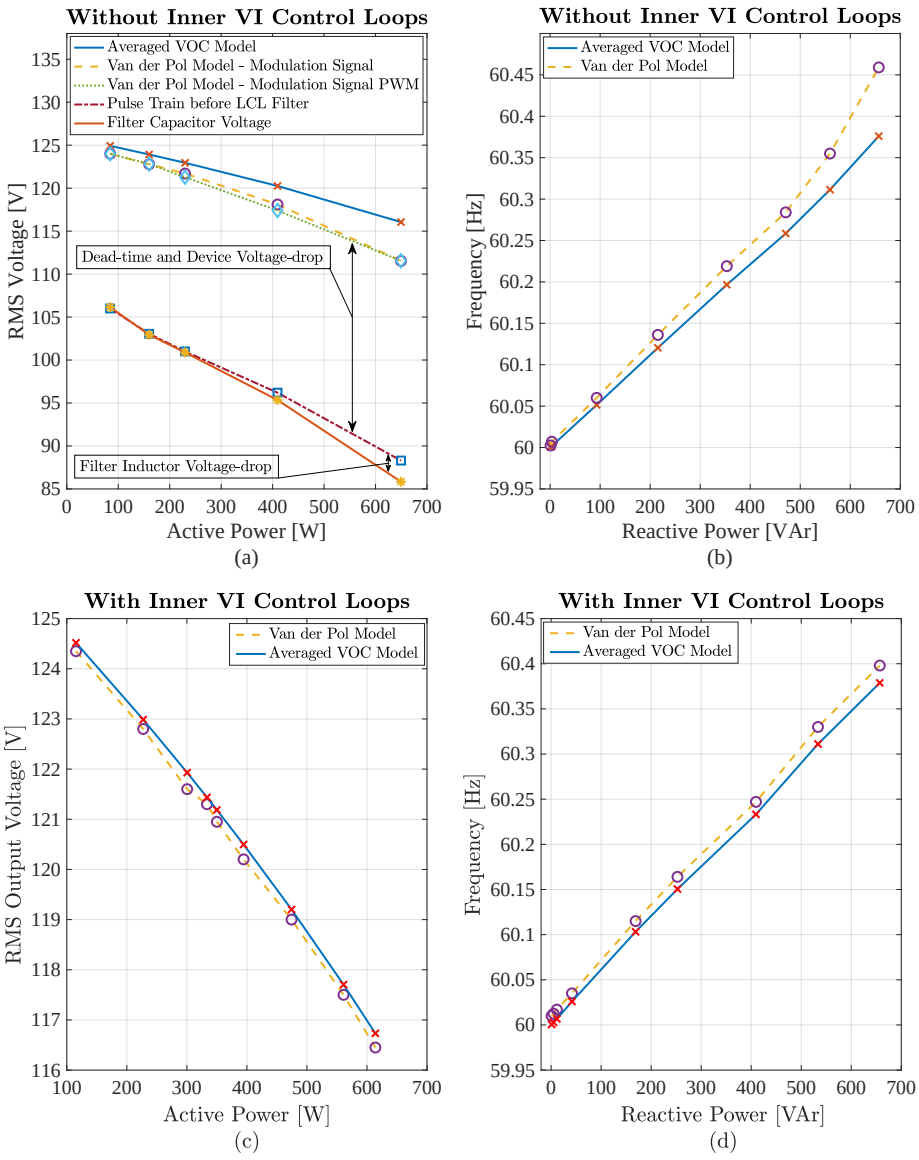

Figure 6.13: A comparison of experimentally determined droop-characteristics of an inverter with and without inner control loops. The results are for a dead-time $T_D = 4\,\mu$s and $\epsilon' = \epsilon = \sqrt{L/C}$: (a) $V - P$ droop-characteristics without inner control loops, (b) $\omega - Q$ droop-characteristics without inner control loops, (c) $V - P$ droop-characteristics with inner control loops, (d) $\omega - Q$ droop-characteristics with inner control loops.

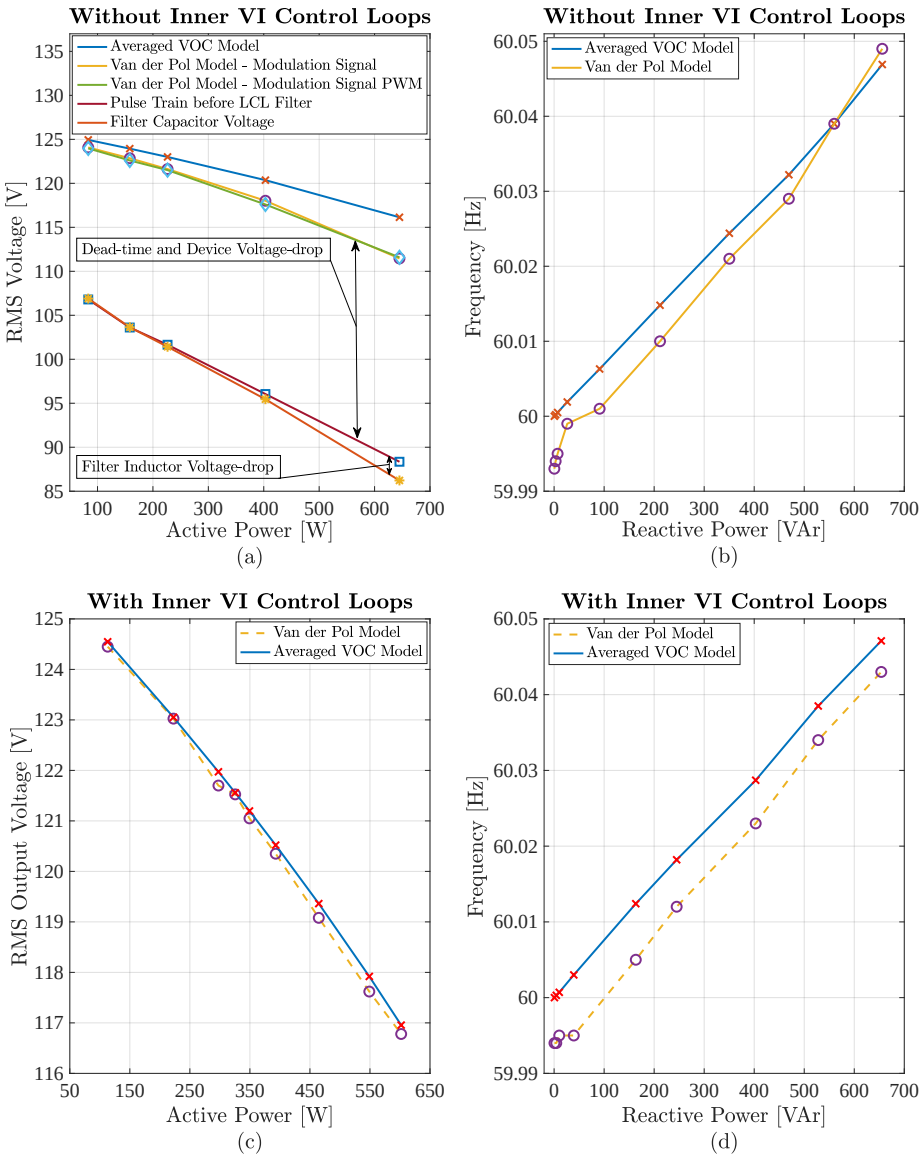

Figure 6.14: A comparison of experimentally determined droop-characteristics of an inverter with and without inner control loops. The results are for a dead-time $T_D = 4\,\mu$s and $\epsilon' = \epsilon/8 = \frac{\sqrt{L/C}}{8}$: (a) $V - P$ droop-characteristics without inner control loops, (b) $\omega - Q$ droop-characteristics without inner control loops, (c) $V - P$ droop-characteristics with inner control loops, (d) $\omega - Q$ droop-characteristics with inner control loops.

6.5 Droop Characteristics with Inner Control Loops

In this section, the effects of dead-time, semiconductor voltage-drop and inverter side filter inductor voltage-drop on the droop-characteristics of the virtual oscillator-controlled inverters are analysed in detail. A comparison is presented between the droop-characteristics embedded within the averaged VOC dynamics (6.4)-(6.5) and experimental results for the actual VOC dynamics (6.1). The droop-characteristics are compared for two different values of dead-time and VOC design parameter ϵ' (resulting in four comparison cases) for a system with and without inner control loops. In order to quantify the effects of dead-time (including the semiconductor voltage-drop) and inverter side filter inductor voltage-drop, the $V - P$ droop-characteristics are plotted for the RMS voltage of:

- averaged VOC model.
- modulation signal generated by the Van der Pol oscillator (that is used for the experimental prototype by programming its discretised dynamics on a digital signal processor).
- PWM signals (without dead-time) corresponding to the modulation signal generated by Van der Pol oscillator.
- pulse train before the output LCL filter that includes the effects of dead-time and semiconductor voltage-drop.
- LCL filter capacitor voltage.

Note that in Fig.6.11-6.14, the dead-time (including the semiconductor voltage-drop) has a major contribution in the voltage difference between the averaged VOC model and the actual voltage that appears at output LCL filter capacitor. The inverter side filter inductor voltage-drop depends on the load current and increases with the increase in output active power. Moreover, there is a difference between the averaged

VOC model and Van der Pol model $V - P$ droop-characteristics. This difference is due to the unmodelled dead-time and semiconductor voltage-drop that are not taken into account while synthesising the averaged VOC dynamics. The detailed comparison results are presented in the following sections.

6.5.1 Dead-time $T_D = 2\,\mu$s

6.5.1.1 Case 1

In this section, the effects of dead-time, semiconductor voltage-drop and inverter side filter inductor voltage-drop on the droop-characteristics of a virtual oscillator-controlled inverter are presented for a dead-time $T_D = 2\,\mu$s. The comparison is made between the embedded droop-characteristics within the averaged VOC dynamics (6.4)-(6.5) and experimental results for the actual VOC dynamics (6.1). In Fig. 6.11, the comparison is presented for $\epsilon' = \epsilon = \sqrt{L/C}$. Note that for the case when inner control loops are not used, the inverter does not follow the intrinsic droop-characteristics as in Fig. 6.11(a). There is a significant voltage loss that increases further with the increase in active power demand. On the other hand, the utilisation of inner control loops compensate for the effects of dead-time, semiconductor voltage-drop and inverter side filter inductor voltage-drop. Note that in Fig. 6.11(c)-6.11(d), the inverter closely follows the desired intrinsic droop-characteristics.

6.5.1.2 Case 2

In Fig. 6.12, the comparison is presented for $\epsilon' = \epsilon/8 = \frac{\sqrt{L/C}}{8}$. A smaller value of ϵ' results in a smaller frequency deviation for the nominal value ω^* as evident in Fig. 6.12(b) and Fig. 6.12(d). In Fig. 6.12(a) and Fig. 6.12(c), it can be seen that the inner control loops enable the inverter to follow the desired intrinsic droop-characteristics.

6.5.2 Dead-time $T_D = 4\,\mu$s

6.5.2.1 Case 3

In this scenario, a comparison is made between the embedded droop-characteristics within the averaged VOC dynamics (6.4)-(6.5) and experimental results for the actual VOC dynamics (6.1) for a dead-time $T_D = 4\,\mu$s. The comparison between the droop-characteristics is presented in Fig. 6.13 for $\epsilon' = \epsilon = \sqrt{L/C}$. The inner control loops compensate for the effects of dead-time, semiconductor voltage-drop and inverter side filter inductor voltage-drop as in Fig. 6.13(c) compared to the Fig. 6.13(a), where there is a significant voltage loss. Note that the voltage loss in this case is more compared to the voltage loss in Section 6.5.1 with a smaller value of dead-time $T_D = 2\,\mu$s.

6.5.2.2 Case 4

A comparison between the droop-characteristics for a virtual oscillator-controlled inverter with and without inner control loops is presented in Fig. 6.14 for $\epsilon' = \epsilon/8 = \frac{\sqrt{L/C}}{8}$. In Fig. 6.14(b) and Fig. 6.14(d), it can be noted that the deviation of the system's frequency ω as a function of reactive power from the nominal grid frequency ω^* is quite small as expected for a smaller value of ϵ'. The proposed inner control loops compensate for the effects of dead-time, semiconductor voltage-drop and inverter side filter inductor voltage-drop, resulting in the virtual oscillator-controlled inverter following the desired droop-characteristics, as in Fig. 6.14(c).

Note that the dead-time, semiconductor voltage-drop and inverter side filter inductor voltage-drop result in a voltage loss that mainly affects the $V - P$ droop-characteristics of the virtual oscillator-controlled inverter. However, these voltage losses do not affect the $\omega - Q$ droop-characteristics of the inverter noticeably.

Table 6.1: System Parameters

Symbol	Parameter	Inverter 1	Inverter 2	Unit
k_i	Current feedback gain	[control variable]	0.152	A/A
k_v	Voltage scaling factor	[control variable]	126	V/V
σ	Conductance	6.09	6.09	Ω^{-1}
α	Cubic-current source coefficient	4.06	4.06	A/V^3
L	Virtual oscillator inductance	39.09	39.09	μH
C	Virtual oscillator capacitance	0.18	0.18	F

6.6 Power Dispatch with Inner Control Loops

In order to validate the effectiveness of the proposed inner control loops, power dispatch results are presented in this section. Note that the proposed control loops minimise the steady-state offset-error in the control inputs (reported earlier in Chapter 4) by regulating the filter current and capacitor voltage according to the desired reference set-points. In Fig. 6.15, it can be seen that the proposed control loops compensate for the effects of dead-time, semiconductor voltage-drop and inverter side filter inductor voltage-drop by regulating the voltages at the output filter capacitor close to the desired reference values. A system of two parallel-connected single-phase virtual oscillator-controlled inverters is considered for the power dispatch results. The power is dispatched for Inverter 1 while Inverter 2 supplies the remaining load power. Simultaneous active and reactive power regulation is achieved by the use of two PI controllers for Inverter 1, as described in Section 6.3.3. A number of power dispatch scenarios are considered and described in the following sections. The simulations are performed in MATLAB.

6.6.1 Case 1

Initially at $t = 0$ s, both the inverters are sharing equal active and reactive power demand. Moreover, the voltage scaling factor $k_{v,1}$ and current feedback gain $k_{i,1}$ are

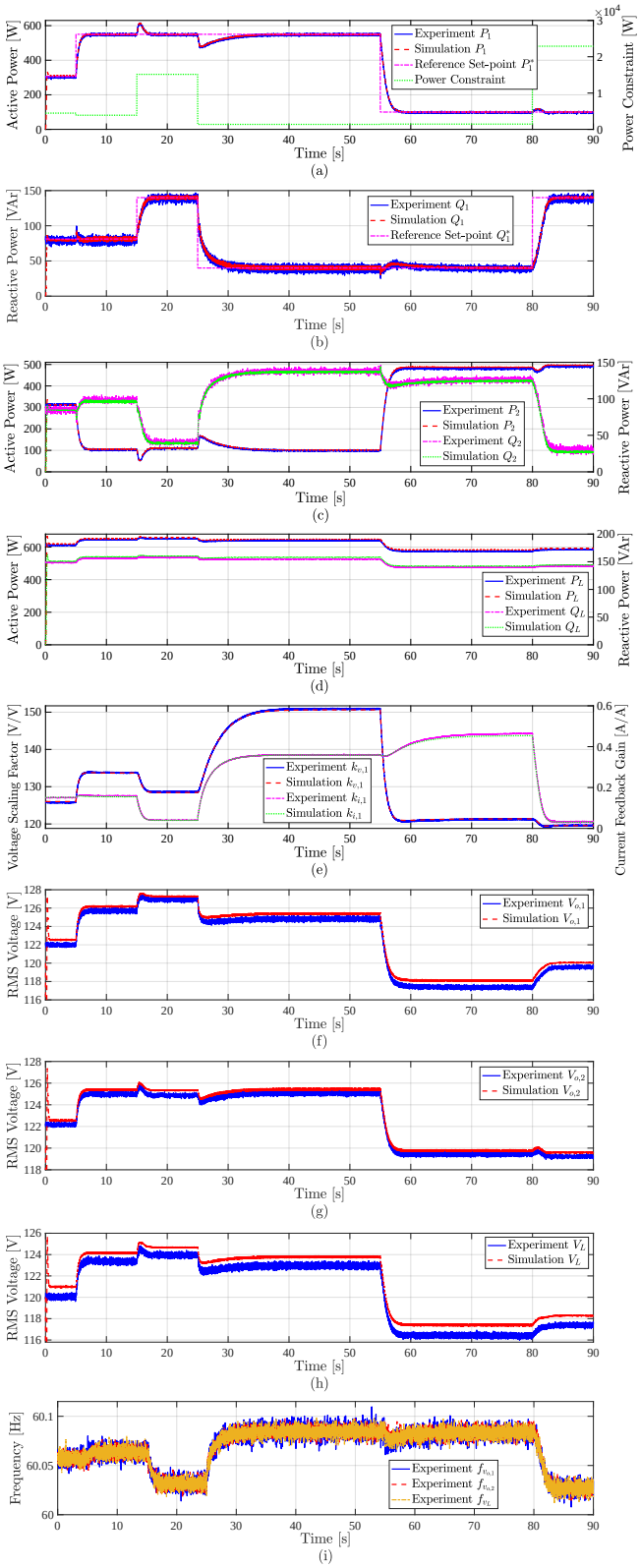

Figure 6.15: A comparison between the experimental and simulation power dispatch results: (a) set-point P_1^*, active power P_1 and power constraint (4.26), (b) set-point Q_1^* and reactive power Q_1, (c) Inverter 2 active power P_2 and reactive power Q_2, (d) load active power P_L and reactive power Q_L, (e) control variables $k_{v,1}$ and $k_{i,1}$, (f) Inverter 1 RMS voltage, (g) Inverter 2 RMS voltage, (h) load RMS voltage, (i) frequency.

Table 6.2: AC Performance Specifications

Symbol	Parameter	Value	Unit
$\overline{V}_{oc}$	RMS open-circuit voltage	126	V
$\overline{V}_{rated}$	RMS rated grid voltage	120	V
$\overline{V}_{min}$	RMS rated power voltage	114	V
$\overline{P}_{rated}$	Rated real power	750	W
$\lvert\overline{Q}_{rated}\rvert$	Rated reactive power	750	VAr
ω^*	Nominal oscillator frequency	$2\pi 60$	rad/s
$\lvert\Delta\omega\rvert_{max}$	Maximum frequency offset	$2\pi 0.5$	rad/s
t_{rise}^{max}	Maximum rise time	0.2	s
$\delta_{3:1}^{max}$	3^{rd} to 1^{st} harmonic ratio	1.5	%

the same as the fixed gains ($k_{v,2}$ and $k_{i,2}$) for Inverter 2 as in Fig. 6.15.

6.6.2 Case 2

A step-up change in the active power set-point $P_1^* = 305 \rightarrow 550$ W is applied at $t = 5$ s while the reactive power set-point is the same $Q_1^* = 81.2$ VAr. Inverter 1 tracks and reaches the desired power set-point at $t = 6.6$ s. In this case, Inverter 1 is supplying a major portion of load active power demand. The corresponding changes in the control inputs ($k_{v,1}, k_{i,1}$) can be seen in Fig. 6.15.

6.6.3 Case 3

At $t = 15$ s, a step-up change is applied in the reactive power set-point $Q_1^* = 81.2 \rightarrow$ 140 VAr while the active power set-point is the same $P_1^* = 550$ W. The inverter follows and reaches the new set-point at $t = 16.7$ s. In this case, Inverter 1 is supplying a major portion of both the active and reactive power demand.

6.6.4 Case 4

A step-down change in the reactive power set-point $Q_1^* = 140 \rightarrow 40$ VAr is applied at $t = 25$ s and the active power set-point is the same $P_1^* = 550$ W. Inverter 1 reaches the new set-point at $t = 28.4$ s and tracks it effectively. In this case, Inverter 1 supplies most of the active power while Inverter 2 supplies most of the reactive power demand.

6.6.5 Case 5

In this case, a step-down change in the active power set-point $P_1^* = 550 \rightarrow 100$ W is applied at $t = 55$ s while the reactive power set-point is fixed at $Q_1^* = 40$ VAr. In Fig. 6.15, Inverter 1 effectively tracks the new set-point and reaches it at $t = 58.1$ s. In this case, Inverter 2 supplies most of the active and reactive power demand.

6.6.6 Case 6

At $t = 80$ s, a step-up change in the reactive power set-point $Q_1^* = 40 \rightarrow 140$ VAr is applied while the active power set-point is fixed at $P_1^* = 100$ W. Inverter 1 reaches the desired set-point at $t = 82.8$ s. In this case, Inverter 1 is supplying most of the reactive power to the load while Inverter 2 is supplying most of the active power demand.

Note that in all of the aforementioned power dispatch cases, the experimental results are close to the simulation results. The proposed inner control loops compensate for the effects of dead-time, semiconductor voltage-drop and inverter side filter inductor voltage-drop, thus resulting in the desired voltages appearing at the output LCL filter capacitors. This minimises the steady-state offset-error in the control inputs

between the simulation and experimental results, as reported earlier in Chapter 4.

6.7 Conclusion

Inner voltage and current control loops are proposed to compensate for the effects of dead-time, semiconductor voltage-drop and inverter side filter inductor voltage-drop for virtual oscillator-controlled inverters. The dead-time results in a voltage loss/gain at each switching cycle that is not considered in existing models of virtual oscillator-controlled inverters. Moreover, the voltage drops across the switching devices and inverter side filter inductor are also not considered. As a result, in experiments, the VO-controlled inverters do not follow the desired droop-characteristics and the voltages that appear at the output of the inverters are lower than expected. The voltage losses also result in a steady-state offset-error between the control inputs when comparing the experimental and simulation results for dispatchable virtual oscillator control. The experimental and simulation results presented in this chapter validate the effectiveness of the proposed inner control loops that enable the inverters to follow the desired droop-characteristics. Experimental results for the (i) black-start operation to form a power grid, (ii) synchronisation and power sharing capability to connect/disconnect a power source and (iii) load transients, demonstrate the merits of the proposed control technique. Further, these inner control loops also minimise the steady-state offset-error in the control inputs for the power dispatch scenario by regulating the output LCL filter capacitor voltage close to the desired reference value. In order to implement the inner control loops, the virtual oscillator dynamics are used to recover the inverter's instantaneous phase angle and frequency information, thus avoiding the need for a phase-locked loop. This helps in avoiding the unnecessary delays and complexities associated with the implementation of phase-locked loops, and retaining the fast dynamics of the virtual oscillator controller.

Chapter 7

Power Sharing Dynamics of Parallel Connected Virtual Oscillator Controlled and Droop Controlled Inverters in an AC Microgrid

Accurate active and reactive power control is of utmost importance in an inverter-interfaced AC microgrid. Power droop control has been proven as a good design trade-off and communication free technique for achieving controllable load sharing. Implementation of power droop control requires both the voltage and current measurement at the inverter output to calculate the power, and to achieve synchronisation with rest of the system. On the other hand, recall from Chapter 2, that the recently proposed virtual oscillator controller (VOC) features inherent synchronisation using only current measurement. However, VOC being a non-linear oscillator, introduces harmonic distortion in the output. This chapter investigates power sharing capability, dynamic response and harmonic profile for a system consisting of a parallel-connected (i) droop-controlled inverter and (ii) virtual oscillator-controlled inverter. It is demonstrated that power sharing between these two different control techniques can be achieved by properly designing both the droop controller and VOC

parameters. The harmonic distortion present in the output of a VO-controlled inverter results in harmonic currents flowing between the two inverters. The harmonic distortion can be reduced by designing a tightly regulated VO-controlled inverter. However, this results in a slower dynamic response. Several features, including synchronisation capability, response to step change in load, and the trade-off between dynamic response and harmonic content present in the VOC output, are demonstrated through simulations[1].

7.1 Introduction

In a microgrid, inverters are not necessarily controlled by the same control technique. Hence, a need arises to investigate systems consisting of multiple inverters operating in parallel with heterogeneous control techniques. To the best of our knowledge, this issue has not been addressed in the literature except for [121]. Most of the literature on inverter control techniques considers that all inverters present in the system are controlled by the same control technique.

In this chapter, a system consisting of two parallel-connected inverters: (i) droop-controlled inverter and (ii) virtual oscillator-controlled inverter are considered. Note that this chapter deals with the three-phase inverters. It is demonstrated that proportional power sharing between two parallel-connected inverters being controlled by two different control techniques can be achieved by properly designing both the droop controller and VOC parameters. Moreover, a discussion is carried out to identify the possible reasons for unequal reactive power sharing in the case of heterogeneously controlled inverters. Several scenarios demonstrating the synchronisation

[1]This chapter is based on conference paper [2]. The primary author, Mr. Muhammad Ali worked on the virtual oscillator controller part of the research work, whereas the co-author, Mr. Animesh K. Sahoo worked on the droop controller part of the research work. The co-authors, Dr. Hendra I. Nurdin (joint supervisor), Associate Professor Jayashri Ravishankar (PhD supervisor of the co-author Mr. Animesh K. Sahoo) and Professor John E. Fletcher (primary supervisor) supervised the research work.

capability, step change in load, and dynamic response of the system are considered. It is demonstrated that on turning-ON the virtual oscillator-controlled inverter, it synchronises with the droop-controlled inverter, and shares the power proportionally. Further, the design trade-off between the dynamic response and harmonic distortion present in the system is also demonstrated. Simulation results show that the reduction of harmonic content present in the output of VO-controlled inverters, results in reduced harmonic circulating currents. However, this is achieved at the cost of slower transient response.

The chapter is organised as follows. In Section 7.2, a system consisting of two parallel-connected inverters with heterogeneous control techniques is described. In Section 7.3, detailed modelling of both the droop-controlled inverter and virtual oscillator-controlled inverter is presented. In Section 7.4, simulation results are presented for power sharing, transient response and harmonic distortion present in the system. In Section 7.5, possible future work is discussed and a conclusion is drawn.

7.2 System Description

A system consisting of two three-phase inverters operating in parallel with heterogeneous control techniques is considered, as shown in Fig. 7.1. One inverter is droop-controlled and the other is virtual oscillator-controlled. An LCL filter is used at the output of each inverter. The $z_f = R_f + \jmath\omega^* L_f$, $z_g = R_g + \jmath\omega^* L_g$ and $z_C = R_C + \frac{1}{\jmath\omega^* C_f}$ denote the LCL filter impedances, where ω^* denotes the fundamental grid frequency. The line impedance is denoted by $z_l = R_l + \jmath\omega^* L_l$. The inverters are connected to a common RL load $z_L = R_L + \jmath\omega^* L_L$ at the point of common coupling (PCC). In the case of the droop-controlled inverter, outer power and inner voltage/current control loops are used, whereas in the case of the virtual oscillator-controlled inverter, only inner voltage/current control loops are used (as

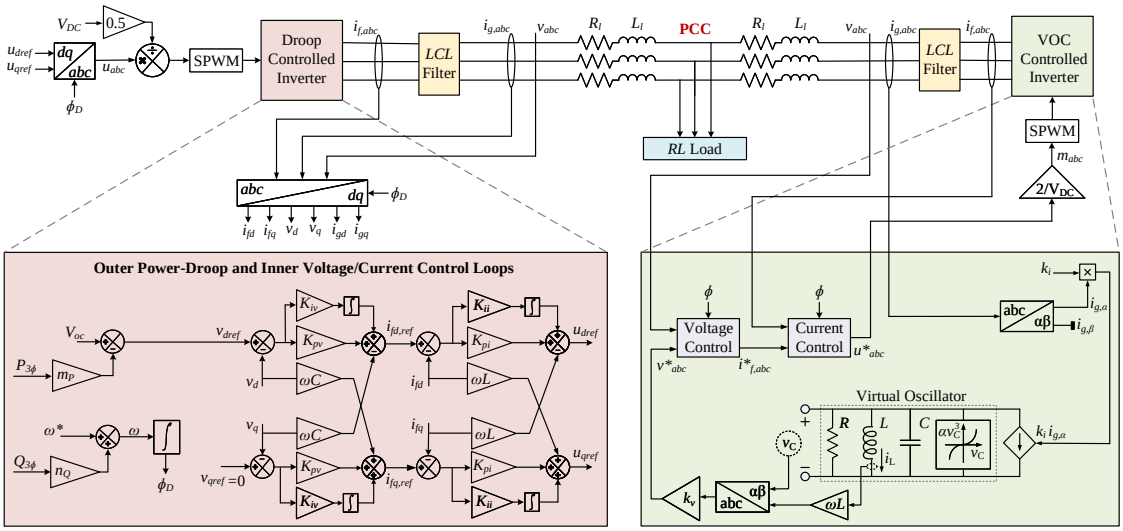

Figure 7.1: A system consisting of two parallel-connected three-phase inverters with heterogeneous control techniques: (i) a droop-controlled inverter and (ii) a virtual oscillator-controlled inverter. The inverters are connected to an RL load z_L at the point of common coupling (PCC) through line impedance $z_l = R_l + \jmath\omega^* L_l$. Inner voltage/current control loops are used for both the inverters.

proposed in Chapter 6) to compensate for the effects of dead-time, semiconductor voltage-drop and inverter side filter inductor voltage-drop.

7.3 System Modelling

This section briefly describes both the droop controller and virtual oscillator controller used to control the inverters.

7.3.1 Virtual Oscillator Controller

Recall from Chapter 2, the following differential equations describe the virtual oscillator controller [76]:

$$\begin{aligned}\frac{dV}{dt} &= \frac{\epsilon\omega^*}{\sqrt{2}}\Big(\sigma g\big(\sqrt{2}V\cos(\phi)\big) - k_v k_i i\Big)\cos(\phi),\\ \frac{d\phi}{dt} &= \omega^* - \frac{\epsilon\omega^*}{\sqrt{2}V}\Big(\sigma g\big(\sqrt{2}V\cos(\phi)\big) - k_v k_i i\Big)\sin(\phi),\end{aligned} \tag{7.1}$$

where V is the RMS output voltage magnitude and ϕ is the instantaneous phase angle. Again recalling from Chapter 2, as the VOC design parameter $\epsilon \searrow 0$, the harmonic content present in the VOC output voltage decreases and there is smaller frequency deviation $\Delta\omega$ from the nominal value ω^*. However, as $\epsilon \searrow 0$, the dynamic response becomes slower. In Section 7.4, the effects of ϵ on the transient response and harmonic distortion are discussed. In order to implement the inner voltage and current control loops, the load dependent system frequency ω and instantaneous phase angle ϕ required for the conversion from an *abc* to a *dq* reference frame can be recovered using the actual VOC dynamics (7.1).

7.3.2 Averaged Model of VOC Inverter

Recall from Chapter 2, averaging the actual VOC dynamics (7.1) over an ac-cycle $\frac{2\pi}{\omega^*}$ results in the following averaged VOC model [76]:

$$\frac{d}{dt}\overline{V} = \frac{\sigma}{2C}\left(\overline{V} - \frac{\beta}{2}\overline{V}^3\right) - \frac{k_v k_i}{2C\overline{V}}\overline{P}, \tag{7.2}$$

$$\frac{d}{dt}\overline{\theta} = \omega^* - \omega + \frac{k_v k_i}{2C\overline{V}^2}\overline{Q}, \tag{7.3}$$

where $\overline{P}$ and $\overline{Q}$ are the averaged active and reactive output power of the virtual oscillator-controlled inverter, respectively. The averaged RMS output voltage magnitude is denoted by $\overline{V}$ and $\overline{\theta}$ denotes the phase-offset with respect to wt. The equilibrium points corresponding to the averaged VOC dynamics are reviwed in Chapter 2.

7.3.3 Droop Controller

In the case of a droop-controlled inverter, the active power $P_{3\phi}$ and reactive power $Q_{3\phi}$ are calculated using the *dq*-components of the three-phase inverter output voltage v_{abc} (i.e. v_d and v_q) and current $i_{g,abc}$ (i.e. i_{gd} and i_{gq}), as per *dq*-reference

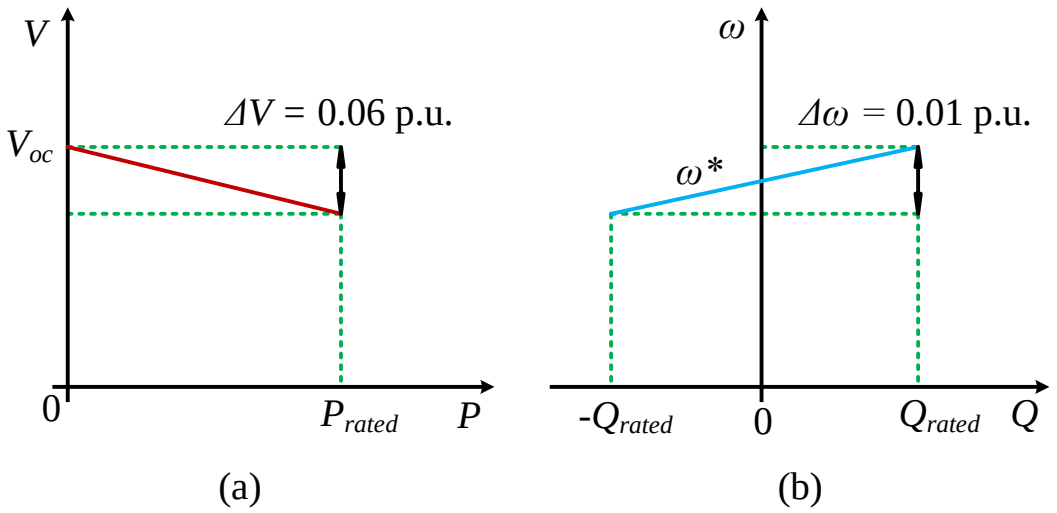

Figure 7.2: The $P-V$ and $Q-\omega$ droop-characteristics for low voltage microgrid.

frame theory. The angle ϕ_D required for the conversion from *abc*-to-*dq* reference frame is obtained using the droop-equations (7.6)-(7.7), which are updated at every switching-cycle as per the load sharing dynamics. The three-phase active and reactive power can be calculated using the Park transformation of three-phase voltage v_{abc} and current $i_{g,abc}$ as follows:

$$P_{3\phi} = 1.5(v_d i_{gd} + v_q i_{gq}), \tag{7.4}$$

$$Q_{3\phi} = 1.5(v_d i_{gq} - v_q i_{gd}). \tag{7.5}$$

In this chapter, the power droop-curves corresponding to a low voltage microgrid are implemented as shown in Fig. 7.2 [122]. The droop-characteristics are given by:

$$\omega = \omega^* + n_Q Q_{3\phi}, \tag{7.6}$$

$$V = V_{oc} - m_P P_{3\phi}, \tag{7.7}$$

where V_{oc} is the open-circuit RMS output voltage magnitude of the droop-controlled inverter. In these equations, the calculated three-phase active and reactive power

demand is shared based on the droop-coefficients i.e. n_Q for reactive power $Q_{3\phi}$ and m_P for active power $P_{3\phi}$.

7.3.4 Discussion

In order to match the droop-characteristics of both the droop-controlled and virtual oscillator-controlled inverters, the droop gains are designed to keep the voltage and frequency deviations within the range of 6% and 1% of their nominal values, respectively, when each inverter is supplying power at the maximum of its rated capacity. It is to be noted that for the three-phase virtual oscillator-controlled inverter, the three-phase output current $i_{g,abc}$ is transformed into the $\alpha\beta$-reference frame (i.e. $i_{g,\alpha\beta}$) and only the $i_{g,\alpha}$ component is fed back to the virtual oscillator controller, as shown in Fig. 7.1. Hence, while designing the VOC parameters to match the embedded droop-characteristics with those of the droop-controlled inverter, single-phase rated active power $\overline{P}_{1\phi,rated}$ and rated reactive power $\overline{Q}_{1\phi,rated}$ should be used. This is in contrast with the droop controller, where we should use the three-phase rated active and reactive power, as in (7.9)-(7.10).

To change the VOC parameter $\epsilon = \sqrt{\frac{L}{C}}$ while keeping the fundamental grid frequency $\omega^* = \frac{1}{\sqrt{LC}}$ constant, the capacitance value C for the virtual oscillator controller needs to be re-designed. The re-designing of the capacitance value C in turn affects the upper bound on the maximum permissible frequency deviation $|\Delta\omega|_{max}$ from the fundamental grid frequency ω^* for the VO-controlled inverter [76]. As a result, it needs the droop-coefficient n_Q for the droop-controlled inverter to be recalculated accordingly. Recall from Section 2.7.3.3, the upper bound on the maximum permissible frequency deviation $|\Delta\omega|_{max}$ for the virtual oscillator-controlled inverter can be determined as follows:

$$|\Delta\omega|_{max} \leq \frac{1}{2C}\frac{\overline{V}_{oc}}{\overline{V}_{min}}\frac{|\overline{Q}_{1\phi,rated}|}{\overline{P}_{1\phi,rated}}, \tag{7.8}$$

where $\overline{V}_{oc}$ denotes the open-circuit RMS output voltage magnitude and $\overline{V}_{min}$ denotes the RMS output voltage magnitude corresponding to the $\overline{P}_{1\phi,rated}$ for the virtual oscillator-controlled inverter. Subsequently, the droop-coefficients n_Q and m_P for the droop-controlled inverter can be determined as follows:

$$n_Q = \frac{|\Delta\omega|_{max}}{Q_{3\phi,rated}}, \tag{7.9}$$

$$m_P = \frac{V_{oc} - V_{min}}{P_{3\phi,rated}}, \tag{7.10}$$

where V_{min} denotes the RMS output voltage magnitude corresponding to the $P_{3\phi,rated}$ for the droop-controlled inverter, as defined in Table 7.1.

7.3.5 Inner Voltage and Current Control Loops

In the cascaded voltage and current controllers for the inverters, both the d-axis and q-axis components are controlled using separate control loops. The capacitor voltage is controlled to ensure high power quality in stand-alone operations of the voltage source inverter. The bandwidth of the voltage control loop is kept between 25% and 75% of the current control loop to have a slower transient response compared to the innermost current control loop. Based on this bandwidth selection criterion, the proportional gain K_{pv} and integral gain K_{iv} for the voltage controller are designed. Similarly, K_{pi} and K_{ii} are the proportional and integral gains used for the current controllers. These two gains are designed based on the bandwidth of the current controller which is chosen as $\frac{1}{20}$ to $\frac{1}{10}$ of the inverter switching frequency [49, 123]. The switching frequency chosen for inverters is 10 kHz. The transient response speed, disturbance rejection capability and stability margin of the closed-loop inverter control decides the bandwidth of the current controller [49]. As in the case of a dq-reference frame, all the components are DC values, the deviation of the measured voltage and current values from their reference values for both the $dq-$axes are tracked using the respective PI controllers. To remove the strong coupling that

Table 7.1: AC Performance Specifications

Symbol	Parameter	Value	Unit
$\overline{V}_{oc}, V_{oc}$	RMS open-circuit voltage	240	V
$\overline{V}_{min}, V_{min}$	RMS rated power voltage	226	V
$\overline{P}_{3\phi,rated}, P_{3\phi,rated}$	Rated active power	5.5	kW
$\lvert\overline{Q}_{3\phi,rated}\rvert, \lvert Q_{3\phi,rated}\rvert$	Rated reactive power	5.5	kVAr
ω^*	Nominal oscillator frequency	$2\pi 50$	rad/s
$\lvert\Delta\omega\rvert_{max}$	Maximum frequency offset	$2\pi 0.5$	rad/s
t_{rise}^{max}	Maximum rise time	0.2	s
$\delta_{3:1}^{max}$	3^{rd} to 1^{st} harmonic ratio	2	%

exists between the d-axis and q-axis components, decoupling terms are added in the corresponding axis for both the voltage and current control loops [7]. The voltage and current control loops are described by the following equations:

$$\begin{aligned}
i_{fd,ref} &= K_{pv}(v_{dref} - v_d) + \int K_{iv}(v_{dref} - v_d)dt - \omega C_f v_q, \\
i_{fq,ref} &= K_{pv}(v_{qref} - v_q) + \int K_{iv}(v_{qref} - v_q)dt + \omega C_f v_d, \\
u_{dref} &= K_{pi}(i_{fd,ref} - i_{fd}) + \int K_{ii}(i_{fd,ref} - i_{fd})dt - \omega L_f i_{fq}, \\
u_{qref} &= K_{pi}(i_{fq,ref} - i_{fq}) + \int K_{ii}(i_{fq,ref} - i_{fq})dt + \omega L_f i_{fd}.
\end{aligned} \tag{7.11}$$

Recall from Chapter 6, the higher bandwidth associated with the VOC (for being a time domain controller) as compared to the conventional outer power-droop control loop, and the non-linear characteristics of VOC, complicate the inner control loops design procedure [85]. Hence, investigating the inner control loops design techniques for virtual oscillator-controlled inverters is possible future work and is not considered in this thesis. In this chapter, for both the droop-controlled and virtual oscillator-controlled inverters, the PI controller gains are determined through trial and error to implement the inner control loops, while achieving an adequate dynamic response.

Table 7.2: System Parameters

Symbol	Parameter	Droop Control	VOC	Unit
k_i	Current feedback gain	-	0.1233	A/A
k_v	Voltage scaling factor	-	240	V/V
σ	Conductance	-	9.3877	Ω^{-1}
α	Cubic-current source coefficient	-	6.2585	A/V^3
L	Virtual oscillator inductance	-	48.248	μH
C	Virtual oscillator capacitance	-	0.21	F
n_Q	Droop coefficient	4.5968×10^{-4}	-	rad/VAr-s
m_P	Droop coefficient	0.0025	-	V/W
K_{pi}	Current proportional gain	1	-	V/A
K_{ii}	Current integral gain	50	-	V/A
K_{pv}	Voltage proportional gain	1	-	A/V
K_{iv}	Volatge integral gain	10	-	A/V
R_f	Filter inductor resistance	0.135	0.135	Ω
L_f	Filter inductance	2.45	2.45	mH
R_g	Filter inductor resistance	0.08	0.08	Ω
L_g	Filter inductance	0.9	0.9	mH
R_C	Filter capacitor resistance	3.3	3.3	Ω
C_f	Filter capacitance	4.7	4.7	μF
R_l	Line resistance	2	2	Ω
L_l	Line inductance	0.1	0.1	mH

7.4 Simulation Results

Simulation results are presented for several scenarios demonstrating the synchronisation capability, load power sharing, transient response and harmonic distortion due to the inherent non-linearity present in the output voltage of the virtual oscillator-controlled inverter. It is observed that for a smaller value of $\epsilon \searrow 0$, the harmonic content reduces in the output of the virtual oscillator-controlled inverter. However, this results in a slower transient response and inverters take a relatively longer time to reach the steady-state. The ac-performance specifications and system parameters are given in Table 7.1 and Table 7.2, respectively. An RL load with $R_L = 50\,\Omega$ and $L_L = 60\,\text{mH}$ is used. The simulations are performed using MATLAB/SIMULINK.

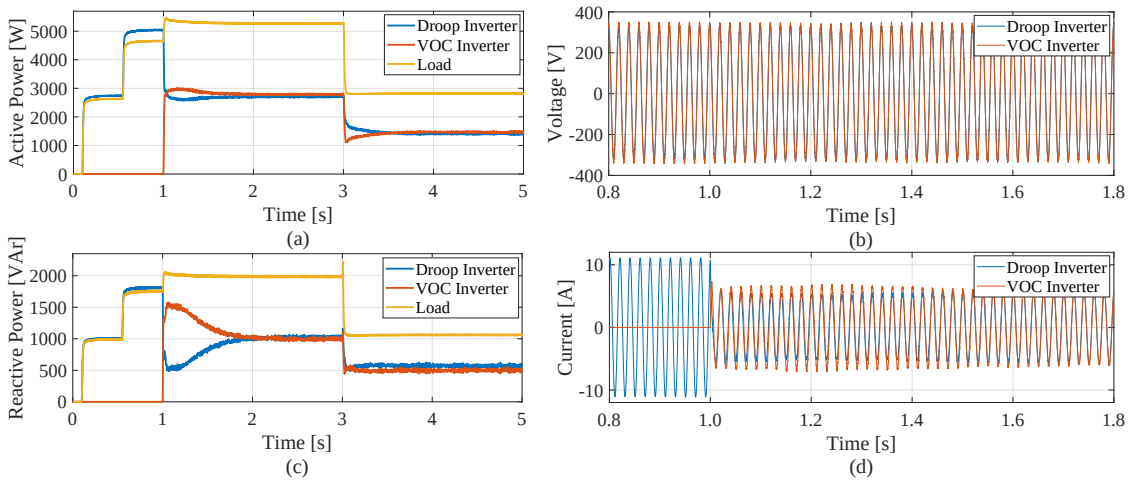

Figure 7.3: Synchronisation and power sharing capability of the virtual oscillator-controlled inverter due to its self-synchronising property for the case $\epsilon' = \epsilon/10$: (a) active power (b) inverter output voltage, (c) reactive power, (d) inverter output current.

Recall from Chapter 2, in order to implement the virtual oscillator controller, the VOC dynamics can be discretised using the trapezoidal rule of integration [76]. The first order low-pass filter with a cut-off frequency of 25 Hz is used to filter out the dq-components of inverter side inductor current $i_{f,abc}$, LCL filter capacitor voltage v_{abc}, and load side filter current $i_{g,abc}$.

7.4.1 Synchronisation Capability

Due to the self-synchronisation property of the VO-controlled inverter, when connected to the system, it synchronises with the droop-controlled inverter. As shown in Fig. 7.3, the droop-controlled inverter is turned ON at $t = 0.1$ s. At $t = 0.55$ s, a step-up change is applied in the load and the droop-controlled inverter is supplying all the load power. At $t = 1.0$ s, the VOC inverter with $\epsilon' = \frac{\epsilon}{10} = \frac{\sqrt{L/C}}{10}$ is connected to the system. It takes around 700 ms for the two inverters to start sharing the power proportionally. At $t = 3$ s, a step-down change is applied in the load and it again takes around 700 ms for the two inverters to start sharing the power proportionally. Through these scenarios, the plug-n-play capability of both the source and load is

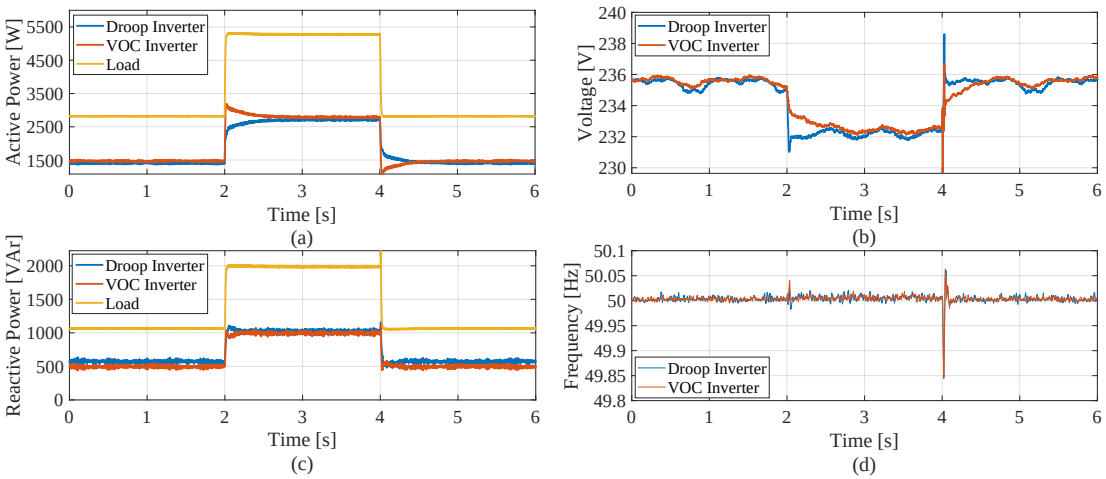

Figure 7.4: Power sharing dynamics in case of parallel-connected droop-controlled and VO-controlled inverters for VOC parameter $\epsilon' = \epsilon/10$: (a) active power (b) RMS output voltage magnitude, (c) reactive power, (d) output frequency.

well demonstrated. A pre-synchronisation circuit, similar to the one discussed in Chapter 2 and presented in [16] is used to synchronise the VOC inverter with the droop-controlled inverter before connecting it with the system. This reduces the transients at the time of connection, as can be seen in Fig. 7.3(d).

7.4.2 Dynamic Response

In Fig. 7.4-7.6, the dynamic response of the system as a function of the VOC parameter ϵ' is presented. The three different cases with $\epsilon' \in \{\epsilon/10, \epsilon/5, \epsilon\}$ are considered. Initially at $t = 0$ s, the two inverters are operating in steady-state and sharing power proportionally. At $t = 2$ s, a step-up change in the load is applied and the load is nearly doubled. Similarly, at $t = 4$ s, at step-down change in the load is applied and the load is halved. From Fig. 7.4-7.6, it can be seen that as $\epsilon' \searrow 0$, the settling time after the step change in load is increased from approximately 50 ms to 700 ms. For the case $\epsilon' = \epsilon = \sqrt{L/C}$, the dynamic response is fastest. In contrast, for the case $\epsilon' = \epsilon/10$, the dynamic response is slowest.

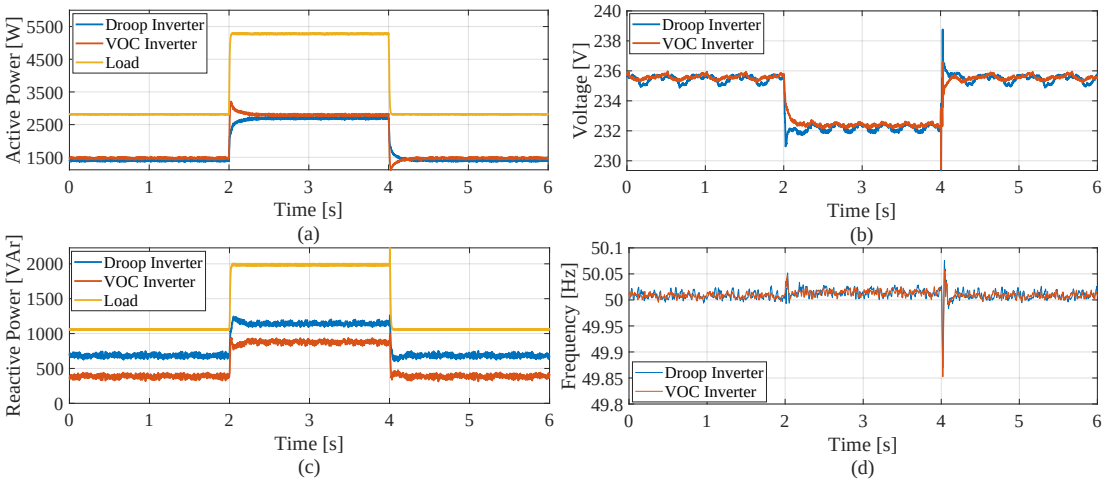

Figure 7.5: Power sharing dynamics in the case of parallel-connected droop-controlled and VO-controlled inverters for VOC parameter $\epsilon' = \epsilon/5$: (a) active power (b) RMS output voltage magnitude, (c) reactive power, (d) output frequency. It can be seen that the dynamic response of the system becomes faster as compared to the case with $\epsilon' = \epsilon/10$. The unequal reactive power sharing is possibly due to the mismatch between the droop-characteristics of two heterogeneously controlled inverters and the design procedure for the droop-coefficient n_Q, as discussed in Section 7.4.4.

7.4.3 Harmonic Distortion

The total harmonic distortion (THD) variation in the Van der Pol oscillator output as a function of ϵ' is demonstrated in this section starting with an inverter modelled as an ideal voltage source. In Fig. 7.8, the harmonic content and THD variations in the output of the VO-controlled inverter as a function of ϵ' are presented for an open-circuit inverter and an inverter connected to an RL load. Note that in both the cases, the harmonic content and THD decrease with the decrease in the value of ϵ' in a consistent (monotonic) manner.

Similarly, the harmonic content and THD variations in the output of the Van der Pol oscillator as a function of ϵ' for switching inverters, is demonstrated in Fig. 7.9 for an open-circuit inverter and an inverter connected to an RL load. Note that compared to the previous case of an inverter modelled as an ideal voltage source, the harmonic content and THD has increased for the switching inverter. Moreover, the decrease in the harmonic content with the decrease in ϵ' is less consistent (non-

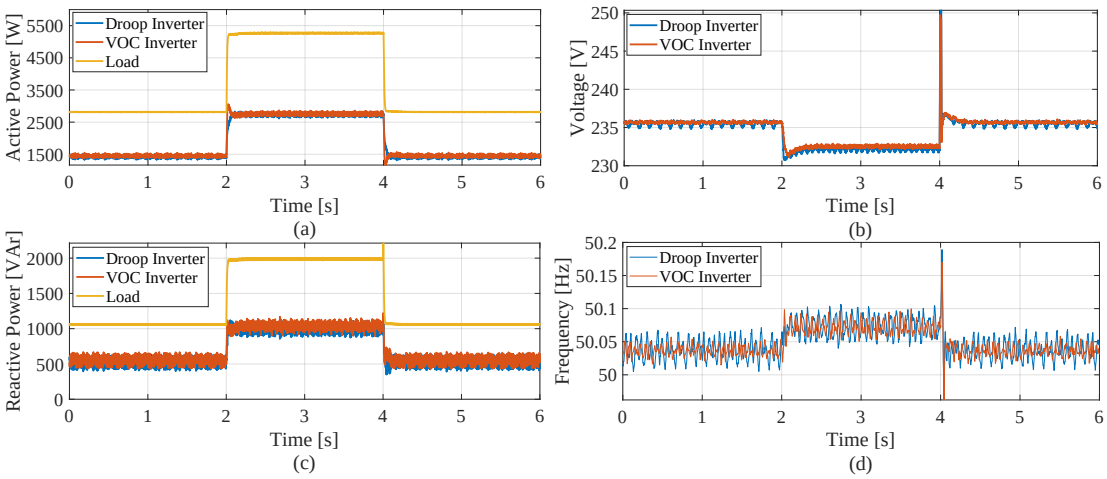

Figure 7.6: Power sharing dynamics in the case of parallel-connected droop-controlled and VO-controlled inverters for VOC parameter $\epsilon' = \epsilon$: (a) active power (b) RMS output voltage magnitude, (c) reactive power, (d) output frequency. The increase in the value of ϵ' results in a fast dynamic response as compared to the other cases at the expense of higher ripple in the output power due to the increased harmonic distortion present in the output of the VO-controlled inverter.

monotonic) compared to the case with an inverter modelled as an ideal voltage source.

So far we have discussed the variations in harmonic content and THD as a function of ϵ' for both the ideal and switching VOC inverters. Finally, the variations in harmonic content and THD for a heterogeneous system of virtual oscillator-controller and droop-controller are demonstrated in Fig. 7.10 for switching inverters. Note that in Fig. 7.10(a) (similar to the case of a switching VO-controlled inverter), the decrease in harmonic content of the virtual oscillator-controlled inverter is not consistent with the decrease in ϵ'. The decrease in harmonic content with ϵ' is non-monotonic and does not improve/become better rapidly. Since they are connected together, the virtual oscillator-controlled inverter also introduces harmonics in the droop-controlled inverter. The corresponding variations in the harmonic content of droop-controlled inverter are presented in Fig. 7.10(b). The harmonic distortion present in the output voltage of the virtual oscillator-controlled inverter increases with the increase in the value of ϵ'. This results in increased harmonic circulating currents flowing between the two inverters. Further, the output currents of the two

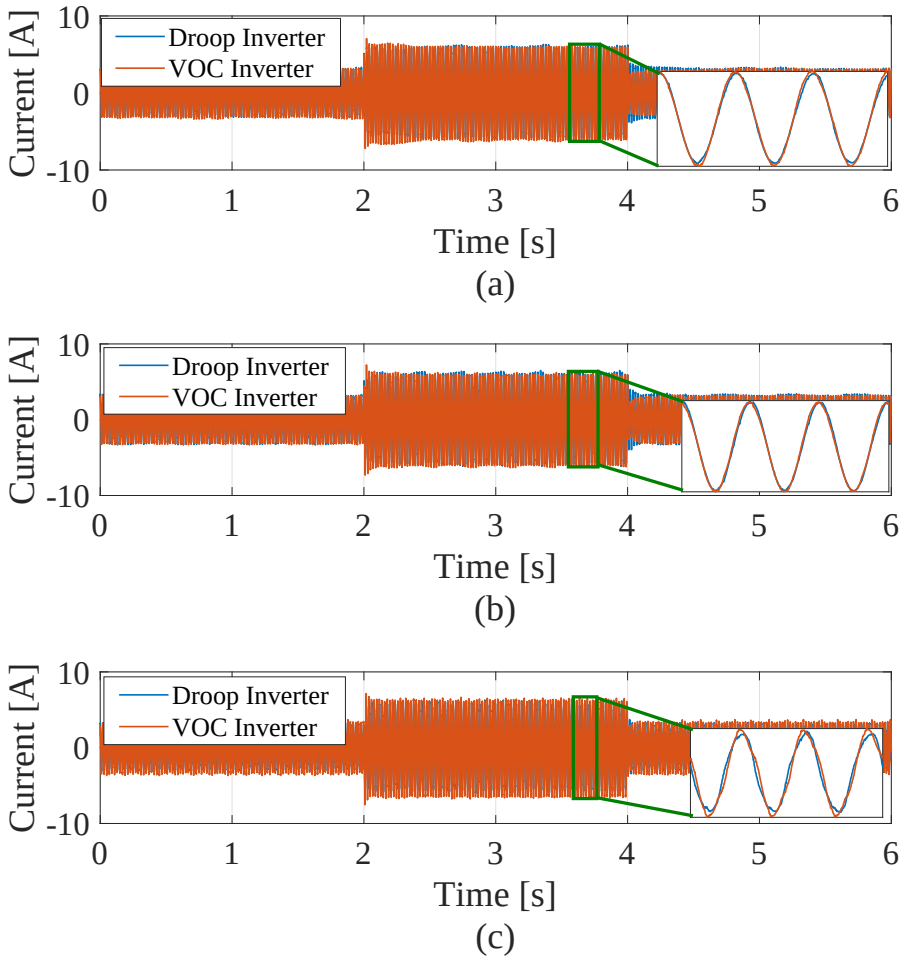

Figure 7.7: Harmonic distortion variations in the inverter output current for parallel-connected droop-controlled and VO-controlled inverters as a function of VOC parameter ϵ': (a) $\epsilon' = \epsilon/10$, (b) $\epsilon' = \epsilon/5$, (c) $\epsilon' = \epsilon$. The harmonic content in the output voltage of the VO-controlled inverter in turn also affects the output voltage of the droop-controlled inverter. This results in two currents being distorted and out of phase.

inverters are no longer sinusoidal as shown in Fig. 7.7. Note that in Fig. 7.4-7.6, there is a ripple in the RMS output voltage magnitude and frequency of the VO-controlled inverter, which in turn induces the same non-linearity in the droop-controlled inverter RMS output voltage magnitude and frequency.

7.4.4 Unequal Reactive Power Sharing

In the case of droop-controlled inverters, unequal reactive power sharing is a known issue. Recall from Chapter 2, a virtual impedance technique to overcome the un-

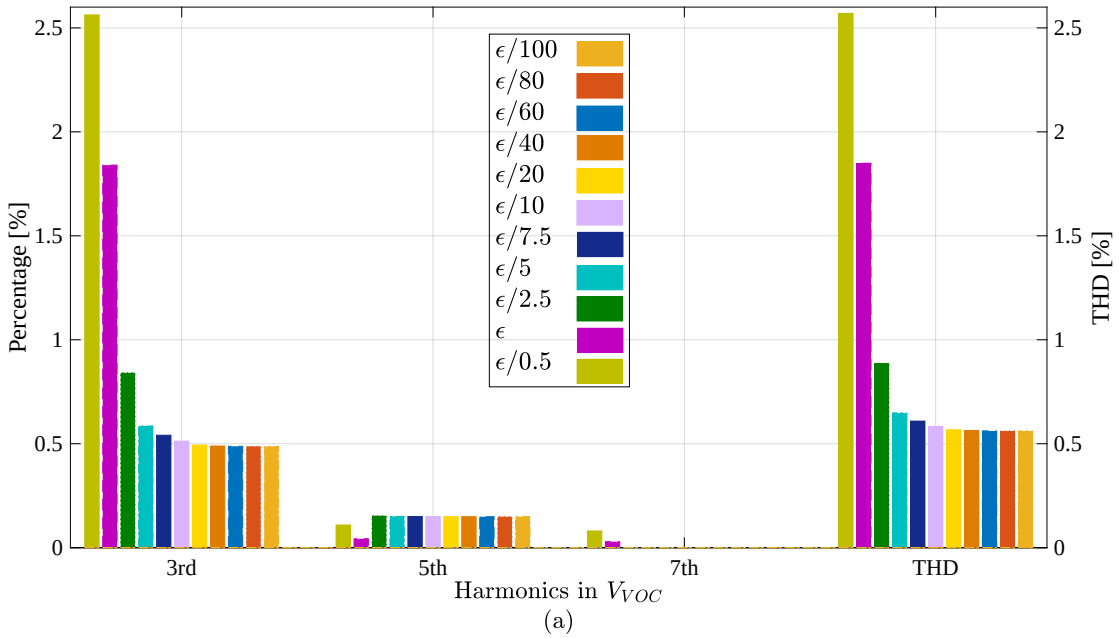

(a)

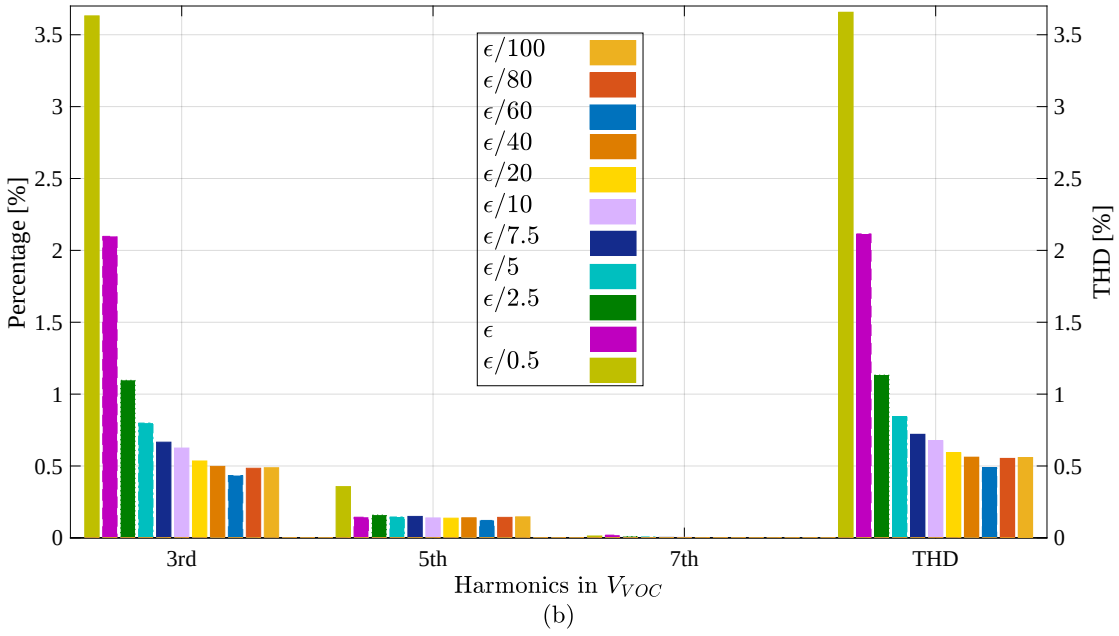

(b)

Figure 7.8: The harmonic content and THD variations as a function of ϵ' for: (a) an open-circuit virtual oscillator-controlled inverter, (b) a virtual oscillator-controlled inverter connected to an RL load. The inverters are modelled as an ideal voltage source. Note that the harmonic distortion in the output voltage of VO-controlled inverter decreases consistently as $\epsilon' \searrow 0$. The THD is computed for the first 10 odd harmonics.

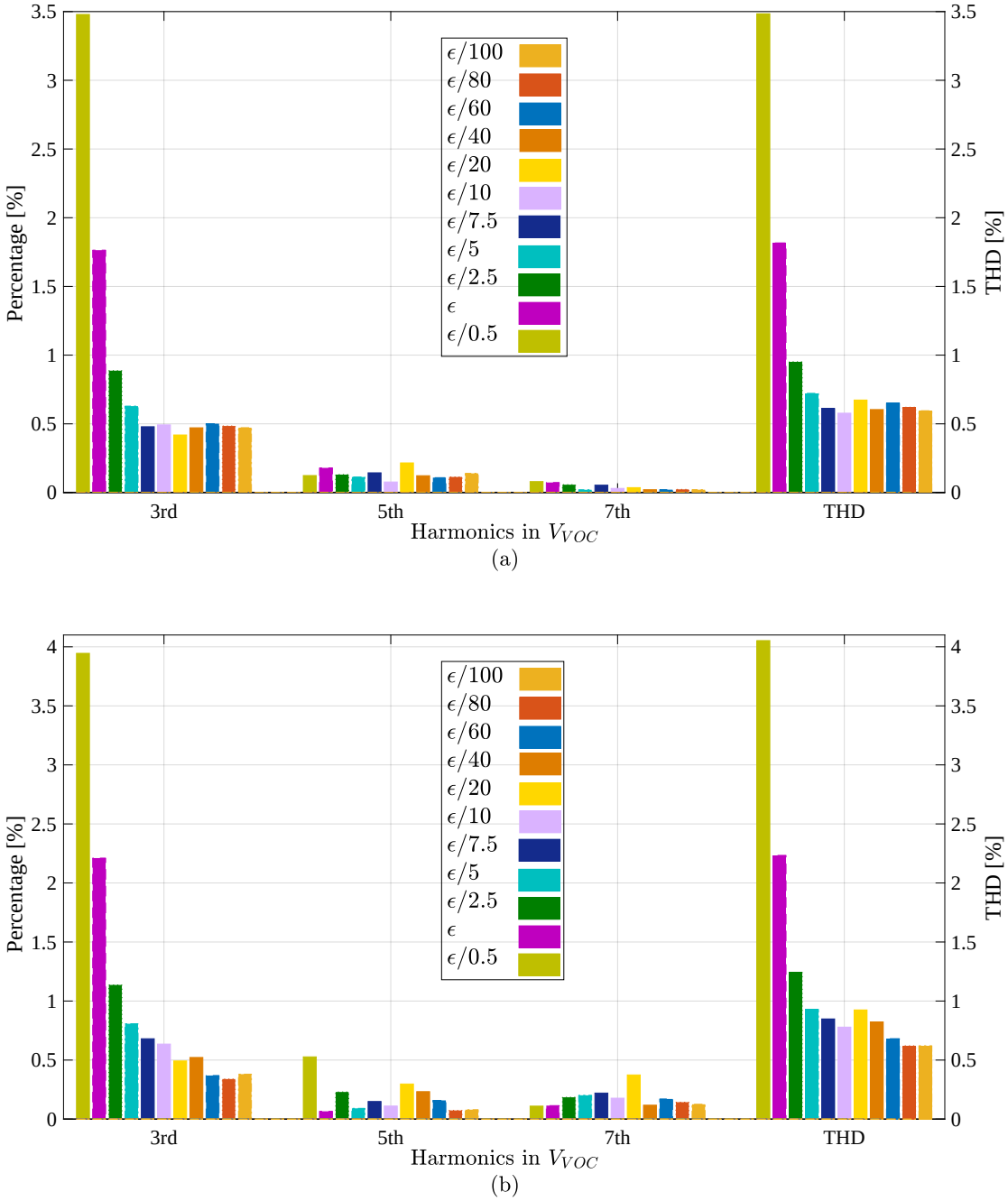

Figure 7.9: The harmonic content and THD variations as a function of ϵ' for: (a) an open-circuit virtual oscillator-controlled switching inverter, (b) a virtual oscillator-controlled switching inverter connected to an RL load. Note that in contrast to the case with inverter modelled as an ideal voltage source, the harmonic distortion in the output voltage of a VO-controlled inverter does not decrease consistently in this case of switching inverters as $\epsilon' \searrow 0$. The THD is computed for the first 10 odd harmonics.

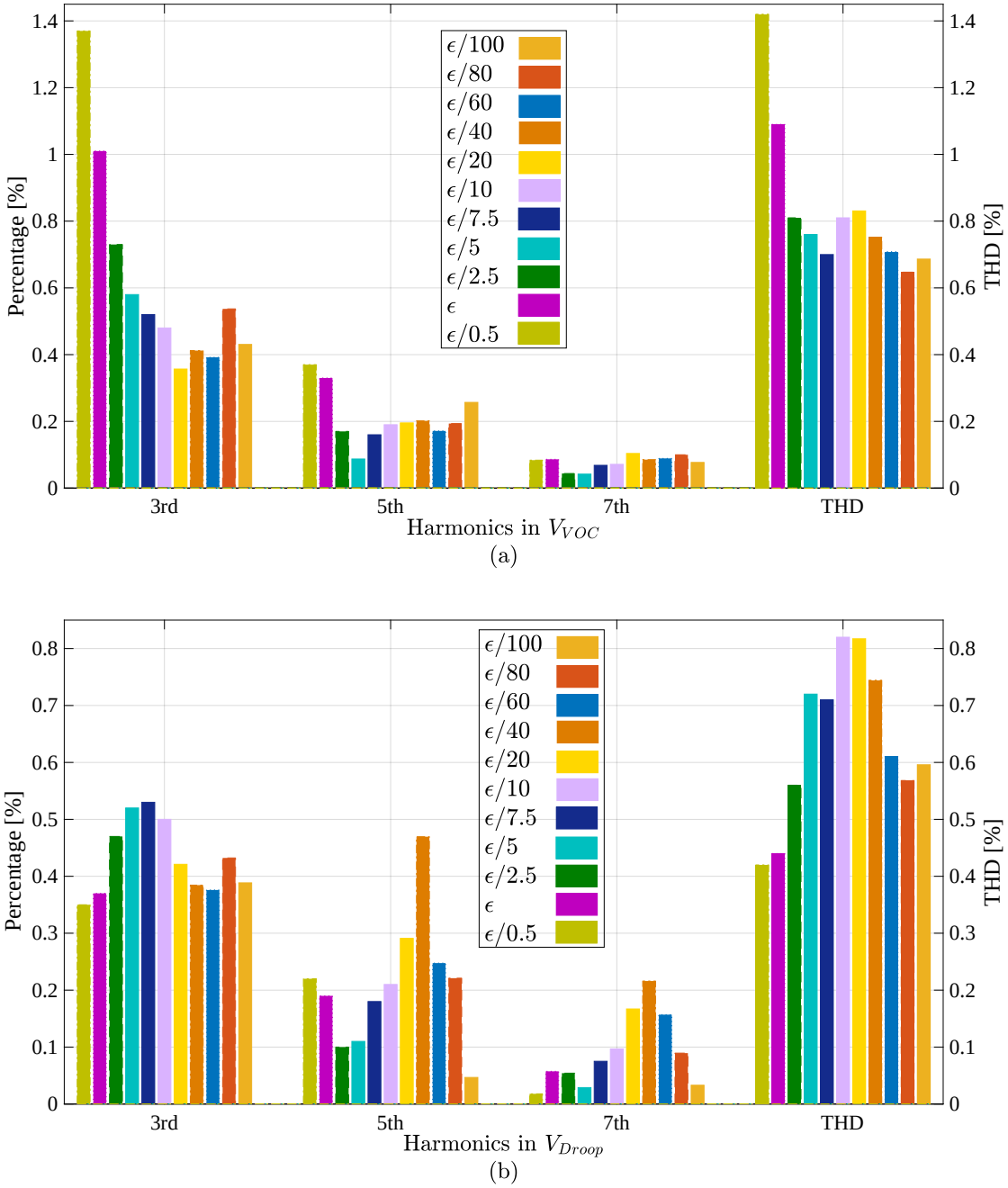

Figure 7.10: The harmonic content and THD variations as a function of ϵ' for a heterogeneous system including: (i) a virtual oscillator-controlled switching inverter, and (ii) a droop-controlled switching inverter. Note that the harmonic distortion in the output voltage of the VO-controlled inverter does not decrease consistently (monotonically) for this heterogeneous system as $\epsilon' \searrow 0$. The THD is computed for the first 10 odd harmonics.

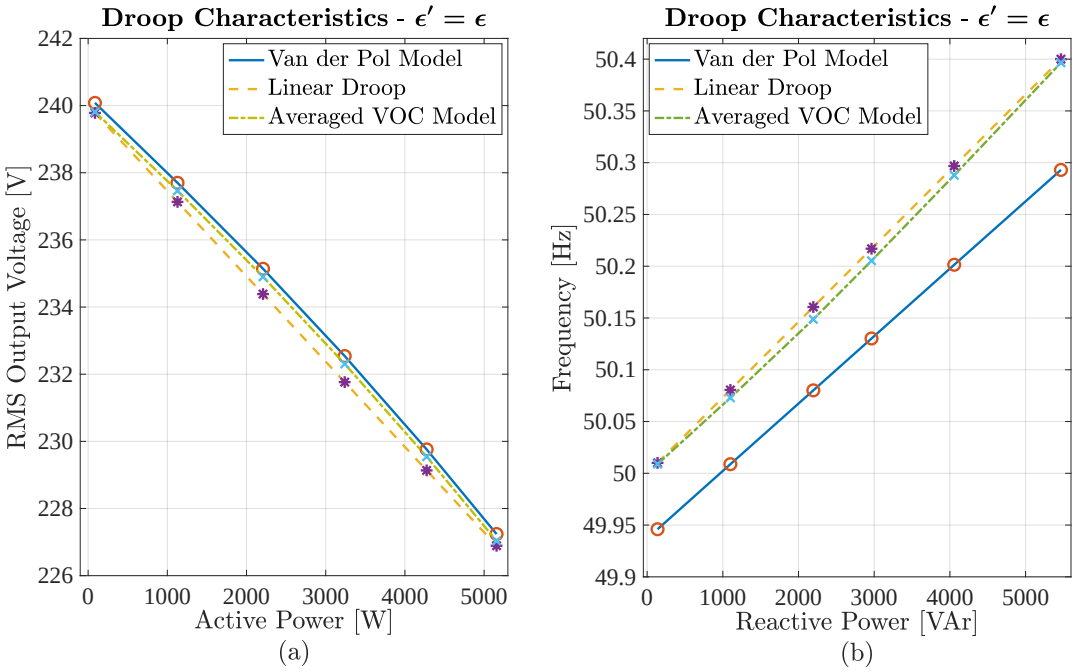

Figure 7.11: The droop-characteristics comparison for the averaged VOC model, Van der Pol oscillator and droop controller for $\epsilon' = \epsilon$.

equal reactive power sharing issue due to the mismatch between the filter and line impedance values for parallel-connected droop-controlled inverters in a microgrid is presented in [66, 67]. Moreover, a robust droop controller to address the reactive power sharing issue for parallel-connected droop-controlled inverters with different per-unit impedance values, is presented in [124].

In contrast to the above known issues of unequal reactive power sharing for droop-controlled inverters, the unequal reactive power sharing in Fig. 7.5 is possibly due to the following reasons, as we have used the same parameters for the filter and line impedances for both heterogeneously controlled inverters in this chapter.

In order to investigate the possible cause of unequal reactive power sharing, the droop-characteristics as a function of $\epsilon' \in \{\epsilon, \epsilon/5, \epsilon/10\}$ are presented in Fig. 7.11-7.13 for the averaged VOC model, Van der Pol oscillator, and droop controller. Note that the droop-characteristics for these three models are not exactly the same.

Considering the $V-P$ droop-characteristics in Fig. 7.11-7.13, the averaged VOC

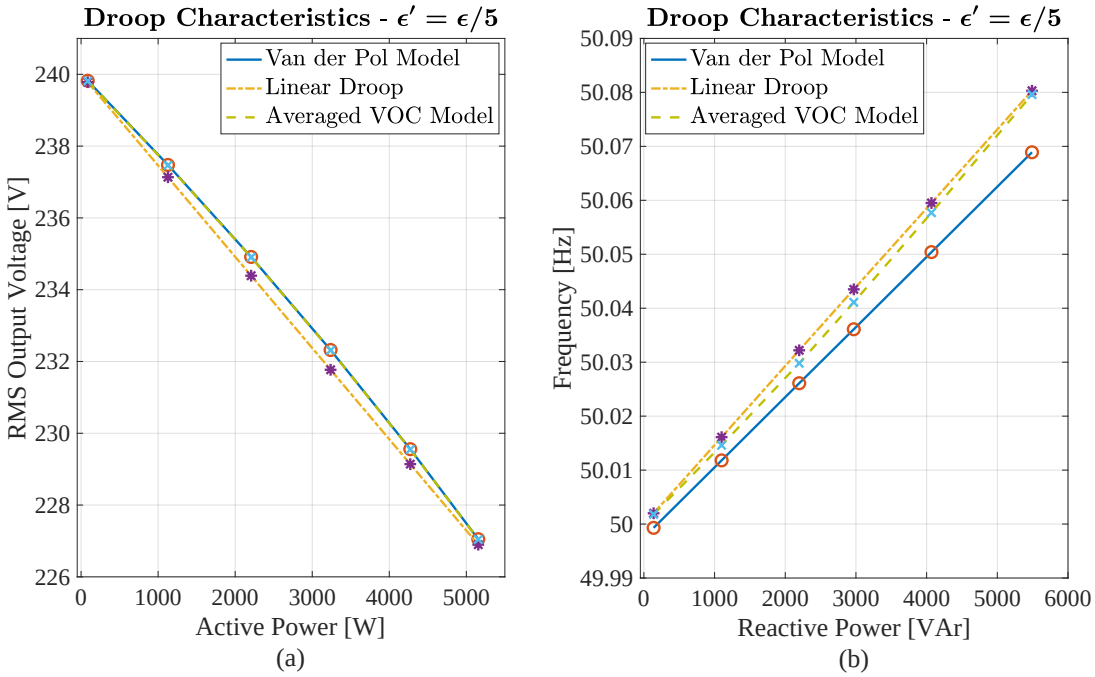

Figure 7.12: The droop-characteristics comparison for the averaged VOC model, Van der Pol oscillator and droop controller for $\epsilon' = \epsilon/5$.

model and Van der Pol model are quite close to each other and start to overlap with the decrease in ϵ'. However, a slight difference is always there between the droop controller and both VOC models (i.e. averaged VOC model and Van der Pol model) even with the decrease in the value of ϵ'.

Similarly, the $\omega - Q$ droop-characteristics are also quite different for the averaged VOC model, Van der Pol oscillator, and droop controller. The difference in the $\omega - Q$ droop-characteristics of the two heterogeneously controlled inverters results in the different steady-state frequency values for a particular reactive power set-point. Therefore, it can be a possible reason for unequal reactive power sharing between the two heterogeneously controlled inverters.

In addition to the above mentioned possible reason for unequal reactive power sharing, another reason could be the design procedure for the droop-coefficient n_Q in (7.9). Recall from Chapter 2 and (7.8), the $|\Delta\omega|_{max}$ only provides an upper bound on the maximum frequency deviation from the nominal value ω^* and the virtual oscillator-controlled inverter may not reach this maximum allowable frequency de-

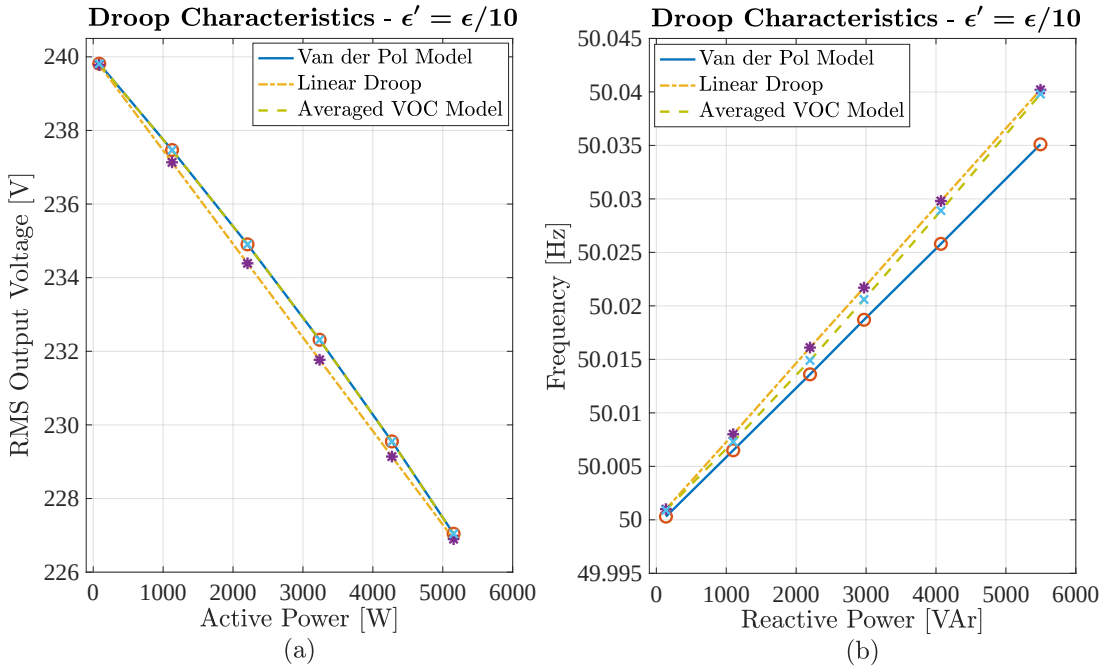

Figure 7.13: The droop-characteristics comparison for an averaged VOC model, Van der Pol oscillator and droop controller for $\epsilon' = \epsilon/10$.

viation, even when supplying the rated reactive power. Hence, the n_Q in (7.9) is designed based on an upper bound on the maximum frequency deviation instead of an exact value specified by the ac-performance specifications. This can result in a mismatch between the $\omega - Q$ droop-characteristics of the two heterogeneously controlled inverters and subsequently lead to unequal reactive power sharing.

Validating the above-mentioned possible causes of unequal reactive power sharing through theoretical/analytical analysis and investigating other possible reasons for unequal reactive power sharing in the case of heterogeneously controlled inverters, is a direction for possible future work and is not pursued in this thesis.

7.5 Conclusion and Future Directions

Power sharing dynamics for two parallel-connected inverters with heterogeneous control techniques including: (i) droop control and (ii) virtual oscillator control are considered in this chapter. By properly designing the droop-coefficients and VOC

parameters, proportional power sharing between the two inverters can be achieved. The dynamic response of the two inverters for a step change in load is demonstrated. Further, the impact of VOC design parameter ϵ on the transient response and steady-state behaviour is considered. It is observed that for $\epsilon \searrow 0$, the harmonic content present in the output of VO-controlled inverters decreases. This results in lower harmonic circulating currents between the two inverters. On the other hand, the dynamic response of the system becomes slower as $\epsilon \searrow 0$. The synchronisation and power sharing capability of the VO-controlled inverter due to its self-synchronising property, is also demonstrated. As the inverters are parallel-connected, the harmonic distortion present in the output of a VO-controlled inverter also affects the output voltage of a droop-controlled inverter. The third harmonic component in the output voltage varies significantly for both the VO-controlled and droop-controlled inverters, as a function of VOC design parameter ϵ. A systematic design approach for the droop-coefficients and VOC parameters to avoid power mismatch during steady-state due to the non-linear droop-characteristics of the VO-controlled inverter (as compared to the linear droop-characteristics of the droop-controlled inverter) and experimentally validating the parallel operation of two heterogeneously controlled inverters, is an avenue for future work.

Chapter 8

Conclusion and Future Directions

The research work presented in this thesis proposed a dispatchable inverter control technique to simultaneously regulate both the active and reactive output power of multiple parallel-connected virtual oscillator-controlled inverters in an islanded microgrid. Moreover, power security constraints were proposed to identify the feasible operating region. Control laws were derived to determine the control inputs for each dispatchable inverter corresponding to the desired set-points for active and reactive power.

In order to address inverters with current feedback after the output LC/LCL filter (as is the case with most practical inverters), a new version of averaged virtual oscillator dynamics was derived, and the proposed power dispatch technique was extended to this new version of averaged VOC dynamics.

Inner voltage and current control loops were proposed to compensate for the inverter non-linearities, including voltage loss/gain at each switching cycle due to the dead-time, semi-conductor voltage-drop, and inverter side filter inductor voltage-drop.

Finally, a system of heterogeneously controlled inverters was investigated, and proportional power sharing was demonstrated between i) a droop-controlled inverter

and ii) a virtual oscillator-controlled inverter.

The main motivations behind the proposed research work in this thesis were to enable better energy source utilisation, increased efficiency, reduced line losses and stress on the distribution network. The increased penetration of renewable energy sources into the power system has raised the need for dispatchable inverter control techniques.

8.1 Conclusion

The main conclusions drawn from the reported research work in this thesis are as follows.

8.1.1 Power Dispatch of Islanded Virtual Oscillator Controlled Inverters

In Chapter 3, a power dispatch technique was presented to regulate the output power of an islanded virtual oscillator-controlled inverter connected to an RL load. The output power regulation was achieved by using a PI controller that tuned the current feedback gain according to the desired power set-point. The system's stability was analysed using the system linearisation and eigenvalues analysis, and constraints were identified on the system parameters. Moreover, the global stability of the system was investigated using the sum-of-squares technique for a particular power set-point. The conclusion drawn is as follows.

1. The output power regulation of an islanded virtual oscillator-controlled inverter can be achieved by tuning the current feedback gain. In the case of an islanded (single) virtual oscillator-controlled inverter connected to a fixed impedance RL load, either active power or reactive power regulation can be

achieved at any one time. Simultaneous regulation of both the active and reactive output power cannot be achieved in this case as the only control variable is the output voltage magnitude, and the phase angle does not play a role in this case.

2. The parametric constraints derived using the system linearisation and eigenvalue analysis ensure the local stability of the system under parametric variations that satisfy these constraints.

8.1.2 Dispatchable Inverter Control Technique for Parallel-Connected Virtual Oscillator-Controlled Inverters

A dispatchable inverter control technique to simultaneously regulate both the active and reactive output power of multiple parallel-connected single-phase virtual oscillator-controlled inverters was proposed in Chapter 4. The simultaneous regulation of both the active and reactive output power was achieved by using two PI controllers for each dispatchable inverter. The PI controllers tuned the voltage and current gains of the virtual oscillator-controlled inverter. A line and filter parameter design procedure was discussed to enable the non-dispatched inverters to share the remaining load demand proportional to their power ratings. The main conclusion is given below.

1. The virtual oscillator-controlled inverters can be dispatched by using the proposed power dispatch technique. The dispatched inverters effectively track both the desired active and reactive power set-points. The voltage and current gains tuning is achieved by using two PI controllers for each dispatchable inverter.

2. The non-dispatchable inverters accurately share the remaining load demand proportional to their power ratings by designing the line and filter parameters

according to the proposed design procedure in Chapter 4.

8.1.3 Feasible Operating Region and Power Security Constraints

In light of the power dispatch techniques proposed in Chapter 3 and Chapter 4, the power security constraints were derived to identify the feasible operating region i.e. the power set-points that can be achieved by a particular dispatchable inverter using the proposed power dispatch technique. Knowledge of the feasible operating region is of crucial importance to plan and optimise the power generation and load flow. Further, the control laws were proposed to determine the control inputs for each dispatchable inverter corresponding to the desired power set-points. An iterative numerical method was developed to solve the load flow analysis, determine the feasible operating region and control inputs corresponding to the desired power set-points. The conclusion drawn is as follows.

1. The proposed power security constraints effectively portray the feasible operating region, and the dispatchable virtual oscillator-controlled inverters can achieve these feasible power set-points by tuning the voltage and current gains.

2. The proposed iterative numerical method can be used to solve the load flow analysis, and determine the voltage magnitude and angle for each bus in the network. This information can then be used to determine the feasible operating region, and control inputs to achieve a particular power set-point.

8.1.4 New Version of Averaged Virtual Oscillator Controller Dynamics for Inverters with Current Feedback after the Output *LC/LCL* Filter

In Chapter 5, a new version of averaged virtual oscillator dynamics was derived for virtual oscillator-controlled inverters with current feedback after the output LC/LCL filter (see Appendix A for a detailed derivation). Moreover, based on this new version of averaged VOC dynamics, a parameter design procedure was proposed to design the VOC parameters according to the desired ac-performance specifications and enable proportional power sharing between the parallel-connected inverters. The proposed power dispatch technique in Chapter 4 was extended to this new version of averaged VOC dynamics, and corresponding power security constraints and control laws were derived. The stability of the high voltage solution of the proposed new version of averaged VOC dynamics was also investigated in Appendix B. The conclusion drawn, follows.

1. The proposed new version of an averaged VOC model predicts the actual VOC (Van der Pol oscillator) dynamics more accurately compared to the existing averaged VOC model for a virtual oscillator-controlled inverter with current feedback after the output LC/LCL filter.

2. The voltage and frequency regulation (according to the desired ac-performance specifications) of the virtual oscillator-controlled inverter with current feedback after the output LC/LCL filter can be achieved by designing the VOC parameters according to the proposed design procedure in Chapter 5. Further, this results in the virtual oscillator-controlled inverters sharing power proportionally.

3. The proposed power security constraint based on this new version of averaged VOC dynamics accurately defines the feasible operating region for a virtual

oscillator-controlled inverter with current feedback after the output LC/LCL filter. The proposed control laws can be used to determine the control inputs for each dispatchable inverter according to the desired power set-points.

4. The high voltage solution for the new averaged VOC dynamics is a stable equilibrium point.

8.1.5 Inner Control Loops to Compensate for Inverter Non-linearities

In order to compensate for the virtual oscillator-controlled inverter non-linearities, including the voltage loss/gain at each switching cycle, semi-conductor voltage drop and inverter side filter inductor voltage-drop, inner voltage and current control loops were proposed in Chapter 6. The instantaneous frequency and phase angle information was recovered from the VOC dynamics, and a phase-locked loop was not required. This helped in avoiding the computations and delays associated with the phase-locked loops, and retaining the fast dynamics of a virtual oscillator controller. The main conclusion is given below.

1. The inner control loops compensate for the virtual oscillator-controlled inverter non-linearities and enable the inverter to closely follow the embedded droop-characteristics designed according to the desired ac-performance specifications.

2. The proposed inner control loops minimise the steady-state offset error in the control inputs between the simulation and experimental results in the case of power dispatch, as discussed earlier in Chapter 4.

3. The proposed inner control loops are validated through experimental results for a number of scenarios, including black-start operation, synchronisation and power sharing capability, and power dispatch.

8.1.6 A System of Heterogeneously Controlled Inverters

In Chapter 7, a heterogenous system of parallel-connected inverters controlled using different types of inverter control techniques was considered. The inverter control techniques included i) droop-control and ii) virtual oscillator control. A parameter design procedure was discussed to enable the heterogeneously controlled inverters to share the power proportionally. Moreover, the effects of VOC design parameter ϵ on the system's harmonic profile and transient response were also considered. The proposed control strategy was validated through simulation results for a number of scenarios demonstrating synchronisation capability, and the dynamic response of the system under source and load transients. The following conclusion is drawn.

1. The heterogeneously controlled inverters can be made to work in parallel and follow the droop-characteristics based on the desired ac-performance specifications by designing the controller parameters as discussed in Chapter 7.

2. The harmonic profile of the overall system mainly depends on the harmonic content present in the output of the virtual oscillator-controlled inverter. The harmonic distortion in the output of the virtual oscillator-controlled inverter can be reduced by making $\epsilon \searrow 0$ at the expense of a slower dynamic response of the overall system.

3. The possible reasons for unequal reactive power sharing include the mismatch between the droop-characteristics of the two heterogeneously controlled inverters and the design procedure of the droop-coefficient n_Q based on the upper bound on the maximum permissible frequency deviation from the nominal value, as discussed in Chapter 7.

8.2 Directions for Future Work

The potential extensions to the research work in this thesis and suggested future directions to be investigated, are as follow.

1. A major aspect of possible future work includes systematic procedure to design the PI controller gains to achieve the desired dynamic behaviour of the dispatchable virtual oscillator-controlled inverters. Recall from Chapter 3 and Chapter 4, the PI controllers were used to tune the voltage and current gains according to the desired set-points for active and reactive power for each dispatchable inverter.

2. Although the proposed dispatchable inverter control technique was developed considering the frequency synchronisation conditions for the virtual oscillator-controlled inverters (recall Remark 4.1) and was validated through the experimental results as in Section 4.7, an explicit analytical analysis to prove the synchronisation of virtual oscillator-controlled inverters (employing the proposed dispatchable inverter control technique) and identifying the corresponding synchronisation conditions, can be considered as potential future work.

3. Another major aspect of possible future work includes investigating the global stability analysis of a generalised system consisting of m-controlled and n-uncontrolled parallel-connected VOC inverters as discussed in Chapter 4. Moreover, in the context of an evolving power system, the online evaluation of stability margins and stability conditions without having access to the detailed model of the system can be pursued as future work. Recent literature on the online stability analysis of the power system can be found in [125–129].

4. A potential avenue for future work includes Investigating a dispatchable inverter control structure or improving the proposed dispatchable inverter control technique such that a decoupled active and reactive power control can be

achieved.

5. A bandwidth selection criterion can be investigated for inner voltage and current control loops proposed in Chapter 6 when the external (relatively slower) power-droop control loop is replaced by a (relatively faster) virtual oscillator control loop. Moreover, small-signal stability analysis and determining the stability margins for a system of VO-controlled inverters with inner voltage and current control loops can be investigated.

6. Recall from Chapter 2, the change of modelling perspective from averaged to instantaneous results in a complex non-linear VOC model with nearly sinusoidal periodic trajectories that are hard to analyse and requires a deeper and challenging mathematical analysis. In-depth analysis using the instantaneous model to get more insight into the time-domain properties of the VOC is potential future work.

7. An analysis characterising and comparing the behaviour of non-linear droop-control and VOC can be considered as future work.

8. Investigating the operation of VO-controlled inverters under non-linear loads or connected to the bus with background harmonics is potential future work.

Appendix A

Derivation of the Averaged VOC Model with an Output LCL Filter

Consider an inverter with current feedback after the output LC/LCL filter, as shown in Fig. 5.1. Let us denote a phasor associated with a time domain variable (.) by $\overrightarrow{(.)}$. The $\overrightarrow{V}$ denotes the voltage before the output LC/LCL filter, the $\overrightarrow{V_o}$ denotes the filter capacitor voltage and the $\overrightarrow{V_g}$ denotes the voltage after the output LC/LCL filter. Similarly, the $\overrightarrow{I_f}$ denotes the current flowing through the filter inductor L_f, the $\overrightarrow{I_c}$ denotes the filter capacitor current and the $\overrightarrow{I_g}$ is the current flowing through the filter inductor L_g. Solving the network equations, we have:

$$\overrightarrow{I_f} = \overrightarrow{I_c} + \overrightarrow{I_g} = \frac{\overrightarrow{V_o}}{z_c} + \overrightarrow{I_g}. \tag{A.1}$$

Replacing $\overrightarrow{V_o} = \overrightarrow{V} - \overrightarrow{I_f} z_f$, we get:

$$\overrightarrow{I_g} = \begin{bmatrix} Z_\alpha \angle\theta_\alpha & Z_\beta \angle\theta_\beta \end{bmatrix} \begin{bmatrix} \overrightarrow{I_f} \\ \overrightarrow{V} \end{bmatrix}, \tag{A.2}$$

where $z_\alpha = R_\alpha + \jmath X_\alpha = Z_\alpha \angle\theta_\alpha = \frac{z_c+z_f}{z_c}$ and $z_\beta = R_\beta + \jmath X_\beta = Z_\beta \angle\theta_\beta = \frac{-1}{z_c}$ are the impedance constants defined at ω^*. Further, we have [76]:

$$\frac{d}{dt}\phi = \omega^* + \frac{d}{dt}\theta^* = \omega + \frac{d}{dt}\theta, \tag{A.3}$$

where the instantaneous phase angle is denoted by ϕ, the nominal grid frequency is denoted by ω^* and the load dependent steady-state frequency is denoted by ω. The angles θ^* and θ denote the phase offset with respect to $\omega^* t$ and ωt, respectively. The inverter output voltage is given by:

$$v(t) = \sqrt{2}V(t)\cos\left(\omega^* t + \theta^*(t)\right). \tag{A.4}$$

The instantaneous active and reactive output power of the inverter in terms of $v(t)$ and $i(t)$ is given by:

$$P(t) = v(t)i(t), \qquad Q(t) = v\left(t - \frac{\pi}{2}\right)i(t). \tag{A.5}$$

The averaged active and reactive power over an ac-cycle $\frac{2\pi}{\omega^*}$ is defined as:

$$\overline{P}(t) = \frac{\omega^*}{2\pi}\int_{s=t}^{t+2\pi/\omega^*} P(s)ds, \qquad \overline{Q}(t) = \frac{\omega^*}{2\pi}\int_{s=t}^{t+2\pi/\omega^*} Q(s)ds. \tag{A.6}$$

In order to derive the averaged VOC dynamics (5.2)-(5.3), a change of variable is made from $t \to \tau = \omega^* t$ and $\theta^*(\tau) = \phi(\tau/\omega^*) - \tau$. Expressing the actual VOC dynamics (5.1) as a function of θ^*, we have [76]:

$$\begin{aligned}
\frac{dV}{d\tau} &= \frac{\epsilon}{\sqrt{2}}\Big(\sigma g\big(\sqrt{2}V\cos\left(\tau+\theta^*\right)\big) - k_v k_i i\Big)\cos\left(\tau+\theta^*\right),\\
\frac{d\theta^*}{d\tau} &= -\frac{\epsilon}{\sqrt{2}V}\Big(\sigma g\big(\sqrt{2}V\cos\left(\tau+\theta^*\right)\big) - k_v k_i i\Big)\sin\left(\tau+\theta^*\right).
\end{aligned} \tag{A.7}$$

The dynamics in (A.7) are 2π periodic functions in τ. The averaged dynamics in the quasi-harmonic limit $\epsilon \searrow 0$ (following [76, Eq. 12]) are given by:

$$\begin{aligned}\begin{bmatrix} \dot{\overline{V}} \\ \dot{\overline{\theta}}^* \end{bmatrix} &= \frac{\epsilon\sigma}{2\pi\sqrt{2}} \int_0^{2\pi} g\left(\sqrt{2}\overline{V}\cos\left(\tau+\overline{\theta}^*\right)\right) \begin{bmatrix} \cos\left(\tau+\overline{\theta}^*\right) \\ \frac{-1}{\overline{V}}\sin\left(\tau+\overline{\theta}^*\right) \end{bmatrix} d\tau \\ &\qquad - \frac{\epsilon k_v k_i}{2\pi\sqrt{2}} \int_0^{2\pi} i \begin{bmatrix} \cos\left(\tau+\overline{\theta}^*\right) \\ \frac{-1}{\overline{V}}\sin\left(\tau+\overline{\theta}^*\right) \end{bmatrix} d\tau, \\ &= \frac{\epsilon\sigma}{2} \begin{bmatrix} \overline{V} - \frac{\beta}{2}\overline{V}^3 \\ 0 \end{bmatrix} - \frac{\epsilon k_v k_i}{2\pi\sqrt{2}} \int_0^{2\pi} i \begin{bmatrix} \cos\left(\tau+\overline{\theta}^*\right) \\ \frac{-1}{\overline{V}}\sin\left(\tau+\overline{\theta}^*\right) \end{bmatrix} d\tau. \end{aligned} \tag{A.8}$$

Changing the coordinates from τ to t in (A.8) and keeping the $\mathcal{O}(\epsilon)$ terms only, we have:

$$\frac{d}{dt}\begin{bmatrix} \overline{V} \\ \overline{\theta}^* \end{bmatrix} = \frac{\sigma}{2C} \begin{bmatrix} \overline{V} - \frac{\beta}{2}\overline{V}^3 \\ 0 \end{bmatrix} - \frac{k_v k_i \omega^*}{2\pi\sqrt{2}C} \int_0^{\frac{2\pi}{\omega^*}} i(t) \begin{bmatrix} \cos\left(\omega^* t+\overline{\theta}^*\right) \\ \frac{-1}{\overline{V}}\sin\left(\omega^* t+\overline{\theta}^*\right) \end{bmatrix} dt. \tag{A.9}$$

Let us define the impedance constants $C_\alpha = Z_\alpha \cos\theta_\alpha$, $C_\beta = Z_\beta \cos\theta_\beta$, $S_\alpha = Z_\alpha \sin\theta_\alpha$ and $S_\beta = Z_\beta \sin\theta_\beta$. The current $i = \sqrt{2} I \cos\left(\omega^* t + \theta_i^*\right)$ where I is the RMS current magnitude and θ_i^* is the phase-offset with respect to $\omega^* t$. Let $\overrightarrow{I_g}^{\Re}$ denotes the real part of the current $\overrightarrow{I_g}$ and according to (A.2) is given by:

$$\overrightarrow{I_g}^{\Re} = \Re\{\overrightarrow{I_g}\} = \sqrt{2}\left(Z_\alpha I \cos\left(\omega^* t + \theta_i^* + \theta_\alpha\right) + Z_\beta V \cos\left(\omega^* t + \theta^* + \theta_\beta\right)\right). \tag{A.10}$$

In order to derive the averaged VOC model, the current $i = i_g$ is replaced by its real part $\overrightarrow{I_g}^{\Re}$ in (A.9), we get:

$$\frac{d}{dt}\begin{bmatrix}\overline{V}\\ \overline{\theta}^*\end{bmatrix} = \frac{\sigma}{2C}\begin{bmatrix}\overline{V}-\frac{\beta}{2}\overline{V}^3\\ 0\end{bmatrix} - \frac{k_v k_i \omega^*}{4\pi C}\int_0^{\frac{2\pi}{\omega^*}}\begin{bmatrix}\frac{Z_\alpha}{\overline{V}}\sqrt{2}V(t)\cos(\omega^* t+\theta^*)\sqrt{2}I(t)\cos(\omega^* t+\theta_i^*+\theta_\alpha)\\ \frac{-Z_\alpha}{\overline{V}^2}\sqrt{2}V(t)\sin(\omega^* t+\theta^*)\sqrt{2}I(t)\cos(\omega^* t+\theta_i^*+\theta_\alpha)\end{bmatrix} + \begin{bmatrix}+2Z_\beta\overline{V}\cos(\omega^* t+\theta^*+\theta_\beta)\cos(\omega^* t+\theta^*)\\ -2Z_\beta\cos(\omega^* t+\theta^*+\theta_\beta)\sin(\omega^* t+\theta^*)\end{bmatrix} dt. \tag{A.11}$$

Using the trigonometric identities and definition of instantaneous active and reactive power (A.5), we get:

$$\frac{d}{dt}\begin{bmatrix}\overline{V}\\ \overline{\theta}^*\end{bmatrix} = \frac{\sigma}{2C}\begin{bmatrix}\overline{V}-\frac{\beta}{2}\overline{V}^3\\ 0\end{bmatrix} - \frac{k_v k_i \omega^*}{4\pi C}\int_0^{\frac{2\pi}{\omega^*}}\begin{bmatrix}\frac{1}{\overline{V}}\left(C_\alpha P(t)+S_\alpha Q(t)\right)+Z_\beta\overline{V}\left(\cos\theta_\beta+\cos\left(2\omega^* t+2\theta^*+\theta_\beta\right)\right)\\ \frac{-1}{\overline{V}^2}\left(C_\alpha Q(t)-S_\alpha P(t)\right)-Z_\beta\left(\sin\left(2\omega^* t+2\theta^*+\theta_\beta\right)-\sin\theta_\beta\right)\end{bmatrix} dt. \tag{A.12}$$

The averaged VOC dynamics (5.2)-(5.3) are recovered by evaluating the integral in (A.12) and using (A.3) as follows:

$$\frac{d}{dt}\overline{V} = \frac{\sigma}{2C}\left(\overline{V}-\frac{\beta}{2}\overline{V}^3\right) - \frac{k_v k_i}{2C}\left(\frac{C_\alpha\overline{P}}{\overline{V}}+\frac{S_\alpha\overline{Q}}{\overline{V}}+C_\beta\overline{V}\right), \tag{A.13}$$

$$\frac{d}{dt}\overline{\theta} = \omega^*-\omega+\frac{k_v k_i}{2C}\left(\frac{C_\alpha\overline{Q}}{\overline{V}^2}-\frac{S_\alpha\overline{P}}{\overline{V}^2}-S_\beta\right). \tag{A.14}$$

Appendix B

Stability of the High Voltage Solution

The small-signal stability analysis of the high voltage equilibrium solution to (5.22) is considered in this appendix. It is demonstrated that the high voltage root in (5.26) is locally asymptotically stable by analysing the linearised averaged VOC dynamics around the equilibrium point. The dependence of active and reactive power on the averaged RMS voltage magnitude and phase dynamics can be expressed as $\overline{P}_\gamma := p_\gamma(\overline{V}, \overline{\theta})$ and $\overline{Q}_\gamma := q_\gamma(\overline{V}, \overline{\theta})$, respectively. Linearising the averaged VOC dynamics (5.22) and (5.23) around the equilibrium point $(\overline{V}_{eq}, \overline{\theta}_{eq})$, we get the following Jacobian matrix $J \in \mathbb{R}^{2\times 2}$ with entries as follows:

$$[J]_{1,1} = \frac{\sigma}{2C}\left(1 - \frac{3\beta}{2}\overline{V}^2\right) + \frac{k_v k_i \overline{P}_\gamma}{2C\overline{V}^2} - \frac{k_v k_i}{2C\overline{V}}\frac{\partial \overline{P}_\gamma}{\partial \overline{V}} - \frac{k_v k_i C_\beta}{2C}, \tag{B.1}$$

$$[J]_{1,2} = -\frac{k_v k_i}{2C\overline{V}}\frac{\partial \overline{P}_\gamma}{\partial \overline{\theta}}, \tag{B.2}$$

$$[J]_{2,1} = -\frac{k_v k_i \overline{Q}_\gamma}{C\overline{V}^3} + \frac{k_v k_i}{2C\overline{V}^2}\frac{\partial \overline{Q}_\gamma}{\partial \overline{V}}, \tag{B.3}$$

$$[J]_{2,2} = \frac{k_v k_i}{2C\overline{V}^2}\frac{\partial \overline{Q}_\gamma}{\partial \overline{\theta}}. \tag{B.4}$$

In case of ideal LC/LCL filters with zero equivalent series resistance of inductors and capacitors (i.e. $R_f = R_c = R_g = 0$), the imaginary part of the impedance

constant $z_\alpha = R_\alpha + \jmath X_\alpha$ is zero (i.e. $X_\alpha = 0$). Further, in case of practical LC/LCL filters with small (almost negligible) equivalent series resistance of inductors and capacitors, the imaginary part $X_\alpha \approx 0$. Under this reasonable, practical assumption, (5.19) can be re-written as follows:

$$\begin{bmatrix} P_\gamma \\ Q_\gamma \end{bmatrix} \approx R_\alpha \begin{bmatrix} P \\ Q \end{bmatrix}. \tag{B.5}$$

In order to determine the stability of the non-zero RMS voltage magnitude equilibrium point, the following assumption is made to decouple the linearised dynamics of the averaged RMS voltage magnitude and phase of the virtual oscillator-controlled inverter:

$$\frac{\partial p_\gamma(\overline{V}_{eq}, \overline{\theta}_{eq})}{\partial \overline{\theta}} \approx R_\alpha \frac{\partial p(\overline{V}_{eq}, \overline{\theta}_{eq})}{\partial \overline{\theta}} = 0. \tag{B.6}$$

Note that for low voltage power grids with resistive lines, (B.6) provides a standard power-flow decoupling assumption. Under assumption (B.6), the stability of averaged RMS voltage magnitude dynamics can be guaranteed for the following condition on the entry of the Jacobian matrix:

$$[J]_{1,1} = \frac{\sigma}{2C}\left(1 - \frac{3\beta}{2}\overline{V}^2\right) + \frac{k_v k_i \overline{P}_\gamma}{2C\overline{V}^2} - \frac{k_v k_i}{2C\overline{V}}\frac{\partial \overline{P}_\gamma}{\partial \overline{V}} - \frac{k_v k_i C_\beta}{2C} < 0. \tag{B.7}$$

Let us now consider a particular load with constant averaged power over an ac-cycle; when also satisfying the decoupling assumption in (B.6), we have:

$$\overline{P}_\gamma = p_\gamma(\overline{V}, \overline{\theta}) = \overline{P}_{\gamma,eq}. \tag{B.8}$$

The two possible solutions of the averaged RMS voltage magnitude dynamics (5.22) at equilibrium are given by:

$$\overline{V}_{eq}^{low} = k_v \sqrt{\frac{\sigma_\beta - \sqrt{\sigma_\beta^2 - 6\alpha\,(k_i/k_v)\,\overline{P}_{\gamma,eq}}}{3\alpha}}, \tag{B.9}$$

$$\overline{V}_{eq}^{high} = k_v \sqrt{\frac{\sigma_\beta + \sqrt{\sigma_\beta^2 - 6\alpha\,(k_i/k_v)\,\overline{P}_{\gamma,eq}}}{3\alpha}}. \tag{B.10}$$

Using (B.7) and (B.8), the averaged RMS voltage magnitude at equilibrium should satisfy the following condition to be stable:

$$\frac{3\sigma\beta}{2}\overline{V}_{eq}^4 - \sigma_\beta \overline{V}_{eq}^2 - k_v k_i \overline{P}_{\gamma,eq} > 0. \tag{B.11}$$

For $\overline{P}_{\gamma,eq} > 0$, the condition (B.11) holds for all $\overline{V}_{eq}$, satisfying the following condition:

$$\overline{V}_{eq} > \sqrt{\frac{\sigma_\beta + \sqrt{\sigma_\beta^2 + 6\alpha\beta k_i k_v \overline{P}_{\gamma,eq}}}{3\alpha\beta}} = k_v \sqrt{\frac{\sigma_\beta + \sqrt{\sigma_\beta^2 + 18(k_i/k_v)\alpha \overline{P}_{\gamma,eq}}}{9\alpha}} =: \overline{V}_{lim}, \tag{B.12}$$

where $\beta = \frac{3\alpha}{k_v^2 \sigma}$ is substituted in (B.12). The stable equilibrium RMS voltage magnitude $\overline{V}_{eq}$ should satisfy the condition in (B.12) for a particular equilibrium power $\overline{P}_{\gamma,eq} < S_{cr}$, where S_{cr} is defined in (5.6). The $\overline{V}_{lim}$ can be bounded by replacing $\overline{P}_{\gamma,eq} = S_{cr}$ in (B.12) as follows:

$$\overline{V}_{lim} < k_v \sqrt{\frac{\sigma_\beta + \sqrt{\sigma_\beta^2 + 3\sigma_\beta^2}}{9\alpha}} = k_v \sqrt{\frac{\sigma_\beta}{3\alpha}} = \overline{V}_{cr}. \tag{B.13}$$

Considering the two possible equilibria (B.9) and (B.10), the $\overline{V}_{eq}^{high} > \overline{V}_{cr}$. Further, from the inequality in (B.13), it follows that $\overline{V}_{eq}^{high} > \overline{V}_{lim}$; hence, establishing the local asymptotic stability of the high voltage solution of averaged RMS voltage magnitude.

References

[1] M. Ali, J. Li, L. Callegaro, H. I. Nurdin, and J. E. Fletcher, "Regulation of active and reactive power of a virtual oscillator controlled inverter," *IET Generation, Transmission & Distribution*, vol. 14, no. 1, pp. 62–69, 2019.

[2] M. Ali, A. Sahoo, H. Nurdin, J. Ravishankar, and J. Fletcher, "On the power sharing dynamics of parallel-connected virtual oscillator-controlled and droop-controlled inverters in an ac microgrid," in *IECON 2019-45th Annual Conference of the IEEE Industrial Electronics Society*, IEEE, vol. 1, 2019, pp. 3931–3936.

[3] S. Chowdhury and P. Crossley, *Microgrids and active distribution networks*. The Institution of Engineering and Technology, London, United Kingdom, 2009.

[4] R. H. Lasseter, "Microgrids," in *Power Engineering Society Winter Meeting, 2002. IEEE*, IEEE, vol. 1, 2002, pp. 305–308.

[5] N. Hatziargyriou, H. Asano, R. Iravani, and C. Marnay, "Microgrids," *IEEE power and energy magazine*, vol. 5, no. 4, pp. 78–94, 2007.

[6] N. Hatziargyriou, *Microgrids: architectures and control*. John Wiley & Sons, West Sussex, United Kingdom, 2014.

[7] N. Pogaku, M. Prodanovic, and T. C. Green, "Modeling, analysis and testing of autonomous operation of an inverter-based microgrid," *IEEE Transactions on power electronics*, vol. 22, no. 2, pp. 613–625, 2007.

[8] K. De Brabandere, B. Bolsens, J. Van den Keybus, *et al.*, "A voltage and frequency droop control method for parallel inverters," *IEEE Transactions on power electronics*, vol. 22, no. 4, pp. 1107–1115, 2007.

[9] J. M. Guerrero, J. C. Vasquez, J. Matas, L. G. De Vicuña, and M. Castilla, "Hierarchical control of droop-controlled ac and dc microgrids—a general approach toward standardization," *IEEE Transactions on industrial electronics*, vol. 58, no. 1, pp. 158–172, 2010.

[10] E. Barklund, N. Pogaku, M. Prodanovic, C. Hernandez-Aramburo, and T. C. Green, "Energy management in autonomous microgrid using stability-

constrained droop control of inverters," *IEEE Transactions on Power Electronics*, vol. 23, no. 5, pp. 2346–2352, 2008.

[11] A. Engler and N. Soultanis, "Droop control in lv-grids," in *Future Power Systems, 2005 International Conference on*, IEEE, 2005, 6–pp.

[12] R. Teodorescu, F. Blaabjerg, M. Liserre, and P. C. Loh, "Proportional-resonant controllers and filters for grid-connected voltage-source converters," *IEE Proceedings-Electric Power Applications*, vol. 153, no. 5, pp. 750–762, 2006.

[13] H. Cha, T.-K. Vu, and J.-E. Kim, "Design and control of proportional-resonant controller based photovoltaic power conditioning system," in *Energy Conversion Congress and Exposition, 2009. ECCE 2009. IEEE*, IEEE, 2009, pp. 2198–2205.

[14] A. V. Timbus, M. Ciobotaru, R. Teodorescu, and F. Blaabjerg, "Adaptive resonant controller for grid-connected converters in distributed power generation systems," in *Applied Power Electronics Conference and Exposition, 2006. APEC'06. Twenty-First Annual IEEE*, IEEE, 2006, 6–pp.

[15] R. Teodorescu, F. Blaabjerg, and M. Liserre, "Proportional-resonant controllers. a new breed of controllers suitable for grid-connected voltage-source converters," *Proc. Optim*, vol. 3, pp. 9–14, 2004.

[16] B. B. Johnson, S. V. Dhople, A. O. Hamadeh, and P. T. Krein, "Synchronization of parallel single-phase inverters with virtual oscillator control," *IEEE Transactions on Power Electronics*, vol. 29, no. 11, pp. 6124–6138, 2014.

[17] B. B. Johnson, S. V. Dhople, J. L. Cale, A. O. Hamadeh, and P. T. Krein, "Oscillator-based inverter control for islanded three-phase microgrids," *IEEE Journal of Photovoltaics*, vol. 4, no. 1, pp. 387–395, 2014.

[18] B. B. Johnson, S. V. Dhople, A. O. Hamadeh, and P. T. Krein, "Synchronization of nonlinear oscillators in an lti electrical power network," *IEEE Transactions on Circuits and Systems I: Regular Papers*, vol. 61, no. 3, pp. 834–844, 2014.

[19] B. B. Johnson, M. Sinha, N. G. Ainsworth, F. Dörfler, and S. V. Dhople, "Synthesizing virtual oscillators to control islanded inverters," *IEEE Transactions on Power Electronics*, vol. 31, no. 8, pp. 6002–6015, 2016.

[20] M. Sinha, F. Dörfler, B. B. Johnson, and S. V. Dhople, "Uncovering droop control laws embedded within the nonlinear dynamics of van der pol oscillators," *IEEE Transactions on Control of Network Systems*, vol. 4, no. 2, pp. 347–358, 2017.

[21] P. Tielens and D. Van Hertem, "The relevance of inertia in power systems," *Renewable and Sustainable Energy Reviews*, vol. 55, pp. 999–1009, 2016.

[22] J. P. Lopes, N. Hatziargyriou, J. Mutale, P. Djapic, and N. Jenkins, "Integrating distributed generation into electric power systems: A review of drivers, challenges and opportunities," *Electric power systems research*, vol. 77, no. 9, pp. 1189–1203, 2007.

[23] R. Shah, N. Mithulananthan, R. Bansal, and V. Ramachandaramurthy, "A review of key power system stability challenges for large-scale pv integration," *Renewable and Sustainable Energy Reviews*, vol. 41, pp. 1423–1436, 2015.

[24] Z. Shuai, Y. Sun, Z. J. Shen, *et al.*, "Microgrid stability: Classification and a review," *Renewable and Sustainable Energy Reviews*, vol. 58, pp. 167–179, 2016.

[25] A. Ulbig, T. S. Borsche, and G. Andersson, "Impact of low rotational inertia on power system stability and operation," *IFAC Proceedings Volumes*, vol. 47, no. 3, pp. 7290–7297, 2014.

[26] E. Bitar, P. P. Khargonekar, and K. Poolla, "Systems and control opportunities in the integration of renewable energy into the smart grid," *IFAC Proceedings Volumes*, vol. 44, no. 1, pp. 4927–4932, 2011.

[27] E. J. Coster, J. M. Myrzik, B. Kruimer, and W. L. Kling, "Integration issues of distributed generation in distribution grids," *Proceedings of the IEEE*, vol. 99, no. 1, pp. 28–39, 2011.

[28] P. Basak, S. Chowdhury, S. H. nee Dey, and S. Chowdhury, "A literature review on integration of distributed energy resources in the perspective of control, protection and stability of microgrid," *Renewable and Sustainable Energy Reviews*, vol. 16, no. 8, pp. 5545–5556, 2012.

[29] R. Majumder, "Some aspects of stability in microgrids," *IEEE Transactions on power systems*, vol. 28, no. 3, pp. 3243–3252, 2013.

[30] S. K. Kaper and N. K. Choudhary, "A review of power management and stability issues in microgrid," in *Power Electronics, Intelligent Control and Energy Systems (ICPEICES), IEEE International Conference on*, IEEE, 2016, pp. 1–6.

[31] M. Ali, H. I. Nurdin, and J. E. Fletcher, "Output power regulation of a virtual oscillator controlled inverter," in *2018 IEEE 18th International Power Electronics and Motion Control Conference (PEMC)*, IEEE, 2018, pp. 1085–1090.

[32] M. Ali, H. I. Nurdin, and J. E. Fletcher, "Simultaneous regulation of active and reactive output power of parallel-connected virtual oscillator controlled inverters," in *IECON 2018-44th Annual Conference of the IEEE Industrial Electronics Society*, IEEE, 2018, pp. 4051–4056.

[33] M. Ali, H. I. Nurdin, and J. Fletcher, "Dispatchable virtual oscillator control for single-phase islanded inverters: Analysis and experiments," *to ap-*

pear in IEEE Transactions on Industrial Electronics, [Online] Available: doi: 10.1109/TIE.2020.2991996.

[34] M. Ali, H. I. Nurdin, and J. E. Fletcher, "Synthesizing averaged virtual oscillator dynamics to control inverters with an output lcl filter," in *accepted in IECON 2020-46th Annual Conference of the IEEE Industrial Electronics Society*, IEEE, 2020.

[35] H. Jiayi, J. Chuanwen, and X. Rong, "A review on distributed energy resources and microgrid," *Renewable and Sustainable Energy Reviews*, vol. 12, no. 9, pp. 2472–2483, 2008.

[36] M. Colombino, D. Groß, and F. Dörfler, "Global phase and voltage synchronization for power inverters: A decentralized consensus-inspired approach," in *2017 IEEE 56th Annual Conference on Decision and Control (CDC)*, IEEE, 2017, pp. 5690–5695.

[37] M. Colombino, D. Groß, J.-S. Brouillon, and F. Dörfler, "Global phase and magnitude synchronization of coupled oscillators with application to the control of grid-forming power inverters," *IEEE Transactions on Automatic Control*, 2019.

[38] J.-S. Brouillon, M. Colombino, D. Groß, and F. Dörfler, "The effect of transmission-line dynamics on a globally synchronizing controller for power inverters," in *2018 European Control Conference (ECC)*, IEEE, 2018, pp. 2242–2247.

[39] D. Groß, M. Colombino, J.-S. Brouillon, and F. Dörfler, "The effect of transmission-line dynamics on grid-forming dispatchable virtual oscillator control," *IEEE Transactions on Control of Network Systems*, vol. 6, no. 3, pp. 1148–1160, 2019.

[40] G.-S. Seo, M. Colombino, I. Subotic, *et al.*, "Dispatchable virtual oscillator control for decentralized inverter-dominated power systems: Analysis and experiments," in *2019 IEEE Applied Power Electronics Conference and Exposition (APEC)*, IEEE, 2019, pp. 561–566.

[41] P. Kundur, N. J. Balu, and M. G. Lauby, *Power system stability and control*. McGraw-hill New York, 1994, vol. 7.

[42] P. Kundur, J. Paserba, V. Ajjarapu, *et al.*, "Definition and classification of power system stability ieee/cigre joint task force on stability terms and definitions," *IEEE transactions on Power Systems*, vol. 19, no. 3, pp. 1387–1401, 2004.

[43] "Rate of change of frequency (rocof) modification to the grid code," The Commision for Energy Regulation, Decision Paper, April 2014. Online Available: www.cer.ie.

[44] B.-I. Craciun, S. Spataru, T. Kerekes, D. Sera, and R. Teodorescu, "Power ramp limitation and frequency support in large scale pvpps without storage,"

in *Photovoltaic Specialists Conference (PVSC), 2013 IEEE 39th*, IEEE, 2013, pp. 2354–2359.

[45] F. Shahnia, A. Ghosh, G. Ledwich, and F. Zare, "Voltage unbalance reduction in low voltage distribution networks with rooftop pvs," in *Power Engineering Conference (AUPEC), 2010 20th Australasian Universities*, IEEE, 2010, pp. 1–5.

[46] A. Ulbig, T. S. Borsche, and G. Andersson, "Impact of low rotational inertia on power system stability and operation," *arXiv preprint arXiv:1312.6435*, 2013.

[47] S. I. Gkavanoudis, K. O. Oureilidis, and C. S. Demoulias, "Fault ride-through capability of a microgrid with wtgs and supercapacitor storage during balanced and unbalanced utility voltage sags," in *Renewable Energy Research and Applications (ICRERA), 2013 International Conference on*, IEEE, 2013, pp. 231–236.

[48] A. Bidram and A. Davoudi, "Hierarchical structure of microgrids control system," *IEEE Transactions on Smart Grid*, vol. 3, no. 4, pp. 1963–1976, 2012.

[49] M. Ramezani, S. Li, and S. Golestan, "Analysis and controller design for stand-alone vsis in synchronous reference frame," *IET Power Electronics*, vol. 10, no. 9, pp. 1003–1012, 2017.

[50] S. M. Silva, B. M. Lopes, R. P. Campana, W. Bosventura, *et al.*, "Performance evaluation of pll algorithms for single-phase grid-connected systems," in *Conference Record of the 2004 IEEE Industry Applications Conference, 2004. 39th IAS Annual Meeting.*, IEEE, vol. 4, 2004, pp. 2259–2263.

[51] L. N. Arruda, S. M. Silva, *et al.*, "Pll structures for utility connected systems," in *Conference Record of the 2001 IEEE Industry Applications Conference. 36th IAS Annual Meeting (Cat. No. 01CH37248)*, IEEE, vol. 4, 2001, pp. 2655–2660.

[52] S. M. Silva, "Wide bandwidth single and three-phase pll structures for utility connected systems," in *Proc. of 9th European Conference on Power Electronics and Applications (EPE 2001), 8*, 2001.

[53] M. Ciobotaru, R. Teodorescu, and F. Blaabjerg, "Improved pll structures for single-phase grid inverters," *Proc. of PELINCEC*, vol. 5, no. 6, 2005.

[54] M. Ciobotaru, R. Teodorescu, and F. Blaabjerg, "A new single-phase pll structure based on second order generalized integrator," in *2006 37th IEEE Power Electronics Specialists Conference*, IEEE, 2006, pp. 1–6.

[55] H. Han, Y. Liu, Y. Sun, M. Su, and J. M. Guerrero, "An improved droop control strategy for reactive power sharing in islanded microgrid," *IEEE Transactions on Power Electronics*, vol. 30, no. 6, pp. 3133–3141, 2015.

[56] C.-L. Chen, Y. Wang, J.-S. Lai, Y.-S. Lee, and D. Martin, "Design of parallel inverters for smooth mode transfer microgrid applications," *IEEE Transactions on Power Electronics*, vol. 25, no. 1, pp. 6–15, 2010.

[57] J. C. Vasquez, J. M. Guerrero, M. Savaghebi, J. Eloy-Garcia, and R. Teodorescu, "Modeling, analysis, and design of stationary-reference-frame droop-controlled parallel three-phase voltage source inverters," *IEEE Transactions on Industrial Electronics*, vol. 60, no. 4, pp. 1271–1280, 2013.

[58] J. W. Simpson-Porco, Q. Shafiee, F. Dörfler, *et al.*, "Secondary frequency and voltage control of islanded microgrids via distributed averaging," *IEEE Transactions on Industrial Electronics*, vol. 62, no. 11, pp. 7025–7038, 2015.

[59] J. W. Simpson-Porco, F. Dörfler, and F. Bullo, "Synchronization and power sharing for droop-controlled inverters in islanded microgrids," *Automatica*, vol. 49, no. 9, pp. 2603–2611, 2013.

[60] A. M. Bouzid, J. M. Guerrero, A. Cheriti, *et al.*, "A survey on control of electric power distributed generation systems for microgrid applications," *Renewable and Sustainable Energy Reviews*, vol. 44, pp. 751–766, 2015.

[61] P. Piagi and R. H. Lasseter, "Autonomous control of microgrids," in *Power Engineering Society General Meeting, 2006. IEEE*, IEEE, 2006, 8–pp.

[62] J. M. Guerrero, L. G. De Vicuna, J. Matas, M. Castilla, and J. Miret, "A wireless controller to enhance dynamic performance of parallel inverters in distributed generation systems," *IEEE Transactions on power electronics*, vol. 19, no. 5, pp. 1205–1213, 2004.

[63] M. C. Chandorkar, D. M. Divan, and R. Adapa, "Control of parallel connected inverters in standalone ac supply systems," *IEEE Transactions on Industry Applications*, vol. 29, no. 1, pp. 136–143, 1993.

[64] C.-T. Lee, C.-C. Chu, and P.-T. Cheng, "A new droop control method for the autonomous operation of distributed energy resource interface converters," *IEEE Transactions on Power Electronics*, vol. 28, no. 4, pp. 1980–1993, 2013.

[65] B. Shoeiby, D. Holmes, B. McGrath, and R. Davoodnezhad, "Dynamics of droop-controlled microgrids with unequal droop response times," in *Power Engineering Conference (AUPEC), 2013 Australasian Universities*, IEEE, 2013, pp. 1–6.

[66] J. M. Guerrero, J. Matas, L. G. de Vicuna, M. Castilla, and J. Miret, "Decentralized control for parallel operation of distributed generation inverters using resistive output impedance," *IEEE Transactions on industrial electronics*, vol. 54, no. 2, pp. 994–1004, 2007.

[67] W. Yao, M. Chen, J. Matas, J. M. Guerrero, and Z.-M. Qian, "Design and analysis of the droop control method for parallel inverters considering the impact of the complex impedance on the power sharing," *IEEE Transactions on Industrial Electronics*, vol. 58, no. 2, pp. 576–588, 2011.

[68] T. L. Vandoorn, B. Meersman, J. D. De Kooning, and L. Vandevelde, "Transition from islanded to grid-connected mode of microgrids with voltage-based droop control," *IEEE transactions on power systems*, vol. 28, no. 3, pp. 2545–2553, 2013.

[69] J. C. Vasquez, J. M. Guerrero, A. Luna, P. Rodriguez, and R. Teodorescu, "Adaptive droop control applied to voltage-source inverters operating in grid-connected and islanded modes," *IEEE transactions on industrial electronics*, vol. 56, no. 10, pp. 4088–4096, 2009.

[70] B. Shoeiby, R. Davoodnezhad, D. Holmes, and B. McGrath, "Voltage-frequency control of an islanded microgrid using the intrinsic droop characteristics of resonant current regulators," in *Energy Conversion Congress and Exposition (ECCE), 2014 IEEE*, IEEE, 2014, pp. 68–75.

[71] B. Shoeiby, R. Davoodnezhad, D. Holmes, and B. McGrath, "A new current control droop strategy for vsi-based islanded microgrids," in *Power Electronics Conference (IPEC-Hiroshima 2014-ECCE-ASIA), 2014 International*, IEEE, 2014, pp. 1482–1489.

[72] B. Shoeiby, R. Davoodnezhad, D. Holmes, and B. McGrath, "A resonant current regulator based microgrid control strategy with smooth transition between islanded and grid-connected modes," in *Power Electronics for Distributed Generation Systems (PEDG), 2014 IEEE 5th International Symposium on*, IEEE, 2014, pp. 1–8.

[73] A. Vidal, F. D. Freijedo, A. G. Yepes, *et al.*, "Assessment and optimization of the transient response of proportional-resonant current controllers for distributed power generation systems," *IEEE Transactions on Industrial Electronics*, vol. 60, no. 4, pp. 1367–1383, 2013.

[74] B. Shoeiby, "Current regulator based control strategy for islanded and grid-connected microgrids," *PhD Thesis, RMIT Australia*, 2015.

[75] D. Holmes, T. Lipo, B. McGrath, and W. Kong, "Optimized design of stationary frame three phase ac current regulators," *IEEE Transactions on Power Electronics*, vol. 24, no. 11, pp. 2417–2426, 2009.

[76] B. B. Johnson, M. Sinha, N. G. Ainsworth, F. Dörfler, and S. V. Dhople, "Synthesizing virtual oscillators to control islanded inverters," *IEEE Transactions on Power Electronics*, vol. 31, no. 8, pp. 6002–6015, 2016.

[77] M. Sinha, F. Dorfler, B. Johnson, and S. Dhople, "Uncovering droop control laws embedded within the nonlinear dynamics of van der pol oscillators," *IEEE Transactions on Control of Network Systems*, 2015.

[78] M. Sinha, F. Dörfler, B. B. Johnson, and S. V. Dhople, "Virtual oscillator control subsumes droop control," in *American Control Conference (ACC), 2015*, IEEE, 2015, pp. 2353–2358.

[79] S. V. Dhople, B. B. Johnson, and A. O. Hamadeh, "Virtual oscillator control for voltage source inverters," in *Communication, Control, and Computing (Allerton), 2013 51st Annual Allerton Conference on*, IEEE, 2013, pp. 1359–1363.

[80] A. Rosse, R. Denis, and C. Zakhour, "Control of parallel inverters using nonlinear oscillators with virtual output impedance," in *Power Electronics and Applications (EPE'16 ECCE Europe), 2016 18th European Conference on*, IEEE, 2016, pp. 1–10.

[81] H. K. Khalil and J. Grizzle, "Nonlinear systems, vol. 3," *Prentice hall Upper Saddle River*, 2002.

[82] M. Awal and I. Husain, "Unified virtual oscillator control for grid-forming and grid-following converters," *arXiv preprint arXiv:2007.06042*, 2020.

[83] G.-S. Seo, M. Colombino, I. Subotić, *et al.*, "Dispatchable virtual oscillator control for decentralized inverter-dominated power systems: Analysis and experiments," *arXiv preprint arXiv:1811.08842*, 2018.

[84] M. Lu, S. Dutta, V. Purba, S. Dhople, and B. Johnson, "A grid-compatible virtual oscillator controller: Analysis and design," in *2019 IEEE Energy Conversion Congress and Exposition (ECCE)*, IEEE, 2019, pp. 2643–2649.

[85] M. Awal, H. Yu, H. Tu, S. M. Lukic, and I. Husain, "Hierarchical control for virtual oscillator based grid-connected and islanded microgrids," *IEEE Transactions on Power Electronics*, vol. 35, no. 1, pp. 988–1001, 2019.

[86] M. Awal, H. Yu, I. Husain, W. Yu, and S. M. Lukic, "Selective harmonic current rejection for virtual oscillator controlled grid-forming voltage source converters," *IEEE Transactions on Power Electronics*, vol. 35, no. 8, pp. 8805–8818, 2020.

[87] H. Yu, M. Awal, H. Tu, *et al.*, "A virtual impedance scheme for voltage harmonics suppression in virtual oscillator controlled islanded microgrids," in *2020 IEEE Applied Power Electronics Conference and Exposition (APEC)*, IEEE, 2020, pp. 609–615.

[88] H. Yu, M. Awal, H. Tu, I. Husain, and S. Lukic, "Comparative transient stability assessment of droop and dispatchable virtual oscillator controlled grid-connected inverters," *IEEE Transactions on Power Electronics*, 2020.

[89] D. Raisz, T. T. Thai, and A. Monti, "Power control of virtual oscillator controlled inverters in grid-connected mode," *IEEE Transactions on Power Electronics*, 2018.

[90] Z. Shi, J. Li, H. I. Nurdin, and J. E. Fletcher, "Comparison of virtual oscillator and droop controlled islanded three-phase microgrids," *IEEE Transactions on Energy Conversion*, vol. 34, no. 4, pp. 1769–1780, 2019.

[91] Z. Shi, H. I. Nurdin, J. E. Fletcher, and J. Li, "Similarities between virtual oscillator controlled and droop controlled three-phase inverters," in *2018 IEEE 18th International Power Electronics and Motion Control Conference (PEMC)*, IEEE, 2018, pp. 434–439.

[92] Z. Shi, J. Li, H. I. Nurdin, and J. E. Fletcher, "Transient response comparison of virtual oscillator controlled and droop controlled three-phase inverters under load changes," *IET Generation, Transmission & Distribution*, vol. 14, no. 6, pp. 1138–1147, 2020.

[93] T. H. Summers, C. Yu, S. Dasgupta, and B. D. Anderson, "Control of minimally persistent leader-remote-follower and coleader formations in the plane," *IEEE Transactions on Automatic Control*, vol. 56, no. 12, pp. 2778–2792, 2011.

[94] J. Carr, *Applications of centre manifold theory*. Springer Science & Business Media, 2012, vol. 35.

[95] S. Sastry, *Nonlinear systems: analysis, stability, and control*. Springer Science & Business Media, 2013, vol. 10.

[96] S. Wiggins, *Introduction to applied nonlinear dynamical systems and chaos*. Springer Science & Business Media, 2003, vol. 2.

[97] H. I. Nurdin, "Stability analysis of the sinusoidal orbits of a nonlinear proportional and resonant current regulator for islanded microgrids," in *2019 Australian & New Zealand Control Conference (ANZCC)*, IEEE, 2019, pp. 42–47.

[98] K. J. Palmer, "Linearization near an integral manifold," *J. Math. Anal. Appl.*, vol. 51, pp. 243–255, 1975.

[99] A. Papachristodoulou and S. Prajna, "A tutorial on sum of squares techniques for systems analysis," in *American Control Conference, 2005. Proceedings of the 2005*, IEEE, 2005, pp. 2686–2700.

[100] A. Papachristodoulou and S. Prajna, "On the construction of lyapunov functions using the sum of squares decomposition," in *Decision and Control, 2002, Proceedings of the 41st IEEE Conference on*, IEEE, vol. 3, 2002, pp. 3482–3487.

[101] N. W. Bauer, P. J. Maas, and W. Heemels, "Stability analysis of networked control systems: A sum of squares approach," *Automatica*, vol. 48, no. 8, pp. 1514–1524, 2012.

[102] S. Boyd, L. El Ghaoui, E. Feron, and V. Balakrishnan, *Linear matrix inequalities in system and control theory*. SIAM, 1994, vol. 15.

[103] B. Stott and O. Alsac, "Fast decoupled load flow," *IEEE transactions on power apparatus and systems*, no. 3, pp. 859–869, 1974.

[104] R. A. Van Amerongen, "A general-purpose version of the fast decoupled load flow," *IEEE Transactions on Power Systems*, vol. 4, no. 2, pp. 760–770, 1989.

[105] F. Wu and S. Kumagai, "Steady-state security regions of power systems," *IEEE Transactions on Circuits and Systems*, vol. 29, no. 11, pp. 703–711, 1982.

[106] S. Bolognani and S. Zampieri, "On the existence and linear approximation of the power flow solution in power distribution networks," *IEEE Transactions on Power Systems*, vol. 31, no. 1, pp. 163–172, 2016.

[107] B. C. Lesieutre, P. W. Sauer, and M. Pai, "Existence of solutions for the network/load equations in power systems," *IEEE Transactions on Circuits and Systems I: Fundamental Theory and Applications*, vol. 46, no. 8, pp. 1003–1011, 1999.

[108] M. IliC, "Network theoretic conditions for existence and uniqueness of steady state solutions to electric power circuits," in *[Proceedings] 1992 IEEE International Symposium on Circuits and Systems*, IEEE, vol. 6, 1992, pp. 2821–2828.

[109] H.-D. Chiang and M. E. Baran, "On the existence and uniqueness of load flow solution for radial distribution power networks," *IEEE Transactions on Circuits and Systems*, vol. 37, no. 3, pp. 410–416, 1990.

[110] D. K. Molzahn, B. C. Lesieutre, and C. L. DeMarco, "A sufficient condition for power flow insolvability with applications to voltage stability margins," *IEEE Transactions on Power Systems*, vol. 28, no. 3, pp. 2592–2601, 2013.

[111] X. Wu, C. Shen, M. Zhao, Z. Wang, and X. Huang, "Small signal security region of droop coefficients in autonomous microgrids," in *2014 IEEE PES General Meeting| Conference & Exposition*, IEEE, 2014, pp. 1–5.

[112] J. A. Mueller and J. W. Kimball, "An efficient method of determining operating points of droop-controlled microgrids," *IEEE Transactions on Energy Conversion*, vol. 32, no. 4, pp. 1432–1446, 2017.

[113] L. Wang, S. Chai, D. Yoo, L. Gan, and K. Ng, *PID and predictive control of electrical drives and power converters using MATLAB/Simulink*. John Wiley & Sons, Singapore, 2015.

[114] J. D. Glover, M. S. Sarma, and T. Overbye, *Power System Analysis & Design, SI Version*. Cengage Learning, Stamford, USA, 2012.

[115] M. Liserre, F. Blaabjerg, and A. Dell'Aquila, "Step-by-step design procedure for a grid-connected three-phase pwm voltage source converter," *International journal of electronics*, vol. 91, no. 8, pp. 445–460, 2004.

[116] P. Channegowda and V. John, "Filter optimization for grid interactive voltage source inverters," *IEEE Transactions on Industrial Electronics*, vol. 57, no. 12, pp. 4106–4114, 2010.

[117] Y. Tang, P. C. Loh, P. Wang, *et al.*, "Generalized design of high performance shunt active power filter with output lcl filter," *IEEE Transactions on Industrial Electronics*, vol. 59, no. 3, pp. 1443–1452, 2012.

[118] N. Mohan, T. M. Undeland, and W. P. Robbins, *Power electronics: converters, applications, and design*. John wiley & sons, USA, 2003.

[119] M. Lu, G.-S. Seo, M. Sinha, *et al.*, "Adaptation of commercial current-controlled inverters for operation with virtual oscillator control," in *2019 IEEE Applied Power Electronics Conference and Exposition (APEC)*, IEEE, 2019, pp. 3427–3432.

[120] B. B. Johnson, S. V. Dhople, J. L. Cale, A. O. Hamadeh, and P. T. Krein, "Oscillator-based inverter control for islanded three-phase microgrids," *IEEE Journal of Photovoltaics*, vol. 4, no. 1, pp. 387–395, 2013.

[121] A. Tayyebi, D. Groß, A. Anta, F. Kupzog, and F. Dörfler, "Interactions of grid-forming power converters and synchronous machines–a comparative study," *arXiv preprint arXiv:1902.10750*, 2019.

[122] H. Han, X. Hou, J. Yang, *et al.*, "Review of power sharing control strategies for islanding operation of ac microgrids," *IEEE Transactions on Smart Grid*, vol. 7, no. 1, pp. 200–215, 2015.

[123] A. Sahoo, M. Ciobotaru, and J. Ravishankar, "A novel communication-less frequency restoration technique in droop controlled inverter-based islanded ac microgrid," in *2018 IEEE International Conference on Power Electronics, Drives and Energy Systems (PEDES)*, IEEE, 2018, pp. 1–6.

[124] Q.-C. Zhong, "Robust droop controller for accurate proportional load sharing among inverters operated in parallel," *IEEE Transactions on Industrial Electronics*, vol. 60, no. 4, pp. 1281–1290, 2011.

[125] J. Yan, C.-C. Liu, and U. Vaidya, "A pmu-based monitoring scheme for rotor angle stability," in *2012 IEEE Power and Energy Society General Meeting*, IEEE, 2012, pp. 1–5.

[126] S. Dasgupta, M. Paramasivam, U. Vaidya, and V. Ajjarapu, "Real-time monitoring of short-term voltage stability using pmu data," *IEEE Transactions on Power Systems*, vol. 28, no. 4, pp. 3702–3711, 2013.

[127] H. Choi and S. Bose, "Transient stability analysis of power systems using koopman operators," Online Available: http://boses.ece.illinois.edu/files/TSKoopman.pdf.

[128] Y. Susuki and I. Mezić, "Nonlinear koopman modes and power system stability assessment without models," *IEEE Transactions on Power Systems*, vol. 29, no. 2, pp. 899–907, 2013.

[129] E. Yeung, S. Kundu, and N. Hodas, "Learning deep neural network representations for koopman operators of nonlinear dynamical systems," in *2019 American Control Conference (ACC)*, IEEE, 2019, pp. 4832–4839.